Università degli Studi di Torino

Scuola di Dottorato in

Scienze della Natura e Tecnologie Innovative

Dottorato in Scienze Farmaceutiche e Biomolecolari (XXX ciclo)

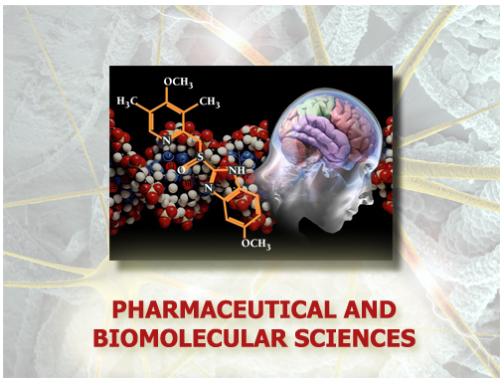

Synthesis, characterization and structure-property relationship of molecular and supramolecular systems for sonodynamic therapy applications

Candidata: Federica Bosca Tutor: Alessandro Barge

Università degli Studi di Torino

Dottorato in
Scienze Farmaceutiche e Biomolecolari

Tesi svolta presso il
Dipartimento di Scienza e Tecnologia del Farmaco

CICLO: XXX

TITOLO DELLA TESI: Synthesis, characterization and structure-property relationship of molecular and supramolecular systems for sonodynamic therapy applications

TESI PRESENTATA DA: Federica Bosca

TUTOR: Alessandro Barge

COORDINATORE DEL DOTTORATO: Gianmario Martra

ANNI ACCADEMICI: 2014 - 2017

SETTORE SCIENTIFICO-DISCIPLINARE DI AFFERENZA*: CHIM/06

Sommario

With deepest gratitude,

ABSTRACT

Sonodynamic therapy (SDT) is an alternative strategy in cancer treatment via the generation of cytotoxic factors during ultrasound-activation of sono-sensitive agents [1]. SDT is based on Photodynamic therapy (PDT) concept. The real molecular mechanism involved in SDT is still unknown, but several hypotheses about possible series of events involved are described in literature[1-2]. In PDT treatment, a given molecule, called "photosensitizer", after light irradiation, is able, during its decay process, to produce oxygen radical species (ROS). Radical species, in turn, result in cell death. The difference between PDT and SDT concerns mainly in the excitation energy source: light (used in PDT) is replaced with ultrasound (US). Hence, SDT approach exploits the thermal effect induced by inertial acoustic cavitation (obtained by ultrasound or shock-waves irradiation) to excite molecules. During the inertial acoustic cavitation, due to the pressure waves, air gas microbubbles are generated, grown in volume, then they violently implode producing "hot spots", characterized by extremely high temperature and pressure in the surrounding, without affecting bulk temperature and pressure. These harsh conditions promote some physico-chemical changes (including thermal excitation) in the next surrounding[3-4]. As it has been touched upon, the SDT requires the contemporary presence of inertial cavitation event, specific molecules able to be excited and oxygen, to produce ROS. Several studies indicate as good candidates for this purpose porphyrins[5-7]. Even macrocyclic tetrapyrrolic structure of natural origin (such as chlorophyll) is considered as an easier source of sensitizing molecules. PDT shows great results in anticancer treatment[8-9], but it possesses two main limitations: low tissue penetration, because of the light as excitation source, and skin photosensitivity after treatment. The first limitation might be overcome by SDT (ultrasounds penetrate more deeply into tissues than light), but skin photosensitivity requires an in-depth study. This research work aims to increase the sonodynamic efficacy, facilitating the inertial cavitation phenomenon, in order to reduce the sonosensitizer dose and limit in this way the skin photo-damage. For this reason, we produce heterogeneous systems combining strategic nanocarriers with porphyrin molecules. Basically, the strategic nanocarrier, because it is a solid dispersed in an aqueous solution, possess the ability in reducing the cavitation threshold on its surface, then if the porphyrin molecule is close enough, the probability to excite it could be increased. So, we need to synthetize *ah-hoc* porphyrin molecules and to link them onto strategic nanosystems.

Graphene, Single Walled Carbon nanotubes (SWCNTs), Solid Lipid Nanoparticles (SLNs), liposomes and nanobubbles (NBs) were considered. We started from carbon based nanosurfaces moving through more biocompatible nanocarriers (liposomes, nanobubbles, SLNs). Among all nanosystems, NB was chosen also because of its ability to act as US contrast agent, so we can obtain a new theranostic agent, combining a real-time SDT with imaging monitoring, enabling future theranostic application based on SDT. NBs particles, indeed, due to their composition and morphology, can act as cavitation nuclei[10]. Changing in nanosystem structure and composition, we can achieve advantages in different fields. Graphene and SWCNTs (carbon based nanomaterials) possess black and rigid surfaces, so they are able to absorb light and to facilitate inertial cavitation. Moreover, porphyrin grafted SWCNT are well-known to promote the electron transfer phenomenon to stabilize the separation charge state (thanks to the extended aromatic surface). In vitro tests are carried out on tumor cell lines (HT-29, LS174 T, PC-3) demonstrating that those obtained hybrid porphyrin-based nanosystems possess all features to make them an efficient model for sonodynamic application in anticancer treatment.

1. INTRODUCTION

Cancer is one of the most important cause of death in economically developed and developing countries[11]. Despite great success with traditional techniques for cancer treatment, the development of new more efficient therapies still remains a challenge. Even if surgery, chemotherapy and radiation therapy are nowadays the major treatment of choice in most human cancers, they suffer from different shortcomings, i.e. system toxicity, low selectivity, drug resistance and potential long-term side effects. Moreover, surgery cannot cure the metastasized tumor; chemotherapy and radiotherapy can effectively kill cancer cells slightly damaging normal tissues. In addition, immunotherapy, an innovative treatment on cancers, is very expensive[12] and the treatment success is not guaranteed successful for all patients undergoing the same immunotherapy . Hence, the development of a highly selective, secure, low cost and minimally invasive anticancer approach is still needed. Recently, an innovative approach, the photodynamic therapy (PDT) has been successfully applied to some tumors (solid tumor). It is based on light irradiation of a pretreated cancer tissue but, because of the low penetration of light, it can be used only to treat superficial tumors. This major shortcoming can be overcome by sonodynamic therapy (SDT), a technique similar to PDT which uses ultrasound waves instead of light to irradiate tumor cells.

1.1 SONODYNAMIC THERAPY VS PHOTODYNAMIC THERAPY

Sonodynamic therapy is a novel, promising, low invasive treatment, which is based on the clinical approved PDT approach. PDT is described as dynamic interaction involving light, photosensitizing agent and oxygen. Upon light excitation, the photosensitizing agent (PS) is promoted from its ground state (S0) to the excited singlet states (S1, S2, …). After internal conversion, the excited sensitizer evolves from S1 level to the more stable T1. Then, to return to the ground state, it can interact with oxygen or with other substrates generating reactive oxygen species (ROS) which initiate the cell death process[12]. When the activated sensitizer directly reacts with surrounding molecules, it changes these molecules to radicals, then they further react to oxygen to produce reactive oxygen species (pathway labelled “type 1” in figure 1). Alternatively, the excited sensitizer can directly interact with oxygen (in its triplet state) transferring the energy and promoting it to its singlet state (pathway labelled “type 2” in figure 1), a highly reactive oxygen species.

Both reactions can occur simultaneously, and the ratio between these processes depends on the type of PS used and on the concentrations of substrate and oxygen. ROS thus produced kill cells by apoptotic and/or necrotic pathway[13].

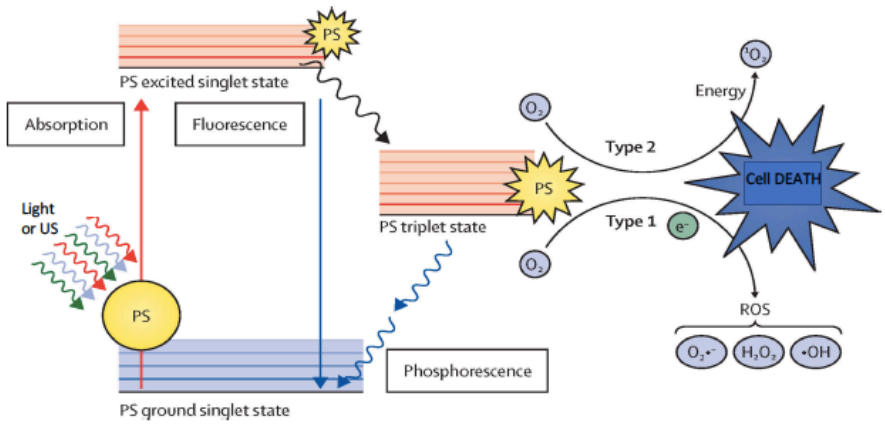

Figure 1. Mechanism of PDT (if light is used as excitation source)/SDT (if US are used as excitation source) action.

PDT has been clinically applied to different types of cancer, including lung, colon and bladder cancer[14-15]. Despite the positive achievements of PDT in clinical application, at least two shortcomings need to be overcome: limited penetration of light into deep tumor tissue (necessary to activate the sensitizer) and a serious side effect, namely skin photosensitivity, due to the retention of the sensitizer in superficial tissue. For this reason, after the administration of the photosensitizer, patients must avoid direct sunlight exposition for several weeks[11]. The use of different energy source than light, to excite the sensitizer, could allow to reach deep tumor and to limit skin photosensitivity. SDT approach has been then proposed as promising, novel strategy to manage solid tumors.

The mechanism of SDT cytotoxicity seems to be very similar to that exploited by PDT. The only difference consists in the sensitizer activation step which is based on acoustic cavitation in the case of SDT. Yumita et al[16] were the first, in 1989, to observe that several hematoporphyrin (HP) derivatives, commonly used in PDT, are also able to induce significant cell damage when they are activated by ultrasound.

Upon US irradiation, inertial acoustic cavitation occurs. The pressure waves generate gas bubbles which grow to a near resonance size and expand to a maximum before collapsing violently. These implosion conditions allow the surrounding microenvironment to reach temperature values up to 10000 K and pressure of 81 MPa (800 atm)[12] . That incredible local heating (hot spot) is enough to thermally excite the sonosensitizer and generate ROS. Singlet oxygen species seems to be the predominant mediator in SDT. In general, highly reactive agents can oxidize surrounding substrates. Once the concentration of singlet molecular oxygen is sufficient, cells will involve in a series of biological events, such as the loss of mitochondrial membrane potential, cytoskeletal shrinkage, membrane damage, and DNA fragmentation[17]. All these physiological responses are ultimately turned into cell death signals. In addition to singlet oxygen, various other free radicals like hydrogen peroxides and superoxide anion radicals can also induce cell damage or apoptosis through chain reaction mechanisms of lipid peroxidation[17].

1.2 ROS DAMAGE

As previously anticipated, the excited sensitizer molecule (in its triplet state, ^3S) can evolve following two concomitant reaction pathways[14, 18] (Figure 2). Pathway type 1 is the reaction between the excited sensitizer (^3S) and biological substrates (A) (such as molecules forming the cell membrane or other molecules inside cell) to give a radical anion or radical cation. These radical ions interact with oxygen to produce oxidized products (Eqn1, Figure 2) which are toxic for cells. Superoxide anion ($O_2^{\bullet -}$) can be generated by electron transfer from the triplet PS state to molecular oxygen (Eqn1*a,* Figure 3). This way seems to be mainly involved.

$$^3S + A \longrightarrow S^{-\bullet} + A^{+\bullet}$$
$$A^{+\bullet} + {}^3O_2 \longrightarrow A_{ox}$$

Figure 2. Equation 1 repots an example of mechanism involved in reaction type 1, ^3S is the excited sensitizer and A is the biological substrates.

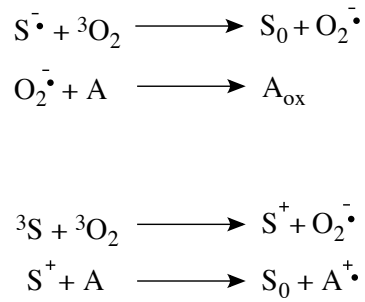

Figure 3. Equation 1*a* reports two possible mechanisms involved in reaction type 1, the excited sensitizer S^- as a radical specie or as excited sensitizer ^3S can interact with O_2 in the triple state.

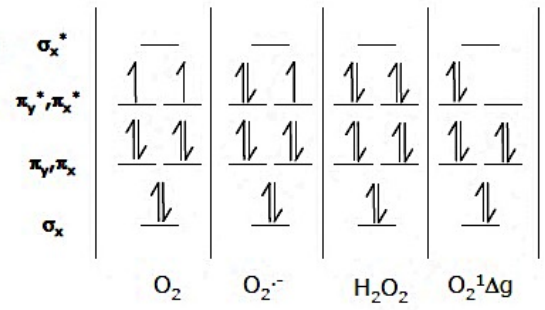

Figure 4. Molecular orbital diagram of oxygen showing the electron distribution of oxygen species.

Superoxide anion ($O_2^{\bullet -}$, Figure 4), is not particularly reactive in biological systems and does not cause, by itself, significant oxidative damage. However, it can react with itself, through a dismutation reaction catalyzed by the superoxide dismutase enzyme (SOD), producing hydrogen peroxide and oxygen. Hydrogen peroxide is important in biological systems since it pass through cell membranes and it cannot be excluded from cells. Hydrogen peroxide is actually necessary to allow many enzymes exerting their function and thus it is required (like oxygen itself) for health. Superoxide anion plays an important role also in the production of the highly reactive hydroxyl radical ($HO^{\bullet}$). In this process, superoxide reduces metal ions (such as ferric iron or Fe^{3+}) which act as catalyst in the conversion reaction from hydrogen peroxide (H_2O_2, Figure 4) to hydroxyl radical ($HO^{\bullet}$). Like hydrogen peroxide, hydroxyl radical ($HO^{\bullet}$) easily passes through cell membranes and cannot be kept out of cells. This highly reactive radical can modify organic substrates, for example fatty acid or other lipids. The hydroxyl radical can also oxidize the organic substrates, that in turn can react with other molecules in a chain reaction.

Via reaction pathway type 2 (Figure 5), mainly singlet oxygen ($^1O_2$, see Figure 4 for molecular orbital diagram) is generated by interaction between the excited sensitizer (in its triplet state) and oxygen (also in its triplet state).

$$^3S + {}^3O_2 \longrightarrow S_0 + {}^1O_2$$
$$A + {}^1O_2 \longrightarrow A_{ox}$$

Figure 5. Equation 2 mechanism involved in reaction type 2.

Independent of the kind of photosensitizer used for PDT or SDT, the efficiency of the treatment is oxygen dependent. All produced ROS are oxidizing agents that can directly react with many biological molecules: amino acid residues in proteins, unsaturated molecules and DNA are the main targets. Since ROS half-life is very short (<40 ns) in order to cause damage, it is necessary, that target molecule or structure are proximal to the area of ROS production.

1.3 ULTRASOUND WAVES

Sonodynamic Therapy approach uses, as energy source to excite the sensitizer, ultrasonic waves. Ultrasounds are mechanical (pressure) waves, characterized by succession of negative and positive pressure peaks with frequencies higher than the audible ones for the human ear (>20 KHz). Ultrasound can be modulated by *frequency* (measured in Hz) and *intensity* (measured in W/cm^2). Frequency directly acts on the wave penetration into the selected medium and also on the cavitation intensity/efficiency, whereas the ultrasound intensity plays a role in the amount of energy delivered to the desired location[19]. When ultrasonic waves are applied to imaging techniques their frequency needs to be carefully considered. Inertial cavitation has to be avoided during imaging acquisition, then frequency has to be higher enough to prevent this phenomenon. Furthermore, frequency is directly proportional to spatial resolution and inversely correlated to the wave penetration (see Figure 6).

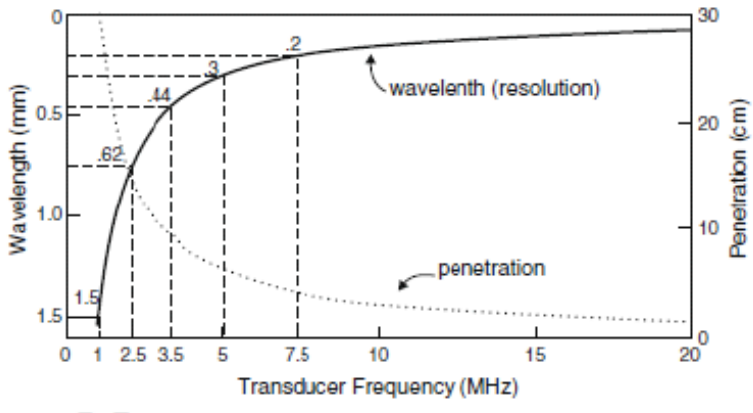

Figure. 6. Behavior of penetration depth and spatial resolution (correlated to the wavelength) as a function of ultrasound frequency[19].

Ultrasound can be classified, on the base of their intensity, in low intensity ultrasound, when the intensity range is between 0.125 and 3 W/cm^2 and high when this value is higher than 3 W/cm^2. High intensity US can induce irreversible biological changes in tissue. Furthermore, ultrasonic waves can be focused or non-focused: non-focused US are typically used in diagnosis, whereas focused US are use in clinical treatment of some pathologies (HIFU – High Intensity Focalized Ultrasounds). Diagnostic ultrasound refers to the imaging of a region of a human or animal body using an ultrasound transducer to generate and receive ultrasonic waves. The transducer addresses US to the target region, then the different tissues reflect in different way the ultrasonic waves which are collected by the same transducer. The electrical signal produced is then elaborated to give a diagnostic image.

Generally, high definition images are obtained using high frequency, with low energy ultrasonic waves. The use of suitable contrast agents can increase the diagnostic power of this technique. US imaging is featured with real-time observation, very low invasiveness, high efficiency, low cost and high safety. Ultrasound has also been used in various therapeutic applications[20] such as hyperthermia (US thermal effects). Hyperthermia involves the insonation of a targeted tumor tissue with focused ultrasonic waves. The acoustic waves are absorbed by tissue and converted in thermal energy. The tissue heating results in a retardation mass growth due to denaturation of proteins, break-down of tumor vasculature and rapid necrosis. HIFU technique is usually exploited for this purpose in clinics; it is able to act on tumor tissue limiting the damage on the surrounding normal one. The target tissue can reach locally temperature up to 80 °C.

Mechanical effects: cavitation

Besides the US irradiation thermal effect, exerted for instance by HIFU, another important US phenomenon that has to be considered is the cavitation. Cavitation occurs when pressure change in a short time by consequence of ultrasound irradiation; it results in the formation of microscopic gas bubbles in fluid bulk. Then bubbles grow until they reach their resonance size and linearly oscillate around this equilibrium diameter. This is called "stable" or "non-inertial cavitation". When the size oscillation is not linear and stable, bubbles are going to collapse violent, with local increasing in pressure and temperature (hot spot). This second phenomenon is called "inertial cavitation".

Usually, the cavitation occurrence probability increases as negative pressure peak increases and it is inversely proportional to US frequency. The selection between the two types of cavitation depends on the local conditions[11, 21]. The most important parameters are frequency, negative pressure peaks, surface tension and the presence of bubbles or cavitation nuclei (and their size) in solution. Cavitation nuclei are usually constituted by heterogeneous phases (gas encapsulated in lipid or polymeric shells, solid micro/nano-particles) present in liquid bulk; they facilitate the transition phase of liquid, lowering in this way the cavitation threshold[21].

1.4 SENSITIZERS

The most explored sonosensitizers (both for photo- and sono-dynamic treatment, since the physico-chemical mechanism involved is very similar) are based on organic molecules whose excited triplet state is accessible (phosphorescent molecules). Among all possible organic molecules, porphyrins are particularly interesting; they were the first derivatives considered in PDT approach and they are identified as first generation of sensitizing agents. Hematoporphyrin (Hp), Photofrin and hematoporphyrin monomethyl ether (HMME) represented in figure 7 are an example of these generation of sensitizing agents[14, 22-23]; some of them are approved in clinic for PDT anticancer treatment[24-25-26].

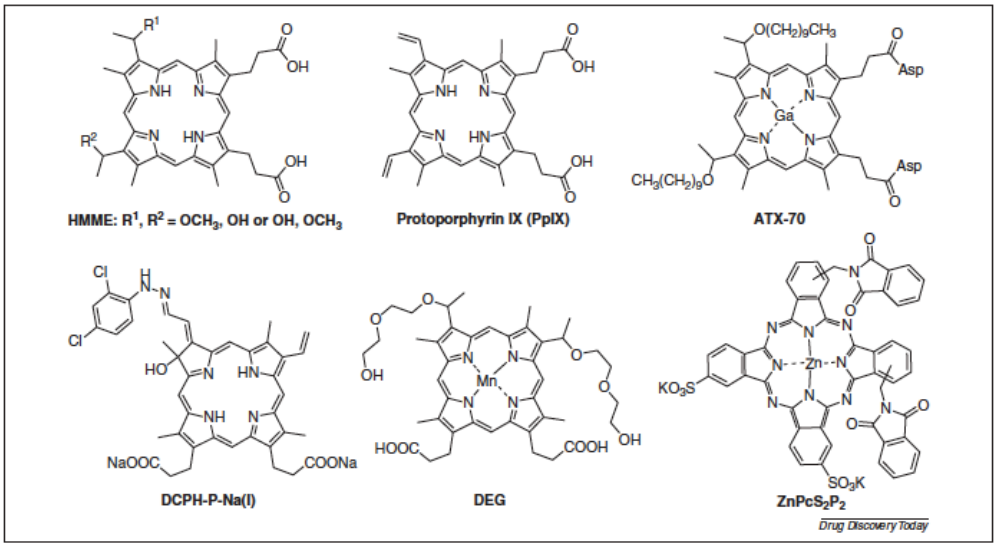

Figure 7. Chemical structures of first generation of porphyrin derivatives: hematoporphyrin monomethyl ether (HMME), protoporphyrin IX (PpIX), ATX-70, DCPH-P-Na(I), DEG and $ZnPcS_2P_2$.

Photofrin® (Porfimer sodium, Figure 8) and Foscan® (Temoporfin, meso-tetra (hydroxyphenyl)porphyrin, Figure 9) are two of the porphyrin based molecules approved for systemic administration; ALA (aminolevulinic acid) and methyl-aminolevulinate (Figure 10), which are porphyrin precursors (they will be converted into porphyrin inside cells), have been approved for topical use. All Porphyrin derivatives are characterized by a typical UV-Vis absorption profile consisting in a strong Soret band around 400nm and a series of weaker satellite, called "Q bands", between 600 and 800nm. Q bands are normally selected to excite the sensitizer in PDT treatment. Another important feature of these compounds is the absence of cellular-toxicity when they are not subjected to proper stimulus (light or US). Their toxicity can be triggered by a suitable external energy source and it is confined in the energy application region.[27]. The cytotoxic species, indeed, are not the sensitizers themselves, but ROS produced during their relaxation period. The interaction between sensitizing molecules (porphyrins) and a specific receptor or cellular epitope is not necessary, as usually occurs with "classical" drugs.

1.4.1 FIRST GENERATION OF PHOTOSENSITIZERS

As previously mentioned, the first generation of photosensitizers class includes different porphyrin molecules, porphyrin-like molecules and porphyrin precursor molecules. Photofrin® is one of the most famous members of this class (Figure 8). It has been approved for use as PDT photosensitizer in advanced and early-stage lung cancers, superficial gastric cancer, esophageal adenocarcinoma, cervical cancer, and bladder cancer and has been used in clinical trials for many other pathologies i.e. for ophthalmology, cardiovascular diseases, dermatology (psoriasis and scleroderma) and rheumatology[28]. Its clinical history covers more than 20 years and the PDT advantages clearly emerged: effective tumors destruction, non-toxicity in the absence of light, easy formulation for intravenous administration, possibility of multiple treatments for patients. However, some problems remains to overcome, first of all skin photosensitivity which required protection from light between drug administration and irradiation (48-72 h)[25]. Important research efforts have been done to identify new, more suitable molecules with improved sensitizing properties.

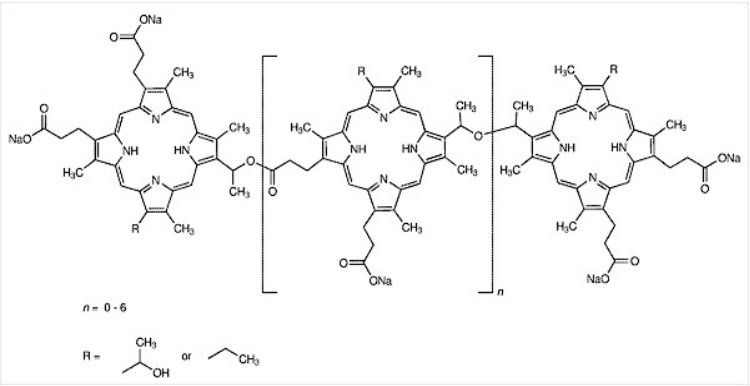

Figure 8. Chemical structure of Photofrin®.

1.4.2 SECOND GENERATION OF PHOTOSENSITIZERS

One of the possible strategies adoptable to reduce the skin photosensitivity concerns the improvement of tumor cells accumulation of porphyrin. And concerning the light penetration shortcoming, the use of electromagnetic radiation with higher wavelength (red region) is necessary. These two goals can be achieved by suitable modifying the porphyrin structure, obtaining the second generation of sensitizers[29 30].

This class includes Foscan®, Verteporfin®, Levulan®, Metvix® and other similar compounds. Foscan® (Tetra(m-hydroxyphenyl) chlorin, mTHPC, in Fig 9) was approved in Europe in 2001 for palliative treatment of head and neck cancer. Among all tetrahydroxyphenyl analogues it is the most active photosensitizer. Verteporfin® (a benzoporphyrin derivative) was approved in Canada in 1999 and later in USA, for PDT treatment and detection of cancer and pre-cancerous lesions in ophthalmology. This treatment strategy, in cardiovascular diseases, dermatology and rheumatology[14], is still under investigation in clinical trials. Most of second generation derivatives possess higher selectivity for tumor tissue than Photofrin®, with consequent higher tumor accumulation and lower skin distribution. The lower drug dose and light intensity required, allow to better damage the tumor mass limiting the adverse effect such as skin photosensitivity.

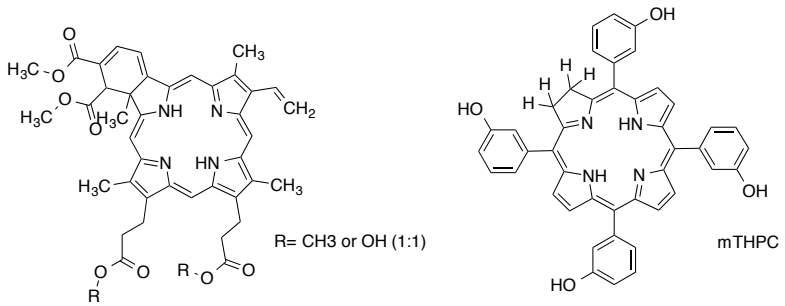

Figure 9. Chemical structure of Temoporfin® (Foscan® right side) and Verteporfin® (left side).

Photosensitizers already approved in clinic are Levulan® (Aminolevulinic acid or ALA, Figure 11), which is licensed in the USA for topical application as a solution and Metvix® (Methyl aminolevulinate, ALA-methyl ester, Figure 11), approved in EU as a cream (after 3h from application it is converted in the corresponding porphyrin based photosensitizing agent[25]).

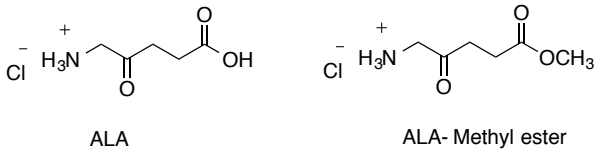

Figure 10. Chemical structure of ALA and ALA-Methyl ester approved drugs.

Levulan® and Metvix® are used in treatment of non-melanoma skin cancer (not in melanoma because the low penetration of light through pigmented lesions). However, new trials are ongoing to allow the approval of ALA for treatment of actinic keratinosis (precancerous lesions that can progress to squamous-cell carcinoma) and for basal-cell carcinoma.

Aminolevulinic acid[31] is an endogenous molecule which is synthesized in the mitochondria *via* enzyme (ALA-synthase) catalyzed condensation of glycine and succinyl CoA. Once synthesized ALA is exported into the cytosol, where it undergoes a series of synthetic steps forming porphobilinogen (PBG), then porphyrinogens, protoporphyrin IX and finally Heme (Figure 11). During the final stages of Heme biosynthesis, the intermediate coproporphyrinogen is transported from the cytosol into the mitochondria and here converted to the first real porphyrin, the protoporphyrin IX (PpIX).

PpIX is a very powerful photosensitize, but it is not administered in clinical practice because it is unable to cause enough photodynamic damage since it is not accumulated in cells. The way to generate large amount of PpIX inside cells pass through the administration of exogenous ALA which will be *in situ* converted in PpIX [32]. When exogenous ALA is given to cells, the Heme biosynthetic pathway becomes temporarily overloaded, all control mechanisms are bypassed and ferrochelatase, which catalyzes iron insertion into PpIX, is unable to complex all PpIX excess. In this way, it is possible to accumulate inside cells enough PpIX exploitable as active sensitizer. Tumor cells usually show low level of ferrochelatase, less readily accessible iron, lower pH than normal cells (different protonated PpIX species are present in this condition which increase porphyrin retention inside cell) and high selective ALA uptake; all these features guarantee selective accumulation of PpIX in tumoral tissues [33].

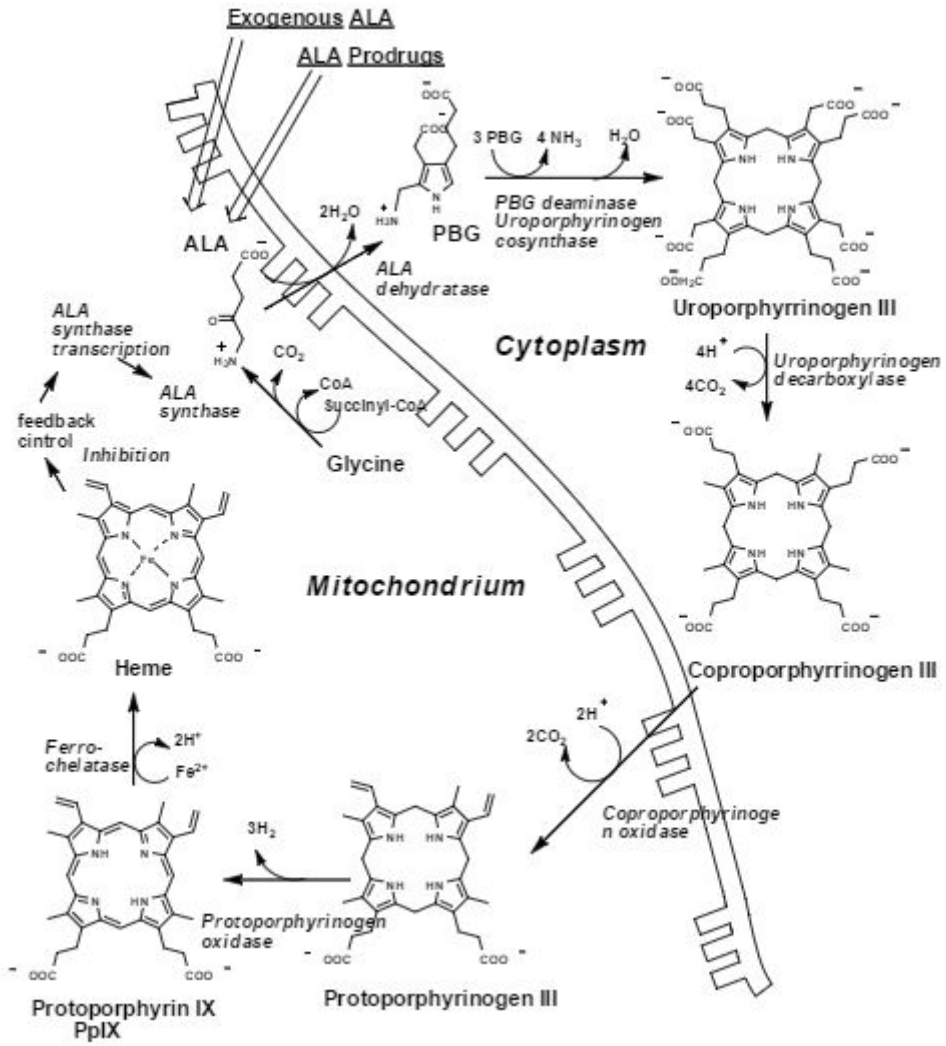

Figure 11. Endogenous ALA is synthesized by ALA Synthase.

1.4.3 ALA ADVATAGES AND DISADVANTES

In contrast to porphyrins, ALA is a small and water-soluble molecule able to penetrate easily into the abnormal stratum corneum overlying skin tumor. ALA is converted in PpIX inside cells and both ALA and PpIX are rapidly cleared from the system, which results in an acceptably short period (2 days compared to 1-1.5 months in the case of Photofrin®) of cutaneous photosensitivity. This results in a short session treatment, without damage of surrounding tissues[34] .

Main limitations of this compound consist in its low stability at physiological pH (it dimerizes to give pyrazine derivatives at physiological pH[35]) and in its inability to cross certain biological barriers (e.g. cellular membranes) because of its low lipid solubility[36]. Moreover, when it is used for topic treatment, it cannot deeply penetrate the skin layers. When it is systemically administered, it can cause, after PDT treatment, mild nausea[37]. These limitations can be overcome by suitably derivatization of its acidic function. The carboxylic group of ALA can be transformed in different esters[38], increasing in this way its lipophilicity (and its ability to cross the cell membrane) and improving its bioavailability. Methyl aminolevulinate (Metvix®) as well as many others esters are examples of this kind of derivatization; their increased lipophilicity enhance their cellular uptake *via* different mechanisms, improving the efficiency of the therapy[39]. These esters must be hydrolyzed to ALA in order to take part of Heme biosynthetic pathway. It was observed that esters longer than C-7 (heptyl ester) produce less efficient PpIX formation.[40-41]

1.4.4 THIRD GENERATION OF SENSITIZERS

Most of therapeutic drugs possess a large distribution in whole body increasing in toxicity and in side-effects. For this reason, targeted delivery of drugs represents the main challenge in pharmaceutical chemistry research. Therefore, one goal in the field of targeted therapies is to develop chemically derivatized drugs or drug vectors able to target defined cells via specific mechanisms[42,43]. Different strategies have been investigated, such as: i) monoclonal antibodies directed against antigens or ligands that are specifically overexpressed on cancer cells; ii) encapsulation in colloidal carriers, such as liposomes, oil-dispersions, polymeric particles and polymers, to facilitate drug delivery and increase the amount of drug released in situ[44]. The same approach can be translated to sensitizer formulation: a given sensitizer can be linked to a defined vector (antibody, protein, peptide, small molecule, …), or it can be included into a colloidal nanoparticle, which can be driven to the target by the conjugation with a specific vector. The obtained sensitizing systems are called "third generation sonosensitizer". Lutsenko et al have conjugated metal-disulfonated phthalocyanines to epithelial grow factor (EGF), obtaining sensitizers with higher specificity, 10 times more efficient than free phthalocyanines in treatment of human breast carcinoma (MCF7) cells[45]. Zhang and coworkers based their approach on the altered sugar metabolism of cancer cells; they functionalized a selected sensitizer with a large variety of sugars such as: xylose, arabinose, glucose, galactose[46].

Important to note that Verteporfin liposomal formulation (Visudyne®) has been approved for the photodynamic treatment for age-related macular degeneration. For the same indication, a Rostaporfin lipoprotein complex (Photrex®) has been proposed. Now Photrex® is in phase III for breast cancer and in phase I/II for basal cell cancer. Both Visudyne® and Photrex® are third generation of sensitizer molecules.

Among different nanostructure suitable to carry a given sensitizer, carbon nanomaterials (carbon nanotubes and graphene), solid-lipid nanoparticles (SLN), liposomes and nanobubbles, are particular interesting nano-supports for sonodynamic application. Their peculiar features could improve efficiency and selectivity of sonosensitizer and reduce side effects.

1.5 CARBON NANOMATERIALS: CNTs and GRAPHENE

One of the fathers of nanotechnology, R. Smalley, said:" *... My own research these days is focused on carbon nanotubes an outgrowth of the research that led to the Nobel Prize a few years ago. These nanotubes are incredible. They are expected to produce fibers 100 times stronger than steel at only 1/6th the weight almost certainly the strongest fibers that will ever be made out of anything strong enough even, to build an elevator to space. In addition, they will conduct electricity better than copper, and transmit heat better than diamond."*

Depending from its hybridization (sp^3, sp^2), Carbon element can form diamond (thermodynamically less stable, for it formation it requires high pressure and temperature) or graphite (the thermodynamically stable form). The ideal diamond structure consists of carbon atoms that are bonded to their nearest neighbor by tetrahedral strong covalent σ bonds arising from superimposition of sp^3 atomic orbitals (Figure 12 (b)), whereas the ideal graphite structure consists of planar layers of hexagonal arrays of carbon (which is in sp^2 hybridization) in an ABAB stacking arrangement (Figure 12 (a)). In graphite, layer planes are bonded to one another by weak Van der Waals forces[47]. Fullerene/C_{60} (Figure 12 (c)) is the third allotropic form of carbon, it possesses a football shape and it was obtained for the first time in the earlier 1985 by Smalley, by vaporizing graphite using laser irradiation. This process produced a remarkably stable cluster consisting of 60 carbon atoms (C_{60}). Graphene (figure 12 (e)) is the thinner carbon-based material; the sp^2 hybridization of carbon and its electron density distribution are the main reasons why graphene possesses, at room-temperature, extraordinary properties such as ultra-high mechanical strength, tunable electronic band gap, excellent thermal and electrical conductivity.

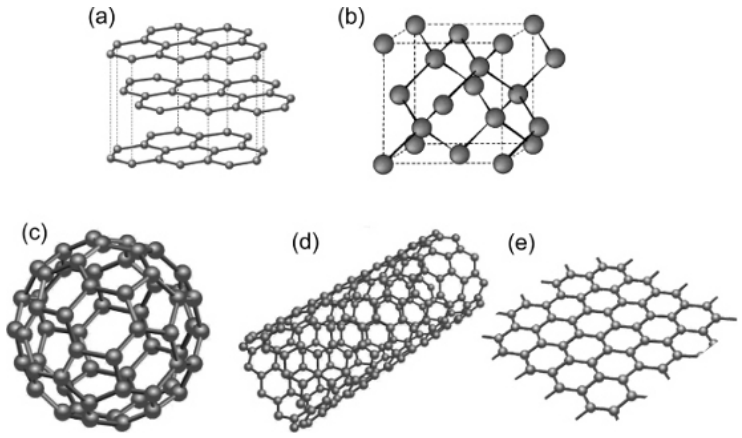

Figure 12 Allotropic structures of Carbon element: Graphite (a), Diamond (b), Fullerene (c), Carbon nanotubes or CNTs (d) and Graphene (e).

Graphene has been experimentally studied for over 40 years[48-49]. It can be synthesized in various ways: mechanical cleaving (exfoliation) or scotch-tape method, chemical exfoliation, chemical synthesis (i.e. graphite oxide exfoliation) and thermal chemical vapor deposition (CVD) synthesis[50].

The chemical exfoliation method (first technique employed to prepare graphene) exploits the insertion of large alkali ions (K^+) between graphite layers in a graphite dispersed alkali solution. Chemical synthesis is similar to chemical exfoliation process. An aqueous suspension of graphite is oxidized and then subjected to ultrasound irradiation. Thanks to sonication, H_2O molecules interlay two graphite oxide sheets causing a total exfoliation in graphene oxide monolayers. Further reduction with hydrazine produce the graphene monolayer. Chemical vapor deposition (CVD) has proved to be the most significant process for large-scale graphene fabrication. Thermal CVD allows the production of an uniform layer that is deposited onto metal surfaces (usually Ni or Cu) evaporated on SiO_2 support. After the synthetic step, metal is chemically removed (for instance by nitric acid dissolution) leaving graphene nanosheets floating inside solution.

Due to its peculiar features (electrical conductivity, ability to absorb visible and NIR light [51], stiffness, tenacious, high strain resistance), graphene is a promising candidates for the realization of composite materials, electronic devices and sensors[52], for the energy conversion[53-54] and, finally, for biomedical applications[55]. Some of these applications are intrinsically dependent on its ability to be suspended in aqueous medium, since it is completely insoluble in all solvents.

So, this carbon nanomaterial needs to be superficially modified by the insertion of suitable functional groups (oxydriles, carbonyls, carboxylic groups, amines, heterocycles, …), or by wrapping it with biopolymers or polymers, surfactants[56]. Another important aspect of this material is its non-biodegradability, which still remain an important question mark about its use in biomedical applications.

When graphene is rolled it can form carbon nanotubes (CNTs, figure 12 (d)), which were discovered by Iijima[57], during the fullerene formation process, in 1991. Carbon nanotubes are classified in Single Walled Carbon Nanotubes (SWCNT) or in Multi Walled Carbon Nanotubes (MWCNT) depending on the number of layers which constitute the tube wall.

SWCNT is made of a single graphene sheet wrapped around to form a cylinder, whereas MWCNT are made of multiple concentrically nested tubes. SWCNT can be visualized as a tube with a middle extended graphene sheet closed in both sides by fullerene moieties allowing the right bending[58]; sometimes these two moieties are not present. The tube diameter range is between 0.7-10 nm and up to few μm of length. MWCNT have diameters up to 100 nm and lengths from 1 to several μm. The high length/diameter ratio allows CNTs to be like a mono-dimensional structure. However, the strong intertube forces keep CNTs together in bundles, making their manipulation, characterization and analytical investigation very difficult.

There are three principal methods to obtain CNTs: arc discharge, laser ablation[59] of graphite and chemical vapor deposition (CVD). The first two methods involve the condensation of hot gaseous carbon atoms generated from evaporation of solid carbon using Co, Ni, Fe or a mixture of them, as metal catalysts. Arc discharge has been used widely for fullerene synthetic process and it was the method through MWCNTs were discovered[60]. Laser ablation method allowed to obtain SWCNTs bundles with high yield 70-90%. Whereas, CVD[61] method involves the decomposition of a gaseous or volatile organic compound (hydrocarbon) catalyzed by metallic nanoparticles, which also serve as nucleation sides for the initiation of carbon nanotubes growth. Typically, after synthetic procedure, purification step is necessary to remove carbonaceous byproducts (graphite, carbon soot, fullerene and other carbon fibers) and metallic components. However, a complete removal of catalyst is not an easy task and a lot of commercially available CNTs still contain not negligible metal amount. As described for graphene, also biomedical applications of CNT require a suitable ability to be suspended in aqueous medium, so surface derivatization is needed (using the same approaches described for graphene).

1.6 LIPID SHELLS: LIPOSOMES, NBs and SLN

Lipid shells are an important and well-studied class of nanoparticles. The great advantage of all these nanosystems is their size that allow to exploit the *Enhanced Permeability and Retention* (EPR) effect[62]. EPR effect consists in extravasation and accumulation of a given nanosystem into tumor region by passive targeting, because of the increased permeability of the vasculature that supplies this pathological tissue[63-64].

Liposomes are nowadays approved for clinical applications in PDT such as Visudyne® (liposomal formulation of Verteporfin in AMD- Age related Macular Degeneration), already described. AmBisome® (liposomal formulation of Amphotericin B) is another example of drug approved as antifungal medication but also used in different infections[65-67] . PEGylated liposomal doxorubicin (Caelyx/Doxil) is one of the most used in metastatic mammary tumor treatment in clinic.

Microbubbles formulations have been approved as US contrast agent (Sonovue®), they are extensively used for this application but, recently, they are also studied as drug carriers and drug delivery systems. The advantage of this type of nanoparticle is to combine the diagnostic properties with therapeutic ones.

Solid Lipid Nanoparticles (*SLNs*) are colloidal carriers developed in the last two decades (from 1991)[68-69] as system replacing the traditional lipidic particles (emulsions, liposomes and polymeric nanoparticles). SLN are a new generation of submicron-sized lipid emulsions where the liquid lipid (oil) has been substituted by a solid lipid. SLN offer unique properties such as small size, large surface area, high drug loading. After an intravenous administration, they possess the ability to cross the human blood brain barrier (BBB)[70-71]. Even if they are very promising, there are not yet formulations in clinical use based on SLNs.

1.6.1 LIPOSOMES

The pioneering work of countless liposome researchers over almost 5 decades led to the development of important technical advances such as remote drug loading, extrusion for homogeneous size, long-circulating (PEGylated) liposomes, triggered release liposomes, liposomes containing nucleic acid polymers, ligand-targeted liposomes and liposomes containing combinations of drugs. These advances have led to numerous clinical trials in diverse areas as the delivery of anti-cancer, anti-fungal and antibiotic drugs, the delivery of gene medicines, and the delivery of anesthetics and anti-inflammatory drugs. A number of liposomes (lipidic nanoparticles) are on the market, and many more are in the pipeline. Lipidic nanoparticles are the first nanomedicine delivery system to make the transition from concept to clinical application, and they are now an established technology platform with considerable clinical acceptance. We can look forward to many more clinical products in the future[72-73].

Liposomes are vesicles consisting of an aqueous core encapsulated by natural or synthetic phospholipids (figure 13). Size shell can be into the 50-250 nm range for unilamellar liposomes; 1–5 μm for multilamellar type.

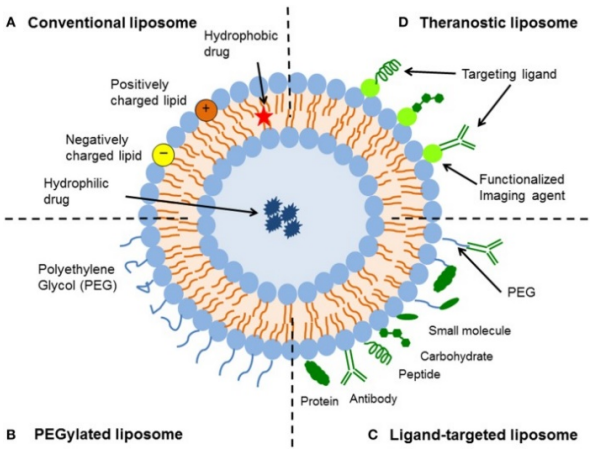

Figure 13. Schematic representation of the different types of liposomal drug delivery systems.

To increase specific cellular and tissue uptake, and to improve the biodistribution of drugs, decreasing in this way their off-sides toxicity, liposome surface can be functionalized with specific vector[62]. Ligand-targeted liposomes (C in figure 13) offer a vast potential for site-specific delivery of drugs to designated cell types *in vivo*, which selectively express or over-express specific ligands.

1.6.2 NANOBUBBLES

Among many novel nano-carriers being developed, echogenic bubble formulations have been gaining lots of attention in recent decades. Bubbles are gas-filled nanoparticles, spherically shaped and stable in aqueous medium. The main features of this nanovectors is the flexible membrane, but also, the presence of a gas core which allows them to be used as US contrast agents[74-75]. Commercial available formulations of ultrasound contrast agents are made of bubbles with dimension in the μm range. They are routinely utilized in clinical diagnostic imaging and are being investigated for drug delivery applications. Microbubbles (MBs) resonates when irradiated with an ultrasound beam; they are rapidly contracted and expanded in response to pressure changes of the sound wave. MBs vibrate strongly at the high frequencies used for diagnostic US imaging, making them several thousand times more reflective than normal body tissues[76-77]. However, the size of MBs may limit their biodistribution in the tumor, local drug delivery and targeting drug delivery hindering subsequent therapy[78 79]. Bubbles formulations should be therefore scaled down in nanosize range dimension (200-400 nm).

1.6.3 SOLID LIPID NANOPARTICLES

Solid lipid nanoparticles (SLN) [80-81] consist in solid lipid aggregates (matrix structure) which can be stabilized by a surfactant or polymer and dispersed in aqueous medium. Their diameter is usually between 50 nm and 1μm. The main advantages are the controlled drug release due to the solid state of lipid matrix, the drug protection from chemical, photochemical, enzymatic and oxidative degradation and the high biocompatibility (like other lipid shell nanoparticles). A very important aspect is the easy scale-up of their formulation, a key step for industrial development of these nanoparticles. SLN have been administered through different ways: topical, parenteral and oral administrations[82-83].

The drug loading capacity of conventional SLN is limited by the solubility of drug in the lipid melt, the structure of the lipid matrix and the polymorphic state of the lipid matrix. More ordered are the lipids less amount of drug can be loaded in. The transition to highly ordered (α to β) lipid particles is also the reason for drug expulsion. Many drugs have been incorporated: prednisolone, doxorubicin, methotrexate[84-85].

2. THE AIM OF THE PROJECT

Given that the main PDT shortcomings impact negatively on the clinical results, it has been proposed to use US irradiation (SDT). This irradiation modality overcomes the first PDT limitation: the light low tissue penetration (that allow limited cutaneous cancer treatment). However, US source is not enough to bypass the second PDT limitation: the skin photosensitivity. To reduce (or better, to eliminate) the skin photosensitivity, two different strategies can be implemented. First, the synthesis of new heterogeneous nanoconstructs able to be excited only, or at list mainly, by ultrasound. Second, the development of new systems easily conjugatable with high affinity vectors for targeting tissues (limiting in this way the sensitizer concentration in skin tissues).

The aim of this project is to explore the combination of the two above mentioned strategies to reduce the skin photosensitivity. The idea is to take advantage from the ability of a particular nanosystem to be modified by vectors (to make them tissue specific) and from the heterogeneity of the engineering nanoconstruct suspension. This last feature can reduce the energy required for acoustic cavitation enhancing the sonodynamic effect.

The nanosystems considered are CNT, graphene, SLN, liposomes and nanobubbles, whose peculiar features are already mentioned.

In particular, carbon based nanosystems (CNT and Graphene) could be interesting because of their additional ability to absorb light (since they are black supports) and because they can promote the electron transfer mechanism, which can enhance ROS production. Both effects could be exploited to selectively amplify the sensitizer excitation after US irradiation. Nanobubbles shell are proposed as interesting systems because of their ability to act as ultrasound contrast agent. This additional feature can make this lipid shell an intriguing support for theranostic applications based on US. Liposomes are considered as last class of nanosystems because they are already well-studied and approved for clinical application.

All these nanoparticles need to be garnish with suitable sensitizer. The chemical structures identified as good sensitizers in SDT are porphyrin molecules, as confirmed by a large number of scientific publications. Since the proposed nanoparticles possess different composition and different surface properties, it is necessary the design of a*d hoc* porphyrin derivatives.

The study strives to evaluate different chemical approaches (from total synthesis to simply modification of commercial porphyrins) in obtaining the most appropriate structure to garnish selected nanoparticles in order to exert a good sonodynamic effect.

The efficiency of porphyrin hybrid-nanosystems in sonodynamic and photodynamic therapy approaches have been evaluated and compared by *in vitro* cellular proliferation, quantification of ROS production.

Because of the multidisciplinary nature of this project, the work has been carried out in collaboration with different research groups:

Drug Science and Technologies Department: Group of Pharmaceutical Technologies (E. Peira, S. Arpicco, F. Dosio, B. Stella, A. Marengo), Pharmacology (L. Serpe, R. Canaparo, F. Foglietta)

Chemistry Department: Group of Inorganic and Physical-Chemistry (F. Turci, I. Corazzari)

American collaboration: Case Western Reserve University, Cleveland – OH (A.A. Exner's lab).

3. RESULT AND DISCUSSION

3.1 Porphyrin conjugated to carbon-based nanomaterials (SWCNT and reduced graphene oxide - rGO)

SWCNT and rGO (reduced Graphene Oxide) are characterized by an extended sp^2 surface which is responsible of their peculiar features. This carbon atom hybridization can also be exploited to covalently conjugate different organic molecules by two different reactions: Diels-Alder cycloaddition and 1,3-dipolar cycloaddition.

Diels-Alder cycloaddition occurs between suitable diene and dienophile; in the case of carbon nanomaterial rGO or SWCNT surface act as dienophile, whereas a furanyl moiety, ad hoc inserted on the porphyrin structure, acts as diene. 1,3-dipolar cycloaddition occurs between a suitable dipole and a dipolarophile which is again represented by carbon surface.

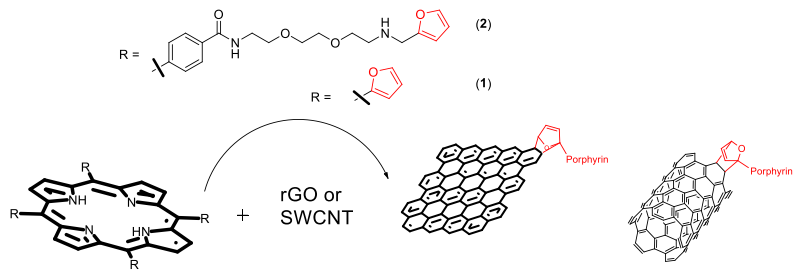

Figure 14. Diels-Alder reactions between carbon nanosupports (rGO and SWCNT) and *ad-hoc* synthetized porphyrin derivatives, compound (**1**) and (**2**).

Both approaches require specific derivatized porphyrins which need to be prepared for these purposes. To exploit Diels-Alder reaction, furanyl moieties have to be inserted on the porphyrin macrocycle; two different structures (compounds (**1**) and (**2**), figure 14) have been designed in order to modulate the distance between carbon surface and porphyrin, which can play a role in the sonodynamic process.

The first challenging task was to chemically realize the *ad-hoc* porphyrin derivative compound (**1**), starting from basic heterocyclic compound (pyrrole and furfural). The obtained porphyrinic nucleus exposes four furanyl moieties directly attached to the macrocycle ring (see figure 14). Compound (**2**) was obtained by derivatization of a commercially available porphyrin.

Cyclocondensation reaction of four furanyl aldehydes and four pyrroles heterocycles, is known to be an arduous synthetic procedure to be performed because of the starting materials sensitivity and for the intrinsic properties of the 'feeble' porphyrinic compound. Porphyrin derivatives are affected by a low solubility in many solvents, photo-sensibility and arduous purification step at the end of reaction. Many attempts, to obtain similar compounds (but not compound (**1**)), were done using different reaction conditions. *Adler-Longo*'s [86-87] (1964) approach was performed using a solution of aldehyde (benzaldehyde) and pyrrole (concentration range was 0.1-0.3 M, in equal molar ratio) in a high-boiling acid solvent (propionic acid or acetic acid), at reflux temperature, in air for 30-60 minutes.

Under these conditions, condensation and oxidation steps occur simultaneously. Using this methodology, porphyrins derivatives were obtained with yield up to 20%. Other procedure 'two-steps one-flask room-temperature', optimized by *Lindsey*[88] (1986) consists in the condensation of starting materials (concentration range 0.1-0.001 M) in non-polar solvent (dichloromethane) in presence of acid (TFA 1-2.5x10 $^{-2}$ M) for 1 h, followed by oxidation of porphyrinogen intermediate . The yields of porphyrins generated under these conditions were improved up to 40% yield. Same yield was reached by using *Dolphin*'s[89] (1970) and *MacDonald*'s[90] (1960) protocols. They proposed the use of the dipyrromethenes as intermediates in porphyrin synthesis since the pioneering and epic work of Hans Fischer in the 1920's. *Hans Fisher* (1920, Nobel prize in 1930) was the first scientist working on protohemin and accomplished the synthesis of chlorophyll *a* pigment.

The latter procedures represent an improvement of *Rothemund*'s reaction (1939) which was the first method[91] to synthetize tetra- aryl porphyrin by reacting benzaldehyde with pyrrole in a sealed tube and using pyridine as solvent, at 220°C for 48 h, usually with less than 5% yield. Rothemund's method is characterized by high reactant concentration, high temperature and no oxidant addition. Further optimizations[92] of these synthetic protocols include the use of an oxidizing co-solvent, oxidizing Lewis acids and various catalysts[93-95]. Among these works, Calvin et al[96] , thanks to the Zn acetate salt in the mixture reaction, were able to double the yield of Rothemund's reaction.

All the synthetic efforts described in literature are relative to aryl-porphyrins whose aryl substituent is not furan. A very few papers[93, 97-98] deal with meso-tetrakys-(furan-2-yl)-porphyrin synthetic procedures. This porphyrin was obtained in low yield (1-12%) with a time consuming and multi-step procedure. Moreover, none of those procedures report the purity of isolated porphyrin.

3.1.1 *Synthesis of Compound (**1**) and its carbon-based SWCNT nanosupport derivatives*

Meso-tetrakys-(furan-2-yl)-porphyrins compound (**1**), a well-engineered porphyrin derivative, was synthesized by microwave (MW) enhanced, acid-catalyzed condensation of four furfurals and four pyrrole molecules. Two different routes have been investigated (see Scheme 1): solid support and solution protocols. Both reaction pathways consider heterogeneous catalysis, in the first case the solid support acts also as acid catalyst, whereas the other one exploit an acidic polymeric resin[99].

Regarding the solid supported protocol, silica gel[100], neutral alumina, a mixture of both (SiO_2/Al_2O_3= 1:1; 1:2; 1:3) and acetic acid (0.1% w/w) on alumina have been investigated as supports. All reactions were carried out under the same reaction conditions (MW irradiation power and modality, temperature, time, reactant ratio and concentration) and meso-tetrakys-(furan-2-yl)-porphyrin was obtained only after oxidation of crude precursors mixture (partially oxidized porphyrin compounds) by 2,3-dichloro-5,6-dicyano-1,4-benzoquinone (DDQ). There were no cases in which we were able to obtain final porphyrin without the oxidation step. When silica gel is used, its double role of support and acid catalyst was evaluated. The amount of un-oxidized porphyrin (porphyrinogen species), partially oxidized porphyrinogen species and porphyrin was measured by HPLC-MS.

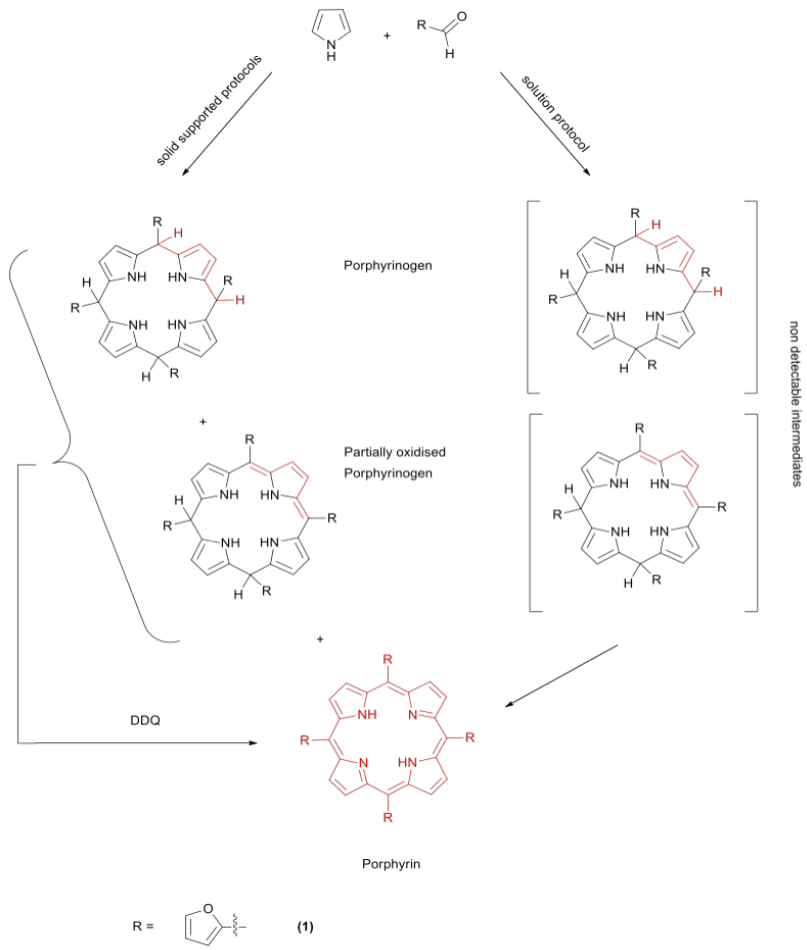

Scheme 1. Two different protocols for *meso*- tetrakys-(furan-2-yl)-porphyrin (compound (**1**)) synthesis: left-side is represented the solid support protocol using DDQ to obtain (**1**) and right-side is showed the solution protocol.

The ratio between porphyrin and the total number of reduced species turns out to be related to the type of solid support involved in the reaction. It was found to be 0.6 (porphyrin/porphyrinogen like species) when pure silica gel was used and reaching 0.3 when only pure alumina is used. When silica and alumina were mixed together (SiO_2/Al_2O_3= 1:1; 1:2; 1:3 ratio), the ratio value was markedly lower than neat alumina (it was 0.1 for the two higher SiO_2/Al_2O_3 ratios and 0.2 for SiO_2/Al_2O_3 = 1: 3, see figure 15). Whereas the ratio reached 0.9 when alumina was adulterated with acetic acid.

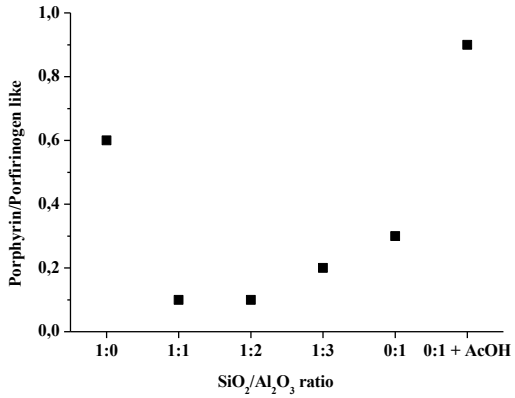

Figure 15. Porphyrin/porphyrinogen-like ratio species *vs* different solid support composition.

This behavior could be also explained considering the morphology of the support and its consequent ability to diffuse O_2 on it (allowing the oxidization step and the final product formation). It was observed that silica gel support has a very vitreous morphology compared to alumina, that looked spongier after MW heating. The sponginess of the support is necessary for the oxygen diffusion. When those two supports are combined, the sponginess of the alumina was lost together with the oxygen diffusion. Probably also the silica acidic behavior was not retained as well. We can observe that the difference in composition of the supports influences the distribution of porphyrin like species, whereas it does not affect the reaction yield trend because in all cases, the isolated product yield was lower than 1% (after DDQ oxidation step).

The optimization of the solid support reaction conditions did not give gratifying results in terms of yield, so we decide to shift to the solution procedure. With this approach, this the final product was synthetized without any oxidation step. The reactants concentration was initially fixed at 1M and the reaction conditions (temperature, pressure and time) are maintained unvaried. Reaction yield was lower than 1% using this concentration (figure 16). That's reasonably because the cyclization reaction mechanism is always in competition with linear polymerization, dilution conditions of reactants are well known to be a good way to promote cyclization reactions. Hence, meso-tetrakys-(furan-2-yl)-porphyrin synthetic pathway was studied at four different reactant concentrations (from 1 to 0.1 M).

As showed in figure 16, the reaction yield of the isolated product increased when reactant concentrations decreased, giving a maximum value of 4% at 0.1 M and 170°C for 20 minutes. Further dilutions do not enhance the reaction yield value.

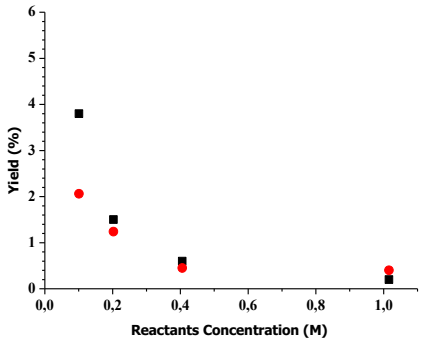

Figure 16. Porphyrin yield *vs* reactant concentration. MW enhanced reactions carried out in dioxane, 50 bar (N_2), 20 min, 140°C (red circle) and 170°C (black square).

In literature, it is reported that not only the use of diluted reactants concentration, but also the presence of metal ions facilitates this kind of reactions (acting a templating agent during macrocycle formation). So, we decided to investigate the role of metal ion and we selected $Zn(AcO)_2$ because it is known to form stable porphyrin complexes. The presence of metal ion in solution mixture, allows to increase the reaction yield up to 5% in the case of metalloporphyrin, in only 10 minutes of MW irradiation at 140°C (figure 17). The reactant concentrations were maintained reasonably low (0.4 M) in order to have enough final product to be analyzed. The role played by $Zn(AcO)_2$ in increasing reaction yield, seems to be related to its acidic behavior[101] and its ability to act as templating agent.

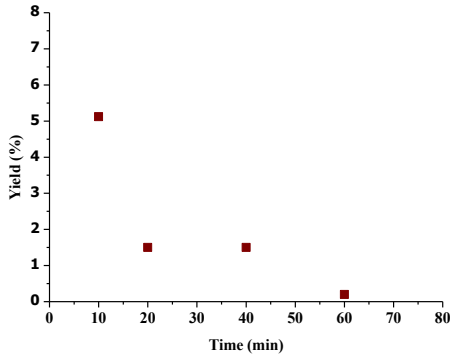

Figure 17. Zn-Porphyrin yield *vs* reaction time (min). MW enhanced reactions carried out in dioxane in the presence of $Zn(AcO)_2$ (0.13 M), 50 bar (N_2), 140°C, reactant concentration 0.4 M.

Analogous results, in terms of reaction kinetic (10 minutes reaction time), were observed with different metals (Cu(II), Fe(III), Mn(II)) but with lower yields. However, even if reaction yield still remains quite low, the solution protocol of aldehyde-pyrrole condensation allows to reduce the synthetic steps because the intermediate species are immediately oxidized. This phenomenon may be due to the better oxygen diffusion in-solution (compared to the diffusion into a solid support) raised up by the high-pressure conditions (a reaction parameter fixed at 50 bar (N_2) for all cases, solid and liquid protocols).

The obtained compound (**1**) and compound (**1**)**-Zn**, were conjugated to SWCNT by using DA cycloaddition. Compound (**1**) was mixed with SWCNT support (2:1 w/w respectively) under MW irradiation at 100°C for 2h in DMF. Same conditions were used for compound (**1**)**-Zn** and SWCNT.

Thermogravimetric analysis (TGA) of grafted nanotubes, allows us to quantify the derivatization degree of this support. SWCNT-compound (**1**) showed a loss weight corresponding to a derivatization of 5.7% (w/w), whereas SWCNT-compound (**1**)**-Zn** functionalization was 10.2% (w/w) (figure 20).

The higher derivatization degree of porphyrin Zn complex could be due to the higher stability of this compound compared to free metal ion porphyrin derivative.

3.1.2 *Synthesis of Compound (**2**) and its carbon-based SWCNT and rGO nanosupports derivatives*

Meso-tetrakis-[4-(2-(2-(2-(furan-2yl-methyl-amino) ethoxy)-ethoxy). ethyl-aminocarbonyl) phenyl] porphyrin (compound (**2**), see scheme 2) is the next porphyrin derivative that we are interested in. The main difference, with compound (**1**), is the presence of the hydrophilic spacer between tetrapyrrole macrocycle and furanyl moieties. The spacer allows to evaluate if the carbon nanosupport-porphyrin distance change the sonodynamic result.

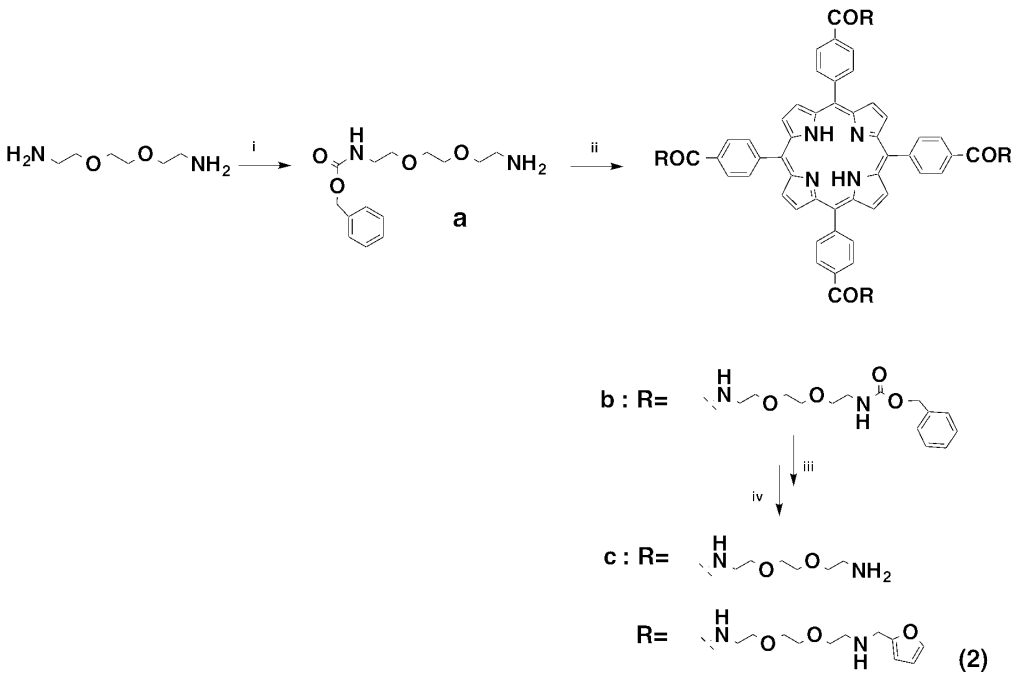

Scheme 2. Synthetic pathway of compound (**2**): *i)* benzyl chloroformiate, H_2O/EtOH/Dioxane, 0°C, pH=7; *ii)* meso tetra-(4-carboxyphenyl) -porphyrin, EDC, DMAP, DCM; *iii)* H_2, Pd/C (10% w/w), MeOH/Dioxane; *iv)* furfural, $Na(AcO)_3BH$, MeOH, pH=5.

Compound (**2**) was obtained through different synthetic steps, starting from the benzyloxycarbonyl monoprotection of 1,2-bis-(2-aminoethoxy) ethane (**a**) and further conjugation to the *meso*-tetra-(4-carboxyphenyl) porphyrin (commercially available) to give product (**b**). The four amino-groups were then deprotected by hydrogenolysis to give (**c**), which was converted in to desired product (**2**) after reductive amination in presence of furfural.

The low solubility of compound (**2**) makes isolation very easy but analytical characterization very difficult to set up (the acquisition time of the analyses are higher because the low concentration of the product).

Compound (**2**) was linked to SWCNTs by using MW enhanced Diels-Alder reaction, carried out at 100°C for 2h in DMF. A functionalization degree of 7.8% (w/w) was determined by TGA. Contemporary rGO was subjected to the same reaction under very similar condition. In this case, thermogravimetric analysis reveals a functionalization degree of about 29%. Probably, the observed differences in functionalization degree are due to the different structure of these two carbon-based nanosupports. In fact, graphene has a planar surface allowing two faces to graft. Whereas, the cylindrical surface of SWCNT exposes lower surface area to accommodate porphyrin derivative.

3.1.3 *Synthesis of Compound (**3**) and its carbon-based SWCNT nanosupports derivative*

To evaluate if the porphyrin arrangement on the nanotube surface has a role in the sonodynamic results, the relative distance between these two entities and also the linking modality used to graft the carbon nanotube surface, have to be considered. To this purpose, the 1,3-dipolar cycloaddition reaction, via azomethine ylide, has been selected. The reaction concerns an imine formation between an α-aminoacid and a suitable aldehyde, followed by decarboxylation and 1,3-dipole formation (figure 18). The dipole reacts with double bond present on SWCNT surface giving a substituted pyrrolidine heterocycle. Meso-tetrakys-(4-(5-amino-5-carboxypentylaminocarbonyl) phenyl) porphyrin derivative (compound (**3**)) was then designed in order to expose four α-amino carboxylic moieties that is required for 5-membered heterocycles (pyrrolidine) formation, see figure 19.

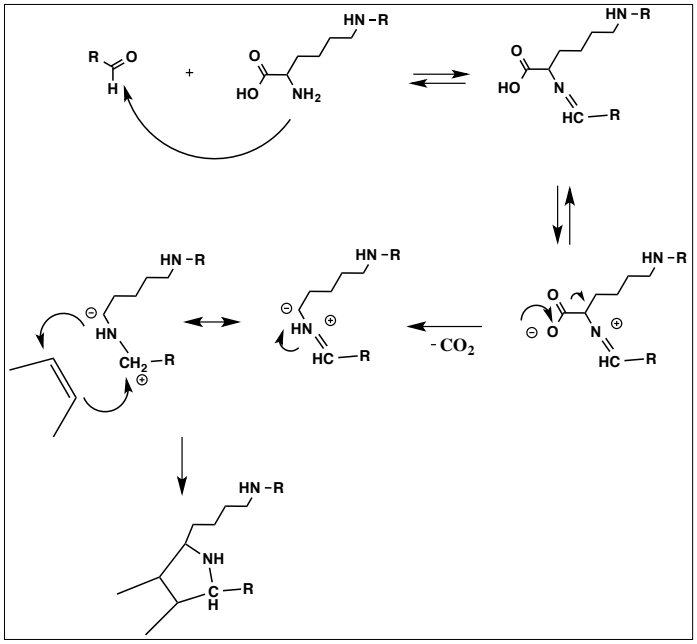

Figure 18. 1,3 dipolar cycloaddition mechanism between general aldehyde and α-aminoacid to form the pyrrolidine moiety with SWCNT (double bond).

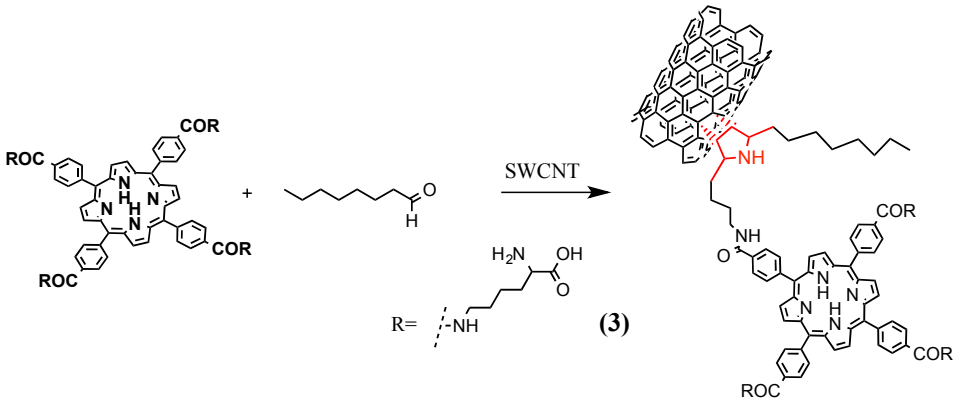

Figure 19. 1,3 dipolar cycloadditions reaction via azomethine ylide to link porphyrin derivate, compound (**3**), with octanal aldehyde is depicted. In red is highlighted the pyrrolidine moiety linked to SWCNT.

Compound (**3**) was obtained by condensation of meso-tetrakis-(carboxyphenyl)-porphyrin with α-Boc-lysine *t*-butylester (**f** derivative) obtaining compound **g** which was further deprotected with TFA in DCM. (see scheme 3).

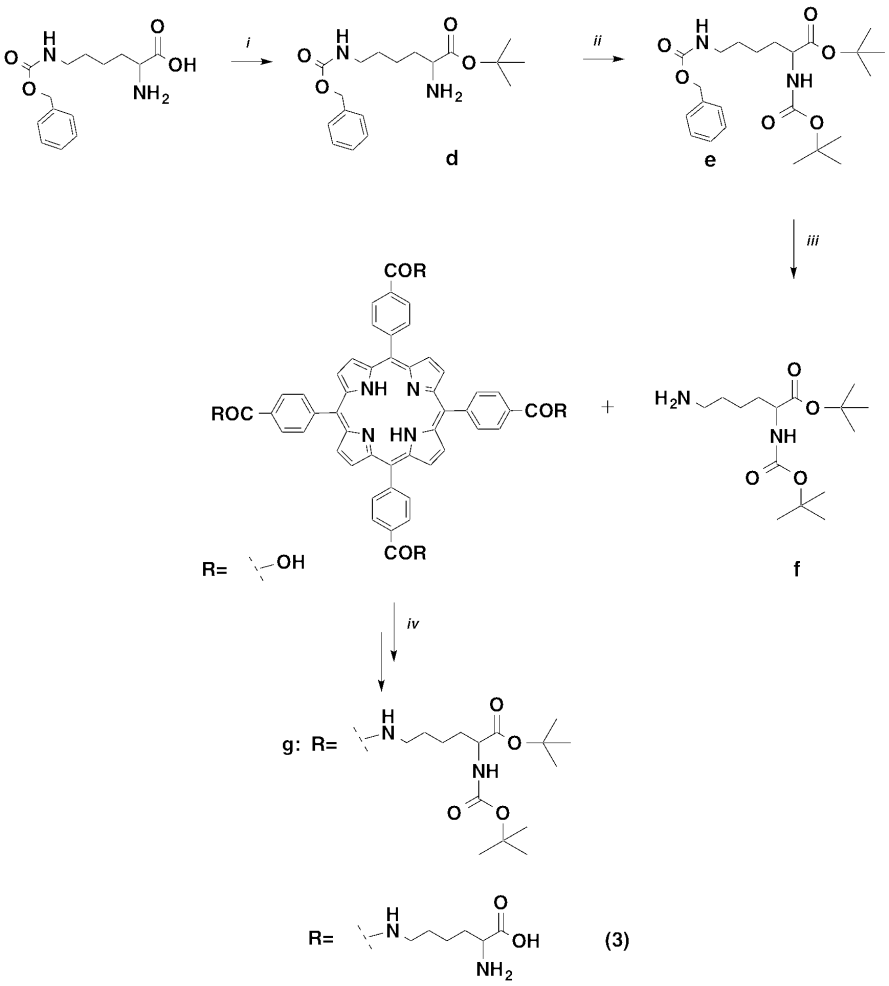

Scheme 3. Synthetic procedure of compound (**3**): *i)* terz-butyl acetate, $HClO_4$, *ii)* Boc_2O, Na_2CO_3 in CH_2Cl_2, *iii)* H_2, Pd/C (10%w/w), MeOH under N_2 atmosphere. *iv)* EDC, DMAP, CH_2Cl_2/THF and following deprotection with TFA in CH_2Cl_2.

SWCNT grafting with compound (**3**) was obtained by reaction of **3** with octanal and nanotube (1:1.5:1 w/w/w respectively) in DMF under MW irradiation at 120°C for 2h. Thermogravimetric analysis provides a functionalization degree value of 9.5% (w/w) (figure 21), which is similar to that obtained by Diels-Alder reaction. This suggest that both synthetic approaches proceed with similar efficiency.

3.2 Physico-chemical characterization of all Porphyrin loaded SWCNT carbon-based nanosupports

Thermogravimetric profiles show a weight loss between 270°C and 600°C related to decomposition of garnishing organic moieties (figure 20). On the basis of loss weight analysis, the derivatization degrees were estimated in 5.7%, 10.2%, 7.8% and 9.5% (w/w) for SWCNT-(**1**), SWCNT-(**1**)**-Zn**, SWCNT-(**2**) and SWCNT-(**3**) respectively. All grafting reactions seem to behave similarly; Diels-Alder or 1,3-dipolar cycloadditions appear to be equally efficient. Expressing the porphyrin loading in terms of moles, allows us to make a more precise idea about the amount of porphyrin grafted on SWCNT surface. This data, in fact, is independent from molecular weight of grafted molecules. $1.0x10^{-1}$ μmol mg^{-1}, $1.6x10^{-1}$ μmol mg^{-1}, $4.7x10^{-2}$ μmol mg^{-1} and $6.7x10^{-2}$ μmol mg^{-1} were determined for **SWCNT-compound (1)**, **SWCNT- compound (1)-Zn**, **SWCNT- compound (2)** and **SWCNT- compound (3)**, respectively. Again, the porphyrin amount grafted on SWCN is very similar for all nanosystem and it is very low in all cases.

When the carbon based nanosupport is changed from SWCNT to rGO, the amount of porphyrin grafted is significantly increased. Using Diels-Alder cycloaddition between compound (**2**) and SWCNT or rGO, the loading passes from 7.8% to 29% (w/w), respectively. This is reasonably due to the double, flat, widespread surface typical of the graphene support which can accommodate a large amount of porphyrin molecules.

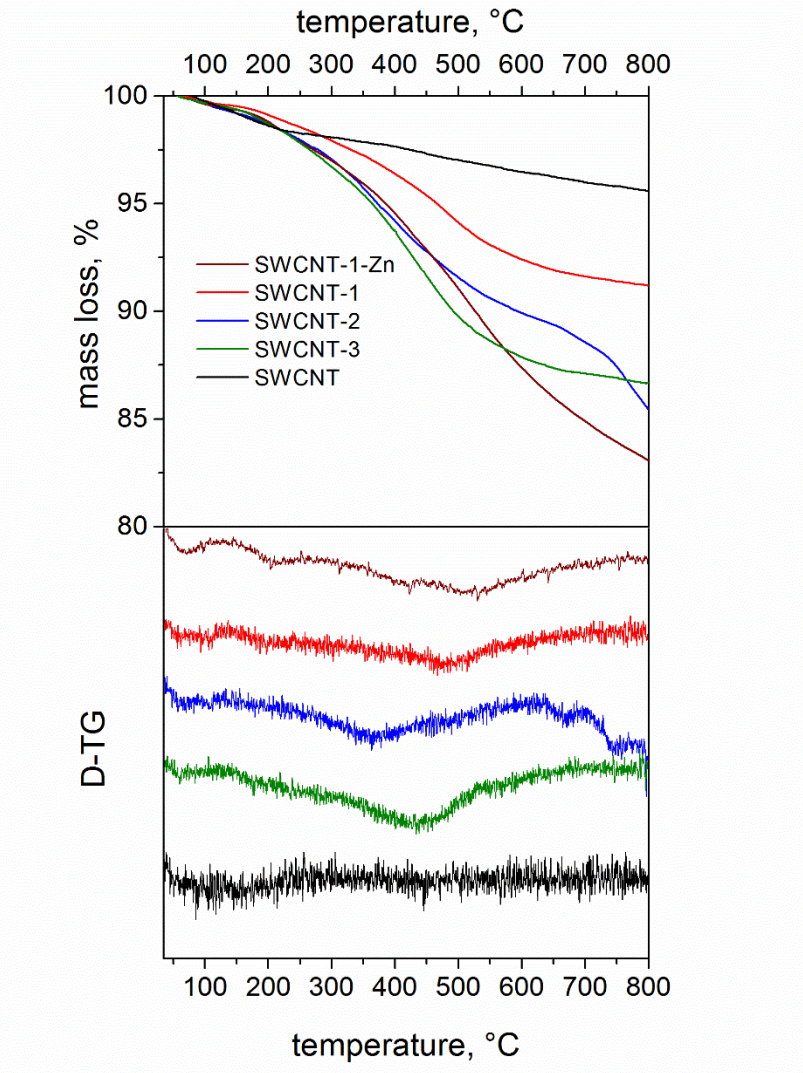

Figure 20. TGA profiles image of all porphyrin loaded SWCNT derivatives, top figure. The thermogram with pristine SWCNT is reported for comparison (black profile).

Raman micro-spectroscopy, and electron and atomic force microscopies (TEM and AFM) were carried out for all SWCNT-derivatives. The effect of surface functionalization on the micro-morphology of SWCNT was assessed by HR-TEM analyses (figure 21). HR-TEM images showed a minimum width of 7 nm (diameter, in according to Sigma data sheet of the pristine). By lower magnification TEM images, it is observed a bundles organization of the materials. High density areas were found to be consistent with metal residues (spots in panel B and D, figure 21) and amorphous carbon attached to SWCNT bundles[102]. The high magnification TEM images didn't show any significant morphological modifications after grafting procedure.

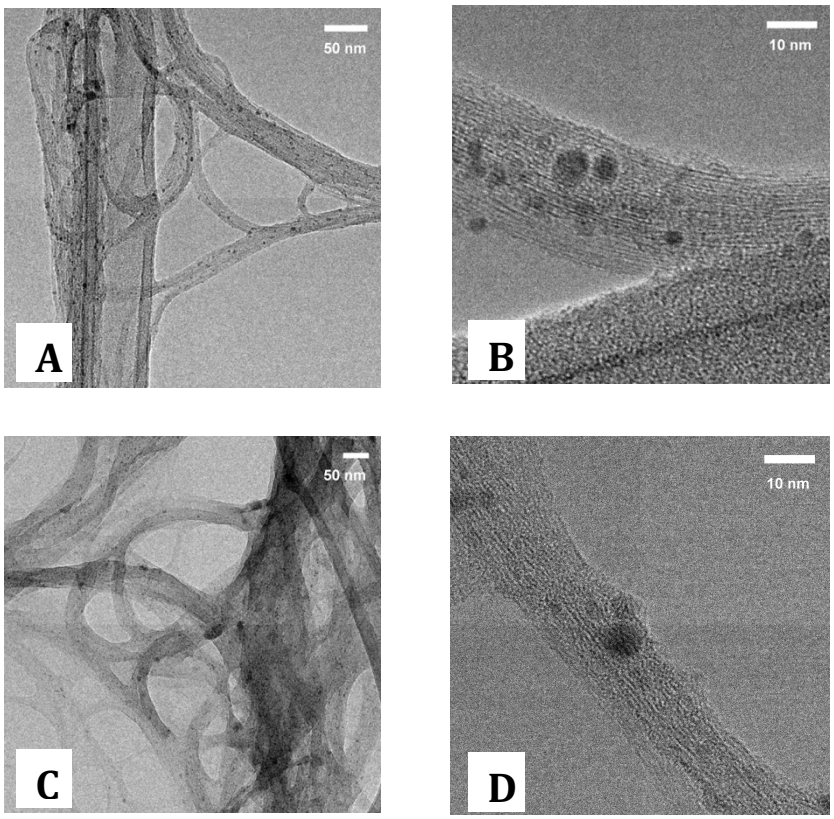

Figure 21. TEM images of **SWCNT-compound 1** (a and b) and pristine **SWCNT** (c and d).

For AFM analysis, samples were suspended in cyclohexane, sonicated and dried at 120°C overnight. Overall, the ribbons' width was in the range 150- 500 nm and their height ranges from 5 nm to 15 nm. In pristine SWCNT sample, some smaller features (approximately 150 nm large and 1.5 nm high) were recognized. No single nanotubes were detected, the smallest structures detected are composed of about 10 single nanotubes. AFM morphological data (figure 22) are consistent with those obtained from HR-TEM microscopy.

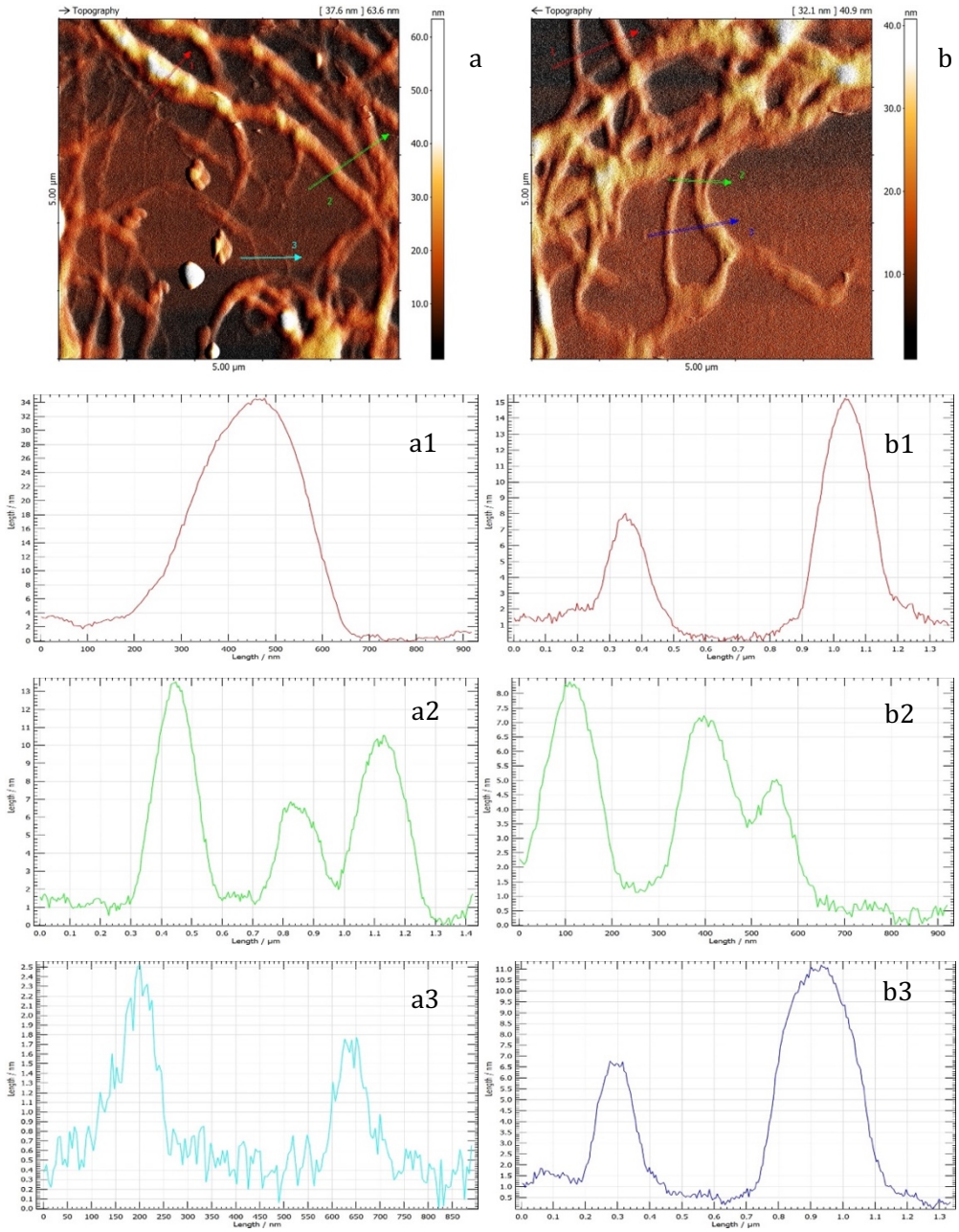

Figure 22. AFM images of pristine **SWCNT** and **SWCNT-compound 1** (a and b respectively) and topographic profiles. In all samples, the ribbons' width ranges from 150 nm to 500 nm and their height ranges from 5 nm to 15 nm (Figure 22 a1, a2 and b1, b2 and b3). In the SWCNT sample, some smaller features (approximately 150 nm large and 1.5 nm high) are recognized (Figure 22 a3).

Raman spectroscopy confirmed that the functionalization process did not modify significantly the SWCNT structure. In details, the normalized intensity I_D/I_G ratio (figure 23) was used to measure the amount of disorder: a slight increase of D-band is observed for **SWCNT-compound 3** conjugate (case of 1,3 dipolar cycloadditions), probably, this is consequence of pyrrolidine insertion.

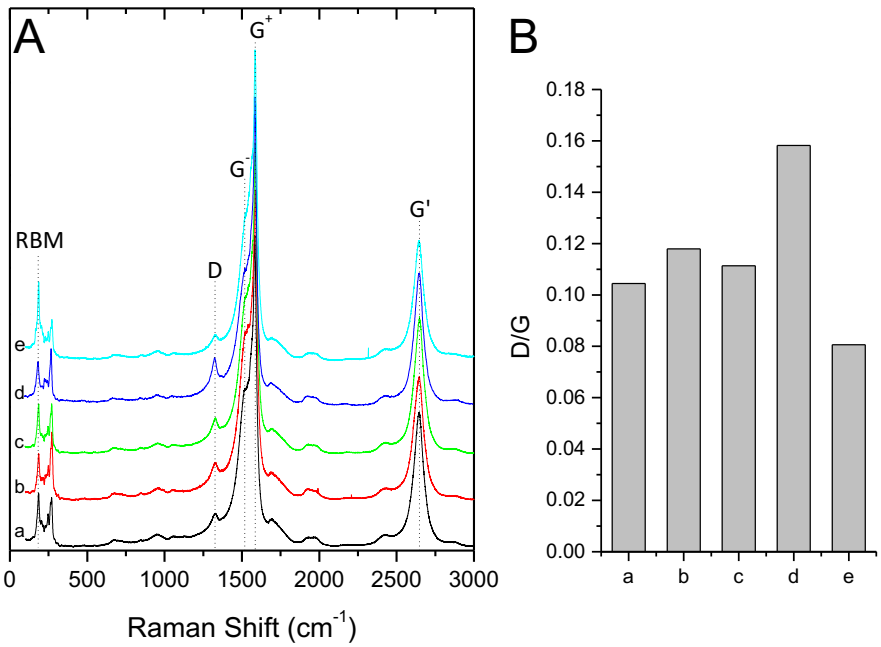

Figure 23. Representative Raman (λ_{ex} = 532 nm) spectra (**A**) and relative intensity of the D-band (**B**) of pristine **SWCNT** (a) and **SWCNT- compound 1** (b), **SWCNT- compound 1-Zn** (c), **SWCNT-compound 2** (e) and **SWCNT- compound 3** (d). Raman graphitic band, split in the two singularities (G^+, for atomic displacements along the tube axis, and G^- for modes with atomic displacement along the circumferential direction), ring breathing modes (RBM), and disorder band (D) were observed in all spectra. For each spectrum, the relative intensity of the disorder band with respect to G^+ band (I_D/I_G) was calculated.

The addition of a pyrrolidine ring provokes an uncovered loss of carbon-based aromaticity, the added ring is not aromatic and is in orthogonal position to SWCNT surface (A side of figure 24). Differently, the furanyl moiety allows the final carbon-based cycle-adduct to cover better the absence of aromaticity thanks to its new double bond (B side in figure 24).

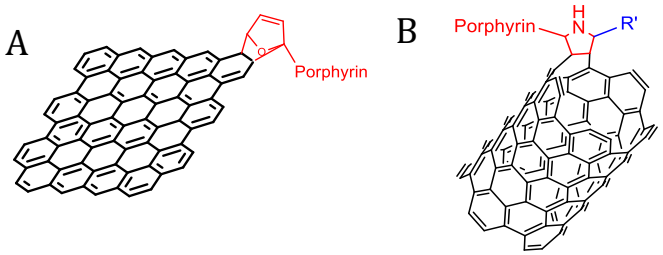

Figure 24. Representation of DA cycloaddition adduct (A) and 1,3 dipolar cycloadditions construct (B) are depicted.

However, the relative intensity and the downshift of G'-band is virtually the same for all samples, indicating that eventually conjugation strain-induced did not significantly affected on the tube curvature.

3.3 Physico-chemical characterization of Porphyrin (2) loaded rGO carbon-based nanosupport

TGA analysis was performed on rGO loaded porphyrin (**2**) derivative. In the temperature range 150-270 °C (region I), rGO-(**2**) exhibited a mass loss which was significantly higher than that observed with pristine rGO. This event was assigned to the thermal decomposition of residual labile functionalities (e.g. OH, COOH) from rGO structure and to the evolution of volatile compounds absorbed on its surface. In the temperature range between 271 and 800 °C (see figure 25), rGO-(**2**) underwent a mass loss of ca. 29%. This thermal decomposition occurs at high temperature (520 °C) showing the presence of stronger interactions between rGO surface and (**2**) because of the presence of covalent bonds.

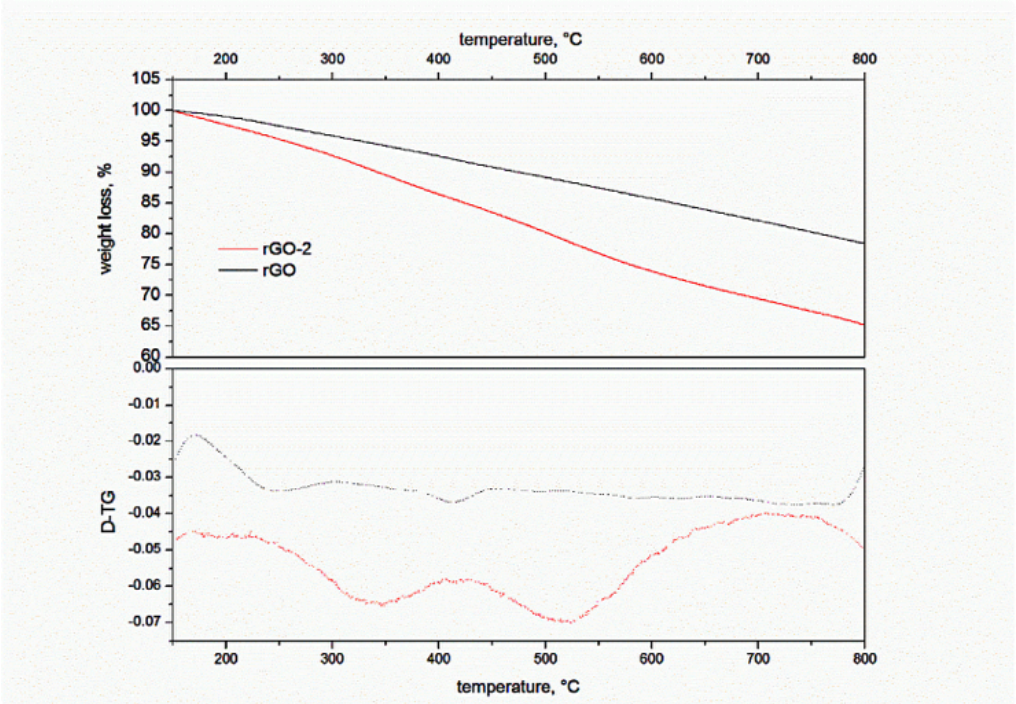

Figure 25. The top panel: TGA analyses of pristine rGO (black line); rGO-(**2**) (red solid line). Lower panel: derivative TG curves of pristine rGO (black dotted line), rGO-(**2**) (red dotted line).

Expressing the amount of porphyrin compound (**2**) grafted on a molar basis (μmol of porphyrin per mg^{-1} of functionalized rGO), the functionalization degree results to be $1.7x10^{-1}$ μmol mg^{-1}, 3.6 times higher than that found in the case of SWCNT grafted with the same compound.

The morphology of rGO-**compound 2** conjugate was analyzed. HR-TEM images of pristine rGO and of rGO-**compound 2** are reported in figure 28. The structure of the pristine rGO exhibits large exfoliated planes where porphyrin grafting may likely occur. The 2-D carbon sheets are occasionally terminated by wrinkles (white arrows) that indicate areas of higher material atomic density (darker portions in the bright field TEM image) and possibly contain a higher number of structural defects. AFM investigation (figures 26-27) of pristine rGO confirmed the large exfoliated nature of the sample by displaying the occurrence of several thin sheets with well-defined geometry (rhombohedral shape), the lateral extension (width) of the aggregates (not well-defined shape, rounded-like) ranges between 0.25 μm and 1 μm in pristine rGO. This analysis proved the pileup of graphene monolayers. If the theoretical monolayer thickness is 0.345 nm (from AFM measurement), the sheet thickness distribution range is, in pristine rGO, from 2.5 to 300 nm (between 7 and 870 monolayers).

The nanoscale morphology of functionalized rGO remains more or less unchanged; a slight increase in denser structures (dark areas) may account for the increase of the piled graphene sheet thickness upon conjugation. This is compatible with the formation of intra-layer cross-linking bridges favoured by the presence of porphyrin pendant chains. The lateral width of the loaded rGO samples structures was lower (0.5μm) than in the pristine.

At the same time, the thickness of the multilayer stacks decreases, ranging from 2.5 to 95 nm (7 to 275 theoretical monolayers). This trend is the opposite of what was expected; this well-defined geometry is higher in the functionalized sample than in the pristine one, meaning that the increased order in stacking is due to the formation of intra-layer cross-linking bridges. Moreover, data could be also explained by consequence of the linking modality chosen: Diels Alder cycloaddition change the C hybridization of carbon-based sheets, breaking up the interconnection between single intra-layer piled graphene sheets (decreasing in sheet thickness).

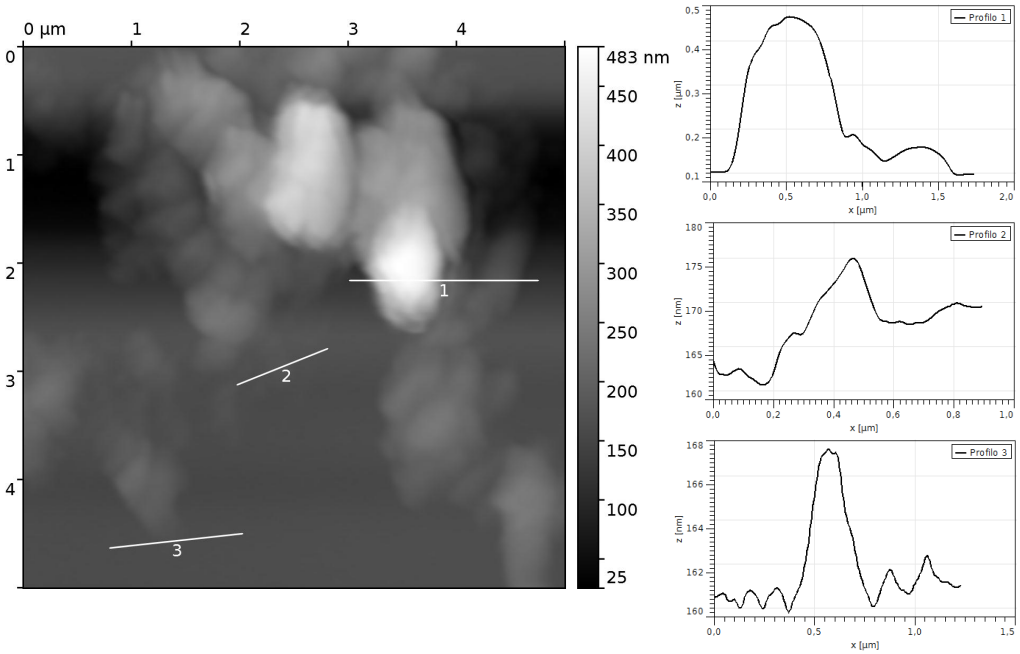

Figure 26. AFM topographic image of pristine sample and AFM height profile of pristine **rGO**. In most cases, especially when the thickness is remarkable (profile 1), the geometry is rounded and not well defined. Profiles 2 and 3 show the height distribution of some thin structures. The thinner structures detectable have a minimum thickness of 2.5 nm (7 monolayers). Relative scale bar: 1 µm.

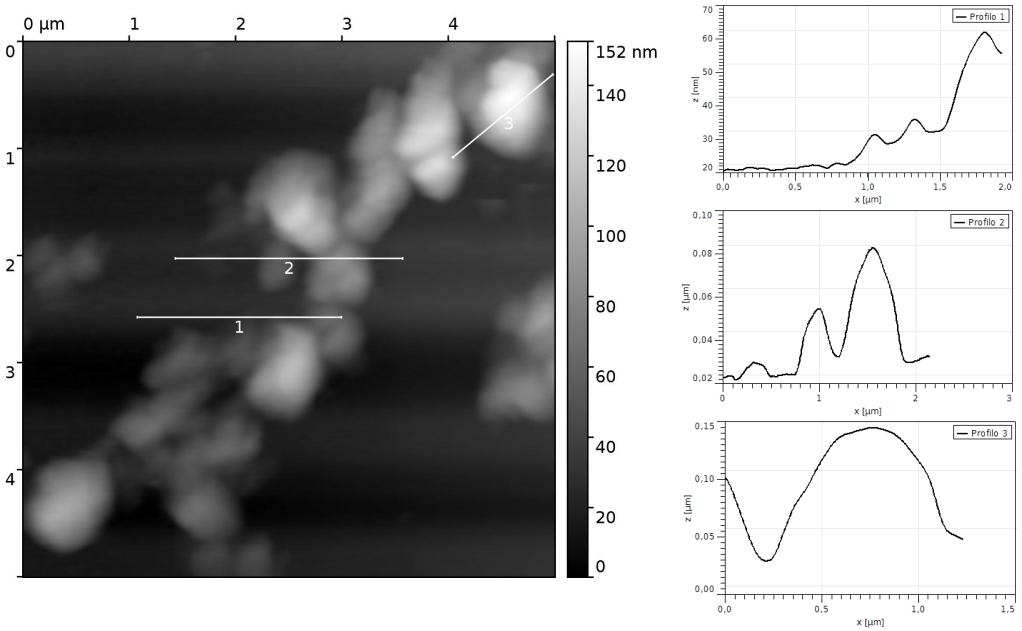

Figure 27. AFM topographic image of the loaded sample and AFM height profile of functionalized compound 2**-rGO.** Profiles 1 and 2 show a sequence of pileup structures with increasing thickness. The minimum stack sequence found is 7 monolayers. In profile 3 the behavior of a very thick structure is reported. The thickness of the structures generally decreases in loaded sample with respect to pristine sample. Relative scale bar: 1 µm.

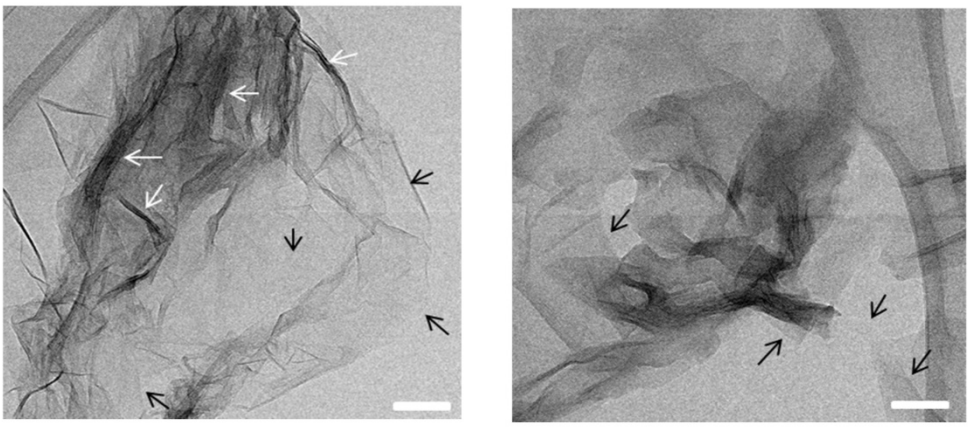

Figure 28. Representative images of pristine rGO (left) and rGO-**compound 2** (right) as seen by TEM. TEM images highlight the exfoliated flat morphology of the rGO sheets (black arrows) in which some denser material (white arrows), due to wrinkles in the graphene sheet, occasionally occurs. Relative scale bar: 5 nm.

Raman spectroscopy confirmed that the functionalization process did not modify significantly rGO structure, the I_D/I_G ratio was calculated on several Raman spectra collected with rGO and rGO-**compound 2**. The measured I_D/I_G ratio was 1.27 ± 0.04 and 1.09 ± 0.04 for pristine rGO and the functionalized one, respectively. The slight decrease in I_D/I_G ratio observed for the functionalized rGO sample clearly indicates that the adopted synthetic approach does not further modify the frame features of the overall carbon-based structure (figure 29).

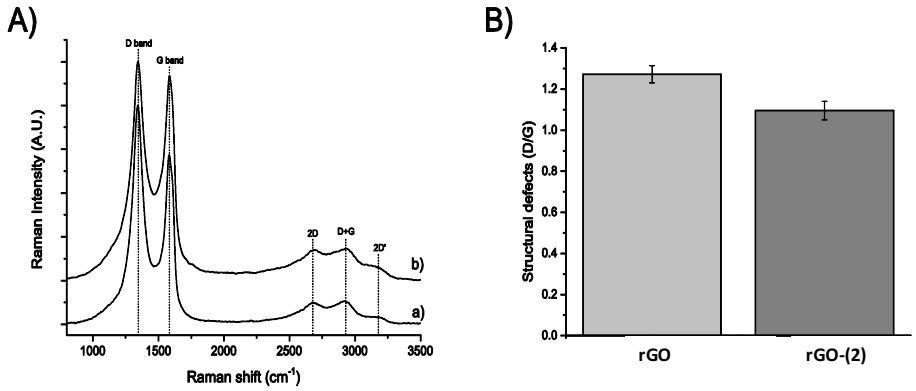

Figure 29. A) Raman spectra of rGO and rGO-**compound 2** (spectra a and b, respectively), and B) evaluation of average graphene sheet defectiveness. All spectra were recorded with an exciting laser wavelength of 523 nm. The position of the G band peak is indicated by a vertical dashed line. The second-order Raman lines are also visible.

3.4 Wrapping procedure for unloaded and loaded-SWCNT derivatives

To evaluate the sonodynamic activity of the reported carbon-based hybrid nanosystems, a series of pilot *in vitro* tests on human colorectal cancer cell line, HT-29 has been carried out. This biological analysis is aimed to compare SDT versus PDT treatment and to understand if the porphyrin distance between the porphyrin nucleus and the hybrid nanosystems surface might have affect in sonodynamic result. However, in order to administrate a suspension of modified SWCNT or rGO, it is mandatory to enhance their water suspension stability and their biocompatibility.

Bare and grafted SWCNT were then wrapped with suitable PEG (polyethylene glycol) chains covalently linked to a phospholipid. To this purpose, SWCNT derivatives suspension in PBS solution of MPEG-DSPE-PEG was sonicated in an US bath (20KHZ, RT, 3 h).

After removal of unbound PEG derivative by ultrafiltration, the wrapped-SWCNT was dispersed in different medium [water, PBS, RPMI (Roswell Park Memorial Institute medium) 1640 and RPMI 1640 +10% FBS (fetal bovine serum)] and then suspension stability was evaluated within 30 days. The hydrophobic lipid chains of the DSPE moiety interact non-covalently with the lipophilic carbon surface, decorating the SWCNT with a PEG sunburst pattern and increasing the stability of SWCNT suspension in all media up to 30 days (no precipitation was observed).

To enhance the suspension stability and avoid/minimize aggregation phenomena, the PEGylated SWCNT were suspended in PBS containing 10% percoll® (colloidal solution of silica coated with polyvinylpyrrolidone), before cell culture investigations.

3.5 Loaded-SWCNT derivatives *in vitro* test on human colorectal cancer cell line (HT-29)

HT-29 cells were previously incubated, for 6, 12 and 24h, with cell medium containing a 1% percoll suspension of PEG-SWCNT (pristine and porphyrin conjugated) and intra/extra cellular fluorescence was measured (FACS). No uptake occurs, the SWCNT remain in the extracellular space, as expected since size and morphology accordingly with literature data.

To evaluate the photo- and sonodynamic activity of each modified and pristine SWCNT, HT-29 cells were detached from plate and mixed with 1% percoll (colloidal solution of silica coated with polyvinylpyrrolidone) suspension PEG-SWCNT derivatives.

Cell suspensions were then exposed to light beam (LB) at 15 mW/cm^2 for 5 min, 405 nm (which cover the excitation profile of porphyrins[99]), or to US at 1.5 W/cm^2 for 5 min, 1.866 MHz. The ultrasound field is generated by a plane wave 2.54 cm transducer (INRIM made) connected to an Amplified Research type AR 100A250A power amplifier and an AGILENT 33250 function generator. A mechanical adaptor filled with ultrapure water has been built to connect the tube (1 cm diameter) containing the cell suspension.

After each treatment, cell proliferation analysis was carried out at 24 and 48 hours. Figure 31 compares cell proliferation with and without external stimuli (LB or US) for all the different formulations.

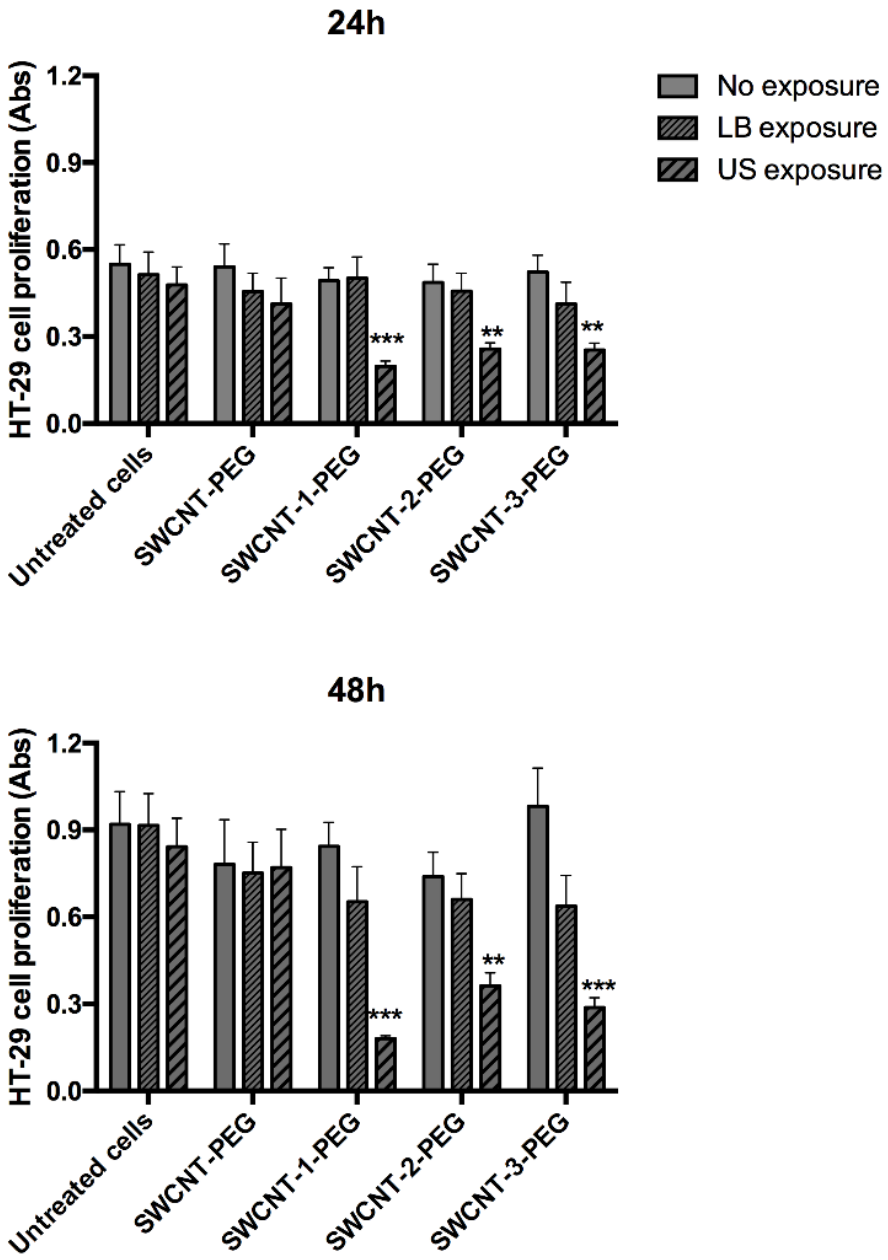

Figure 30. Effect of porphyrin-loaded SWCNT upon LB and US exposure on HT-29 cell proliferation. HT-29 cells were exposed to porphyrin-loaded SWCNT-PEG (SWCNT-**1**-PEG; SWCNT-**2**-PEG and SWCNT-**3**-PEG at 25 μg/mL) and to SWCNT-PEG upon LB (15 mW/cm^2 for 5 min, 405 nm) or US (1.5 W/cm^2, for 5 min, 1.866 MHz). Cell proliferation was evaluated after 24 and 48 h by WST-1 assay. Statistical significance between no exposure (full bars) and LB or US exposure (dashed bars): ** $p < 0.01$, *** $p < 0.001$.

The suspensions of HT-29 with PEG-SWCNT-(**1**), PEG-SWCNT-(**2**) and PEG-SWCNT-(**3**) irradiated by US waves have shown a significant reduction of cellular growth over time (figure 30). No significant alteration of cell proliferation was observed when HT-29 were mixed with SWCNT-**1**, SWCNT-**2** and SWCNT-**3** ("no exposure") and irradiated with LB ("LB exposure"). The US treatment of cells in presence of SWCNT-**1**-PEG, SWCNT-**2**-PEG, and SWCNT-**3**-PEG produces a significant reduction, up to 75%, of the cellular growth over time. On the contrary, LB induced no significant alteration of cell proliferation. This is likely due to the modest porphyrins content compared to the large black SWCNT surface, which absorbs most of the photons. Interestingly, the proliferation reduction is not consequence of the conjugation modality nor from the number of porphyrin molecules loaded (the differences shown in Figure 30 are not statistically relevant), but it is related to the construct itself. The absence of a detectable photo-induced effect may be explained by the peculiar physico-chemical features of SWCNT-porphyrin system, in which a relatively low amount of porphyrin molecules and the occurrence of conjugated rings on SWCNT prevent photo-excitation, yet promoting a remarkable US-induced cellular toxicity. This result evidences that SWCNT-porphyrin behaves as a selective US-activated hybrid nanosystem, possibly minimizing the skin photosensitivity side effect induced by porphyrins. The improvement of this nanohybrid can be further highlighted by comparing cell toxicity induced by our SWCNT-porphyrin system and a porphyrin-decorated polymeric core-shell nanoparticle (PCNP), under the same experimental conditions [6]. A 40-fold lower dose of SWCNT-porphyrin is sufficient to induce a similar cell toxicity. To clarify the mechanism of action of SWCNT-porphyrin system, we assessed the ability of the nanohybrid to generate ROS upon US irradiation.

3.6 ROS production evaluation of Porphyrin (1)-loaded SWCNT

The fluorimetric ROS evaluation was carried out using a well-established method, based on disodium terephthalate assay (TA)[103], applied to a water SWCNT derivatives suspension, using the same US experimental conditions (frequency and intensity) of in vitro biological tests.

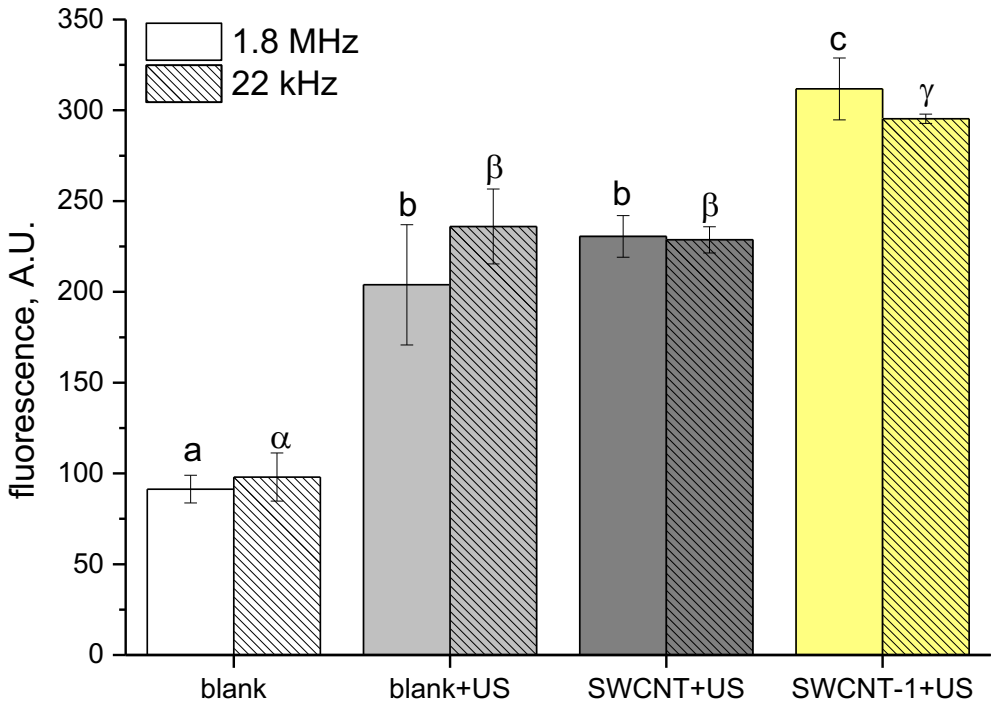

Figure 31. TA hydroxylation induced by SWCNT- **compound 1** sonicated at different frequencies (1.8 MHz and 22 kHz). Pristine SWCNT and porphyrin (**1**)-conjugated SWCNT suspensions and TA only solution (blank) were sonicated (+US) for 5 min and 1 min with an ultrasound probe operated at 1.8 MHz and 22 kHz, respectively. Data are reported as mean ± standard deviation of triplicated experiments. Columns that do not share at least one letter are statistically different (ANOVA, Tukey test $p < 0.05$).

In details, radical hydroxylation reaction of non-fluorescent terephthalate (TA) probe, to give the fluorescent hydroxyterephthalate (TA-OH), was exploited to assess the production of reactive oxygen species (ROS). This test was performed only on SWCNT- compound (**1**) for the higher amount of this product and since there is no difference in cellular viability reduction between the synthetized hybrid-nanosystems.

So, SWCNT-compound 1 in DMSO: water (1:3) suspension was irradiated under two different US conditions: 1.866 MHz and 22 kHz. The first frequency was selected to simulate/reproduce (ex vitro) the same biological experimental conditions, whereas 22 kHz was chosen to verify the behavior of our system in ROS production ability[104]. In Figure 31 the results obtained with porphyrin-grafted nanotubes are reported (SWCNT- compound (**1**) +US) compared with pristine (SWCNT+US) under the same irradiation conditions adopted in cell experiments (1.5 W/cm^2 for 5 min at 1.866 MHz, full columns) and when irradiated with 10 kJ/cm^2 for 1 min at 22 kHz. To prove ROS production by water sonolysis, a blank solution of TA without SWCNT (blank+US) was irradiated under the same conditions. All the results were also compared to a blank solution without sonication (blank), to consider TA autoxidation. Under both US frequencies, ROS generated by SWCNT- compound (**1**) were significantly higher that observed with pristine SWCNT ($p < 0.05$). The collected data indicate a synergistic effect between the carbon-based nanosystem and the grafted porphyrin molecules. Therefore, in such system, the thermal energy, coming from inertial cavitation, is efficiently transferred to the few porphyrin units linked to the nanotube surface, causing molecule excitation. Similarly to what happens in a photo-induced electron transfer (PET) process, the electron transfer between excited porphyrin (electron-donator) and carbon nanotube aromatic surface (electron-acceptor) stabilizes the separated-charge state, increasing the probability of molecular oxygen to react with the excited system and facilitating the ROS production via US excitation (Figure 32).

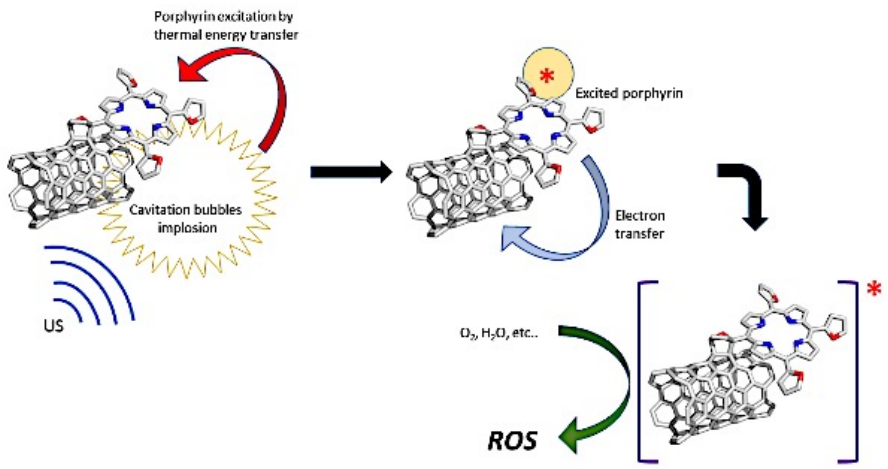

Figure 32. Schematic representation of SWCNT-porphyrin pathway excitation upon US and consequent enhancement of ROS production.

3.7 Porphyrin derivatives loaded on lipidic shells: compounds (4) -(7) and (8) -(11)

Lipid shells represent another interesting class of nanoparticles in SDT application. Liposomes (Visudyne in clinic for PDT ophthalmology application), nanobubbles (NBs) and SLN have been selected to be investigated as porphyrin carrier, because of their physico-chemical features and their biocompatibility. For example, Photofrin, a complex mixture of hydrophobic dimers and oligomers ranging from 2 to 9 porphyrin units primarily linked by ether bonds, proved to be significantly more efficient against a human glioma implanted in rat brain when the photosensitizer was formulated in liposomes as compared to non-liposomal Photofrin[105].

Among the wide variety of nanosystems, NBs nanoparticles have been chosen because of their particular gas-core structure. Thanks to this structure, they possess the ability to operate as an US contrast agent without any further modification and they could act cavitation nuclei if irradiated with proper US frequency. So, we can simultaneously exploit these two peculiarities realizing porphyrin loaded-NBs able to give a real-time visualization target tissues and on-demand activate the sonodynamic effect, obtaining in this way an US-activated theranostic agent. SLN were selected because of their high loading ability, their biocompatibility and their ability to cross the blood brain barrier. Finally, liposomes were chosen thanks to their use in clinically approved protocols and for their physico-chemical feature.

A lipophilic porphyrin derivative is necessary for the non-covalent interaction with nanoparticle shells. Two new classes of porphyrin derivatives were designed. Compounds (**4**) -(**7**) are obtained starting from commercial available meso-tetrakys-(4-hydroxyphenyl)-porphyrin with 1-Bromododecane, obtaining four derivatives with different substitution degree (see scheme 4). Compounds (**8**) -(**11**) (scheme 5) were synthetized from already prepared porphyrin derivative, compound (**c**), and lauryl chloride. These latter obtained derivatives possess a higher overall amphiphilic structure thanks to the presence of four aminoethoxy-ethoxyethyl-amino bridges between porphyrin nucleus and lipophilic chains.

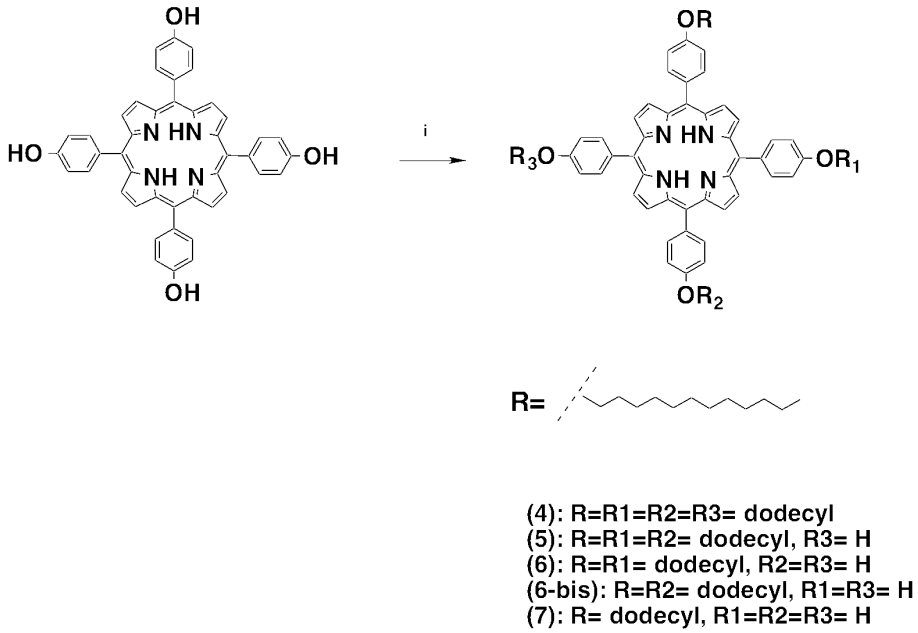

Scheme 4. Synthetic pathway of **compounds (4) -(7)**: *i)* Meso-tetrakys-(4-hydroxyphenyl)-porphyrin, 1-Bromododecane in CH_2Cl_2, DMF, Na_2CO_3 and 18-crow-6 (catalytic amount).

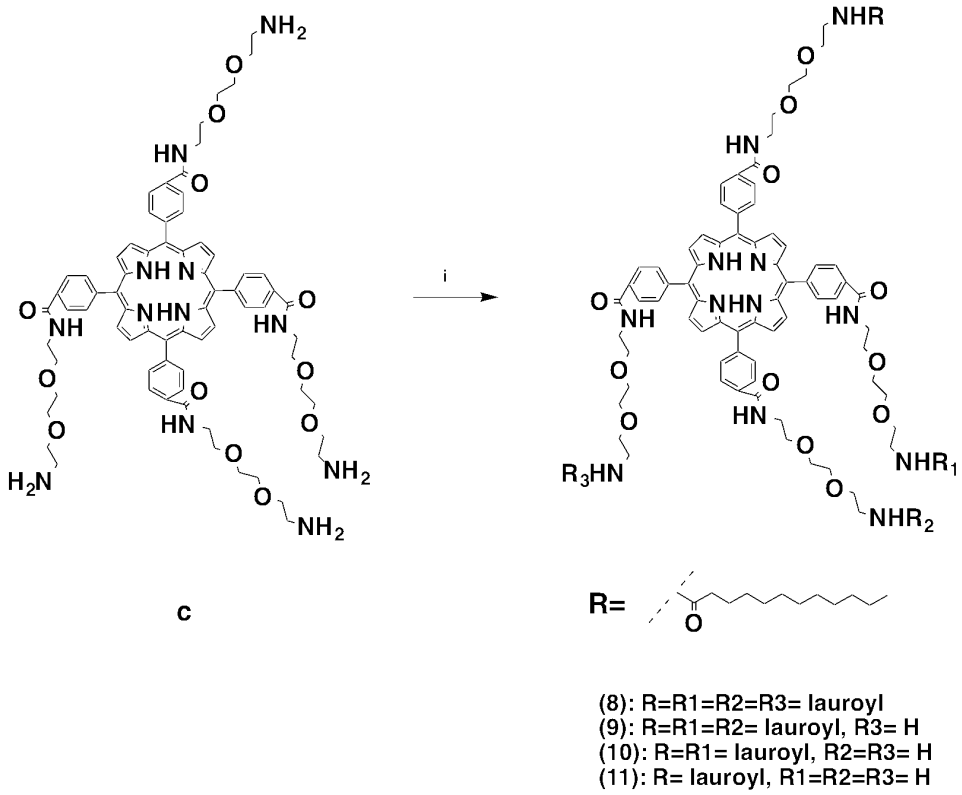

Scheme 5. Synthetic pathway of **compounds (8) -(11)**: *i)* Meso-tetrakis-[4-(aminoethoxy-ethoxyethyl-aminocarbonyl)-phenyl]-porphyrin (compound **c**), lauryl chloride in CH_3CN, Dioxane and CH_3CN, Na_2CO_3.

3.7.1 *Synthetic Porphyrin derivatives loaded-NBs*

Compound (**4**), scheme 4, and compound (**11**), in scheme 5, were selected as model compounds for each class of porphyrin molecules, and they were loaded on NB shells. The interaction between porphyrin and phospholipidic shell (the porphyrin loading) is markedly dependent by the nature of porphyrin lateral chains. The amphiphilic behavior of compound (**11**) seems to be crucial for a correct interaction between sonosensitizer and all key component of NB formulation.

Porphyrin loaded NBs were formulated using a well optimized procedure[106]. To the lipid mixture, L10 Pluronic was added. Non-ionic surfactant Pluronic[107] assumes a peculiar role as NBs size control excipient. L10 Pluronic is a triblock copolymer, hydrophilic ethylene oxide (EO) and hydrophobic propylene oxide (PO) arranged in EO-PO-EO and classified as inactive excipient by the FDA. This specific component turns out to be key element to obtain nanoscale bubbles and to make them more biocompatible[108] together with polyethylene glycol (PEG).

After NB formulation, porphyrin loading was estimated by collecting the entire bubbles layer, washing it and lyophilizing the suspension. After dissolving the residue in a mixture of methanol and chloroform (2:1), to avoid lipid aggregation, the porphyrin content was determined by fluorescence measurement.

The most lipophilic structure (compound **4**) loading on NB is very low and the fluorescent microscopy analysis allows to observe porphyrin mainly as nanoaggregates. A mean of 1800 porphyrin molecules were calculated for each NB. The number of porphyrin molecules per NB was estimated from the overall porphyrin concentration in the bubble layer and the number of nanoparticles determined by nanoparticle tracking analysis (NTA. NanoSight®, Malvern Instruments). Because of the lipophilic structure of compound (**4**), interactions with the lipid monolayer of the NB appeared unlikely. Conversely, compound (**11**), due to its four hydrophilic arms (red lines, Figure 33), one of which functionalized with the lipophilic chain, (blue line, Figure 33) could be loaded more efficiently into NBs than compound (**4**). An average of 3300 porphyrin molecules per NB has been calculated for compound (**11**); fluorescence microscopy does not evidence any porphyrin nanoaggregates and confirm the distribution of (**11**) into the lipidic rim.

The higher loading of compound (**11**) than compound (**4**) in the lipid NBs could be attributed to the amphiphilic nature of side chains in compound (**11**), which have similar structure to Pluronic L10 and to phospholipidic arrangement in the bubble shell (Figure 33).

The data suggest that porphyrin modification has to be tailored ad hoc to the optimized NB formulation, mimicking the phospholipid and additive polar/hydrophobic balance and distribution. More specifically, the porphyrin chain should contain a distal lipophilic region to interact with the non-polar phospholipid tails and Pluronic–PPO in the NB shell. The porphyrin should be amphiphilic to also allow its polar region to interact with the polar phospholipid heads and Pluronic–PEO in the NB shell. Because of porphyrin geometry, only one chain is needed to achieve successful NB incorporation; additional chains are likely not involved in the interaction with NB monolayer components.

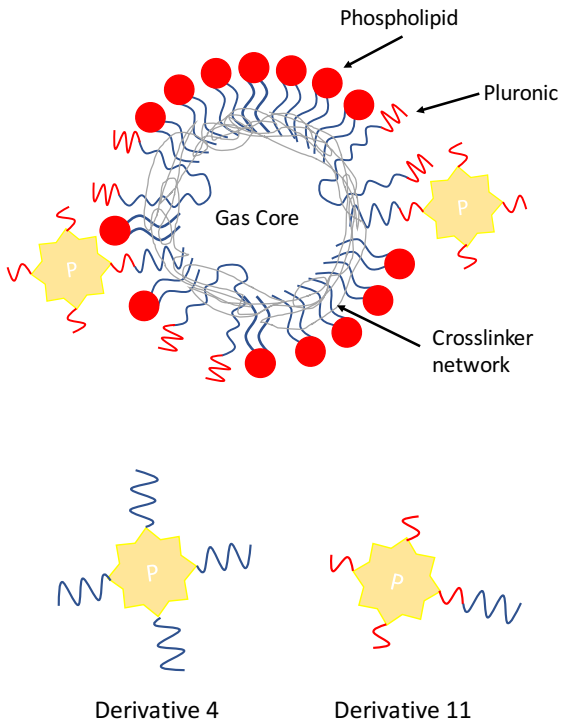

Figure 33. Schematic representation of porphyrin derivatives (**4**) and (**11**) and their interaction with NB monolayer.

Both porphyrin loaded NBs were fully characterized. The mean diameter and polydispersity of Pluronic nanobubbles were measured using nanoparticle tracking analysis (NanoSight®). Without porphyrin, NB diameter was found to be 137.0 ± 16 nm (n=3). When porphyrin was loaded into the bubble shell, the NB diameter changed to 144.66 ± 5.6 nm (n = 3) for compound (**11**) and 199.5 ± 14.6 nm (n = 3) for compound (**4**) (Figure 34 A and 34 B, respectively). When porphyrin is included in the monolayer, an overall diameter increase is observed.

In detail, when the porphyrin derivative contains a "Pluronic-like" structure (compound **11**), the change in size is not so drastic as after compound (**4**) addition. It may be possible that Pluronic L10 is excluded from the NB structure when porphyrin molecules are included in the NB formulation, which can lead to the size increase. If porphyrin is quite different from Pluronic L10 (compound **4**), the change in diameter would be more pronounced than in the presence of a "Pluronic L10-like" porphyrin (compound **11**). Thus, we can assume that the role of Pluronic can be well mimed by the amphiphilic bridge because there is no significant difference between compound (**11**)-loaded NB compared to unloaded NB.

The concentration of NB-(**11**) obtained from the NanoSight® was $4.13 \times 10^{11} \pm 8.74 \times 10^{9}$ particles per ml, while the concentration of NB-(**4**) was $2.98 \times 10^{11} \pm 2.59 \times 10^{10}$ particles per ml. The addition of compound (**11**) seems result in the more stable self-assembly of NBs.

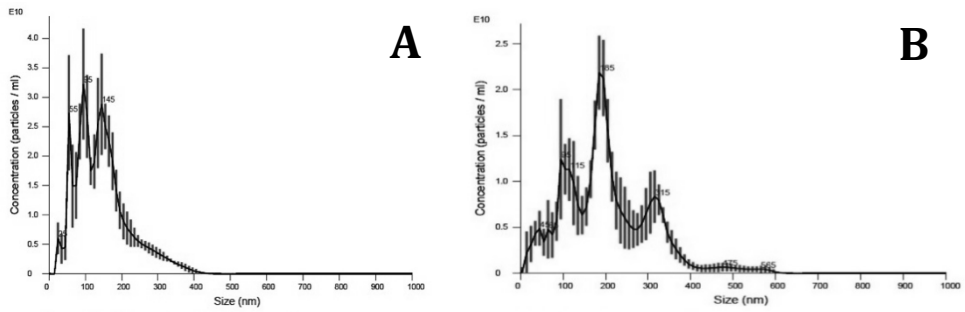

Figure 34. Size distribution of the porphyrin loaded NBs obtained by Nano Sight: compound (**11**)-NBs (**A**) trend and compound (**4**)-NBs (**B**).

Fluorescent microscopy supports the conclusion that compound (**11**) can be more efficiently incorporated into the NB mono-layer than compound (**4**). It is evident that fluorescent signal arising from compound (**11**) is co-localized with bubble shells in suspension. The fluorescent measurements were carried out using a mixture of both nanobubbles and microbubbles (Figure 35). Compound (**4**), which has a completely lipophilic structure, was unable to make efficient interactions with the bubble shell and preferentially self-aggregated into nanocrystals outside the bubbles (figure 35).

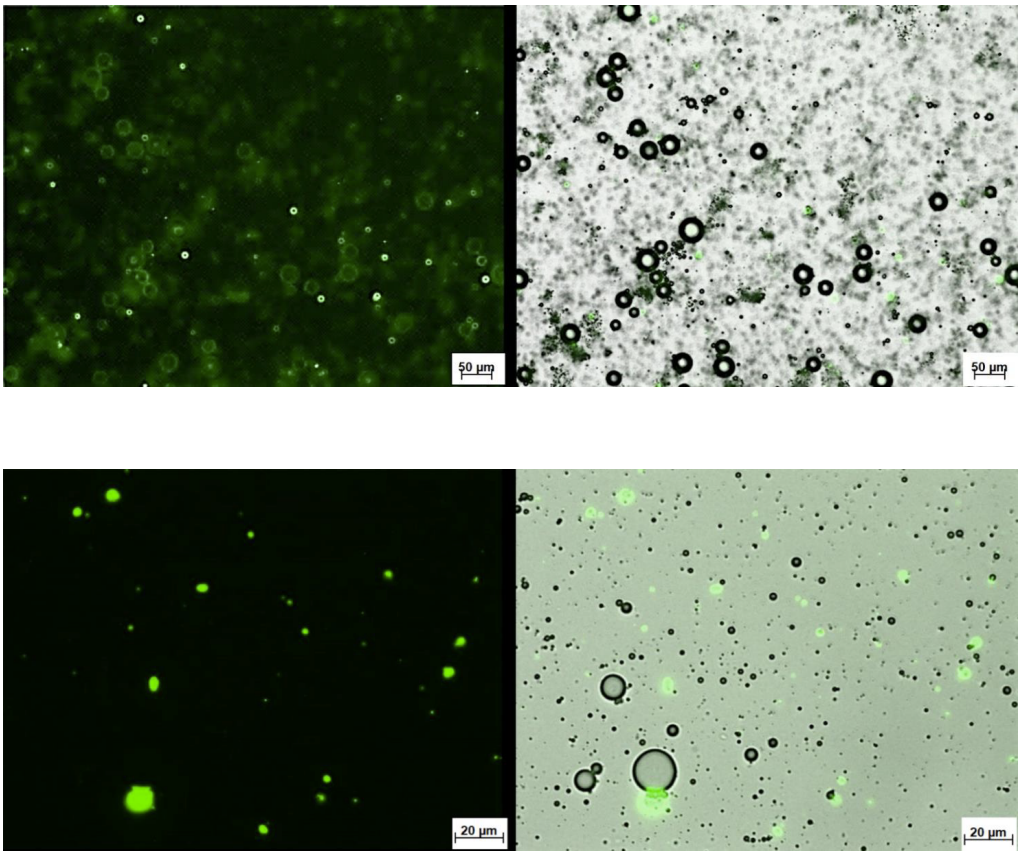

Figure 35. Fluorescent microscopy of amphiphilic compound **11**-bubbles (20X, 50 µm scale bar, upper figure) and of lipophilic compound (**4**)-bubbles (40X, 20 µm scale bar lower figure).

Echogenicity of loaded NBs was evaluated and compared with unloaded ones. The obtained data confirm the retained ability of this system to work as an US contrast agent after porphyrin derivative incorporation (Figure 36). Images were recovered using an AplioXG SSA-790A clinical ultrasound imaging system (Toshiba Medical Imaging Systems, Otawara-Shi, Japan) equipped with a 12 MHz linear array transducer using a contrast harmonic imaging protocol. Images were acquired after diluting nanobubble solution 1:1000 with PBS at pH 7.4 and 700 µl was injected in a custom-made agarose phantom. Phantom was prepared as follow: a 1.5 wt.% agarose gel (BP160-500 from Fisher Reagents) in DI water was prepared inside of a 6-well cell culture plate fitted with a rectangular insert. After gelling, the rectangular insert was removed from phantom and the empty space was filled with NB suspension. The gel was affixed above the US transducer for analysis. The US setup with the transducer placed to the bottom of the phantom gel (see Experimental section).

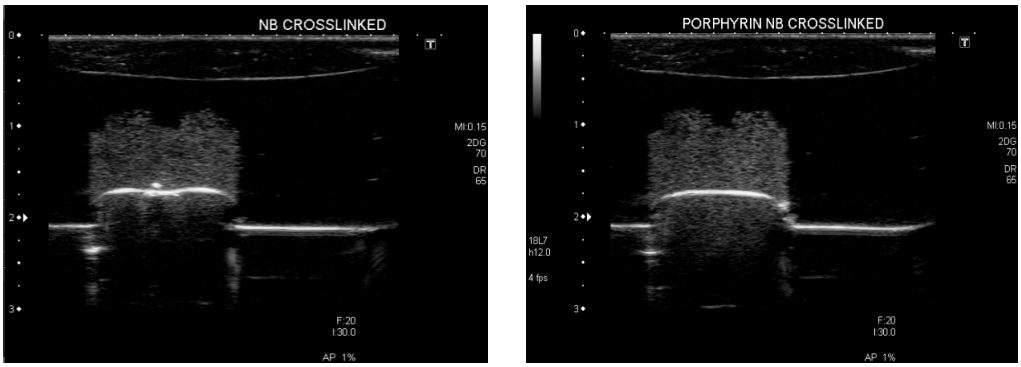

Figure 36. Representative ultrasound images of nanobubbles: unloaded NBs (left) and compound (**11**)-NBs (right). Images are shown inverted due to transducer orientation.

NB stability under US irradiation for imaging purposes was evaluated for both loaded and unloaded bubbles, by measuring the decay in ultrasound signal intensity over time. These data suggest that porphyrin destabilizes the nanoconstruct increasing its signal decay rate to 25% when it is compared to unloaded NB signal (see Experimental section for all details). Sonodynamic activity was preliminary evaluated by a pilot *in vitro* test on human colon adenocarcinoma, LS 174 T cells. Cells were incubated with either unloaded NBs (reference control), 0.1 or 2.5 ug/ml of soluble porphyrin (TPPS, *meso*-tetraphenylporphine-4,4′,4″,4‴ tetrasulfonic acid) in the presence of unloaded NBs, or with compound (**11**) or (**4**)-loaded NBs. Cells were then exposed to US irradiation and, after 3 days, a proliferation test was performed. This biological analysis is aimed to compare the behavior of encapsulated porphyrin with non-encapsulated porphyrin TPPS. Figure 37 clearly shows a statistically significant reduction in cell viability when cells were treated with NB-(**11**), whereas no reduction was observed with unloaded NB and free, soluble TPPS. These results could be explained considering the role of NBs as cavitation nuclei[77] and the distribution of porphyrin in the NB surrounding media. When we consider the case of loaded NB-(**11**) and loaded NB-(**4**)**,** porphyrin molecules are included in the lipidic NB shell (with different derivative content), hence porphyrin molecules are likely very close to the cavitation implosion region. In these cases, porphyrin can be excited more efficiently, allowing to a low number of porphyrin molecules to produce enough ROS [109-111] for cell death. When porphyrin is placed outside the NB (in the case of TPPS-nb), the collapse of bubbles excites less porphyrin molecules (which are away from the cavitation site) causing a lower biological effect.

This suggests that it is sufficient to have a very low amount of porphyrin loaded in NB shell (1800 molecules per NB, 6 ng/ml of porphyrin) to obtain a significant effect on cell viability reduction. Porphyrin excitation is amplified by the action of gas-filled nanosystems which enhance the acoustic cavitation phenomenon.

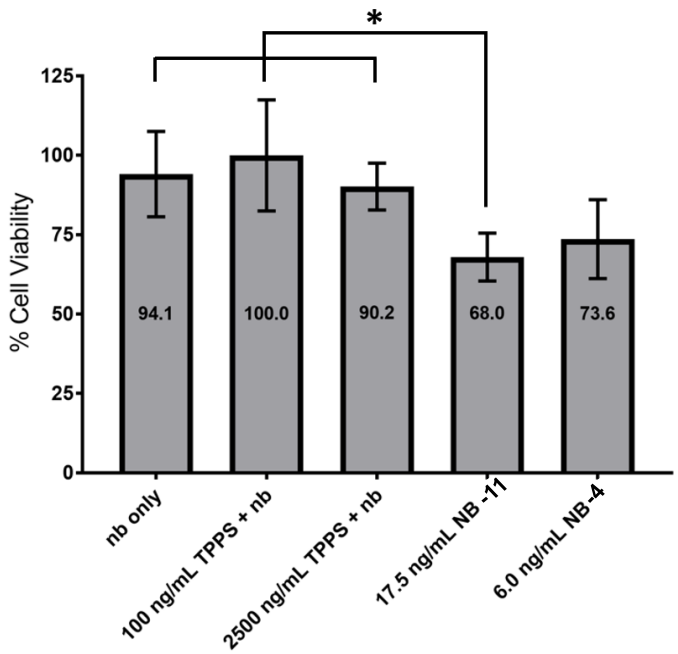

Figure 37. In vitro test on LS 174 T cell line (Human colon adeno-carcinoma) US irradiated for 3 min using 20% duty cycle, 3 MHz transducer, 1.8 W/cm^2 intensity. Studies were carried out under temperature controlled conditions (37°C). Loaded NB: NB-(**11**), total porphyrin content of 17.5 ng/ml; NB-(**4**), total porphyrin content of 6.0 ng/ml. NB particle concentration was kept constant for all wells. "nb" indicates unloaded nanobubbles. * indicates $p < 0.05$ as determined by a student's t-test.

3.7.2 Synthetic Porphyrin derivative (4) loaded on –Liposome and-SLN

Compound (**4**) was also encapsulated in liposomal nanoparticles, thanks to a collaboration with Prof. Silvia Arpicco (DSTF department, University of Turin) and on SLN nanostructures thanks to a collaboration with Dr. Elena Peira (DSTF department, University of Turin). This study aims to investigate the ability of other, lipid nanosystems in loading compound (**4**) and to compare their SDT effect with those obtained from porphyrin derivative (**4**) loaded on NBs. Since NBs and liposomes possess similar matrix lipid composition and features, by consequence we can suppose a similar encapsulation capability. Conversely, SLN nanoparticle, since their entire lipidic matrix composition and their different formulation steps, could show a different loading behavior.

In fact, SLN nanoparticles turned out to be the greatest system in loading porphyrin derivate (**4**) reaching 87.6% of encapsulation efficiency (EE%) and a drug loading (drug incorporated/total lipid ratio (DL%) of 2.1%. This value was obtained by UV analysis (400 nm) after SLN purification by column (gel chromatography). Trilaurin (tridodecanoic acid triglyceride) could be the key component of this system in giving good encapsulation because of the similarity in lipidic chain structure of derivate (**4**) (see Scheme 4) and the three fatty acid groups of trilaurin. Porphyrin (**4**) was encapsulated in SLN by using an optimized procedure (cold dilution of micro emulsion (μE) see experimental section for details) with a lipid/porphyrin ratio of 40:1 w/w, respectively. The main diameter of loaded SLN was 346.4 nm ± 2.1 before column purification and 354.0 nm ± 2.4 after column purification.

As expected, the liposome ability to load porphyrin derivate (**4**), was worse than SLN. This is probably due to do porphyrin geometry and composition and the bilayer formulation of liposome. In fact, the encapsulation efficiency (EE%) was only 0.56% with a drug loading (DL%, drug incorporated/total lipid) of 0.004%. Porphyrin derivate (**4**) was loaded on liposomes by using a well optimized procedure, (see experimental section for details) with a lipid/porphyrin (derivate (**4**), 100 μg) ratio of 134.8:1 w/w. Main liposome diameter was 96.6±1 nm.

Almost the same loading value was achieved using NBs nanoparticles, in this case the encapsulation efficiency (EE%) was found to be 0.5% with a drug loading of 0.07% (lipid/drug ratio of 7:1 w/w).

3.8 Chlorophylls as natural source of porphyrin

Since often the synthetic procedures to obtain porphyrin compounds is very arduous with low yields and sometimes takes long purification steps, Chlorophylls (Chls) have been proposed as natural substitute reserve of synthetic sensitizing agents[112-113]. Chls is a complex mixture of lipophilic magnesium-porphyrins, characterized by an esterified long chain alcohol (C-17), isolated from green plants. They have already been investigated in PDT approach because of their high efficient light-absorption behavior[114].

Chls have several functions in photosynthesis: in absorption light and in charge separation and energy transduction processes. N. Keren et al. showed that as excited states of chlorophyll are very long-lived[115]; in oxygenated environment this means high ROS production after excitation.

Since Chlorophylls are nontoxic derivatives, easily to restock and widespread, we have decided to consider these compounds for SDT applications. And also thanks to the UNI.COO agreement with La Paz (Bolivia), the experimental design starts from an extraction procedure (from alkaloids Evanta plant byproducts made in Bolivia), passes through Chls nanosystems encapsulation and it concludes with preliminary studies of SDT treatment. Literature reports only few studies[113, 116] about the use of chlorophylls as sonosensitizing agent and only ROS generation upon US irradiation has been considered without any biological tests (showing the real effect of this therapy). For this reason, we decided to develop extractive and purification methods to recover Chls from by-products of Evanta alkaloids extraction, which show interesting results in clinical studies for the treatment of cutaneous Leishmaniasis.

3.9 Chlorophylls extraction, characterization and encapsulation in nanoparticles

Chlorophylls extraction were carried out in Bolivia with the support of the Bolivian IIFB's (Instituto de Investigaciones Fármaco Bioquímicas, La Paz). The product purification and characterization were performed in Italy, they were aimed to the obtainment of a purified and well-defined mixture. Chlorophylls mixture was purified by Sephadex LH 20 column chromatography (see Experimental section) and characterized by HPLC-MS (identification of MS-fragments, see Figure 38-39, thanks to the contribution of Prof. Maffei's Lab), then chlorophylls suspension was loaded on selected nanoparticles.

Chlorophyll mixture was analyzed using reverse phase column chromatography C30 (YMC) in acetonitrile/methanol/water 70/20/5 v/v as solvents.

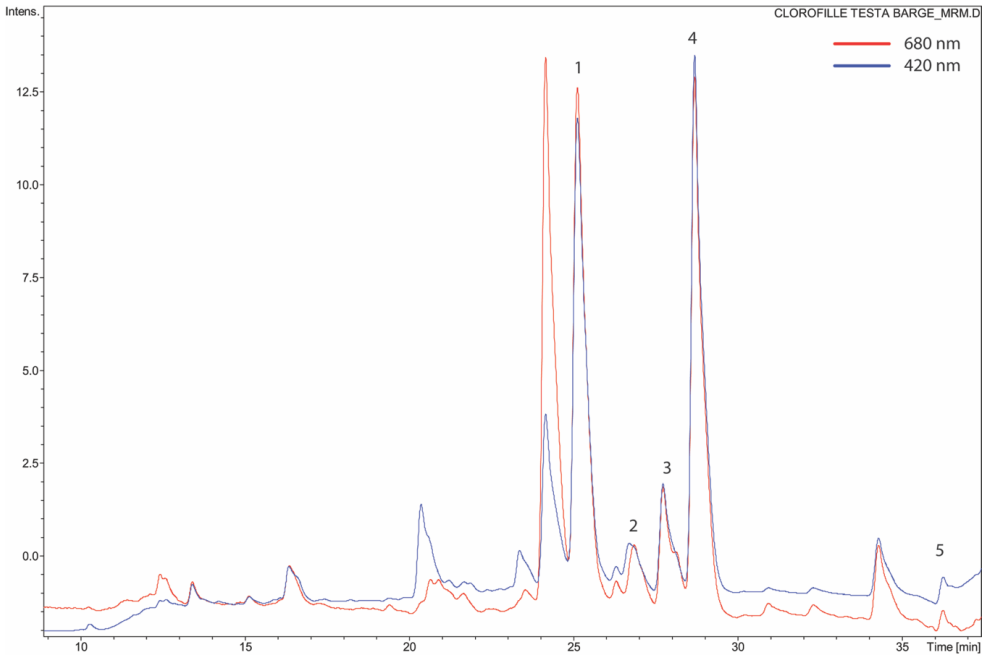

Figure 38. HLPC-MS chromatogram with $[M+H]^+$ mass fragments identification. Chlorophylls mixture for the analysis was dissolved in acetonitrile/methanol/water 70/20/5 v/v.

Compound #	$[M+H]^+$	Fragments MS_2	Identification
1	885	609, 591, 531	Pheophytin b
2	827	550	Pyropheophytin b
3	871	594, 534	Pheophytin a (isomer 1)
4	871	594, 534	Pheophytin a (isomer 2)
5	813	535, 507, 447, 435	Pyropheophytin a

Figure 39. $[M+H]^+$ mass value for each identified peaks/ compound.

Chlorophylls were included in different type of nanoparticles: SLN and liposomes, already tested with porphyrin compound (**4**), and also in micelles and PLGA particles. PLGA nanoparticles were here introduced thanks to a collaboration with Prof. Barbara Stella (DSTF department, University of Turin). They are innovative nanoparticles formed by biodegradable FDA-approved copolymer: poly lactic acid (PLA) and poly glycolic acid (PGA). These polymers are physically strong and highly biocompatible and have been extensively studied as delivery vehicles for drugs[117].

Liposomes (757 μg/ml of chlorophyll mixture in HEPES buffer at pH 7.4, encapsulation efficiency – EE% - of 70% and drug loading -DL% - of 14%, 5:1 lipid/drug ratio), SLN nanoparticles (550 μg/ml of chlorophyll -inside the matrix- with an encapsulation efficiency of 85% and DL% of 5.6%, 15:1 lipid/drug), chlorophyll micelles and PLGA nanoparticles (300 μg/ml in water solution of chlorophyll mixture as final concentration, EE%=100%, DL%=5.0%, 20:1 PLGA/drug) were prepared.

Before proceeding with the evaluation of sonosensitizing ability of chlorophylls loaded nanoparticles, chlorophylls mixture IC50 was measured on PC-3 cell line and it was found to be more than 500 ug/ml (without US irradiation). US cells treatment was firstly carried out using the higher nontoxic chlorophylls concentration determined by IC50 tests (50 μg/ml), but using that concentration no differences in viability reduction were observed with different formulation (viability reduction was more than 85% for all nanoconstructs). To enhance the differences between formulations, due to their intrinsic characteristics, a chlorophylls concentration of 5 μg/ml has been selected for all formulations. The cellular proliferation, upon US irradiation, was evaluated and compared with that measured with unloaded nanoparticles (figure 40).

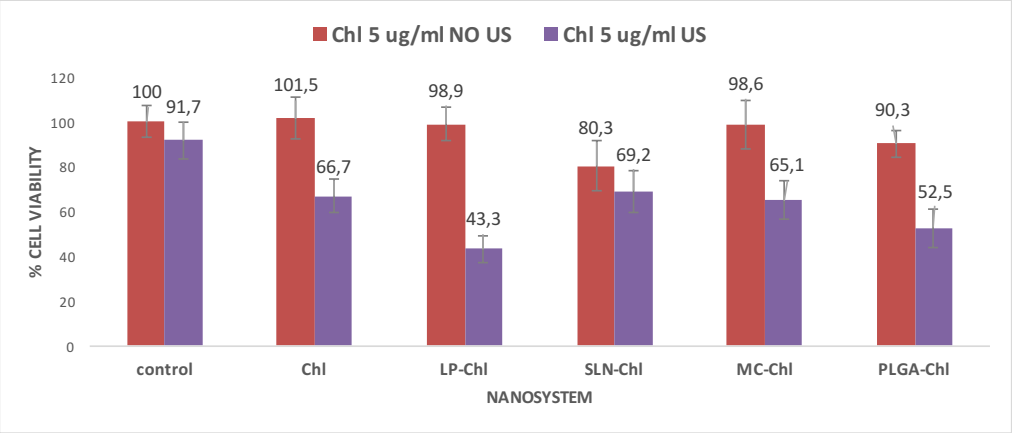

Figure 40. Cellular viability reduction (%) of free Chlorophyll vs loaded Chlorophyll on nanoparticles were *in vitro* tested on PC-3 cell line upon US irradiation (violet bar) and without external stimuli (red bar) at 24h.

Chlorophyll acts as a good sonosensitizer under these experimental conditions. Chlorophyll loaded liposomes turn out to be the most efficient system in increasing the sonodynamic efficacy (reducing the cellular viability up to 60%). Since all these systems can be included into cells, the cellular uptake was also evaluated at different times (1, 3, 6, 12 and 24 h, figure 41 and see Experimental section for details). Moreover, ROS quantification analysis was performed after 5 minutes of US irradiation (figure 42 and see Experimental section for details).

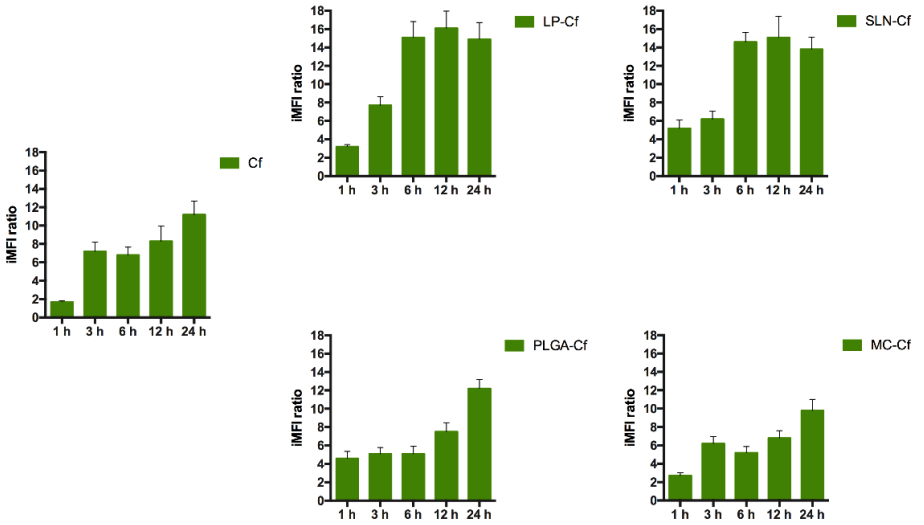

Figure 41. Cellular uptake at 1, 3, 6, 12 and 24h of free Chlorophyll (Cf) and loaded-Chlorophyll.

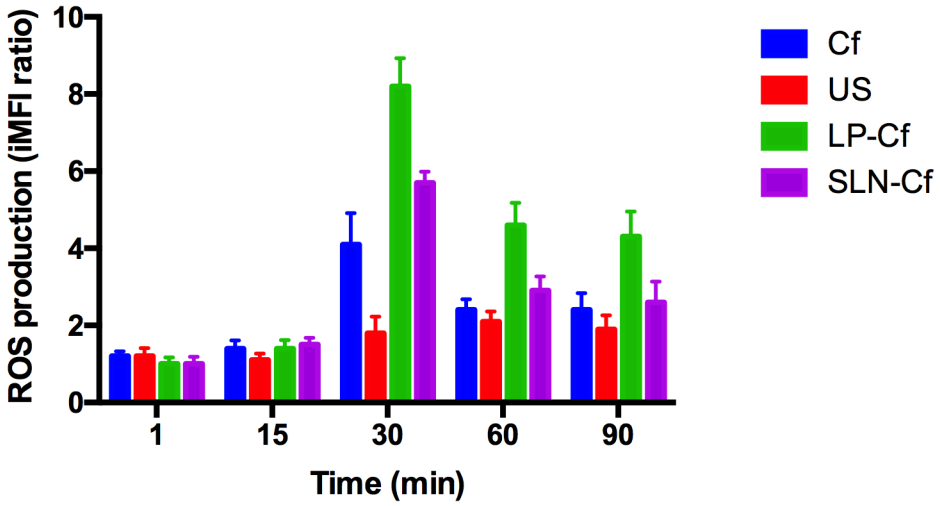

Figure 42. ROS produiction at t1, 15, 30, 60, 90 min after US irradiation for 5 min.

Liposomes and SLN are the loaded nanosystems exerting the highest sonodynamic effect, due to highest ROS production. They also show the highest cellular uptake. On the basis of this data, sonodynamic efficacy in cells seems to be correlated with cellular uptake. Differently to what is observed with carbon based-nanotubes (no cellular uptake), here, the chlorophyll loaded nanosystems need to be firstly encapsulated into cell in order to induce the cytotoxic effect.

4 MATERIALS AND METHODS

Where not otherwise specified, the reagents and solvents were purchased from Sigma (Milan, Italy) and used without further purification. Meso-tetrakis(4-carboxyphenyl) porphyrin and Meso-tetrakys-(4-hydroxyphenyl)-porphyrin were purchased from Frontier Scientific (Logan, Utah, USA). Pure HiPco single walled carbon nanotube was purchased from Unidym (Sunnyvale, CA). Disodium terephthalate (purity ≥ 99%) was from Alfa Aesar (Germany). Ultrapure water was obtained from a Milli-Q water purification system (Merck Millipore, Italy). Furfural was distilled under vacuum prior to use. MW assisted reactions were carried out in a monomode reactor Monowave 300 (Anton Paar Italia Srl, Italy) equipped with a full monitoring system of temperature, pressure and power input. The CombiFlash RfsTeledyne (ISCO) purification system was used to purify all crude reactions on silica gel. Analytical and Preparative HPLC-MS was performed using a FractionLink auto purification system (Waters) equipped with a 2996 photo diode array detector and Micromass ZQ detector (ESCI hybrid ionization source). NMR spectra were recorded on an Avance 300 or on an Avance 600 spectrometers (Bruker) operating respectively at 7T and 14T, dissolving samples in proper deuterated solvent. Chemical shifts were referenced per residual solvent signals. MS spectra were carried out using electrospray ionization (ESI) or by atmospheric pressure chemical ionization (APCI), in positive ion mode, on a Micromass ZQ spectrometer (Waters). TGA analyses were carried out under dynamic nitrogen atmosphere (35 mL min-1) by a Pyris 1 ultra-micro-balance; the gases evolved during the heating ramp were continuously monitored by a Spectrum 100 FTIR spectroscope (Perkin Elmer) The gas evolved during the heating ramp was piped (gas flow 65 mL min-1) via pressurized heated (280 °C) transfer line (Redshift S.r.l. e Vicenza, Italy) and analyzed continuously by the FTIR (Spectrum 100, Perkin Elmer), equipped with a thermostated (280 °C) conventional gas cell. The spectra were acquired in the 4000-600 cm-1 wavenumber range with a resolution of 0.4 cm-1 and analyzed with the Spectrum software (Perkin Elmer). Temperature-resolved infrared profiles of the identified volatiles evolved from samples were obtained from the intensity of a representative peak of the investigated species.

TEM analyses: the morphology of the samples was investigated in the nanometric range by means of a JEOL 3010-UHR transmission electron microscope (TEM) equipped with a LaB6 filament operated at 300 kV, beam current = 114 μA and equipped with a 2k × 2k pixels Gatan US1000 CCD camera.

Micro-Raman spectroscopy: the laser beam of a confocal Raman microscope (Horiba Jobin-Yvon HR800 and Olympus BX41 microscope) has been focused on a 1 μm × 1 μm wide portion of the SC. A polarized solid state Nd laser operating at a wavelength of 532.11 nm and power of 80 mW and a CCD air-cooled detector operating at -70 °C were used. Calibration of the instruments was performed by measuring the Stokes and anti-Stokes bands of the Si band at 520.7 cm-1. Samples were placed on a polished stainless-steel slide and a 50 × objective delivering a power of c. 15 mW on the sample was used. Spectra were acquired with a spectral resolution of ca. 2 cm-1 and an integration time spanning from 100 to 400 seconds.

AFM topography: AFM measurements were performed using a DME SPM Microscope (DME Igloo, Denmark) equipped with a DS95-50E scanner (scan volume 50x50x5μm). The data were acquired using MikroMasch Ultrasharp NSC16/Si3N4 Cr-Au back-coated cantilevers with typical resonance frequency 190 kHz, force constant 45 N/m, tip radius lower than 35 nm and full tip cone angle 40°. Due to the softness of the samples, all measurements were performed in alternated contact mode.

Size dimension: Zetasizer nano (Malvern instruments, UK) for SLN and liposome nanosystems. NanoSight® (NS300, Malvern Instruments) for nanobubbles.

External stimuli (in vitro test): In Italy- A custom system for LB exposure with fixed source-tube positioning and light diffuser all-around cell culture was used. The light-emitting source of the system is based on InGaN light-emitting diodes (Cree Inc., Durham, NC, USA) with 20 mW max radiant power at a central wavelength of 405 nm. The energy fluency rates of the light radiation were adjusted to 15 mW/cm^2 for 5 min, measured using Actinic UV-meter (Jelosil, Le Landeron, CH).

For SWCNT experiments: the ultrasound field is generated by a plane wave 2.54 cm transducer (made by INRIM) connected to an Amplified Research type AR 100A250A power amplifier and an AGILENT 33250 function generator. A mechanical adaptor filled with ultrapure water has been built to connect the tube (1 cm diameter) containing the cell suspension.

In the case of NP-Chlorophyll: the ultrasound field is generated by a plane wave 2.54 cm transducer (made by INRIM) connected to an Amplified Research type AR 100A250A power amplifier and an AGILENT 33250 function generator. The interface between the transducer and the Petri dish (2.5 cm diameter) containing the cell monolayer was daubed with acoustic gel.

In USA- The US field was generated by a plane wave transducer in continuous wave at f0 =1.866 MHz connected to a power amplifier (Type AR 100A250A; Amplifier Research, Souderton, USA) and a function generator (Type 33250; Agilent, Santa Clara, USA). A mechanical adaptor was built to connect the 1 cm diameter polystyrene tube containing the cells suspended in PBS. When filled with ultrapure water, the adaptor creates highly reproducible measurement conditions at a fixed cell tube distance from the transducer.

The therapeutic US apparatus (OMNISOUND® 3000 Pro) with a resonance of 1-3 MHz was used for all US treatments. The transducer with a diameter of 4 cm^2 is horizontally directed to the transparent 24-well plate (TermoFisher Scientific 24 Flat Bottom Transparent) effective output was determined and it was found that intensities of 1.8 W/cm^2 and 20 % of duty cycle.

Cell viability was evaluated by absorbance measurements (450 and 620 nm as reference wavelength) using WST-1 Cell Proliferation Assay (Roche, from Sigma) on a microplate reader (Asys UV340, Biochrom, Cambridge, UK). And by absorbance measurements (450 nm) on Tecan Infinite 200 Microplate Reader.

US images ware recovered using an AplioXG SSA-790A clinical ultrasound imaging system (Toshiba Medical Imaging Systems, Otawara-Shi, Japan) equipped with a 12 MHz linear array transducer.

MICROSCOPIC ANALYSIS. Microscope images were obtained on a Zeiss AxioObserver Z1 microscope using filters: for excitation FITC (450 nm) and Cy5 for emission (670 nm).

ROS QUANTIFICATION Terephthalate solution (8 mM) was prepared dissolving disodium terephthalate in Milli-Q ultrapure water. A stable SWCNT-1 suspension was obtained suspending SWCNT-1 in DMSO (purity $\geq$ 99.9 %). TA solution was added to the DMSO: water (1:3) suspension of SWCNT-1. The concentration of TA and SWCNT-1 in the final mixture was

4.0 mM, and 25 μg/ml, respectively. The suspension was introduced in a polystyrene tube (volume = 3 ml; tube diameter = 1 cm) and exposed to ultrasound (US at 1.866 MHz) under the same experimental conditions employed in cell experiments (namely 0.008 mJ/cm2 for 5 min). Sonication was carried out using different sonotrode frequency (22 kHz): 2 ml of suspension were introduced in polystyrene tubes and exposed to ultrasounds (10 kJ/cm2 for 1 min) employing a sonicator Sonopuls HD3100 equipped with a 73MS probe (Bandelin, Germany). After the US treatment, the suspension was filtered on a cellulose acetate membrane (pore diameter 0.45 μm, Advantec, Japan) and TA-OH fluorescence (λex = 324 nm, λem = ca. 425 nm) was measured on the clear solution by a FLx800 fluorescence reader (BioTek, US). The results were compared to a blank solution without US irradiation and on US-irradiated pristine SWCNT (25 μg/ml) under the same experimental conditions. Three replicates for each experiment were carried out and the results were expressed as the mean values ± SD of the separate determinations and analyzed by a one-way Analysis of Variance (ANOVA) and Tukey's test. $p<0.05$ was considered significant.

HPLC-MS ANALYSIS OF CHLOROPHYLLS MIXTURE IDENTIFICATION: samples were dissolved in tert-methyl-butil-ether. Immediately before the analysis they were diluted in acetonitrile/methanol/water 70/20/5 v/v. The column used for the analysis was reverse phase chromatography C30 (YMC).

Molecules detection was possible thanks to a DAD fixed at 680, 480 e 420 nm using ESI-Ion trap MS_2 with Multi Reaction Monitoring modality.

5 EXPERIMENTAL SECTION

5.1 Synthetic procedures of Porphyrin derivatives

*Meso-tetrakys-(furan-2-yl)-porphyrin (**compound-1**)*

Meso-tetrakys-(furan-2-yl)-porphyrin was obtained using solid-support procedure with yields lower than 1%. The solution protocol was also used and gave better results. A green solid was obtained, at yields up to 3.8%, after HPLC-MS purification. Purification method: min, B%: 0.0, 70%; 2.80, 70%; 4.30, 100%; 8.50, 100%. Preparative HPLC separations were carried out with a Phenomenex Gemini C18 (21.2x100 mm, 5 μm, 110 Å) column, using water (A) and methanol (B) as eluents. Flow rate was 20 mL/min.

HPLC-MS: (method 1) Rt = 14.71 min, purity 80%; ^{1}H NMR (300 MHz, THF-d8, δ 1.73 ppm): δ 9.18 (s, 8H), 8.25 (br. s, 4H), 7.39 (br s, 4H), 7.08 (br s, 4H), -2.55 (s, 2H); APCI-MS +: m/z calcd for $C_{36}H_{22}N_4O_4$, 574.16; found 575.58 [$M+H^+$]; λ max (THF) = 430 nm.

Method 1: min, B%: 0.0, 50%; 7.50, 50%; 22.50, 100%; 32.50, 100%. HPLC-MS analyses were carried out on Waters SunFire (4.6x150, 5 μm) C18 column, using 0.1% trifluoroacetic acid (TFA) aqueous solution (A) and 0.1% TFA in methanol (B) as eluents. Flow rate was 1 mL/min. Product purity was calculated as area ratio on 430 nm and MS TIC traces.

Zn(II)-meso-tetrakys-(furan-2-yl)-porphyrin (**compound-1-Zn**)

The general solution protocol was followed and freshly distilled pyrrole (0.4 M in dioxane) and furfural (0.4 M in dioxane) were used, while $Zn(AcO)_2$ was added to give a final concentration of 0.13 M, at 140°C for 10 min. Amberlyst 15 (2 mg), a strongly acidic resin, was added to the mixture.

After purification, the desired product was recovered as a violet-blue solid (Yield 5.2%).

Purification method: min, B%: 0.0, 70%; 4.30, 100%; 7.50, 100%. Preparative HPLC separations were carried out with a Phenomenex Gemini C18 (21.2x100 mm, 5 μm, 110 Å) column, using water (A) and methanol (B) as eluents. Flow rate was 20 mL/min.

HPLC-MS: (method 2) Rt = 31.22 min, purity 83%; IR (KBr) 3122, 2801, 1676, 1200, 1144, 797, 724 cm^{-1}; ^1H NMR (300 MHz, CDCl3, δ 7.26 ppm): δ 8.60 (s, 8H), 8.37 (s, 4H), 7.82 (d, J= 2.94Hz, 4H), 7.20 (s, 4H); APCI-MS^+: m/z calcd for $C_{36}H_{20}N_4O_4Zn$, 636.08; found 637.60 [$M+H^+$]; λ max (from HPLC-MS analysis, MeOH-TFA, H2O-TFA) = 428, 564, 610 nm.

Method 2: min, B%: 0.0, 65%; 15.00, 65%; 27.50, 100%; 42.50, 100%. HPLC-MS analyses were carried out on Waters SunFire (4.6x150 mm, 5 μm) C18 column, using 0.1% trifluoroacetic acid (TFA) aqueous solution (A) and 0.1% TFA in methanol (B) as eluents. Flow rate was 1 mL/min. Product purity was calculated as area ratio on 428 nm and MS TIC traces.

1-(benzyloxycarbonylaminoethoxy)-2-(aminoethoxy)-ethane (**a**)

1,2-bis-(2-aminoethoxy)-ethane (14 ml, 95.8 mmol) was dissolved in a water/methanol mixture (60ml/30ml) at 0°C.The solution was acidified with HCl 1M until pH=7 and a solution of benzyl choloroformiate (10 ml, 69.7 mmol) in dioxane (72 ml) was slowly added over 10 hours. The temperature was maintained under 10°C and the pH near 7 by adding NaOH 1M. After the addition, the mixture was allowed to reach RT and stirred for additional 30 min. Then solvent was removed in vacuum, the residue dissolved in 40 ml of HCl 0.1M and washed with DCM (20 ml x 2).

The organic phase was washed with HCl 0.1M (20 ml), the aqueous phases were combined and the pH was increased up to 9 by slow addition of concentrated NaOH solution. Compound (**a**) was obtained after extraction of the aqueous phase with DCM (60 ml x 2), dried and used in the next step without further purification (6.0 g, 31% yield).

TLC (silica, DCM/MeOH =9/1) rf = 0.3. ^1H NMR (300 MHz, CDCl3, δ 7.26 ppm): δ 7.34 (s, 5H), 5.59 (br. s, 2H), 5.29 (m, 1H) 5.09 (s, 2H), 3.66-3.52 (m, 4H), 3.52-3.44 (m, 2H), 3.44-3.30 (m, 2H), 2.84 (m, 2H), 1.98-1.81 (m, 2H). ^{13}C NMR (75 MHz, $CDCl_3$, δ 77.16 ppm): δ 156.62, 136.69, 128.53, 128.13, 128.10, 72.70, 70.29, 70.15, 70.11, 66.64, 41.36, 40.89. ESI-MS+: m/z calcd for $C_{14}H_{22}N_2O_4$, 282.16; found 283.53 [$M+H^+$].

Meso-tetrakis-[4-(benzyloxycarbonylaminoethoxy-ethoxyethylaminocarbonyl)-phenyl]-porphyrin (**b**)

Meso-tetrakis-(4-carboxyphenyl)-porphyrin (0.200 g, 0.25 mmol) was dissolved in DCM (50 ml) and left to stir for 1h in the dark. Compound (**a**) (0.564 g, 2.00 mmol), EDCI (0.310g, 2.00 mmol) and DMAP (0.124g, 1.00 mmol) were added to porphyrin solution. The mixture was stirred at RT overnight, under nitrogen atmosphere. Reaction was monitored by TLC (silica, DCM/MeOH 9/1) and MS spectroscopy, and prolonged until disappearance of starting meso-tetrakis-(4-carboxyphenyl)-porphyrin. Reaction mixture was then washed with brine (50 ml x 3) and the organic layer was dried over anhydrous sodium sulfate and filtered.

Solvent was removed under vacuum and the red crude was purified via flash chromatography using pre-packed silica cartridge (RediSep column, 40g) in DCM/MeOH gradient elution (%B, column volume: 0%, 0.0; 0%, 1.0; 15%, 8.0; 65%, 2.0; 65%, 2.0; 100%, 2.0; 100%, 3.3) to give compound (b) (0.323g, 70% yield). TLC (silica, DCM/MeOH =9/1) rf = 0.90. ^{1}H NMR (300 MHz, $CDCl_3$, δ 7.26 ppm): δ 8.73 (s, 8H), 8.14 (m, 16H), 7.35-7.20 (m, 20H), 5.49 (br. s, 4H), 5.08-4.96 (m, 8H), 3.73 (br. s, 16H+4H), 3.62 (br. s, 16H), 3.49 (m, 8H), 3.35 (m, 8H). ^{13}C NMR (75 MHz, $CDCl_3$, δ 77.16 ppm): δ 167.63, 156.56, 145.13, 136.40, 134.60, 134.00, 131.25, 128.51, 128.46, 128.07, 125.60, 119.39, 70.34, 70.12, 66.72, 40.88, 40.04. ESI-MS^{+}: m/z calcd for $C_{104}H_{110}N_{12}O_{20}$, 1847.80; found 1848.96 [M+H^{+}] (from analytic analysis).

Meso-tetrakis-[4-(aminoethoxy-ethoxyethyl-aminocarbonyl)-phenyl]-porphyrin (**c**)

Compound (**b**) (0.240g, 0.13 mmol) was dissolved in methanol/dioxane (100 ml/50 ml) and 24 mg of Pd/C (10%) were added. After air removal, the mixture was vigorously stirred at room temperature (ca. 20°C) for 18 h, then it was filtered and the solvent was evaporated under vacuum.

The crude was purified by preparative HPLC-MS over Waters SunFire C18 column (19 x 100 mm, 5 μm) and using a gradient elution profile (eluent A = water, TFA 0.1%; eluent B = methanol, TFA 0.1%. Gradient, min, B%: 0.0, 50%; 2.1, 70%; 3.5, 70%; 4.2, 100%; 7.0, 100%) with flow rate of 20 ml/min. Compound (**c**) was recovered with 44% yield (75 mg).

^{1}H NMR (300 MHz, CD_3OD, δ 3.31 ppm): δ 8.85 (s, 8H), 8.47 (br. m, 8H), 8.38 (br. m, 8H), 3.89-3.72 (br. m, 16H+16H+8H), 3.18 (t, J = 4.30 Hz, 8H).

^{13}C NMR (75 MHz, CD_3OD, δ 49.00 ppm, from HSQC spectrum): δ 137.03, 131.45, 127.59, 71.10, 67.61, 48.92, 40.56. ESI-MS$^+$: m/z calcd for $C_{72}H_{86}N_{12}O_{12}$, 1311.52; found 1313.20 [M+H$^+$] (from analytic analysis).

Meso-tetrakis-[4-(furan-2yl-methyl-aminoethoxy-ethoxyethyl-aminocarbonyl)-phenyl]-porphyrin (**2**)

Furfural (freshly purified by flash chromatography) (19 μl, 0.228 mmol) was added to a solution of (**c**) (50 mg, 0.038 mmol) in methanol (15 ml) and the pH was increased to 5.5 with NaOH 2M. Then 160 mg of solid $Na(AcO)_3BH$ was added in three portions. Before each addition the pH value was checked ad if necessary it was taken to 5.5. The reaction mixture was allowed to stir overnight. Solvent was removed under reduced pressure and the residue was washed with petrol ether (15 ml x 3). Desired product (**2**) was obtained in 46%. Yield (28.5 mg). ^1H NMR (300 MHz, CD_3OD, δ 3.31 ppm): δ 8.50 (s, 8H), 8.28 (br. t, 4H), 7.96 (br. d, 4H), 7.36 (d, J = 5.64Hz, 8H), 7.31 (br. d, 4H) 6.33 (d, J = 5.84Hz, 8H), 3.66-3.54 (br. m, 16H+16H+8H), 3.07 (br. s, 8H).

Tert-butyl 2-amino-6-(((benzyloxy)carbonyl) amino)-hexanoate (**d**)

Lys-CBz (10 g, 35.7 mmol) was dissolved in terz-butyl acetate (170 ml) and $HClO_4$ (70% in water, 42 mmol, 3.6 ml) was slowly added. The mixture was stirred at RT for 18 h, then water (155 ml) was added. The two phases were separated and the aqueous layer was washed with ethyl acetate (2x 50 ml). The organic layers were then combined and washed with a 5% $NaHCO_3$ solution (2x 100 ml), dried over sodium sulphate and solvent was removed to obtain (**d**) in 94% yield (11.25g).

^1H NMR (300 MHz, DMSO-d6, δ 2.50 ppm): δ 7.32 (m, 5H), 7.19 (t, J= 5.42 Hz, 1H), 4.99 (s, 2H), 3.82 (t, J= 5.95 Hz, 1H) , 3.00 (m, 2H), 1.72 (m, 2H), 1.50-1.15 (overlapped signals, 13H); ^{13}C NMR (75 MHz, DMSO-d6, δ 39.5 ppm): δ 169.6, 156.8, 137.8, 129.0, 128.4, 128.3, 83.5, 80.2, 65.8, 52.9, 30.6, 29.4, 28.1, 22.0; ESI-MS$^+$: m/z calcd for $C_{18}H_{28}N_2O_4$, 336.42; found 337.19 [M+H$^+$].

Tert-butyl 6-(((benzyloxy)carbonyl) amino)-2-((tert-butoxycarbonyl) amino)-hexanoate (**e**)

Compound (**d**) (1.0g, 2.97 mmol) was added to 50 ml of CH_2Cl_2 and heated under reflux until complete dissolution. The solution was allowed to reach ambient temperature and Na_2CO_3 (630 mg, 5.95 mmol) was added.

Mixture was stirred for 1 h then a solution of Boc_2O (1 g, 4.58 mmol) in CH_2Cl_2 (20 ml) was slowly added. The reaction proceeded under stirring overnight, then it was filtered ad washed with 10% $NaHCO_3$ solution (3x 20 ml) and with water (2x 20 ml).

The organic phase was dried over sodium sulphate; solvent was removed under reduced pressure and compound e was collected in 87.5% yield (1.13 g). ^{1}H NMR (300 MHz, $CDCl_3$, δ 7.26 ppm): δ 7.19 (s, 5H), 4.94 (s, 2H+2H), 3.99 (sb, 1H), 3.02 (sb, 2H), 1.73-0.96 (m, 9H+9H+6H); ^{13}C NMR (75 MHz, $CDCl_3$, δ 77.2 ppm): δ 171.8, 156.5, 155.46 146.7, 128.4, 128.0, 127.9, 85.0, 81.6, 79.5, 66.4, 53.7, 32.42, 31.1, 28.3, 27.9, 22.3; ESI-MS$^+$: m/z calcd for $C_{23}H_{36}N_2O_6$, 436.26; found 459.20 [M+Na$^+$].

Tert-butyl 6-amino-2-((tert-butoxycarbonyl) amino)-hexanoate (**f**)

Compound (**e**) (5g, 11.5 mmol) was dissolved in methanol (100 ml) and Pd/C (10%, 500 mg) was added. The mixture was stirred at room temperature under hydrogen atmosphere (atmospheric pressure) for 48h. Then, it was filtered and solvent was removed under reduced pressure obtaining a white solid (2.4g). Acidimetric titration indicates that this solid was formed by compound f (40%) and its carbamic acid form (60%). The solid was dissolved again in methanol, cooled down to 5°C in an ice bath, and aqueous HCl (1M, 4.6 ml) was slowly added. The CO_2 was removed under vacuum, and then NaOH (2M) was added until pH=9. Then methanol was evaporated under reduced pressure and the resulting aqueous phase was extracted with ethyl acetate (3 x 50ml). The organic layer was dried over sodium sulphate and solvent was evaporated to obtain compound (**f**) 15% yield. Acidimetric titration indicates 85% of purity. ^{1}H NMR (300 MHz, $CDCl_3$, δ 7.26 ppm) *: δ 3.82 (sb, 1H), 2.48 (sb, 2H), 1.82-0.70 (overlapped, 6H+18H); ESI-MS$^+$: m/z calcd for $C_{15}H_{30}N_2O_4$, 302.22; found 303.19 [M+H$^+$].

*some impurities were observed; however chemical shifts refer to most abundant compound

Meso-tetrakys-(4-(5-amino-5-carboxypentylaminocarbonyl)-phenyl)-porphyrin (**3**)

Commercial meso-tetrakys-(4-carboxyphenyl)-porphyrin (64 mg, 0.08 mmol) was dissolved in a mixture of CH_2Cl_2 (30 ml) and THF (10 ml), then EDC (165 mg, 0.86 mmol) and DMAP (52 mg, 0.43 mmol) were added. The mixture was stirred at RT for 30 min and a solution of compound (**f**) (306 mg, 85% purity, 0.86 mmol) in CH_2Cl_2 (30 ml) was slowly dropped.

The reaction progress was monitored by TLC (silica, CH_2Cl_2/MeOH=9/1; Rf=0.87), HPLC (Waters SunFire C18 column -4.6x150 mm, 5 μm-; flow=1 ml/min; eluent A= 0.1% TFA in water, B= 0.1% TFA in MeOH, gradient – time, B%- 0.0, 75%; 15, 75%; 27.5, 100%; 42.4, 100%; Rt=29.05 min) and ESI-MS. After 4h the reaction was completed and the mixture was separated by flash chromatography (Silica cartridge 12g, CH_2Cl_2/MeOH: -Column Volume, MeOH%- 0.0, 10.0%; 12.0, 19.6%; 15.3, 19.6%; 17.3, 39.9%; 21.3, 100%; 25.3, 100%) and the product containing fraction was further purified by preparative HPLC-MS (Waters SunFire C18 column -19x100 mm, 5 μm- ; flow=20 ml/min; eluent A= water, B= MeOH, gradient – time, B%- 0.0, 75%; 12.5, 100%; 16.0, 100%) obtaining 50 mg of (**g**) in 34% yield.

The ^{1}H-NMR spectrum shows the presence of (**g**) in mixture with its partially deprotected derivatives which do not compromise its use in the next deprotection step. The solid (**g**) was then dissolved in CH_2Cl_2 (20 ml) and TFA (3 ml) was slowly added. The mixture was stirred overnight, solvent and excess of TFA were evaporated under reduced pressure obtaining compound (**3**), as a blue/green solid (34 mg, yield 53%). ^{1}H NMR (300 MHz, CD_3OD, δ 3.31 ppm): δ 8.82 (s, 8H), 8.31 (m, 16H), 4.07 (sb, 4H), 3.62 (sb, 8H), 2.06 (sb, 8H), 2.29-1.5 (overlapped, 24H); ^{13}C NMR (75 MHz, CD_3OD, δ 49.0 ppm, from HSQC): δ 136.8, 131.4 127.2, 53.5, 40.4, 30.8, 29.9, 23.2; ESI-MS+: m/z calcd for $C_{72}H_{78}N_{12}O_{12}$, 1302.59; found 1304.0 [M+H$^+$], 652.6 [M+2H$^+$].

Synthesis of porphyrin compounds: derivatives (**4**), (**5**), (**6**), (**6bis**) and (**7**)

Meso-tetrakys-(4-hydroxyphenyl)-porphyrin (400 mg, 0.589 mmol) were dissolved in DMF (40 ml) and Na_2CO_3 was added (625 mg, 5.89 mmol). The solution was stirred under inert atmosphere (N_2) for 1h, then a solution of 1-Bromododecane (1.47g, 1.44 ml, 5.89 mmol) in CH_2Cl_2 (10 ml) was dropped.

18-crow-6 (5 mg, 0.019 mmol, catalytic amount) was added to solution which was stirred at ambient temperature and reaction was monitored by HPLC-MS (Phenomenex Gemini hexafluorophenyl 4.6x100 mm, 5 μm; A=0.1% TFA in water, B= 0.1%TFA in MeOH; gradient (time, B%): 0.0, 55%; 2.5, 55%; 4.0, 75%; 10.6, 100%; 15.6, 100%; flow= 1 ml/min) until the maximum amount of tetra-derivative (**4**) was achieved. HPLC-MS (detection at 449.5 nm): (rt – min-, m/z – $APCI^+$) 4.79 min, 679.5 m/z (starting material); 9.38 min, 847.9 $[M+H^+]$ (mono-derivative); 11.88 and 12.22 min, 1016.3 $[M+H^+]$ -508.6 $[M+2H^+]$ (bis-derivative); 13.55 min, 1183.99 $[M+H^+]$ (tris-derivative); 14.7 min, 1352.37 $[M+H^+]$ -677.05 $[M+2H^+]$ (tetra-derivative).

Reaction mixture, which is composed of mono, two isomers of di, tri- and tetra-substituted porphyrin, was concentrated under vacuum and poured in ice-water (200 ml) and it was extracted with CH_2Cl_2 (4x 50 ml). The organic layer was dried using anhydrous sodium sulphate and solvent was removed. The mixture was then firstly purified by column chromatography (silica – 60x4.5 cm – elution with CH_2Cl_2 and then elution with CH_2Cl_2/MeOH=9/1). Mono derivative, two isomers of di-derivatives, tri-derivative and tetra-derivative were collected after further preparative HPLC-MS purification (Phenomenex Gemini hexafluorophenyl 21x100 mm, 5 μm, A=0.1% TFA in water, B= 0.1%TFA in MeOH; gradient (time, B%): 0.0, 55%; 2.6, 55%; 4.1, 75%; 11.0, 100%; 16.0, 100%; flow= 20 ml/min) obtaining 5 mg of compound (**7**) (mono) (yield 1.0%), 33 mg of compound (**6**) (bis 2) (yield 5.5%), 12 mg of compound (**6-bis**) (bis 1) (yield 2.0%), 90 mg of compound (**5**) (tri) (yield 12.9%) and 130 mg of compound (**4**) (tetra) (yield 16.4%).

Meso-tetrakys-(4-dodecyl-oxo-phenyl)-porphyrin (**4**)

^{1}H NMR (300 MHz, $CDCl_3$, δ 7.26 ppm) δ 8.87 (s, 8H), 8.09 (m, 8H), 7.24 (m, 8H), 4.25 (m, 8H), 1.96 (m, 8H), 1.70-1.13 (overlapped, 72H), 0.9 (tb, 12H), -2.76 (s, 2H); ^{13}C NMR (75 MHz, $CDCl_3$, δ 77 ppm, from HSQC) δ 135.4, 130.8, 112.5, 67.2, 31.4, 29.3, 29.2, 26.0, 22.5, 13.9; API-MS$^+$: m/z calcd for $C_{92}H_{126}N_4O_4$, 1350.98; found 1352.37 [M+H$^+$] (from analytic analysis).

5,10,15-tris-(4-dodecyl-oxo-phenyl)-20-(4-hydroxyphenyl)-porphyrin (**5**)

^{1}H NMR (300 MHz, $CDCl_3$, δ 7.26 ppm) δ 8.87 (s, 8H), 8.09 (m, 8H), 7.29(m, 8H), 4.26 (m, 6H), 1.98 (m, 6H), 1.72-1.16 (overlapped, 54H), 0.9 (tb, 9H), -2.77 (s, 2H); ^{13}C NMR (75 MHz, $CDCl_3$, δ 77 ppm, from HSQC) δ 135.6, 131.1, 112.8, 68.4, 31.8, 29.6, 29.5, 26.3, 22.8, 14.1; API-MS$^+$: m/z calcd for $C_{80}H_{102}N_4O_4$, 1182.79; found 1183.99[M+H$^+$].

5,10-bis-(4-dodecyl-oxo-phenyl)-15,20-bis-(4-hydroxyphenyl)-porphyrin (**6**)

^{1}H NMR (300 MHz, $CDCl_3$, δ 7.26 ppm) δ 8.57 (m, 16H), 7.58 (sb, 8H), 4.35 (m, 4H), 2.05 (sb, 4H), 1.67 (sb, 4H),1.30(m, 32H), 0.91 (tb, 6H), -2.76 (s, 2H); ^{13}C NMR (75 MHz, $CDCl_3$, δ 77 ppm, from HSQC) δ 139.9, 127.8, 114.6, 68.6, 31.9, 29.5, 29.3, 26.2, 22.6, 14.1; API-MS$^+$: m/z calcd for $C_{68}H_{78}N_4O_4$, 1014.60; found 1016.33 [M+H$^+$] from preparative analysis.

5,15-bis-(4-dodecyl-oxo-phenyl)-10,20-bis-(4-hydroxyphenyl)-porphyrin (**6-bis**)

^{1}H NMR (300 MHz, CD_3OD, δ 3.31 ppm) δ 8.70 (m, 8H), 8.53 (m, 4H), 8.45 (m, 4H), 7.59 (m, 4H), 7.49 (m, 4H), 4.35 (m, 4H), 2.01 (m, 4H), 1.65 (m, 4H), 1.31 (m, 32H), 0.88 (m, 6H); API-MS$^+$: m/z calcd for $C_{68}H_{78}N_4O_4$, 1014.60; found 1016.33 [M+H$^+$] from preparative analysis.

5-(4-dodecyl-oxo-phenyl)-10,15,20-tris-(4-hydroxyphenyl)-porphyrin (**7**)

^{1}H NMR (300 MHz, $CDCl_3$ /CD_3OD, δ 3.31 ppm) δ 10.48 (s, 8H), 10.24 (d, J=11.4 Hz, 2H), 10.12 (d, J=11.4 Hz, 6H), 8.98 (d, J=11.6 Hz, 2H), 8.87 (d, J=partially overlapped to solvent signal, 6H), 4.66 (t, J=8.9 Hz, 2H), 1.54 (m, 2H), 1.06 (m, 2H), 0.57 (m, 18H), 0.02 (m, 3H).

^{13}C NMR (75 MHz, $CDCl_3$, δ 77 ppm, from HSQC) δ 139.9, 128.7, 115.6, 68.6, 31.6, 29.3, 28.7, 26.3, 22.3, 13.7; API-MS +: m/z calcd for $C_{56}H_{54}N_4O_4$, 846.41; found 847.95 [$M+H^+$] (from analytic analysis).

Synthesis of porphyrin compounds: derivatives (**8**), (**9**), (**10**), and (**11**)

Lauric acid (2.0 g) was dissolved in freshly distilled thionyl chloride (15 ml) and heated under reflux for 2.5h. Excess of thionyl chloride was removed by distillation and the acyl chloride obtained used without further purification.

Meso-tetrakys-[4-(aminoethoxy-ethoxyethyl-aminocarbonyl)-phenyl]-porphyrin (120 mg, 0.092 mmol) was dissolved in acetonitrile (80 ml) and dioxane (30 ml) and heated under reflux under complete dissolution (about 1 h).

The solution was cooled to room temperature under inert atmosphere, then 150 mg of sodium carbonate was added and a solution of lauryl chloride (20 mg, 0.092 mmol) in acetonitrile (20 ml) was slowly dropped. After 2h the same amount (20 mg, 0.092 mmol) of lauryl chloride was dropped again. The reaction was monitored by HPLC-MS (Waters SunFire C18 19x100 mm, 5 μm; A=0.1% TFA in water, B= 0.1%TFA in MeOH; gradient (time; B%): 0.0, 60%; 2.5, 60%; 7.5, 75%; 10, 75%; 12.5, 100%; 22.5, 100%; flow= 1 ml/min). After stirring for 4h the mixture was filtered ad solvent was removed under reduced pressure. The red solid was dissolve in methanol and purified by preparative HPLC-MS (Waters SunFire C18 19x100 mm, 5μm; A=0.1% TFA in water, B= 0.1%TFA in MeOH; gradient (time, B%): 0.0, 80%; 8.7, 100%; 12, 100%; flow= 20 ml/min) isolating tri-derivate, tetra-derivate and a fraction containing mono and bi- derivatives.

Mono- and bi-derivatives were separated from the last fraction by a second preparative HLPC run (Waters SunFire C18 19x100 mm, 5μm; A=0.1% TFA in water, B= 0.1%TFA in MeOH; gradient (time, B%): 0.0, 60%; 2.6, 75%; 9.5, 100%; 12.0, 100%; flow= 20 ml/min). After solvent evaporation, mono-derivative (1.6 mg, yield 1.2%), bi-derivative (2.1 mg, yield 1.4%), tris-derivative (3.0 mg, yield 1.7%) and tetrakys derivative (**8**) (7.3 mg, yield 4.0%) were obtained.

Meso-tetrakys-[4-(lauryl-aminoethoxy-ethoxyethyl-aminocarbonyl)-phenyl]-porphyrin (**8**)

^{1}H NMR (600 MHz, $CDCl_3$, δ 7.26 ppm) δ 8.65 (db, 8H), 8.62 (s, 8H), 8.45 (d, J=6.7 Hz, 8H), 6.13 (sb, 4H), 3.97-3.42 (m, 48H), 2.20 (m, 8H), 1.62 (m, 8H), 1.23 (m, 64H), 0.84 (t, J= 6.75 Hz, 12H); ESI-MS$^+$: m/z calcd for $C_{120}H_{174}N_{12}O_{16}$, 2040.32; found 1021.96 [M+2H^{2+}], 1043.86 [M+2Na^{2+}] (from analytic analysis).

5,10,15-tris-[4-(lauryl-aminoethoxy-ethoxyethyl-aminocarbonyl)-phenyl]-20-(4-aminoethoxy-ethoxyethyl-aminocarbonyl)-phenyl]-porphyrin (**9**)

^{1}H NMR (300 MHz, $CDCl_3$, δ 7.26 ppm) δ 8.61 (m, 16H), 8.43 (d, J=7.43 Hz, 8H), 4.04-3.31 (overlapped, 48H), 2.22 (m, 6H), 1.24 (m, 54H), 0.85 (sb, 9H); ESI-MS$^+$: m/z calcd for $C_{108}H_{152}N_{12}O_{15}$, 1858.15; found 930.57 [M+2H^{2+}] (from analytic analysis).

5,10-bis-[4-(lauryl-aminoethoxy-ethoxyethyl-aminocarbonyl)-phenyl]-15,20-bis-(4-aminoethoxy-ethoxyethyl-aminocarbonyl)-phenyl]-porphyrin and 5,15-bis-[4-(lauryl-aminoethoxy-ethoxyethyl-aminocarbonyl)-phenyl]-10,20-bis-(4-aminoethoxy-ethoxyethyl-aminocarbonyl)-phenyl]-porphyrin (**10**)

^{1}H NMR (300 MHz, $CDCl_3$, δ 7.26 ppm) δ 8.66 (d, J= 5.74 Hz, 8H), 8.58 (s, 8H), 8.44 (d, J=5.46 Hz, 8H), 4.03-3.36 (overlapped, 48H), 2.24 (m, 4H), 1.63 (m, 4H), 1.25 (sb, 32H), 0.86 (tb, 6H); ESI-MS$^+$: m/z calcd for $C_{96}H_{130}N_{12}O_{14}$, 1675.99; found 839.26 [M+2H^{2+}] (from analytic analysis).

5-[4-(lauryl-aminoethoxy-ethoxyethyl-aminocarbonyl)-phenyl]-10,15,20-tris-(4-aminoethoxy-ethoxyethyl-aminocarbonyl)-phenyl]-porphyrin (**11**)

^{1}H NMR (300 MHz, $CDCl_3$, δ 7.26 ppm) δ 8.68 (m, 8H), 8.59 (s, 8H), 8.45 (m, 8H), 4.03-3.22 (overlapped, 48H), 1.25 (s, 20H), 0.88 (s, 3H); ESI-MS$^+$: m/z calcd for $C_{84}H_{108}N_{12}O_{13}$, 1492.82; found 748.02 [M+2H^{2+}] (from analytic analysis).

5.2 Synthetic procedure of SWCNT derivatives

Synthesis of **SWCNT- compound (1)**

SWCNT (20 mg), compound (**1**) (40 mg, 0.07 mmol) and DMF (4 ml) were placed in a specific glass tube (Anton Parr G10). The tube was placed in the MW oven, sealed and heated at 100°C (temperature controlled MW irradiation with max power of 600 W) for 2 h. The mixture was then cooled to RT, centrifuged and washed with DMF (3 ml) and CH2Cl2 (3 x 4 ml). The black solid was recovered and dried at 100°C for 48h (21mg). The final product was characterized by Raman spectroscopy, TGA and AFM analysis.

Synthesis of **SWCNT- compound (1)-Zn**

SWCNT (20 mg), compound (**1**)**-Zn** (30 mg, 0.047 mmol) and DMF (4 ml) were placed in a specific glass tube (Anton Parr G10). The tube was placed in the MW oven, sealed and heated at 100°C (temperature controlled MW irradiation with max power of 600 W) for 2 hours. The mixture was then cooled to RT, centrifuged and washed with DMF (3 ml) and CH_2Cl_2 (3 x 4 ml). The black solid was recovered and dried at 100°C for 48h (30 mg). The final product was characterized by Raman spectroscopy, TGA and AFM analysis.

Synthesis of **SWCNT-compound (2)**

SWCNT (10 mg), compound (**2**) (10 mg, 6 μmol) and DMF (3 ml) were placed in a specific glass tube (Anton Parr G10). The tube was placed in the MW oven, sealed and heated at 100°C (temperature controlled MW irradiation with max power of 600 W) for 2 hours. The mixture was then cooled to RT, centrifuged and washed with DMF (3 ml) and CH_2Cl_2 (3 x 4 ml). The black solid was recovered and dried at 100°C for 48h (14 mg). The final product was characterized by Raman spectroscopy, TGA and AFM analysis.

Synthesis of **rGO-compound (2)**

Compound (**2**) (93 mg, 0,057 mmol) was dissolved in DMF (2 ml) and the solution was put into a specific glass vial (10 ml volume) for Anton Parr microwave reactor, together with a magnetic stir bar. rGO (15 mg) was then added, the vial was sealed with its pressure resistant cap and put in the MW cavity. Reaction mixture was heated under magnetic stirring at 130° for 4h.

After cooling the mixture was centrifuged and the solution separated from solid graphene. Solid was washed several times with DMF (3 ml) and finally with CH_2Cl_2 (3 x 4 ml), then it was dried at 100°C in an oven. Grafted rGO was characterized by TGA, Raman spectroscopy, TEM and AFM imaging.

Synthesis of **SWCNT-compound (3)**

SWCNT (30 mg), octanal (26 mg, 32 μl, 0.20 mmol), compound (**3**) (55mg, 0.04 mmol) and DMF (3 ml) were placed in a specific glass tube (Anton Parr G10). The tube was placed in the MW oven, sealed and heated at 120°C (temperature controlled MW irradiation with max power of 600 W) for 2 h. The mixture was then cooled to RT, centrifuged and washed with DMF (3 ml) and CH_2Cl_2 (3 x 4 ml). The solid was recovered and dried at 100°C for 48 h (34 mg). The final product was characterized by Raman spectroscopy, TGA and AFM analysis.

5.3 Chlorophylls extraction and purification procedure

Leaves of Galipea longiflora (Evanta) were collected by the Gimenez's group (Instituto de Investigaciones Fármaco Bioquímicas - IIFB), together with people of Tacana community, in the region of Sud Yungas in La Paz district (Bolivia). The taxonomical identification was possible by comparing with samples coming from the Herbario Nacional de Bolivia. Evanta leaves were air dried in the shade for several days, at room temperature (RT) and protected from humidity and light.

Milled material (5 Kg) was extracted with ethanol (25 L) for seven days and then filtered. The filtrate was evaporated obtaining residue (6g-10g), which was dissolved in ethanol (100 mL). The ethanol solution was extracted with petroleum ether (2 x 100 mL) and the collected organic phases were dried over sodium sulphate and evaporated obtaining 3 g of crude product.

The crude was re-dissolved in petroleum ether (80 mL) and washed with methanol (2 x 80 mL). Petroleum ether phase was dried over sodium sulphate and solvent was removed under reduced pressure giving a green sticky solid (2.5 g).

First purification was carried out on Sephadex LH 20 column (26 x 560 mm) eluting with $CHCl_3/CH_3OH$ 1:1. Fractions were collected based on their color. UV-Vis analysis allows to group fractions in 5 clusters. Each cluster was characterized by HPLC on a Waters XTerra Phenyl column (4.6 x 150 mm, 5 μm), using 0.1% trifluoroacetic acid solution in water (A) and 0.1% trifluoroacetic acid solution in methanol (B) as eluent. Gradient profile was set as follows: (min, %B) 0.0, 65; 15.0, 65; 27.4, 100; 42.4, 100. The wavelength range observed by PDA detector was between 210 and 700 nm. All fractions displayed the typical absorption bands of Chlorophyll A at 420 and 680 nm and differed only in the high-energy region. Moving from fraction 1 to fraction 5 the absorption band, in the short range 200-300 nm, decreased indicating a higher purity degree of last fraction. In Italy, further characterizations of these fractions, using HPLC analysis, were necessary to clearly identify each component. HPLC analysis (eluted at 100% of MeOH) showed very similar composition (three main peaks with same shape are present) only in terms of Chlorophylls content (at 405 nm, maximum Abs wavelength typical of Chlorophylls) for all analyzed fractions (data not shown). A second purification over Sephadex LH 20 (1.5 x 26 cm; mobile phases 20%, 50%, 80% EtOH in Water) was carried out.

Two final fractions were isolated: one retained/held on Sephadex LH 20 and one eluted with EtOH 100% (washing phase). Content of Chlorophylls is the same (in terms of peaks profile) in both fractions. The fragments identification was possible thanks to a collaboration with Prof. Maffei group (Department of Life Sciences and Systems Biology). Chlorophyll mixture was stored at -20°C in tert-methyl-butil-ether (MTBE) solvent. For the analysis the sample was dissolved in acetonitrile/methanol/water 70/20/5 v/v. Reverse phase chromatography column C30 (YMC).was used. DAD at 680, 480 e 420 nm and ESI-Ion trap MS2 in Multi Reaction Monitoring modality was the set up for the detection of the desired molecules.

5.4 NB formulation

DPPA (1,2-dipalmitoyl-sn-glycero-3-phosphate), DPPC (1,2-dipalmitoyl-sn-glycero-3-phosphocholine), DPPE (1,2-dipalmitoyl-sn-glycero-3-phosphoethanolamine) (Avanti Polar Lipids, Pelham, AL), and mPEG-DSPE (1,2-distearoyl-phosphatidylethanol-amine-methyl-poly ethylene glycol conjugate-2000) (Laysan Lipids, Arab, AL) were dissolved in chloroform in a 4:1:1:1 mass ratio. The solvent was then removed by evaporation, leaving a lipid film. The film was hydrated by adding 1 ml of 0.6 mg/ml Pluronic solution (Sigma Aldrich, Milwaukee, WI) and 0.5% Irgacure (Fisher Scientific; Pittsburgh, PA) in PBS in the presence of glycerol (50µl) at 75 °C for 30 min. Next, NNDEA (Polysciences, Warrington, PA) and BAC (Sigma Aldrich, Milwaukee, WI) (2:1 weight ratio) were added, and air was removed from the sealed vials and replaced with octafluoropropane until the vial pressure was equilibrated. The vial was then placed on a vial shaker for 45s. Porphyrin concentration is in the range between 0.1-0.2 mg/ml.

5.5 NB characterization

SIZE. Measurements size dimension were performed at 25 °C, by diluting a sample 1:2000 with PBS at pH 7.4 (n=3) by using nanoparticle tracking analysis (NanoSight NS300, Malvern Instruments).

PORPHYRIN NB RATIO CALCULATION:

Number of nanobubbles per ml, from NanoSight NS300: $4.13x10^{11}$ (NB with compound 11)

Porphyrin concentration, from fluorescence data: 2.3 nmol/ml (compound (**11**) in NB formulation)- EE% of 25%, from standard curve, DL% of 0.035% with lipid/drug ratio of 7:1.

Number of nanobubbles per ml, from NanoSight NS300: $2.98x10^{11}$ (NB with compound 4)

Porphyrin concentration, from fluorescence data: 0.88 nmol/ml (compound (**4**) in NB formulation)- EE% of 0.5%, from standard curve, DL% of 0.0007% with lipid/drug ratio of 7:1.

Number of porphyrin molecules per ml = porphyrin concentration (expressed in mol/ml) x $6.022x10^{23}$

Number of porphyrin molecules per NB = number of porphyrin molecule per ml / number of NB per ml

$6.022x10^{23}x2.3x10^{-9}$ /$4.13x10^{11}$= 3353 porphyrin molecules (**11**) per NB.

$6.022x10^{23}x0.88x10^{-9}$ /$2.98x10^{11}$= 1778 porphyrin molecules (**4**) per NB.

MICROSCOPIC ANALYSIS. Microscope images were obtained on a Zeiss AxioObserver Z1 microscope using filters: for excitation FITC (450 nm) and Cy5 for emission (670 nm).

US IMAGES were recovered using an AplioXG SSA-790A clinical ultrasound imaging system (Toshiba Medical Imaging Systems, Otawara-Shi, Japan) equipped with a 12 MHz linear array transducer. System acquisition parameters were set to contrast harmonic imaging (CHI) with 12.0 MHz harmonic frequency, 0.15 mechanical index (MI), 4 Hz imaging frame rate, 65 dB dynamic range, and 70 dB gain. Images were acquired after diluting nanobubble solution 1:1000 with PBS at pH 7.4 and 700 µl was injected in a custom-made agarose phantom. Here, a gel of 1.5 wt.% agarose (BP160-500 from Fisher Reagents) in DI water was prepared inside of a 6-well cell culture plate fitted with a rectangular insert.

After gelling, the phantom was removed and contained a sample holder space. The gel was affixed above the US transducer for analysis. The US setup with the transducer placed to the bottom of the phantom gel is depicted in figure E1. Measurements size dimension were performed at 25 °C, by diluting a sample 1:2000 with PBS at pH 7.4 (n=3) by using nanoparticle tracking analysis (NanoSight NS300, Malvern Instruments).

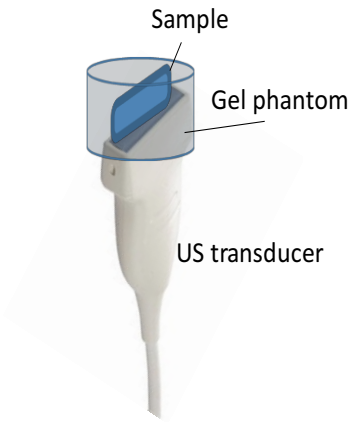

Figure E1. US set up used to image all NB samples.

ECHOGENECITY OVER TIME of loaded and unloaded NB was investigated under the same experimental set up to image the nanosystem (figure E2). System acquisition parameters were set to contrast harmonic imaging (CHI) with 12.0 MHz harmonic frequency, 0.10 mechanical index (MI), 0.2 Hz imaging frame rate, 65 dB dynamic range, and 70 dB gain. Images were acquired after diluting nanobubble solution 1:1000 with PBS at pH 7.4. 700 µl was injected in the agarose phantom. The echogenicity profile is reported in figure E2.

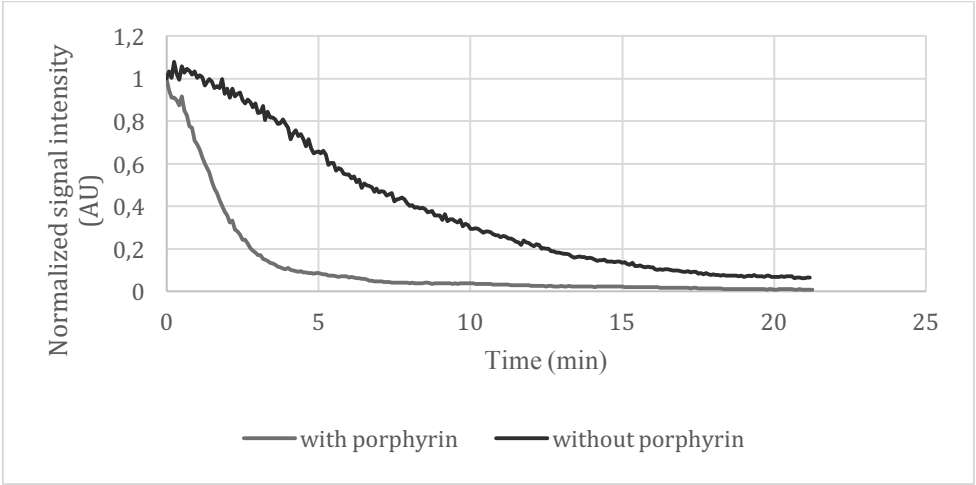

Figure E2. Echogenicity over time profiles for loaded (blue line) and unloaded NB (orange line).

5.6 NBs: Cell culture and cellular treatment

LS174T human colorectal adenocarcinoma cells (ATCC, Manassas, VA) were cultured in complete MEM medium (10% fetal bovine serum, 1% penicillin–streptomycin; Invitrogen, Carlsbad, CA) and placed in a humidified atmosphere at 37 °C and 5% CO_2. At 90% confluence, cells were detached using 0.25% trypsin–EDTA (Invitrogen, Carlsbad, CA) for passaging.

LS 174T cells were seeded at a density of $3x10^4$ cells/ml into a 24-well plate, in Alpha MEM complete media and placed in a humidified atmosphere at 37°C and 5% CO_2. After one day, NBs solution layer was added (4 ml) considering a dilution of 1:200. 24-wells plates (treated and non-treated) were both covered with sterile transparent film (3M Tegaderm sterile transparent film, 4 X 4-3/4 Inch).

An acoustically transparent gel (Aquasonic 100) was placed between the top of ultrasound probe and the film base of the 24-well plate. The therapeutic US apparatus (OMNISOUND® 3000 Pro) with a resonance of 3 MHz was used for all US treatments. The transducer with a diameter of 2 cm^2 is horizontally directed to the transparent 24-well plate (TermoFisher Scientific 24 Flat Bottom Transparent). An intensity of 1.8 W/cm2 and a 20% of duty cycle was used. Treatment was carried out under a temperature controlled environment (37°C).

5.7 Cell proliferation assay: WST-1

Cytotoxicity was evaluated with a colorimetric assay using Cell Proliferation Reagent WST-1. The amount of WST-1 was prepared considering 1:10 final dilution and then was added to the cells in cultured. Cells grown in a 24-well culture plate were incubated at 37 °C for 1 h in a 5% CO_2 incubator. Cell viability was measured at 450 nm (Abs) in a microplate reader (Tecan Infinite 200 Microplate Reader). The adherently growing LS 174T cells line was cultured for 3 days in 24-well plates before adding the reagent. Cytotoxicity of the formulations was expressed as percentage cell viability (measured as WST-1 reduction) compared to control (cells + unloaded NBs + US irradiation).

5.8 Liposome formulation

Liposomes were prepared by thin lipid film hydration and extrusion method. Briefly, a chloroform solution of the lipid components 1,2-distearoyl-sn-glycero-3-phosphocholine (DSPC, Avanti Polar-Lipids), cholesterol (Chol, Sigma-Aldrich) and 1,2-distearoyl-sn-glycero-3-phosphoethanolamine-N [amino (polyethylene glycol)-2000] (DSPE-PEG, ammonium salt from Avanti Polar-Lipids) (70:15:8.5 molar ratios) was mixed with methanol solution of chlorophyll in 20% (mol chlorophyll/mol lipid) ratio and evaporated under reduce pressure using rotary evaporator.

The resulting lipid film was dried under vacuum overnight, hydrated with a 20 mM of 4-(2-hydroxyethyl) piperazine-1-ethanesulforic acid (HEPES) buffer (pH 7.4) and the suspension was vortexed for 10 min and bath sonicated. The formulations were then extruded (Extruder, Lipex, Vancouver, Canada) passing the suspension 5 times under nitrogen through a 400 and a 200nm polycarbonate membrane (Costar, Corning Incorporated, NY), at a set temperature of 5 °C above the phase transition temperature of the lipid mixture. Liposomal preparations were purified from unentrapped chlorophyll through chromatography on Sepharose CL-4B columns, eluting with HEPES buffer. Liposomes were stored at 4 °C.

This procedure has been used also for liposome loaded with compound (4). In this case, the lipid ratio is DPPC (1,2-dipalmitoyl-sn-glycero-3-phosphocholine)/DSPE-PEG (93:7 molar ratio), Cholesterol was not added. Lipid mixture was mixed with chloroform solution of porphyrin compound (4) in 2.5 %(mol porphyrin/mol lipid) ratio.

5.9 Liposome characterization

The mean particle size and polydispersity index (PDI) of the liposomes were determined at 25 °C by dynamic light scattering using a Zeta sizer nano (Malvern instruments, UK). Size measurements were performed at a fixed angle of 173° after dilution of the liposome suspensions in MilliQ® water. Each measurement was carried out in triplicate. The surface charge of liposomes was evaluated by zeta potential measurements after dilution of the suspensions in 10 mM KCl. Phospholipid phosphorous was assessed in each liposome preparation by phosphate assay after destruction with perchloric acid. The amount of encapsulated chlorophyll was determinate by UV-VIS spectrophotometer (figure E3). One hundred µL of liposomal suspension were diluted in 400 µL of methanol and analyzed at 400nm. The drug concentration was calculated from standard curves.

	EE%	DL%	Mean Diameter	Zeta Potential (mV)
Chlorophylls-Liposome	70	14	148.3	-12.0±0.2
*Porphyrin (**4**)-Liposome*	<1	0.56	96.6	-11.5±0.7

Figure E3. *Characterization of liposome formulation: EE (%), DL (%), mean diameter (nm), Zeta potential (mV).*

5.10 SLN formulation

SLN were prepared using "cold dilution of microemulsion (μE)". This method involves, firstly, μE preparation after diluted with a 2% w/w polymeric aqueous solution to precipitate SLN.

μE was obtained with biocompatible GRAS ingredients (Generally Recognized As Safe). A trilaurin solution in ethyl acetate (EA) was chosen as oil phase because of its highest solubility in this partially water miscible solvent. EA and water were mutually pre-saturated before using them in μE preparation. Epikuron® 200 (phosphadityl coline 92%) was chosen as a surfactant together with Cremophor® RH 60 (PEG-60 hydrogenated castor oil) at 3:1 w/w constant ratio. Sodium taurodeoxycholate (Na TdC), was tested as co-surfactants, benzyl alcohol (benzOH) was chosen as a co-solvent to solubilize porphyrin derivative (or chlorophyll).

μE (1,2 ml) was then diluted with a 2% w/w Pluronic®F68 aqueous solution (5 ml) to precipitate SLN. A formulation study was performed to optimize SLN size and encapsulation efficiency.

The finally μE formulation was reported in Table 1, Figure E4.

Component	Quantity
EA	200 μl
trilaurin	60 mg
lecithin	150 mg
cremophor® RH60	50 mg
sodium taurodeoxycholate	30 mg
chlorophyll	4 mg
benzOH	100 μl
waters	700 μl

Figure E4. Composition of SLN.

5.11 SLN characterization

The mean particle size and polydispersity index of the nanoparticles were determined at 25 °C by Dynamic laser light scattering (DLS, Nano ZS zeta sizer (Malvern, UK)). The selected angle was 90°, and the measurement was taken after dilution of the SLN suspensions in MilliQ® water. Each measure was carried out in triplicate (figure E5). The surface charge of SLN was evaluated by zeta potential measurements after dilution of the suspensions in 10 mM KCl. The amount of porphyrin derivative (or Chlorophyll) incorporated in nanoparticles was determined by means of a UV–Vis absorption spectrophotometer at 400 nm. All measurements were carried out at room temperature.

	EE%	DL%	Mean Diameter	Zeta Potential (mV)
T0	95.6	6.4	201.3	-15.3±0.5
T6	70.3	4.7	202.4	-13.9±0.4
T10	73.8	4.9	202.9	-15.4±0.5
T20	69.6	4.6	207.4	-9.8±0.3
T30	72.7	4.8	208.4	-15.9±0.5
T60	72.0	4.8	198.4	-16.1±0.5

Figure E5. *Characterization of different preparation of SLN: EE (%), DL (%), mean diameter (nm), Zeta potential (mV).*

Chlorophyll release from SLN

Three different receiving media were chosen:

- Phosphate Buffer pH 7,4
- Phosphate buffer pH 7,4 + 10 % Ethanol
- Citrate buffer pH 5,0

SLN- Chlorophyll suspension was used as donor formulations in hydrophilic membrane, Servapor® dialysis tubing (Serva, G), cut-off 12000-14000 Da. At fixed times, the receptor solution was tipped out and the cell was then refilled with fresh receiving medium. Drug concentration (figure E6) in the receptor solution was determined by UV-vis spectrophotometer at 400 nm (Beckman coulter DU730 UV/Vis) using a standard curve (figure E7).

RECEIVING MEDIUM	% CHLOR released of at 24 h
Phosphate buffer pH 7.4	35.21
Phosphate buffer pH 7.4 + 10% ethanol	31.07
Citrate buffer pH 5.00	34.63

Figure E6. Value of Chlorophyll % released at 24 h in different media.

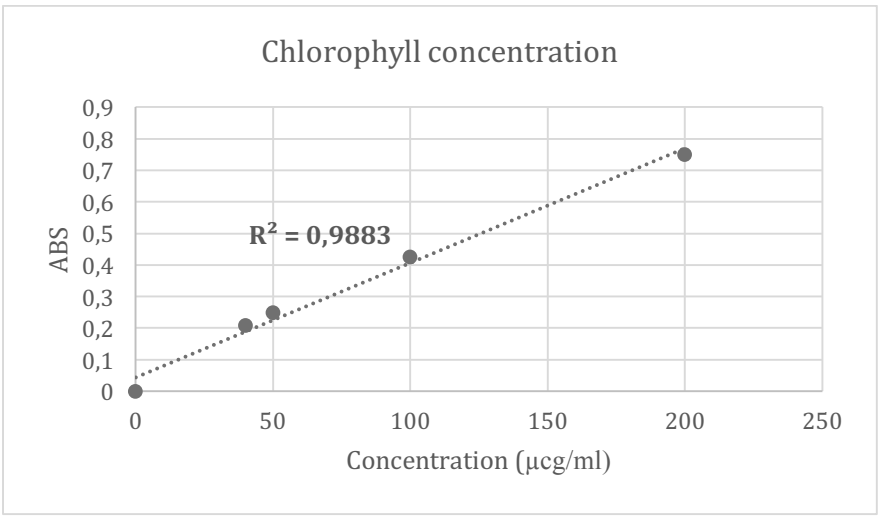

Figure E7. Standard curve of Chlorophyll in MeOH/DCM 1:1.

5.12 PLGA nanospheres and Micelle formulation

Two types of Chlorophyll-containing nanosystems were prepared: PLGA (50:50) nanospheres and micelles.

For the preparation of PLGA (50:50) nanospheres containing chlorophyll, the nanoprecipitation technique[118] was employed. Practically, for each preparation, to 24 mg of PLGA 50:50 dissolved in acetone, an aliquot of an ethanolic stock solution of chlorophyll (8 mg/ml) was added until a total volume of 2 ml. This organic solution was then poured into 4 ml of MilliQ® water under magnetic stirring. Precipitation of particles occurred spontaneously. After solvent evaporation by Rotavapor®, an aqueous suspension of nanospheres was obtained.

Micelles were prepared using the same technique without adding PLGA.

To purify the nanocarriers from non-incorporated chlorophyll, they were extensively dialyzed against MilliQ® water at 4 °C (Spectra/Por® 3500 MWCO dialysis membrane, Spectrum, Huston, TX).

The particles were then stored in the dark at 4 °C.

5.13 PLGA characterization

The average particle size and the polydispersity index of all formulations were determined by dynamic light scattering (DLS) with a Nano ZS zeta sizer (Malvern, UK) at a fixed angle of 173° and at a temperature of 25 °C. The suspensions were diluted 1:10 v/v with MilliQ water before analysis. Each value reported is the average of three measurements.

To determine the zeta potential, the particle samples were diluted 1:10 v/v with MilliQ water and placed in the electrophoretic cell of the Nano ZS zeta sizer at 25 °C. Each sample was analyzed in triplicate.

The colloidal stability of the suspensions was evaluated by measuring the mean size and the zeta potential of the particles over a storage period of 28 days at 4 °C. PLGA 50:50 nanospheres stability was also tested by measuring the mean size after incubation in cell culture medium for 24 h.

The amount of chlorophyll incorporated into nanospheres was determined by UV-Vis measurements (figure E8). Practically, 2 ml of each formulation were purified by dialysis and lyophilized. Then, 200 µl of dichloromethane were added to dissolve the sample and 2 ml of methanol to precipitate PLGA.

After centrifugation (6000 rpm, 15 min), 500 µl of the supernatant were diluted 1:2 with methanol and measured at 400 nm spectrophotometrically (Beckman coulter DU730 UV/Vis). Each value reported is the average of three measurements.

Nanoparticles were also observed by an optical microscope (Leica DM 2500).

FORMULATION PLGA 50:50 6mg/ml	Chlorophyll CONCENTRATION (ug/ml)	SIZE (nm)	Zeta Potential (mV)
	No Chlorophyll	134.4±1.2	-40.3±1.0
	300	123.0±0.9	-40.8±0.4
	500	126.8±0.5	-44.1±2.7
	700	144±0.9	-43.8±0.2

Figure E8. Characterization of Chlorophyll PLGA (50:50) nanospheres

FORMULATION Micelle	Chlorophyll CONCENTRATION (ug/ml)	SIZE (nm)	Zeta Potential (mV)
	300	109.2±10.5	-34.9±3.8
	500	86.6±7.7	-40.7±2.7
	700	47.4±0.9	-32.2±1.4

Figure E9. Characterization of Chlorophyll Micelles.

All suspensions were monodispersed, excepted micelles. In particular, PLGA nanospheres showed a mean diameter in the range 120-150 nm (figure E8). For chlorophyll micelles, the size decreased with the increase of chlorophyll content (figure E9).

All nanosystems have a negative zeta potential (below -30 mV).

Concerning physical stability, all suspensions were stable during storage for 28 days. PLGA 50:50 nanospheres (which were further characterized in vitro) were found to be stable also in cell culture medium for 24 h. The optical microscopy analysis showed the presence of the nanocarriers without aggregates.

The amount of chlorophyll incorporated into PLGA nanospheres was determined by UV-Vis measurements (figure E10) and expressed as:

- Encapsulation Efficiency (EE): ratio between loaded drug and initial drug concentration ×100 (after purification)

- Drug Loading (DL): ratio between loaded drug and lipid ×100 (after purification)

FORMULATION PLGA 50:50 6mg/ml	Chlorophyll CONCENTRATION (ug/ml)	EE%	DL%
	300	100	5.0
	500	100	8.3

Figure E10. Chlorophyll EE% and DL% in PLGA nanospheres.

5.14 Chlorophyll: Cell culture and cellular treatment

The human prostatic carcinoma cell line, PC-3 (ICLC, Interlab Cell Line Collection, Genova, Italy), was cultured in Dulbecco's modified Eagle medium (DMEM) supplemented with 2 mM L-glutamine, 100 UI/mL penicillin, 100 µg/mL streptomycin and 10% (v/v) heat-inactivated fetal calf serum (Sigma-Aldrich, ST Louis, MO, USA) in a humidified atmosphere of 5% CO_2 air at 37°C.

At 85% confluence, cells were harvested with 0.05% trypsin-0.02% EDTA solution (Sigma-Aldrich), suspended in culture medium and seeded at the appropriate cell concentration for the different cell culture experiments. $1x10^5$ PC-3 cells were sub-cultured into Petri dishes (25 mm diameter) and were allowed to attach to the surface for 24 h prior to treatment.

All the chlorophyll formulations were then suspended in the cell culture medium to the appropriate concentration, 5 µM, and incubated for 6 h before US exposure (in figure 11 the US set up). The US field was generated by a plane wave transducer (25 mm diameter) in pulse mode (50% duty cycle) at 1.0 MHz, connected to a power amplifier (Type AR 100A250A; Amplifier Research, PA, USA) and a function generator (Type 33250; Agilent, CA, USA). A mechanical adaptor was built to connect the Petri dish containing the cells and filled with ultrapure water to create highly reproducible measurement conditions, at a fixed Petri dish distance from the transducer (20 mm). US exposure was performed for 5 min, under a dim light, at 1.5 W/cm^2.

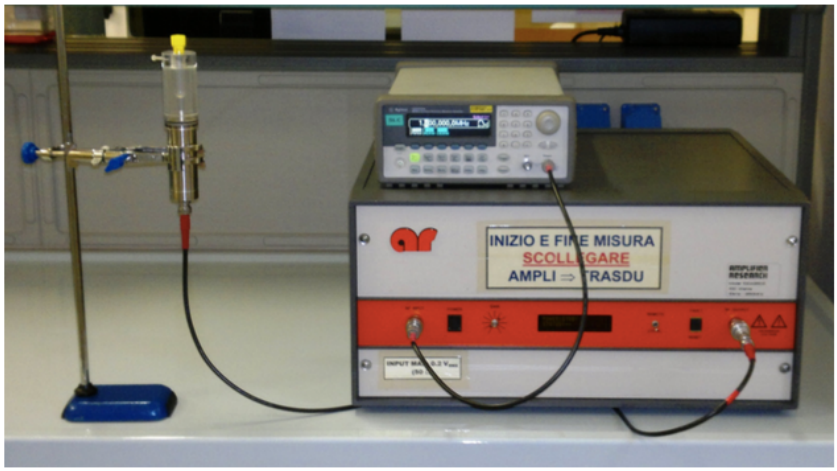

Figure E11. US treatment set up used for *in vitro* tests.

The effect of treatment had on PC-3 cell growth was evaluated using a WST-1 cell proliferation assay (Sigma-Aldrich). After US exposure PC-3 cells were detached with 0.05% trypsin-0.02% EDTA solution (Sigma-Aldrich) and 1.5 x 10^3 cells were seeded in 100 μL of growth medium in replicates (n = 8) in 96-well culture plates (TPP, Trasadingen, Switzerland).

5.15 Cell proliferation assay: WST-1

Cytotoxicity was evaluated by using WST-1 reagent. WST-1 reagent (10 μL/100 μL) was added at 24 and 48 h, and plates were incubated at 37 °C in 5% CO_2 for 90 min. Well absorbance was measured at 450 and 620 nm (reference wavelength) in the microplate reader Asys UV340 (Biochrom, Cambridge, UK). Cell proliferation data were expressed as the ratio between the absorbance of treated and untreated cells.

5.16 Cellular Uptake of Chlorophyll loaded and no **(Flow cytometric analyses)**

The cellular uptake analysis of all the chlorophyll formulations was carried out on C6 flow cytometry equipment (Accuri Cytometers, Milano, Italy). Briefly, 5 x 10^4 cells were plated in 6-well culture plates (TPP) and incubated with each chlorophyll formulations (5 μM) for 1, 3, 6, 12 and 24 h. Cells were detached after each incubation period using a 0.05% trypsin-0.02% EDTA solution (Sigma-Aldrich) and re-suspended in 300 μL PBS (Sigma-Aldrich). They were then run on the C6 flow cytometer (Accuri Cytometers), which considered 10,000 events, using 640 nm excitation to measure the intracellular chlorophyll. Intracellular fluorescence is expressed as integrated median fluorescence intensity (iMFI). This is the product of the frequency of cells that are positive to chlorophyll fluorescence and the median fluorescence intensity of the cells.

Results are expressed as iMFI ratio, i.e. the ratio between the iMFI of treated and untreated cells. The most suitable chlorophyll time of incubation for the US exposure was then chosen according to iMFi ratio.

5.17 ROS evaluation of Chlorophyll loaded nanosystems

Reactive oxygen species (ROS) production was performed at 1, 15, 30, 60 and 90 min after US treatment (5 minutes). Cells were incubated with 10 μM of 2,7-dichlorofluorescein diacetate (DCFH-DA) (Sigma Aldrich) 30 min before the flow cytometric analysis. After DCFH-DA incubation, cells by a C6 flow cytometer (Accuri Cytometers), which evaluated 10,000 events. ROS production was expressed as iMFI ratio.

6 CONCLUSION

Even if SDT is not yet clinically approved, here we show very promising results in tumor cells culture studies using this approach, with an *in vivo* cancer treatment, as future prospective. SDT is based on PDT approach and it maintains all advantages of this technique solving the problem of low tissue penetration of light, replacing light with ultrasound as sensitizer's excitation source. Unfortunately, SDT retain the main limitations, such as the skin photosensitivity due to the sonosensitizer distribution.

This study aims to understand how to overcome this limitation exploiting different nanoparticles as sensitizer carrier. Dimension, rigidity and nature of surface, seem to be key parameters in optimizing sonodynamic effect. However, sonosensitizer structure is not less important. It has to be designed *ad hoc* in order to link the selected particle surface; it is important that the sonosensitizer is properly localized on particle surface. Since the most studied sensitizers are porphyrins, this study has explored different way to synthesize, modify and recover from natural source proper molecules with porphyrin substructure.

All loaded nano-constructs exploited the increase in cavitation efficiency, which enhances the excitation of the sonosensitizer. Carbon nanomaterials (SWCNT) turn out to be very efficient in sonodynamic cell treatment because of their ability to stabilize the charge separated state, generated after sonosensitizer excitation. Nanobubbles are also particularly efficient in exciting sensitizer because of their gas core. In both cases, it is essential that the sensitizer molecule is linked/placed closed enough to the nanoparticles surface. The gas bubble cavitation implosion occurs close to the particle surface and there it exerts the maximum thermal effect.

SLN, liposomes and PLGA particles are particularly suitable to drive sonosensitizer to the region of interest, limiting its concentration in healthy tissues. Differently from SWCNT, these nanoparticles are easily internalized by cells and can exert their effect inside cells. In both cases, extracellular and intracellular activity produce, through different mechanisms, tumor cell death.

7 OUTLOOK

The results here reported would need further detailed investigation, in order to better understand all mechanisms involved in the SDT process. However, based on obtained results, we can surmise that the best sonosensitizer should contain all the features of the nanocarriers reported: small dimension, rigid surface, ability to stabilize radical state, ability to be internalized by cells, biocompatibility, easy surface modification.

Carbon nanodiamonds (CND) can be a good substrate to work with. It combines the nano size dimensions with all carbon nanosupport features. A preliminary reactivity test nanosystem with suitable porphyrin derivatives has been successfully carried out using the well-known DA reaction. Moreover, CND possess, or it can be implanted, N negative vacancy sites which make them luminescent (Abs 530 nm, Ex 650 nm). As proved in NB case, CND could represent another interesting US theranostic agent.

Moreover, all the studied nanosystems and the new porphyrin grafted nanodiamonds, could exert the *passive targeting* for cancer tissue accumulation enhancing the anticancer activity. However, within future prospective, since all these nanoconstruct surfaces are easily modified, an active targeting may be implemented. Different ways to give site specific activities to these systems could include their modification with, for example, monoclonal antibodies, proteins, peptides, hyaluronic acid and folic acid.

SUPPLEMENTARY INFORMATION

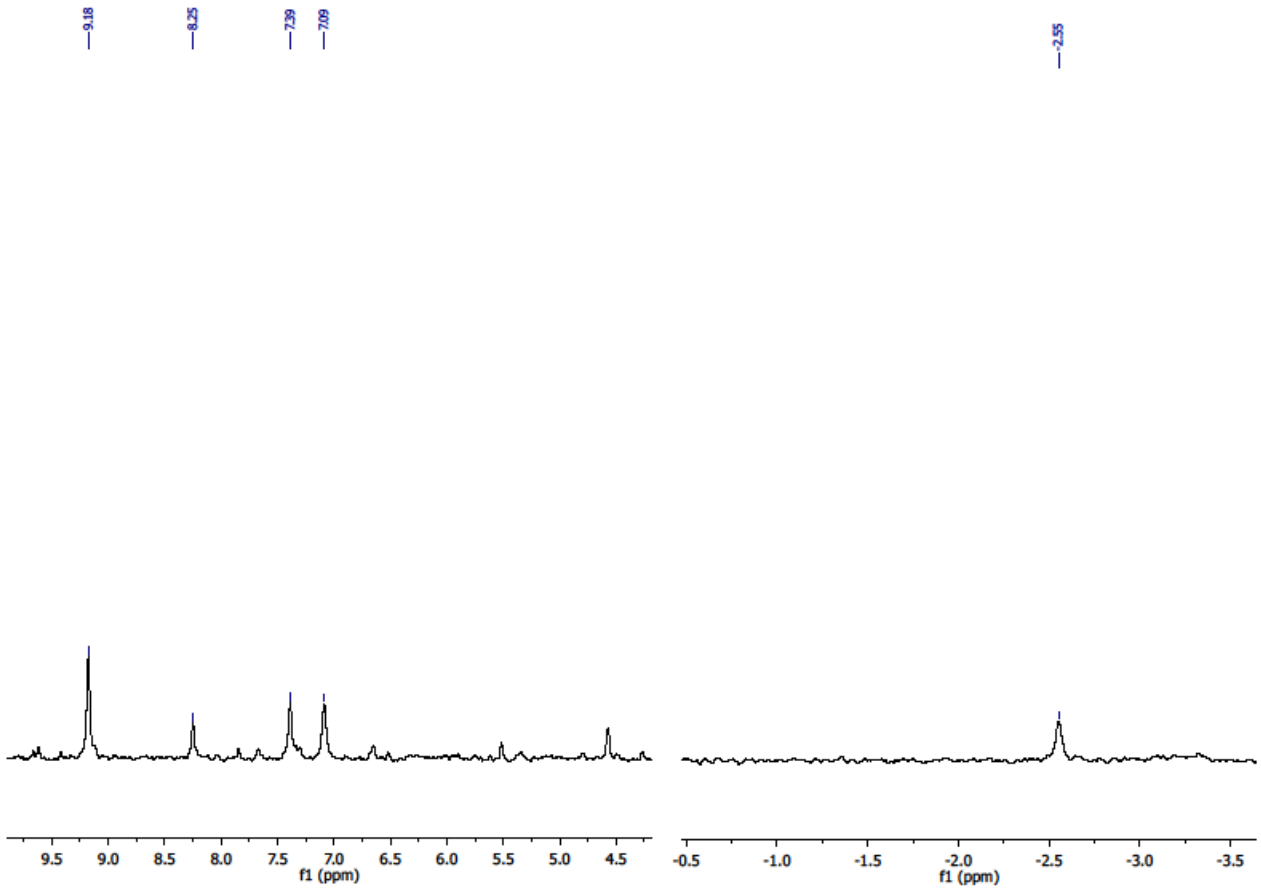

Figure S1. ^{1}H NMR spectrum of compound **1** (300 MHz, THF-d_8).

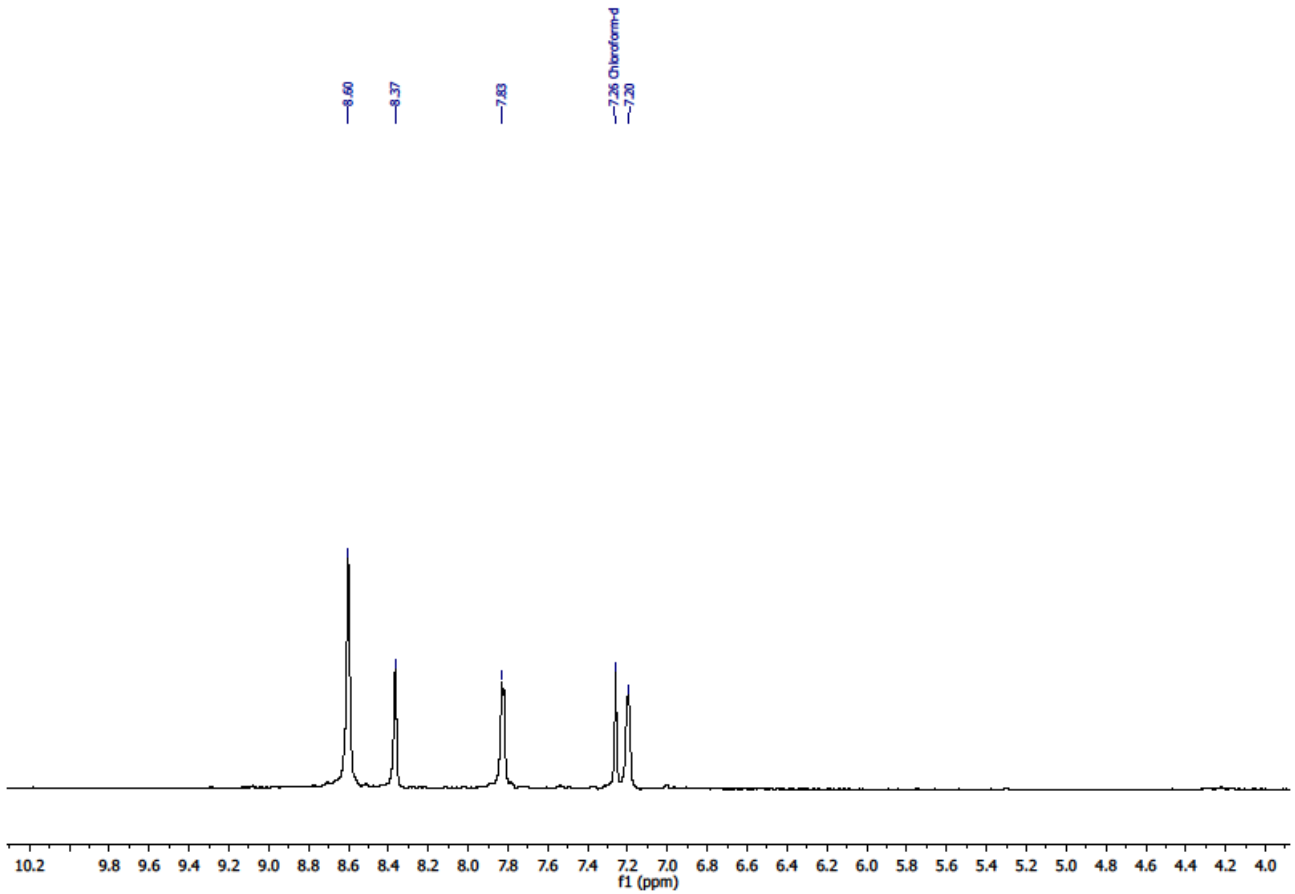

Figure S2. ^{1}H NMR spectrum of compound **1-Zn** (300 MHz, $CDCl_3$)

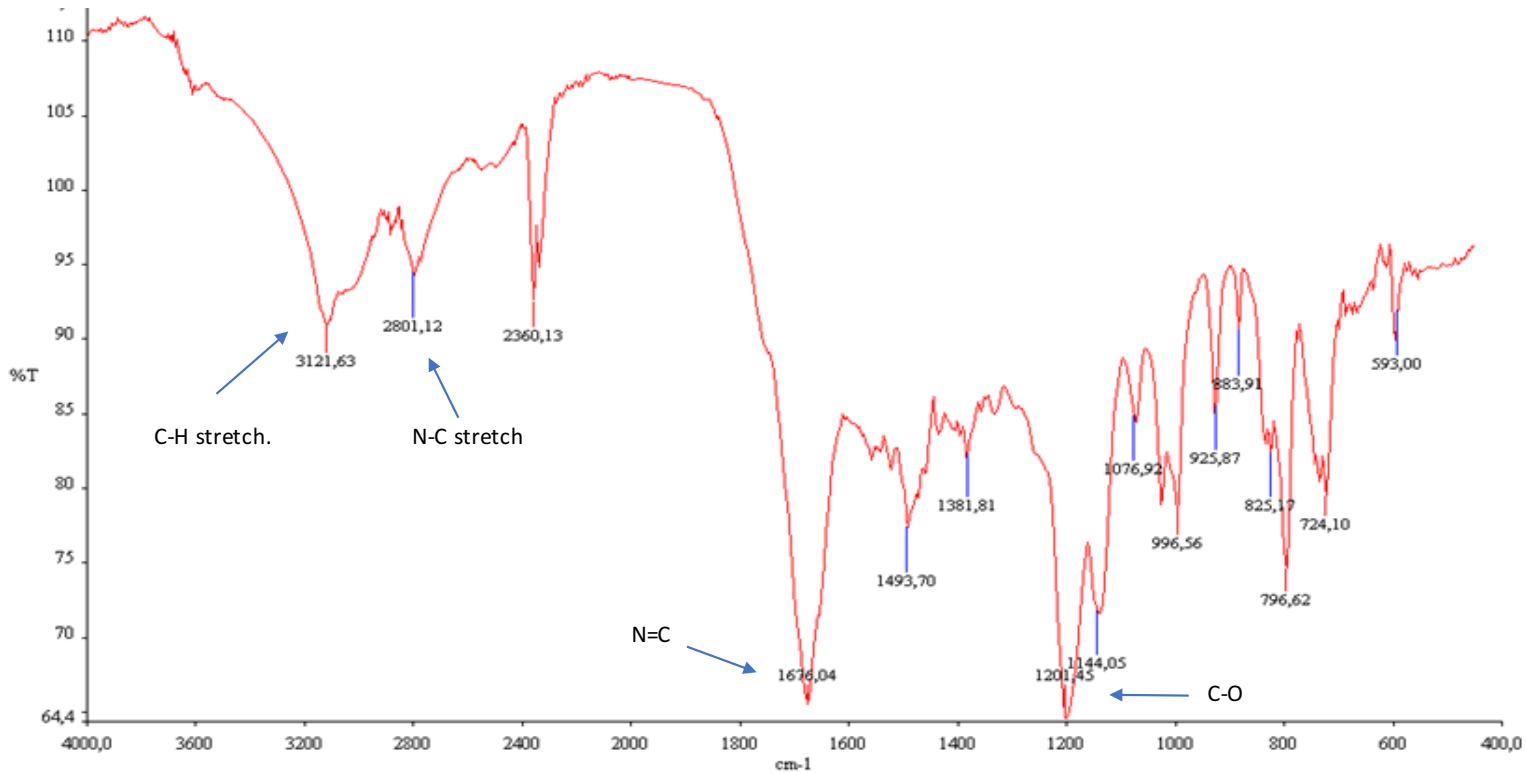

Figure S3. IR spectrum of compound **1-Zn.**

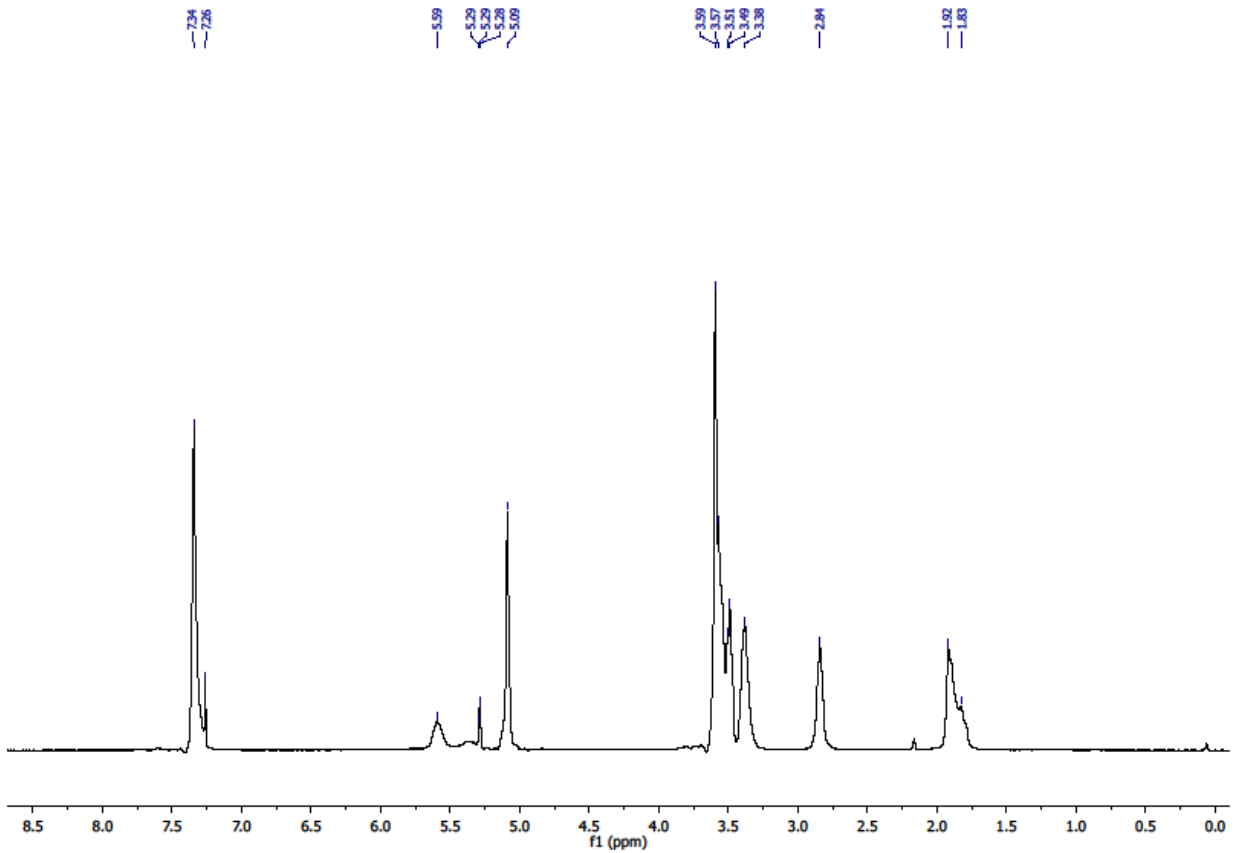

Figure S4. ^{1}H spectrum of compound **a** (300 MHz, CDCl3).

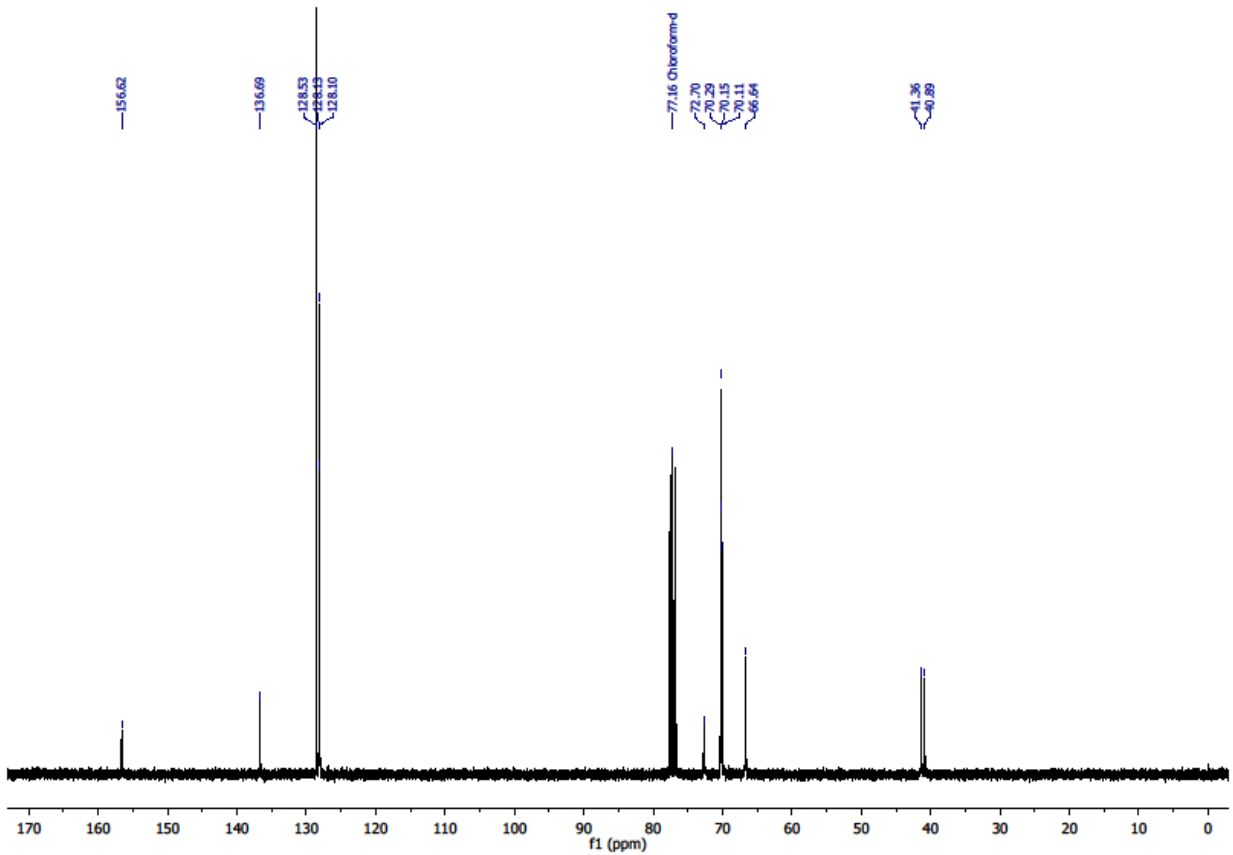

Figure S5. ^{13}C NMR spectrum of compound **a** (300 MHz, CDCl3).

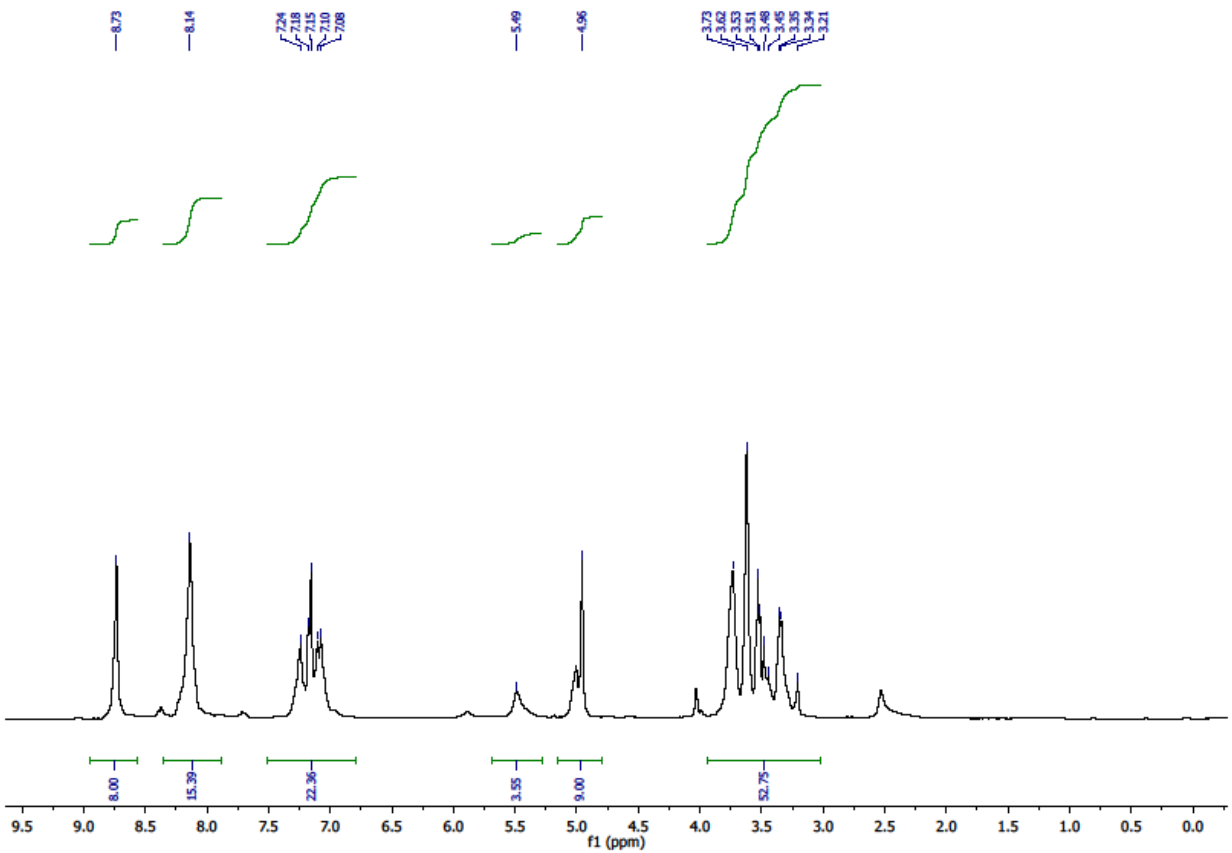

Figure S6. ^{1}H NMR spectrum of compound **b** (300 MHz, CDCl3).

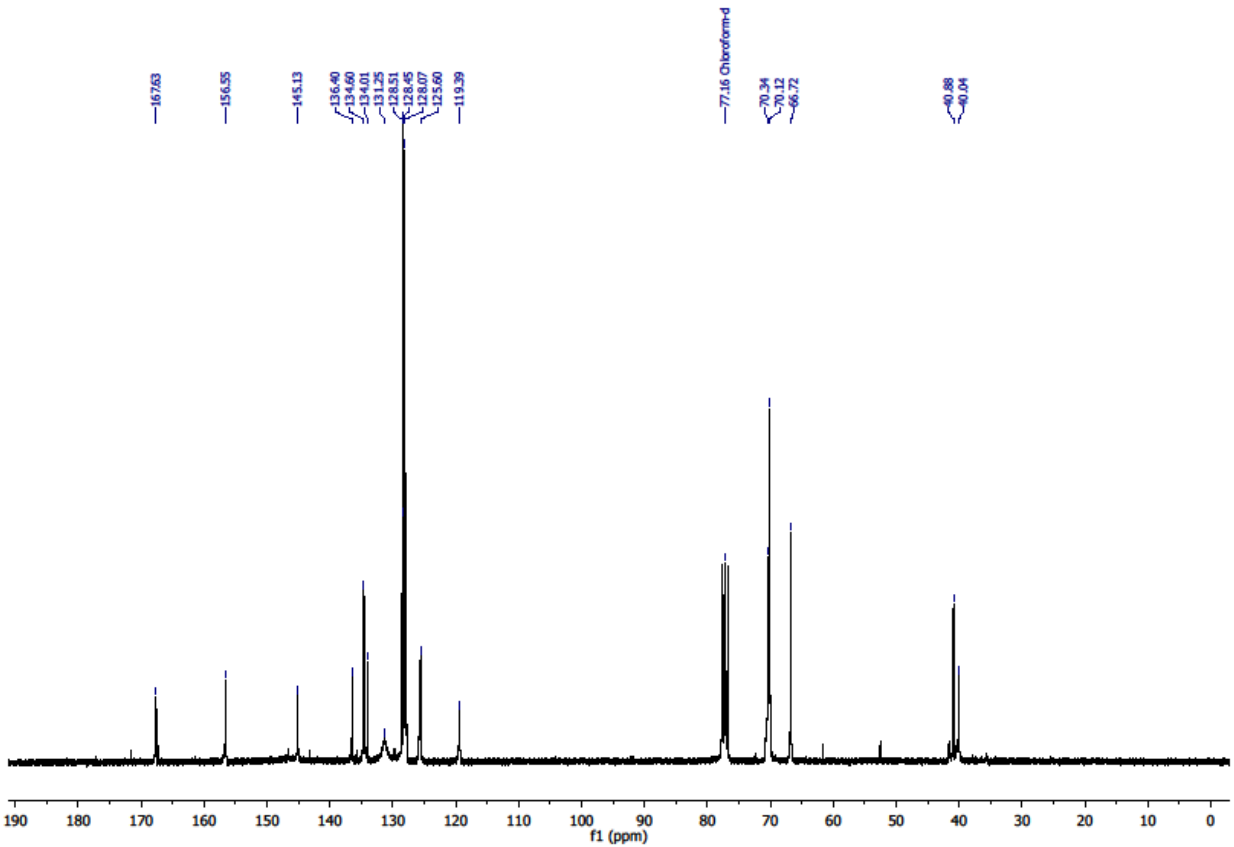

Figure S7. ^{13}C NMR spectrum of compound **b** (300 MHz, CDCl3).

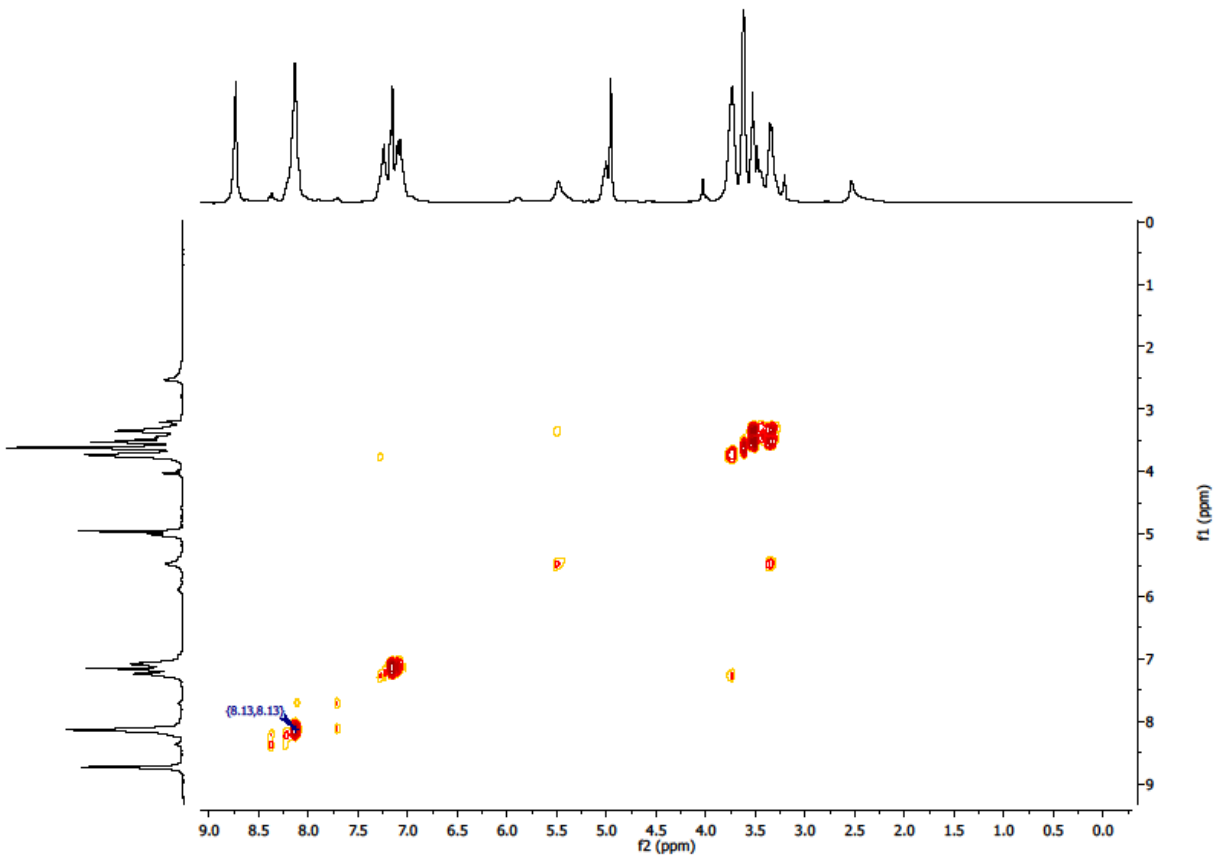

Figure S8. DQF-COSY spectrum of compound **b** (300 MHz, CDCl3).

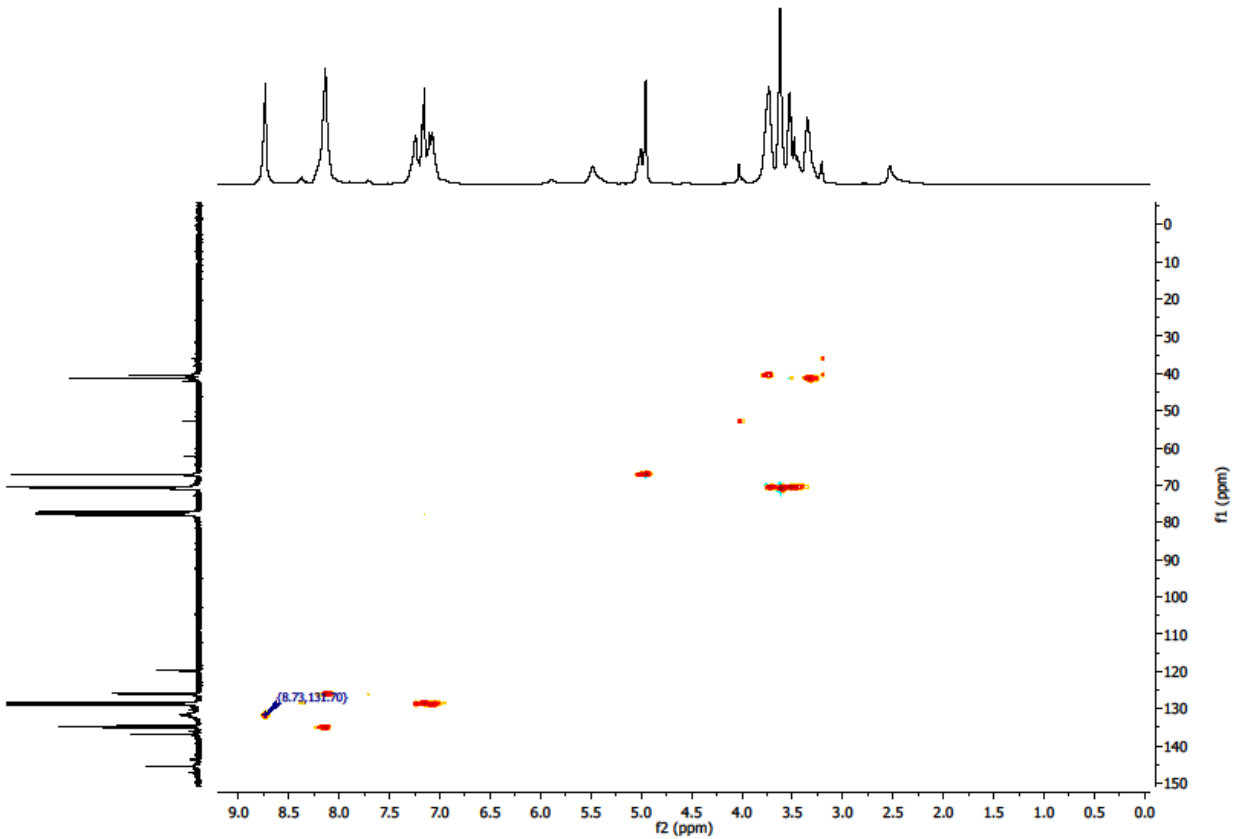

Figure S9. HSQC spectrum of compound **b** (300 MHz, CDCl3).

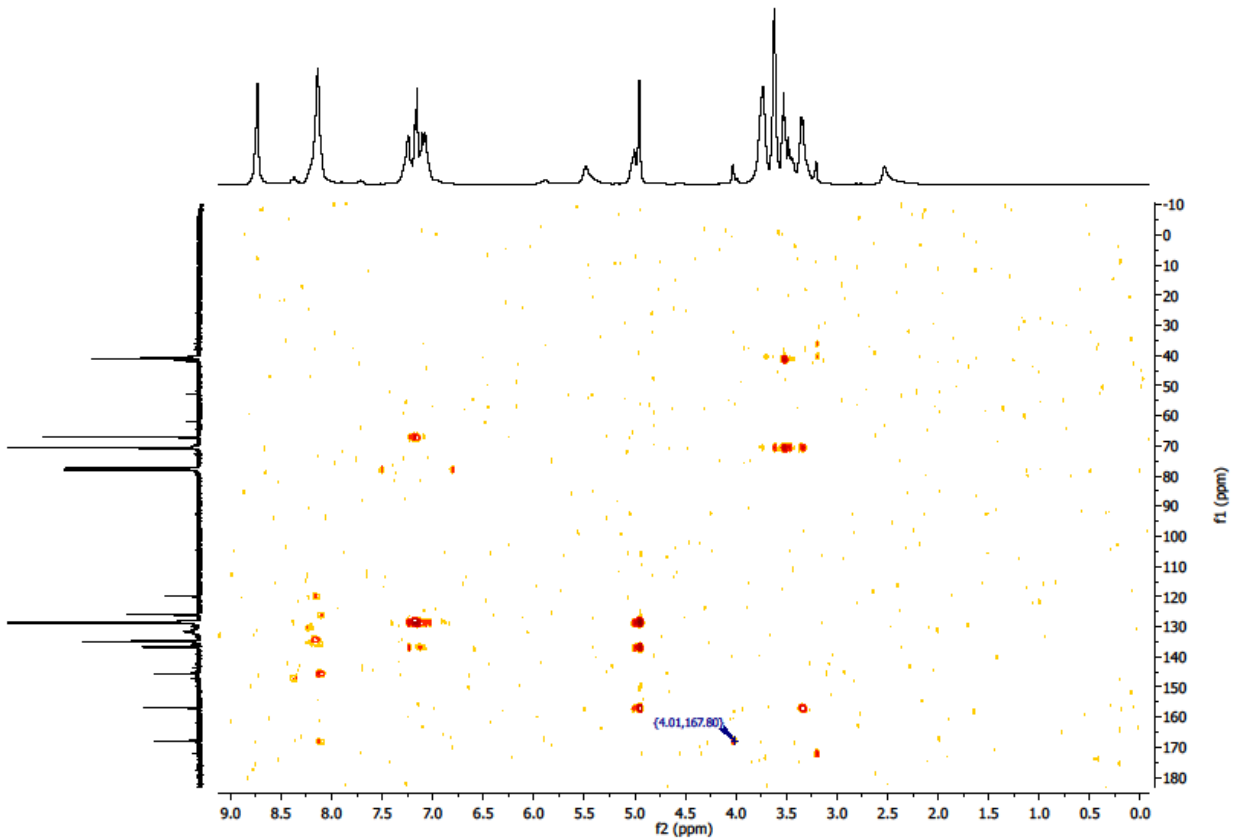

Figure S10. HMBC spectrum of compound **b** (300 MHz, CDCl3).

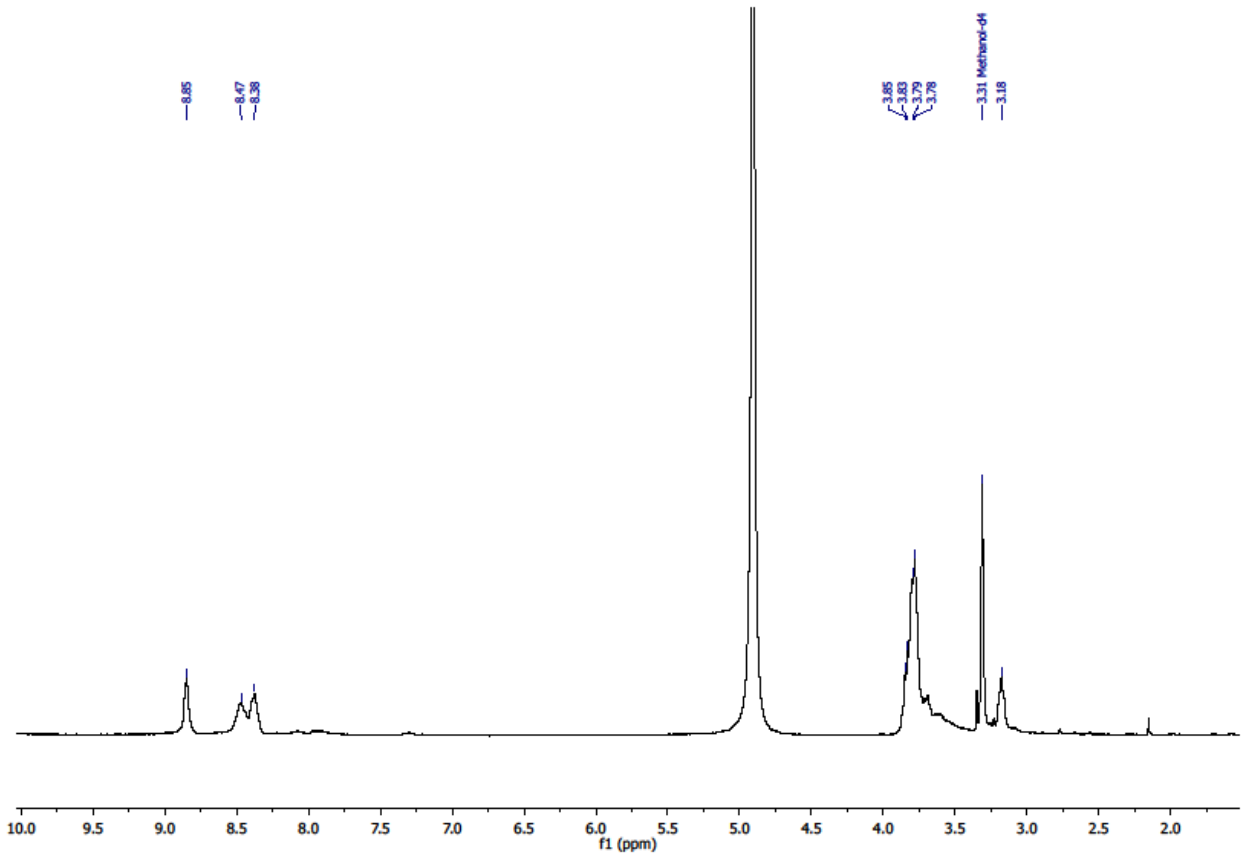

Figure S11. ^{1}H NMR spectrum of compound **c** (300 MHz, MeOD).

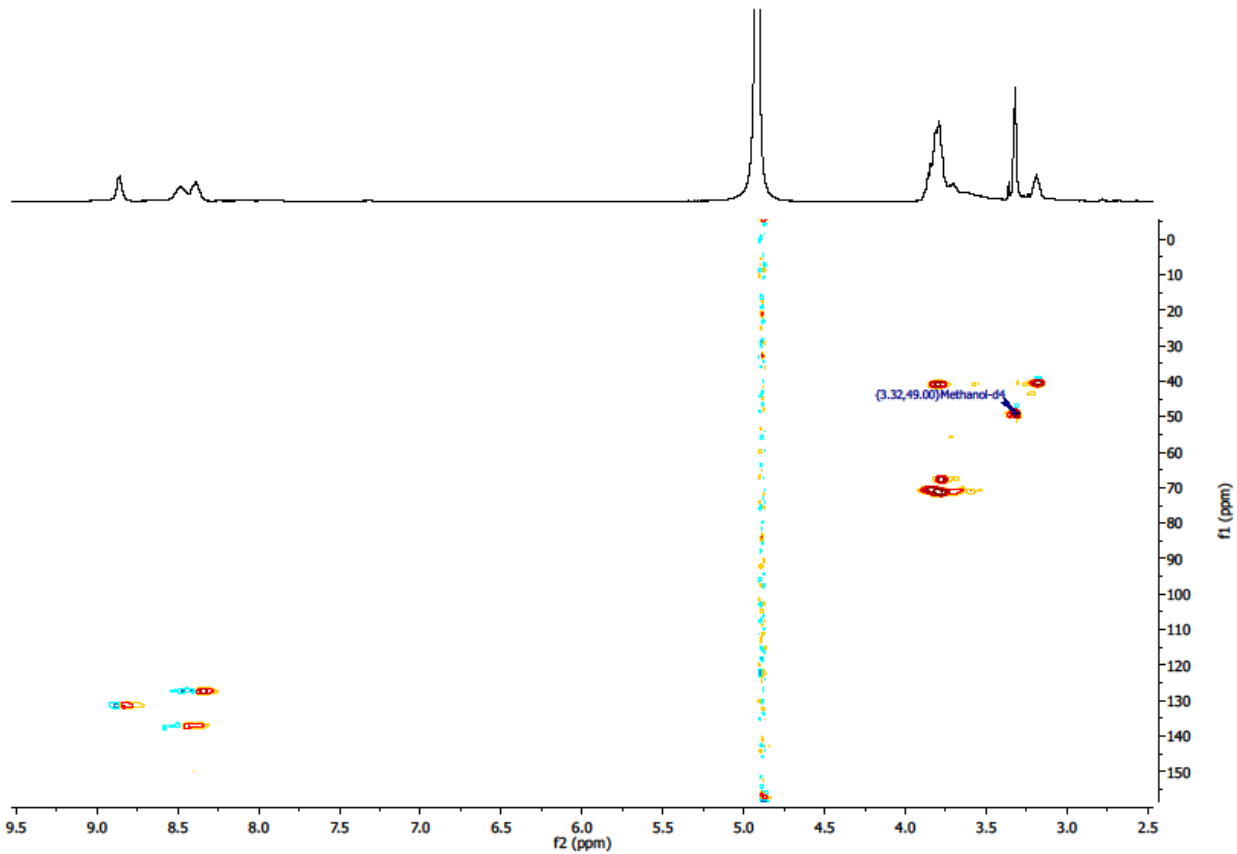

Figure S12**.** HSQC spectrum of compound **c** (300 MHz, MeOD).

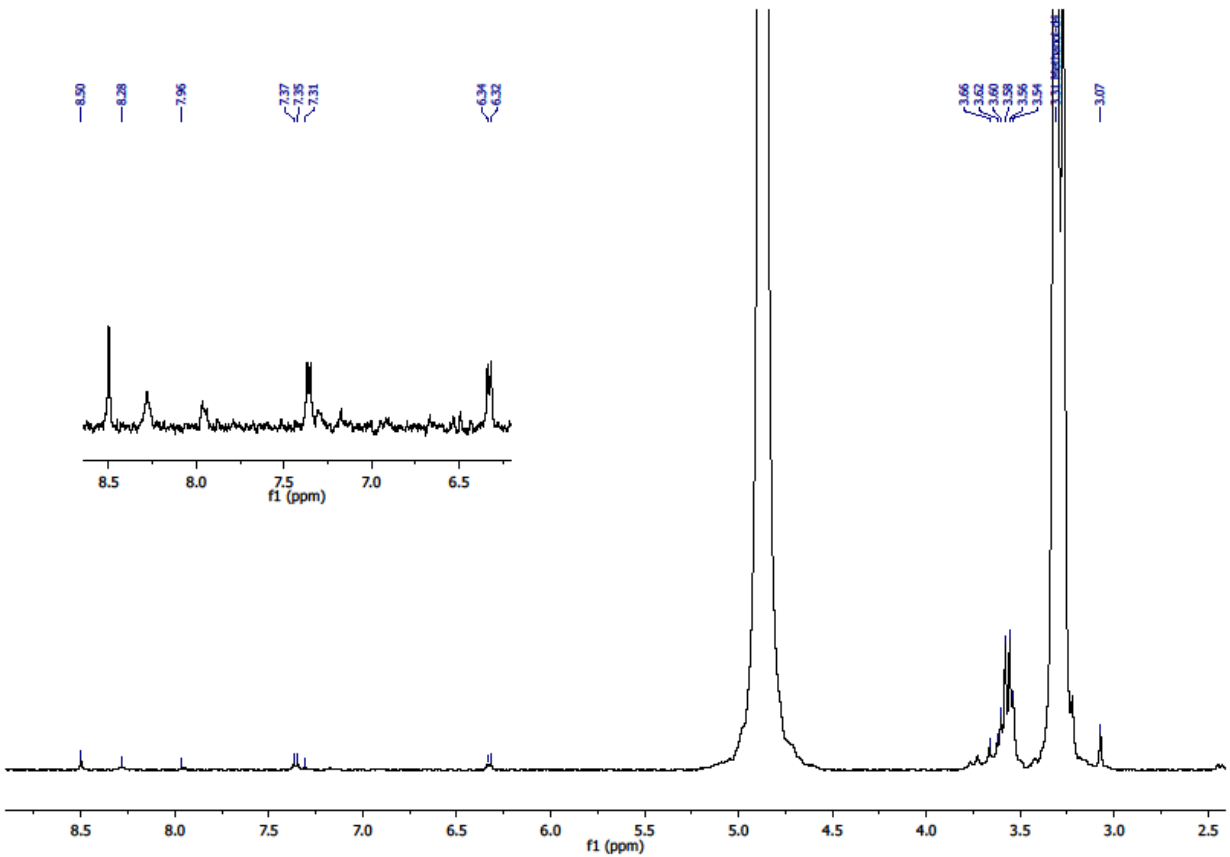

Figure S13. ^{1}H NMR spectrum of compound **2** (300 MHz, MeOD).

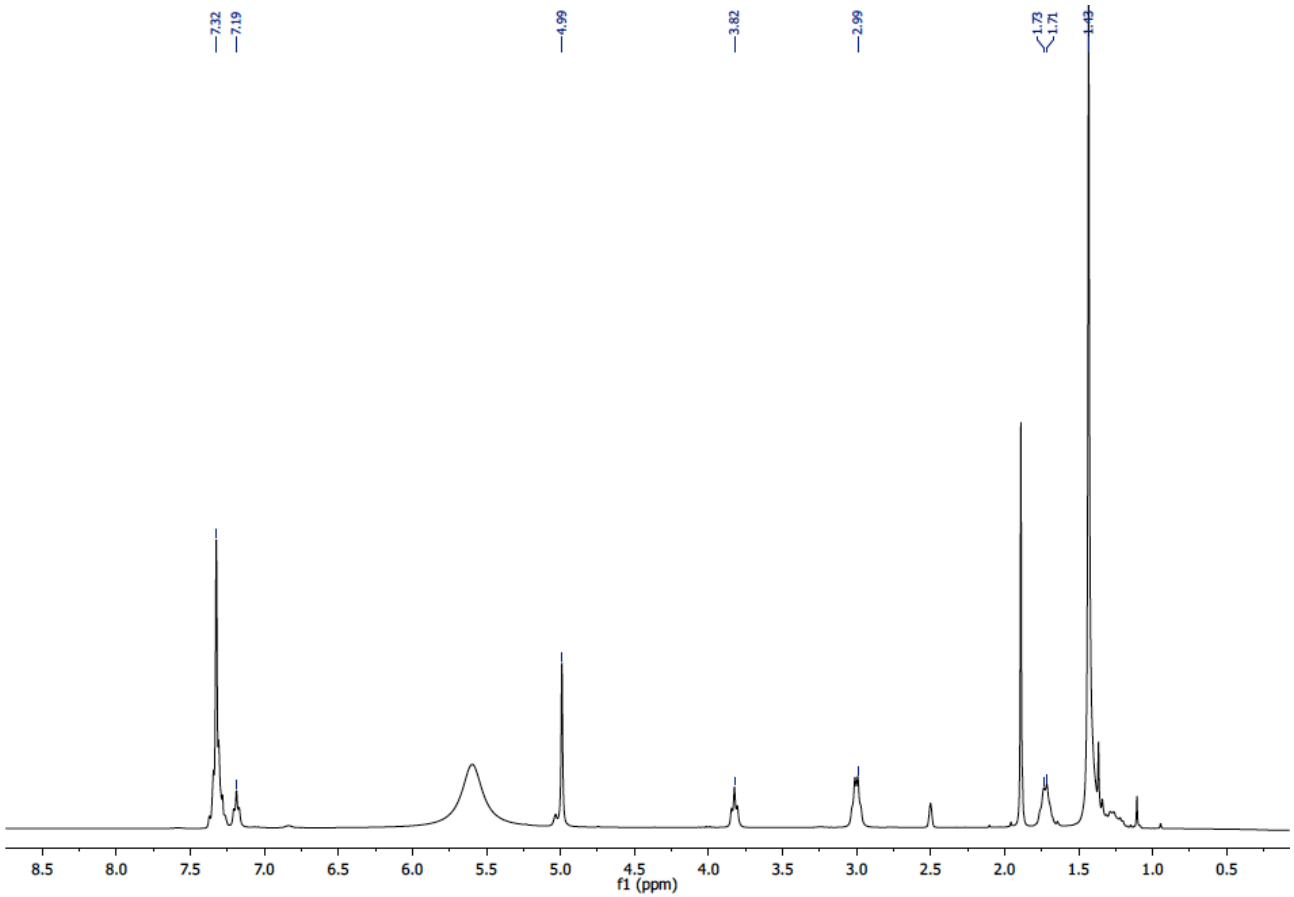

Figure S14. ^{1}H spectrum of compound **d** (300 MHz, DMSO).

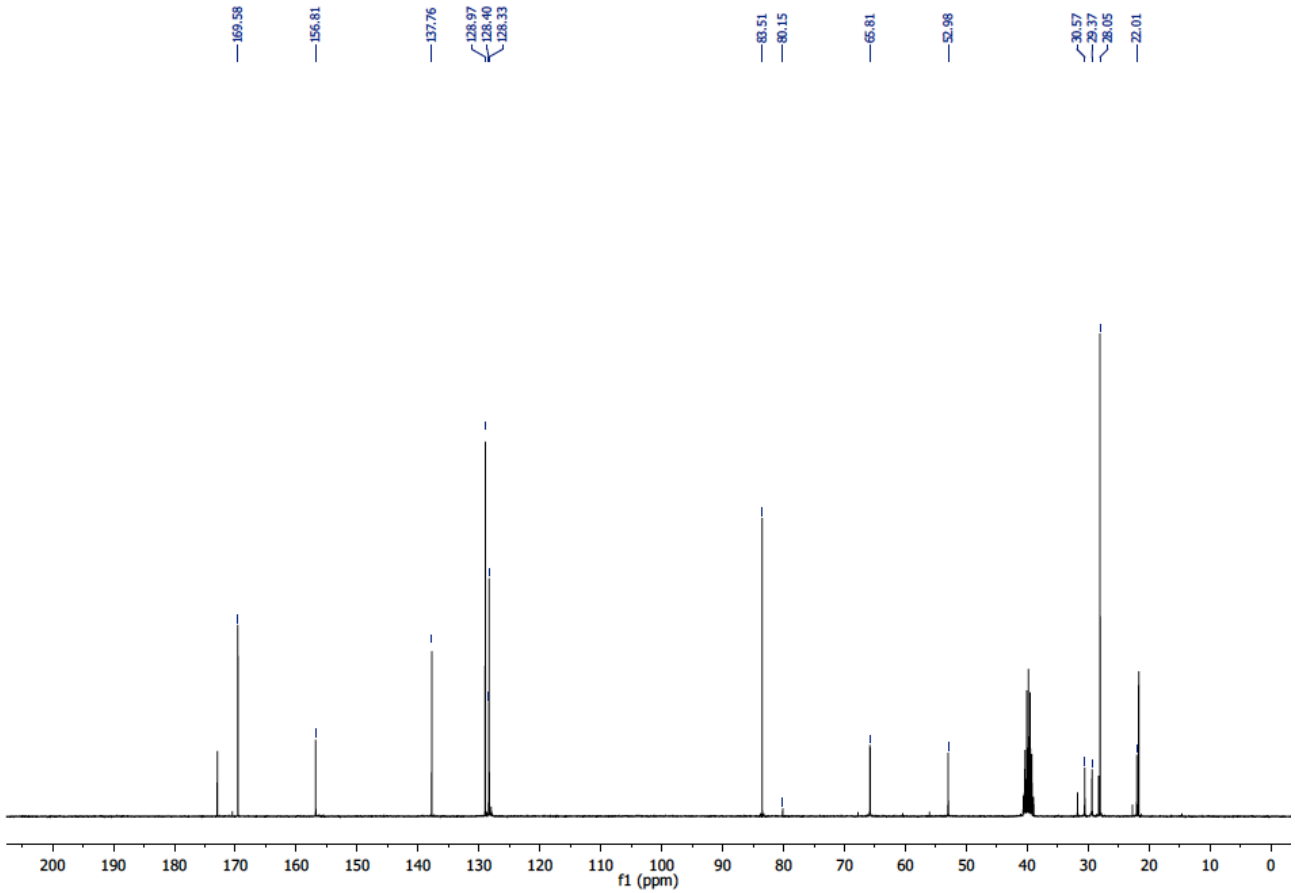

Figure S15. ^{13}C spectrum of compound **d** (300 MHz, DMSO).

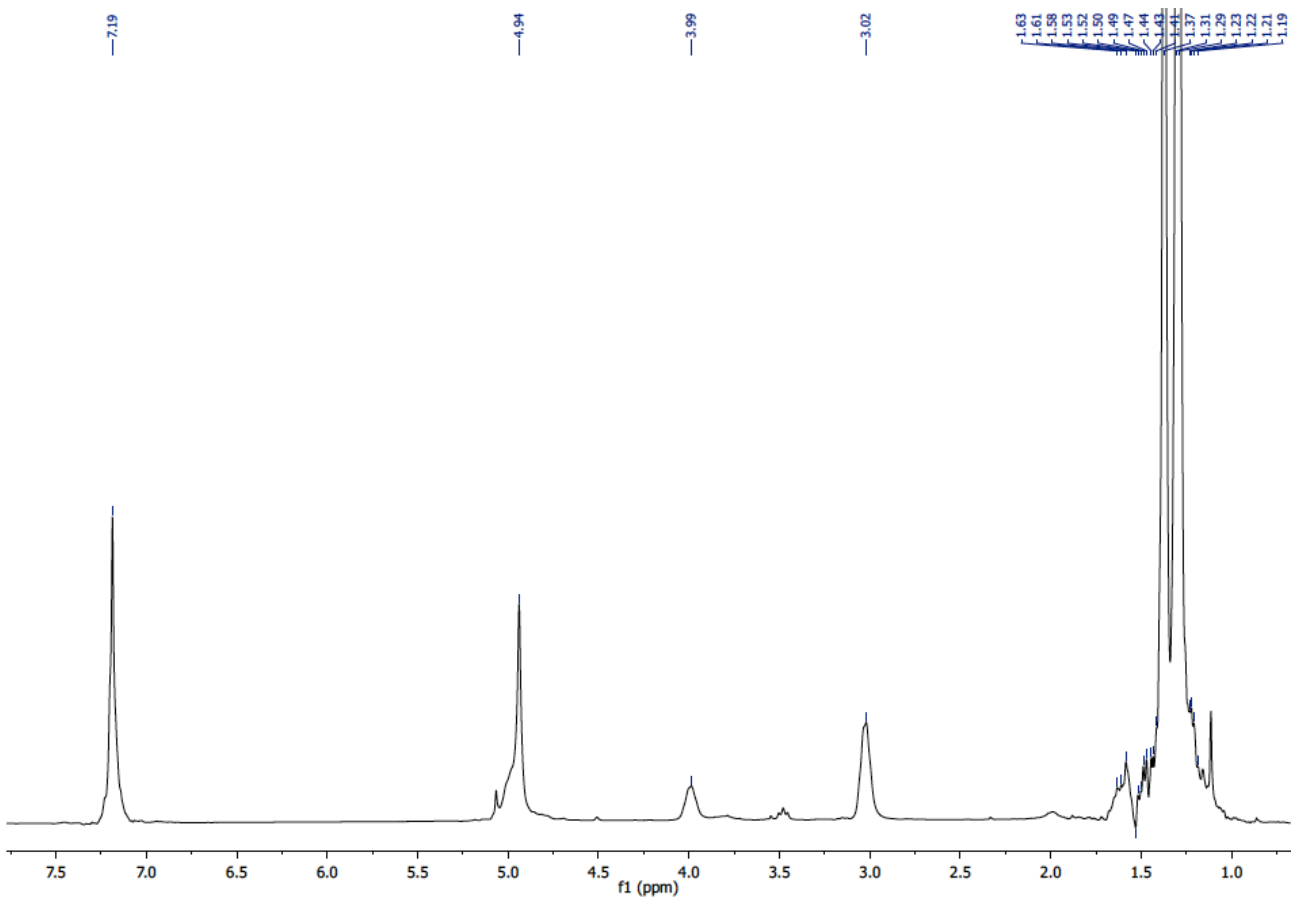

Figure S16. ^{1}H spectrum of compound **e** (300 MHz, MeOD).

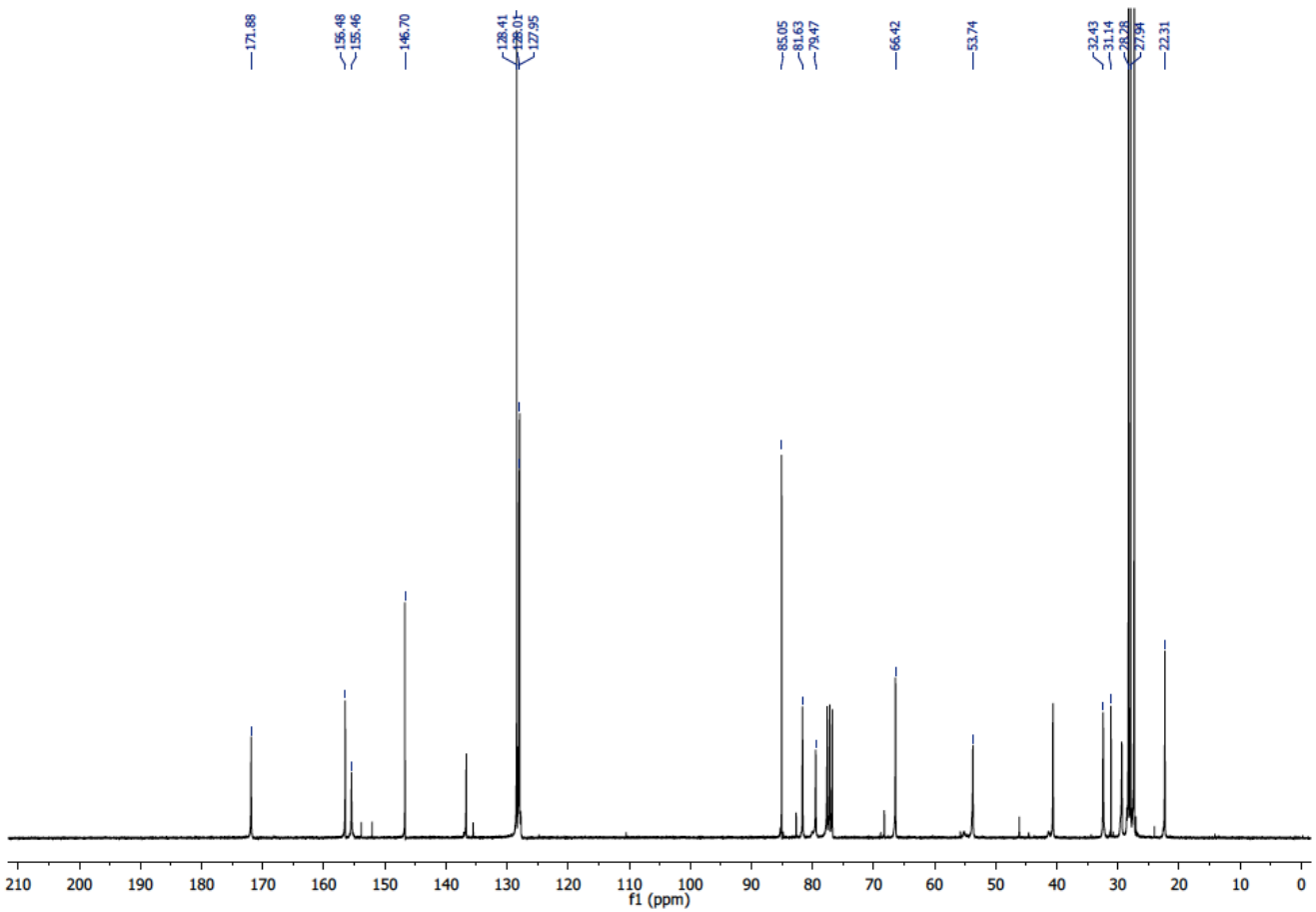

Figure S17. ^{13}C spectrum of compound **e** (300 MHz, MeOD).

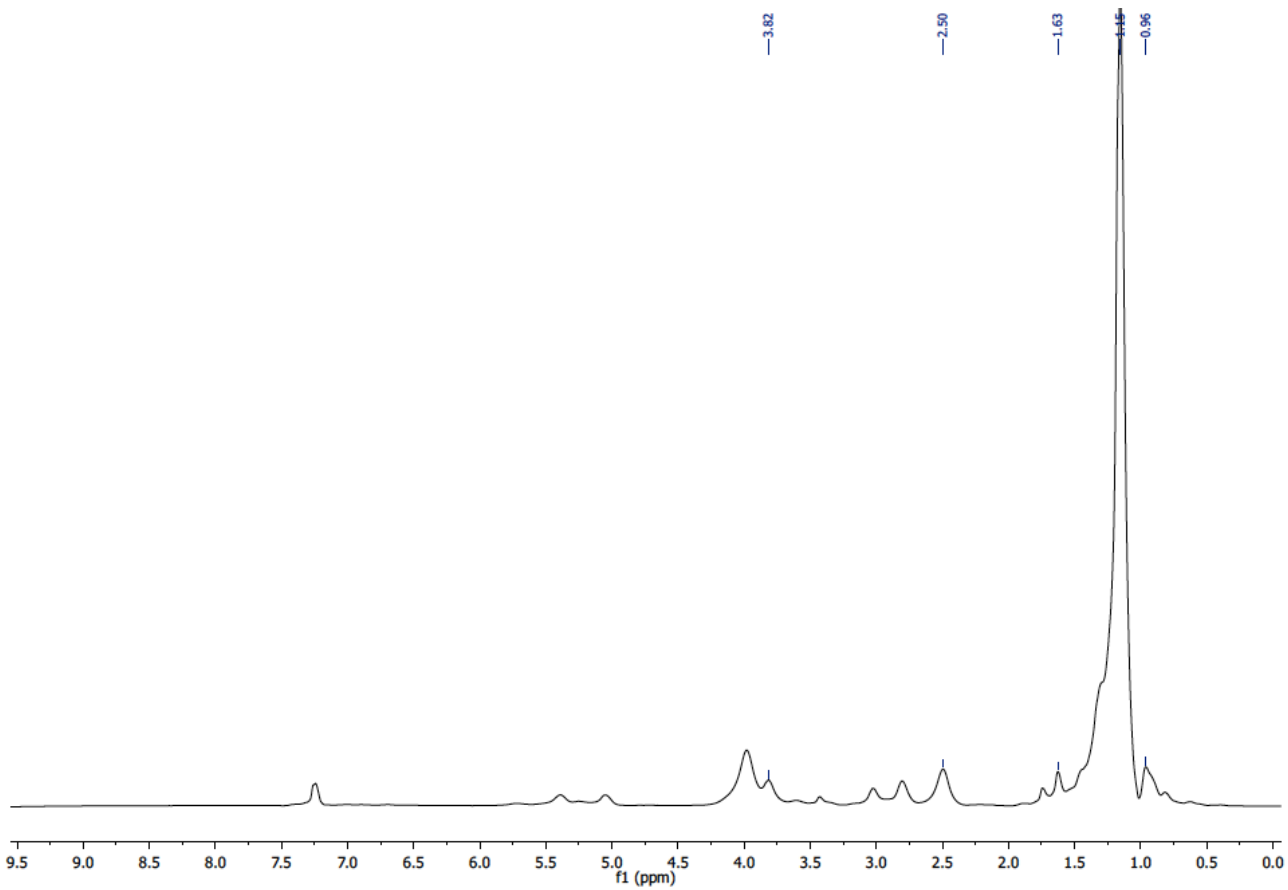

Figure S18 ^{1}H spectrum of compound **f** (300 MHz, $CDCl_3$) *.

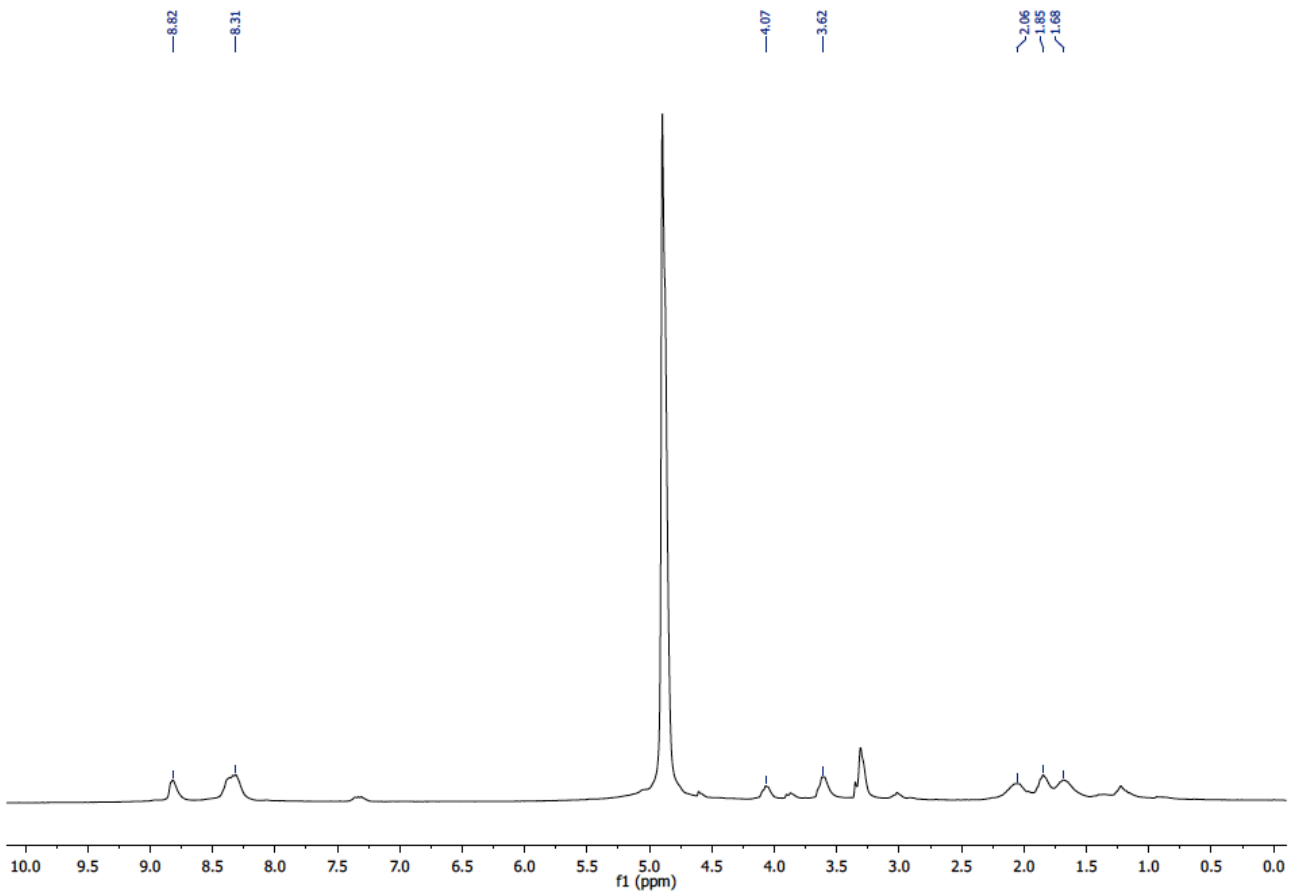

Figure S19. ^{1}H spectrum of compound **3** (300 MHz, MeOD).

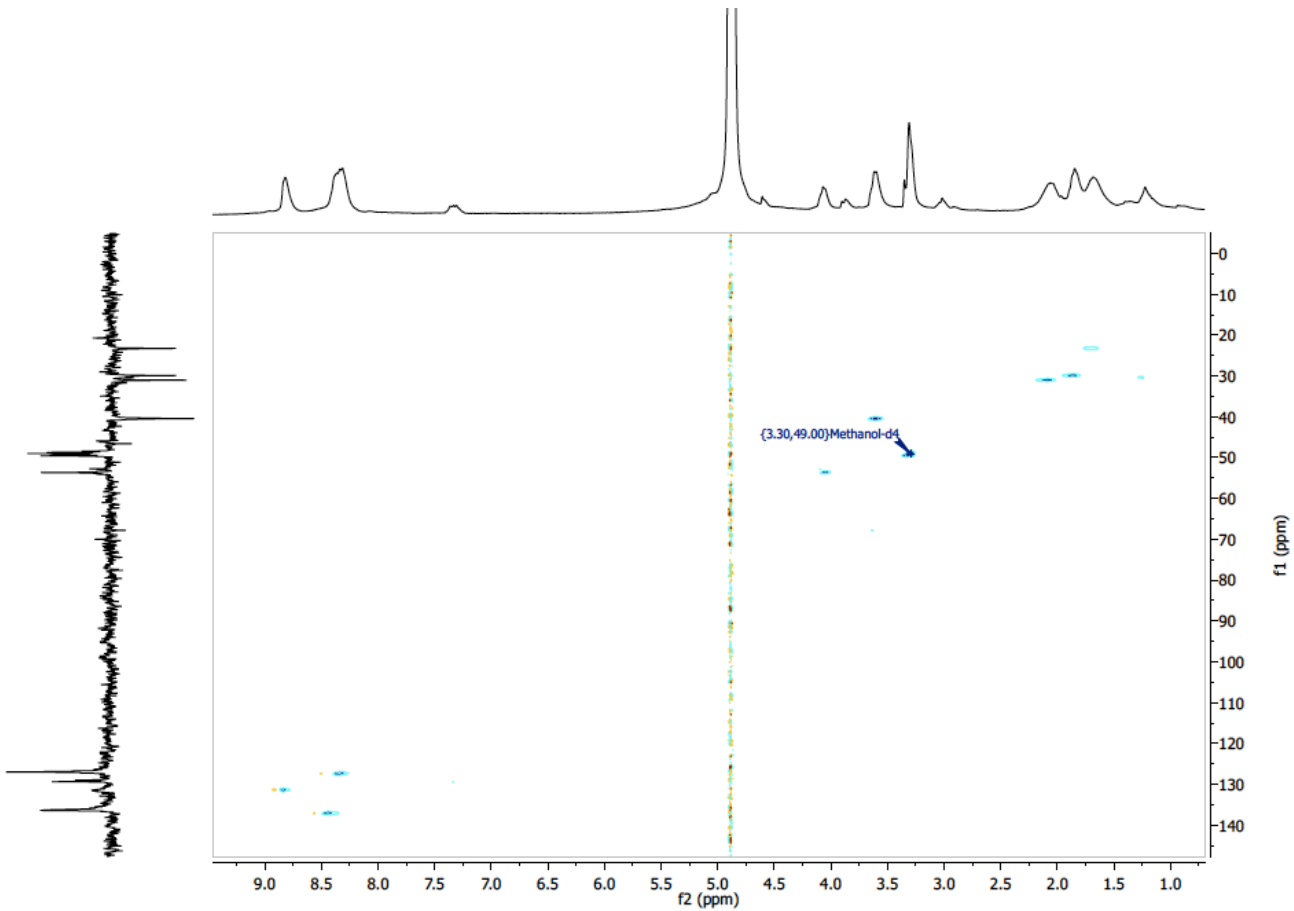

Figure S20. HSQC spectrum of compound **3** (300 MHz, MeOD).

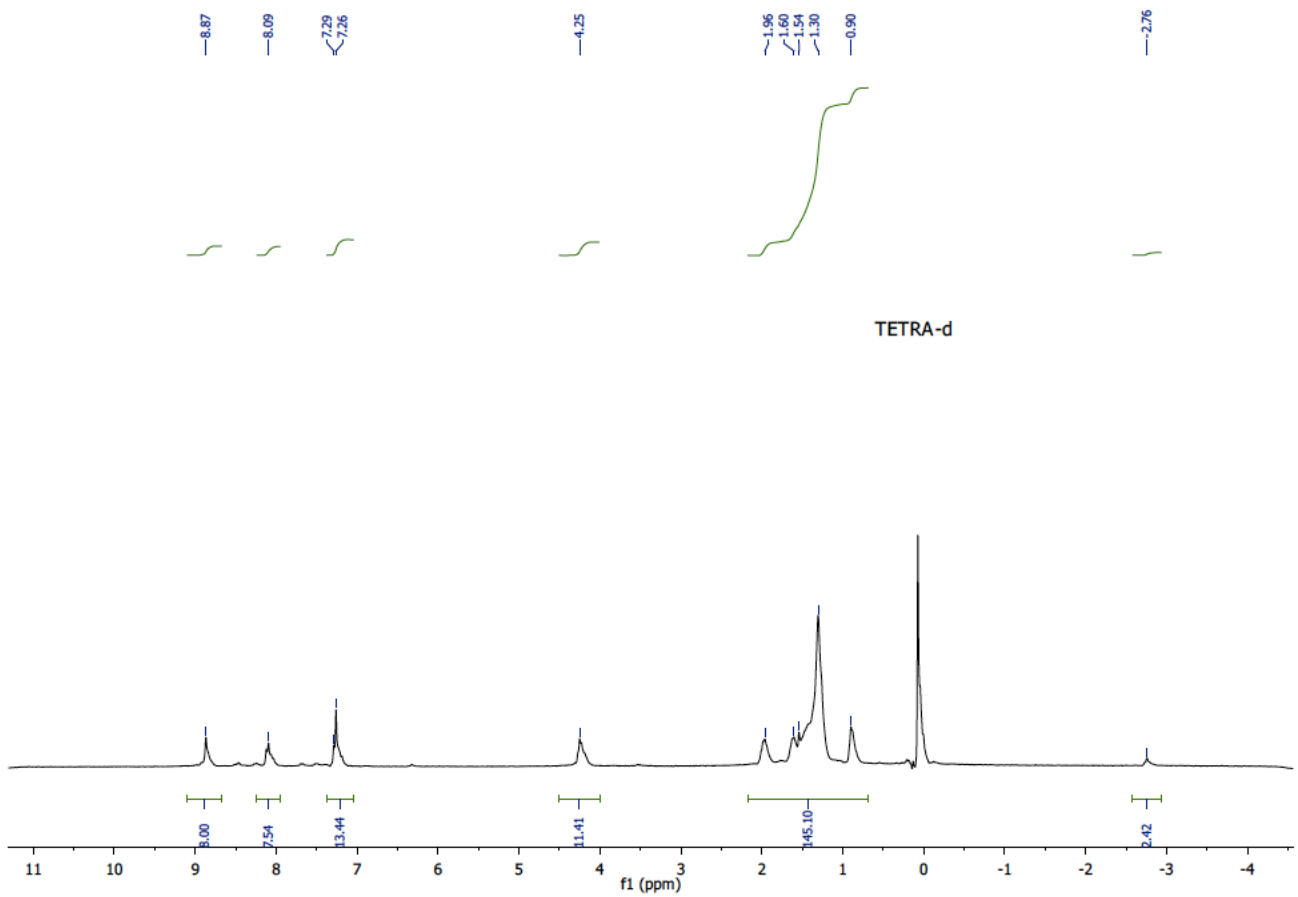

Figure S21. ^{1}H spectrum of compound **4** (300 MHz, $CDCl_3$).

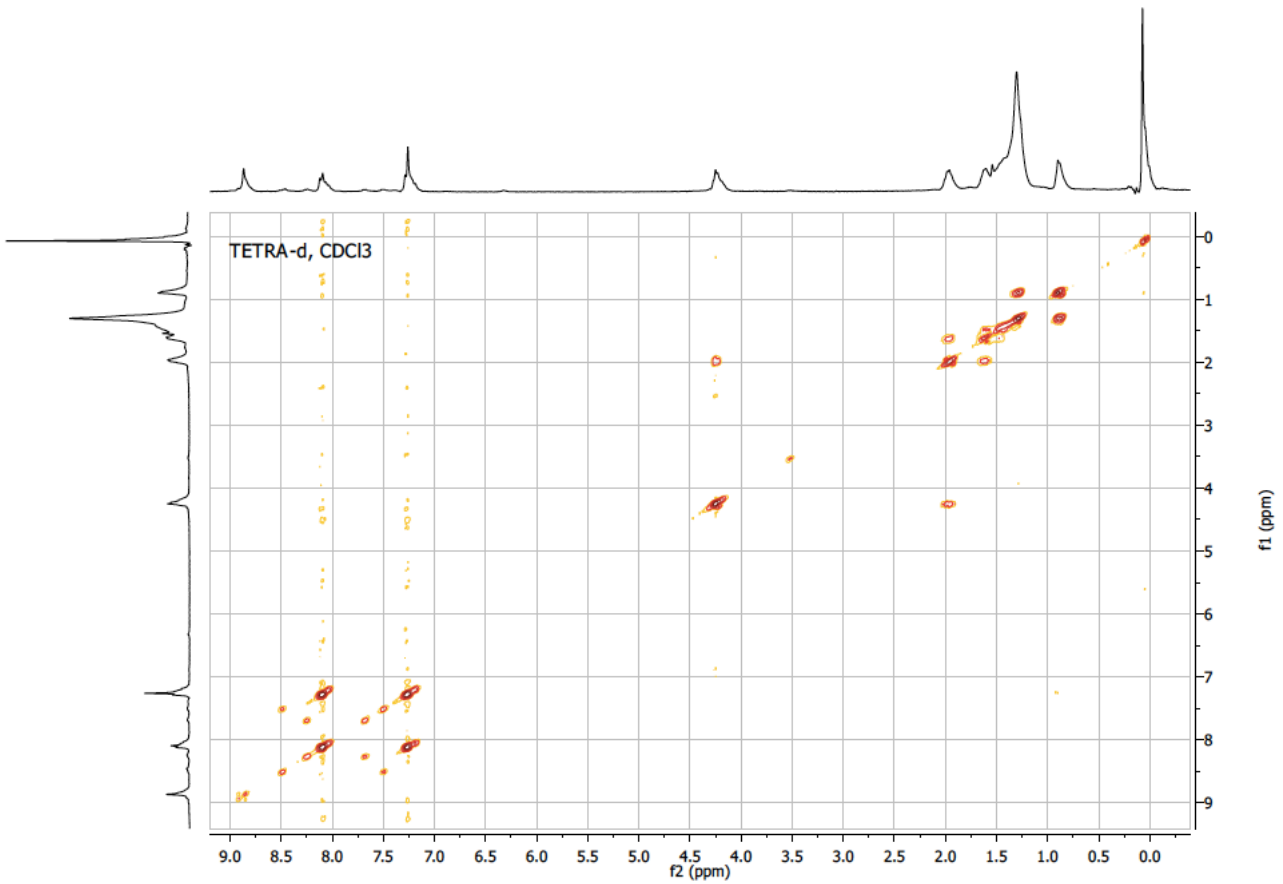

Figure S22. COSY spectrum of compound **4** (300 MHz, $CDCl_3$).

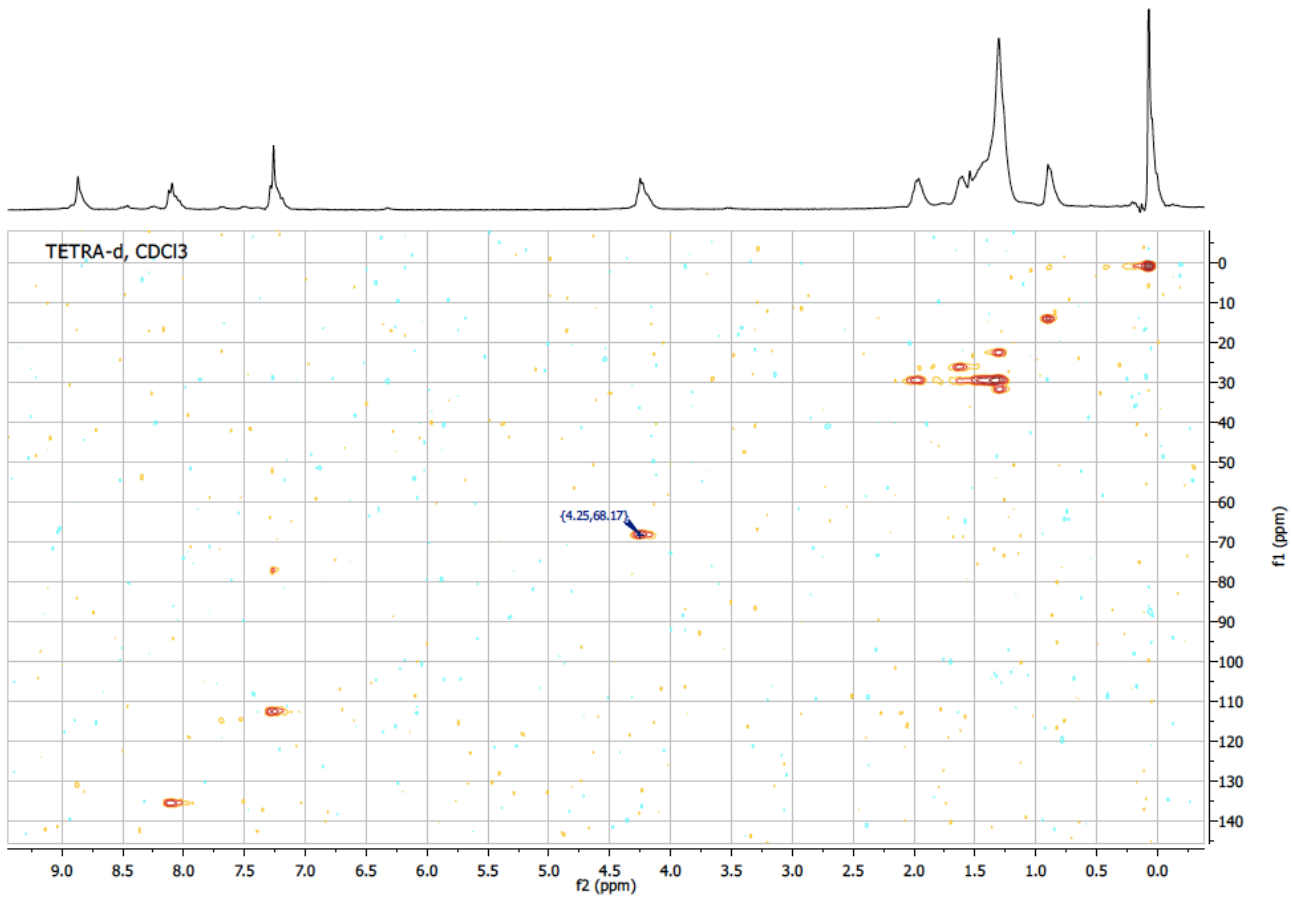

Figure S23. HSQC spectrum of compound **4** (300 MHz, $CDCl_3$).

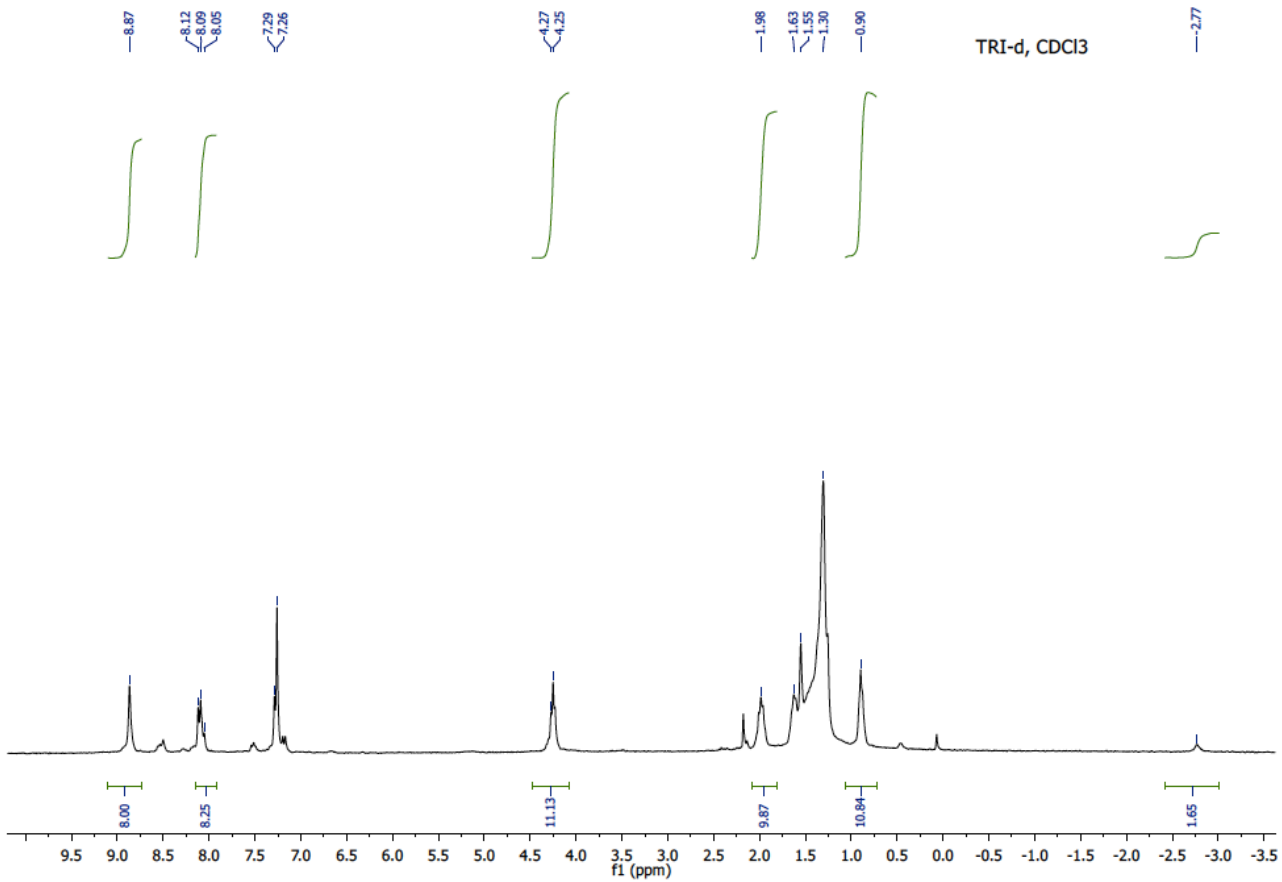

Figure S24. H^1 spectrum of compound **5** (300 MHz, $CDCl_3$).

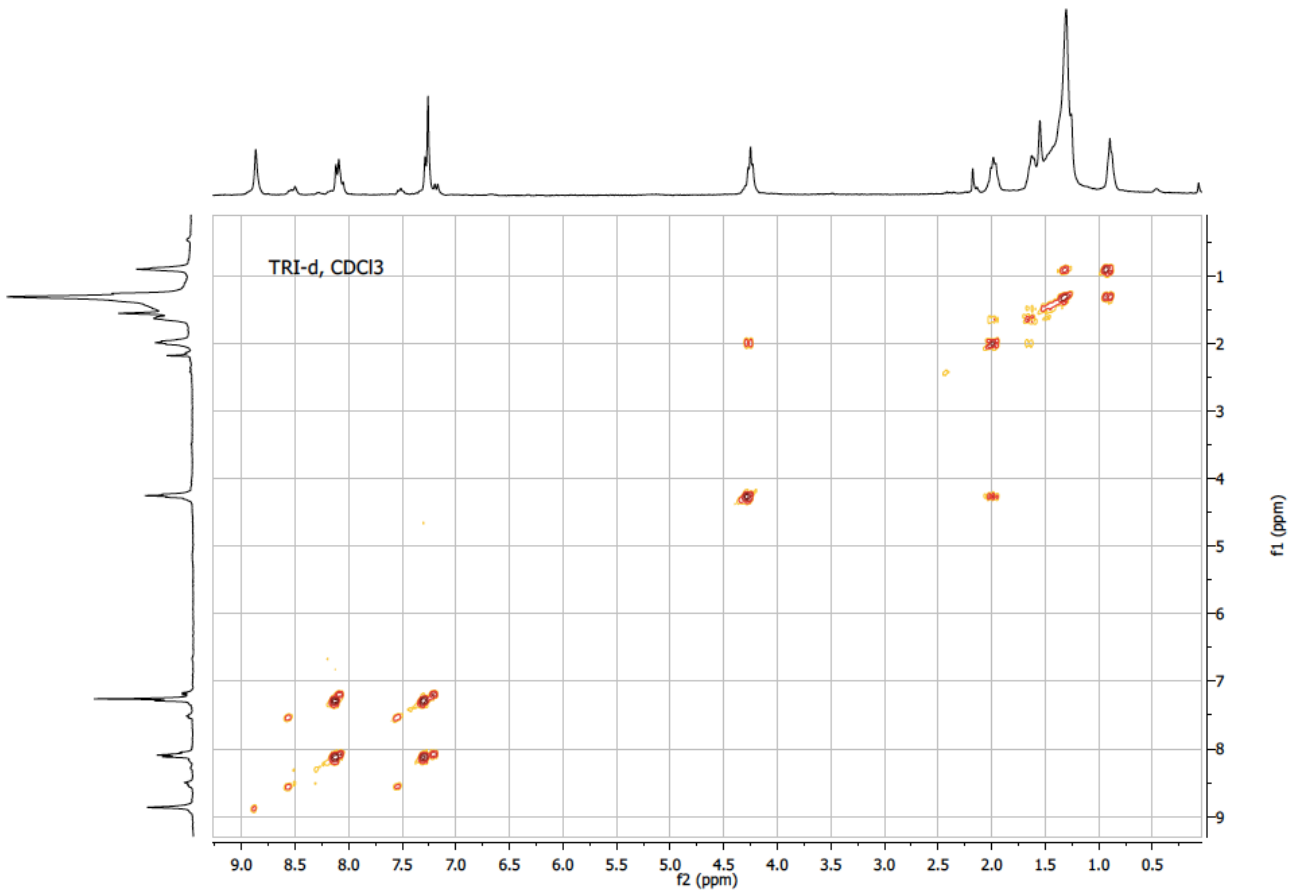

Figure S25. COSY spectrum of compound **5** (300 MHz, $CDCl_3$).

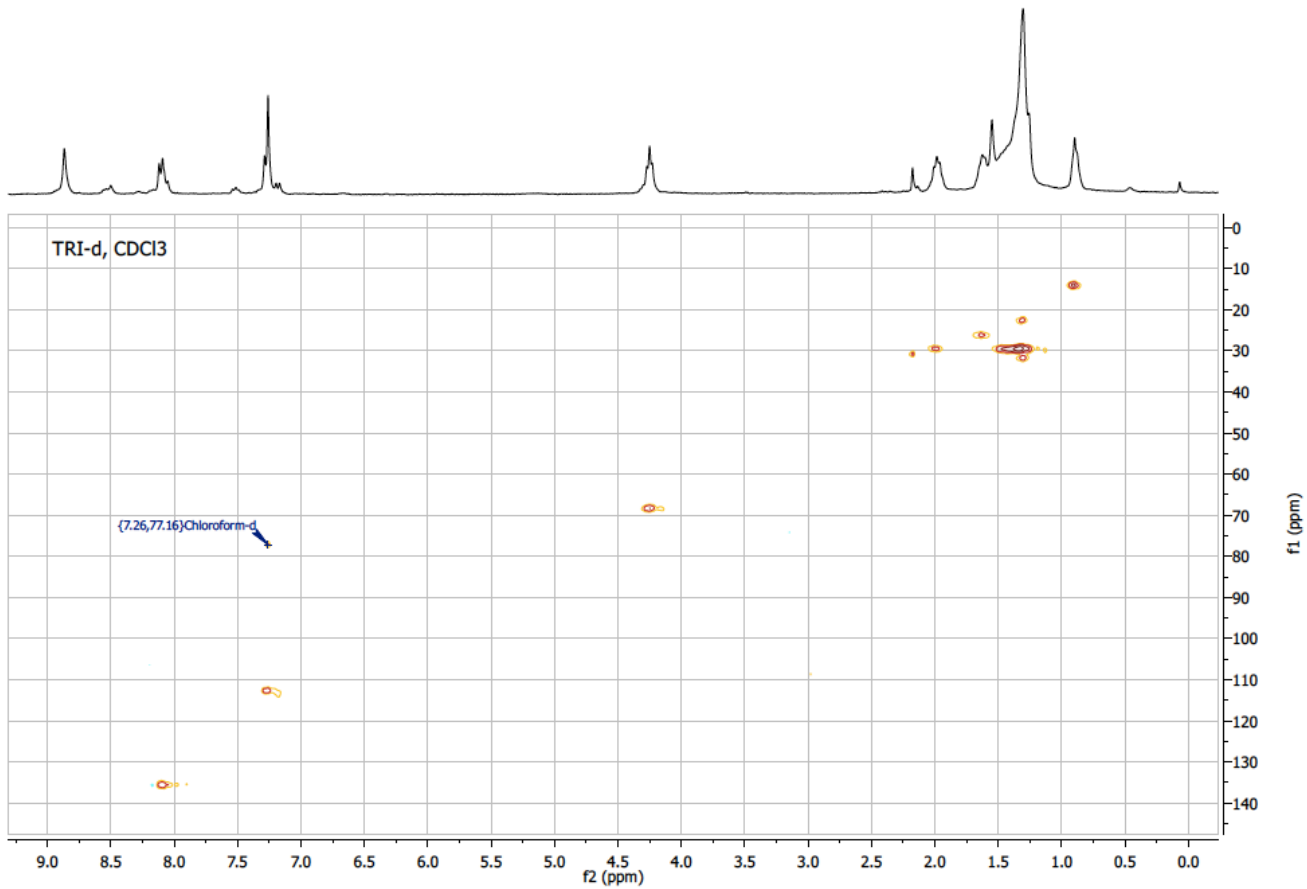

Figure S26. HSQC spectrum of compound **5** (300 MHz, $CDCl_3$).

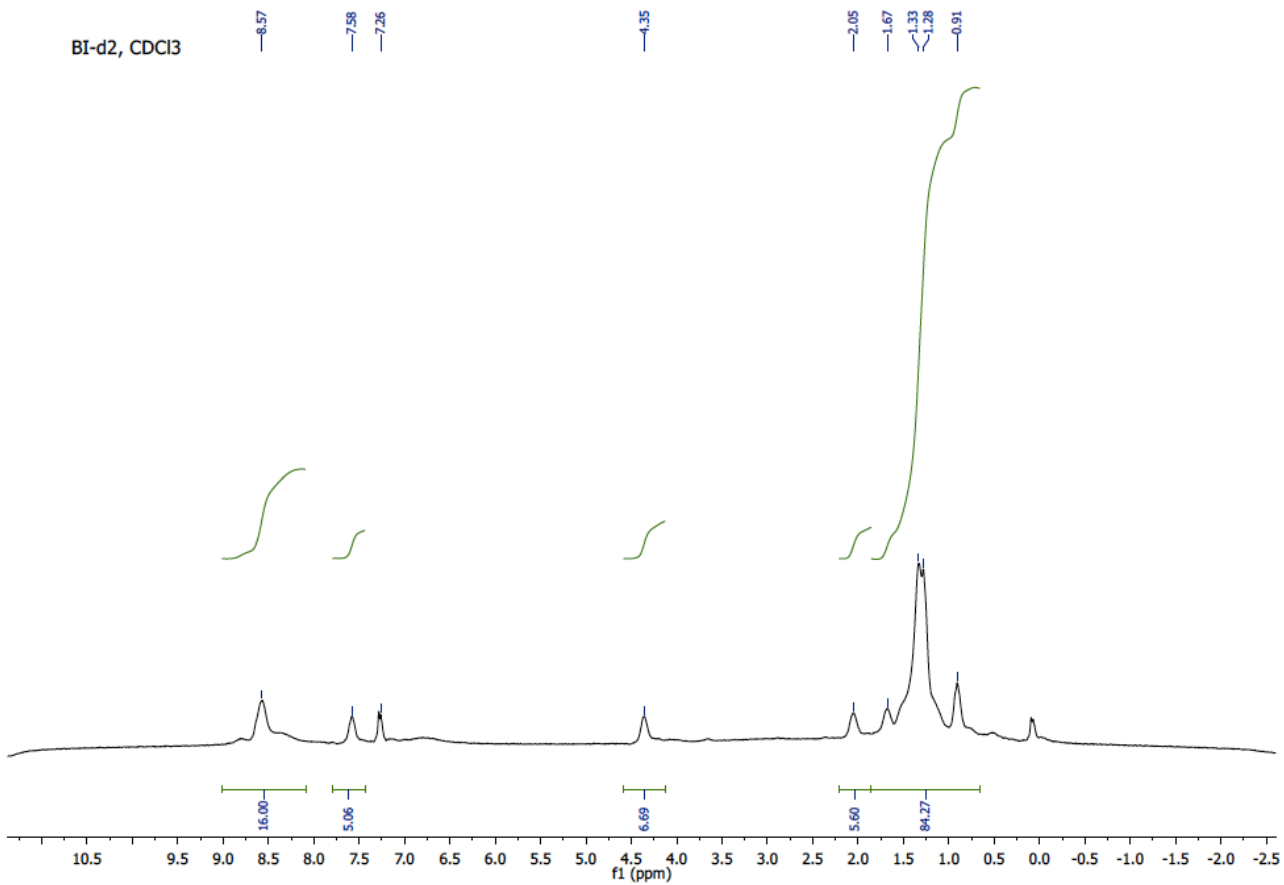

Figure S27. H^1 spectrum of compound **6** (300 MHz, $CDCl_3$).

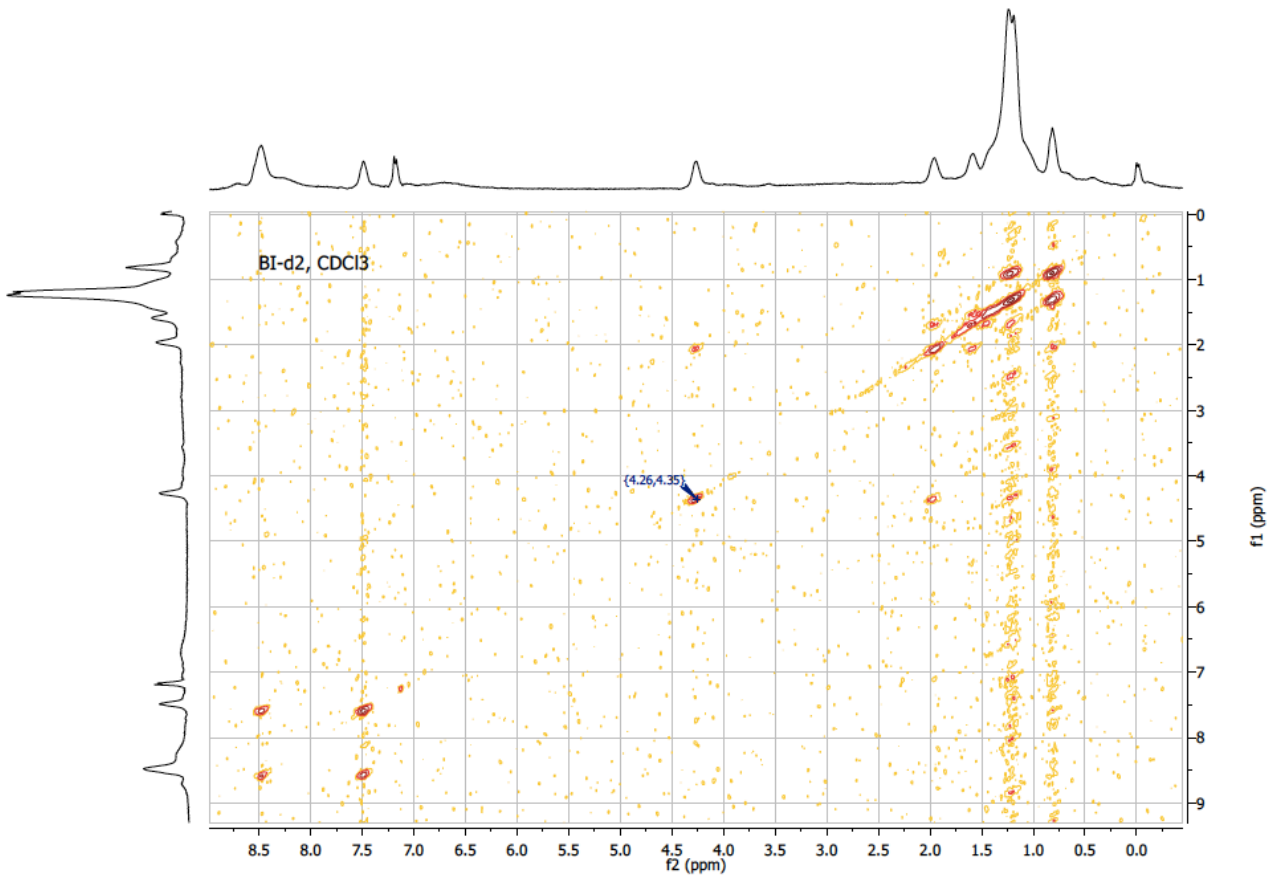

Figure S28. COSY spectrum of compound **6** (300 MHz, $CDCl_3$).

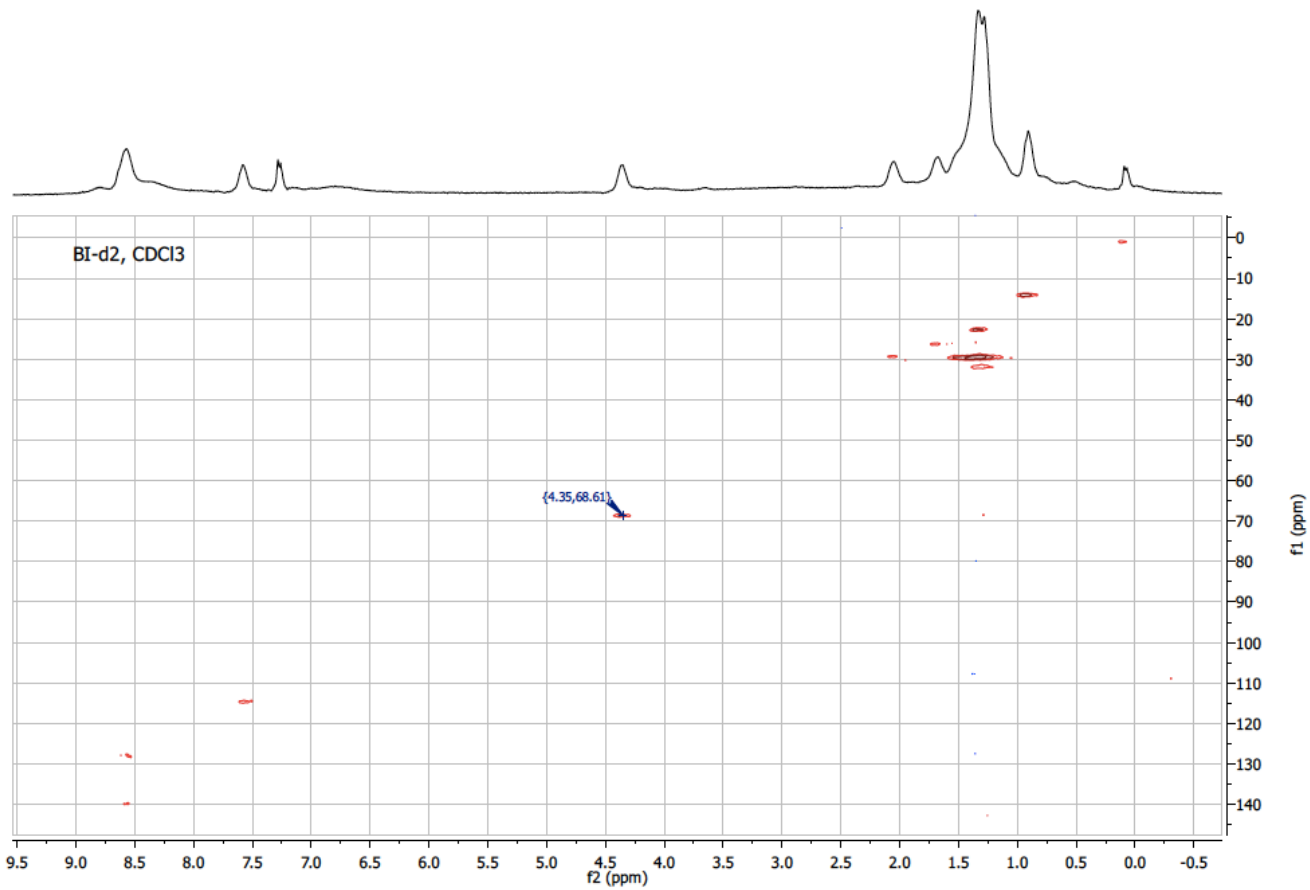

Figure S29. HSQC spectrum of compound **6** (300 MHz, $CDCl_3$).

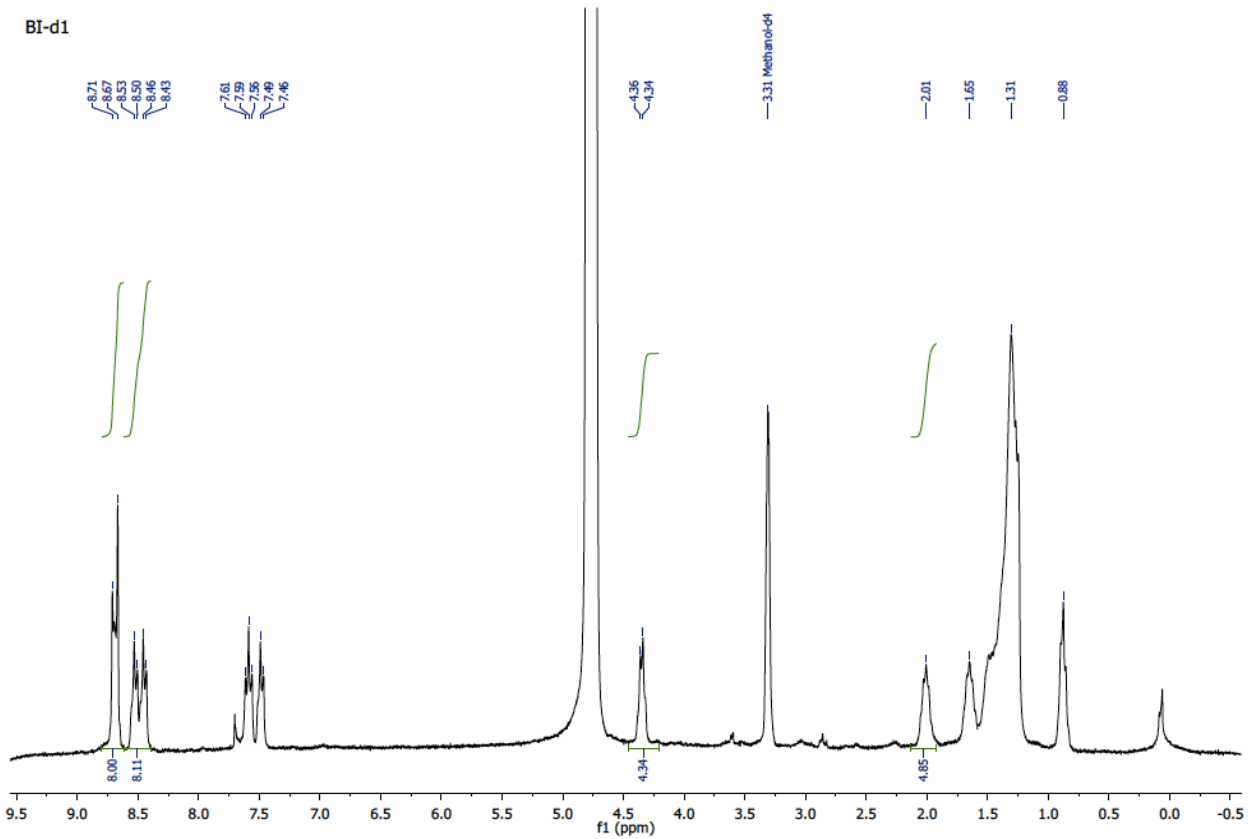

Figure S30. H^1 spectrum of compound **6-bis** (300 MHz, MeOD).

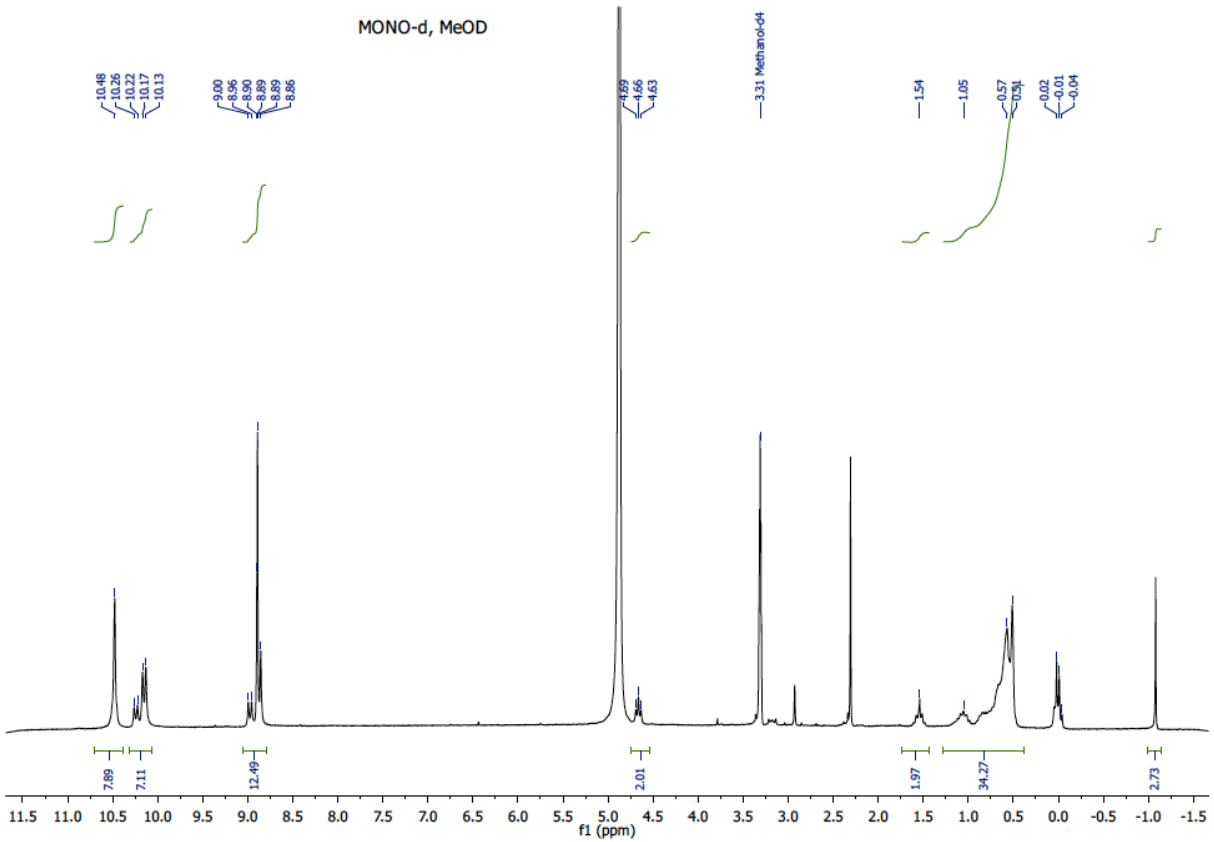

Figure S31. ^{1}H spectrum of compound **7** (300 MHz, MeOD).

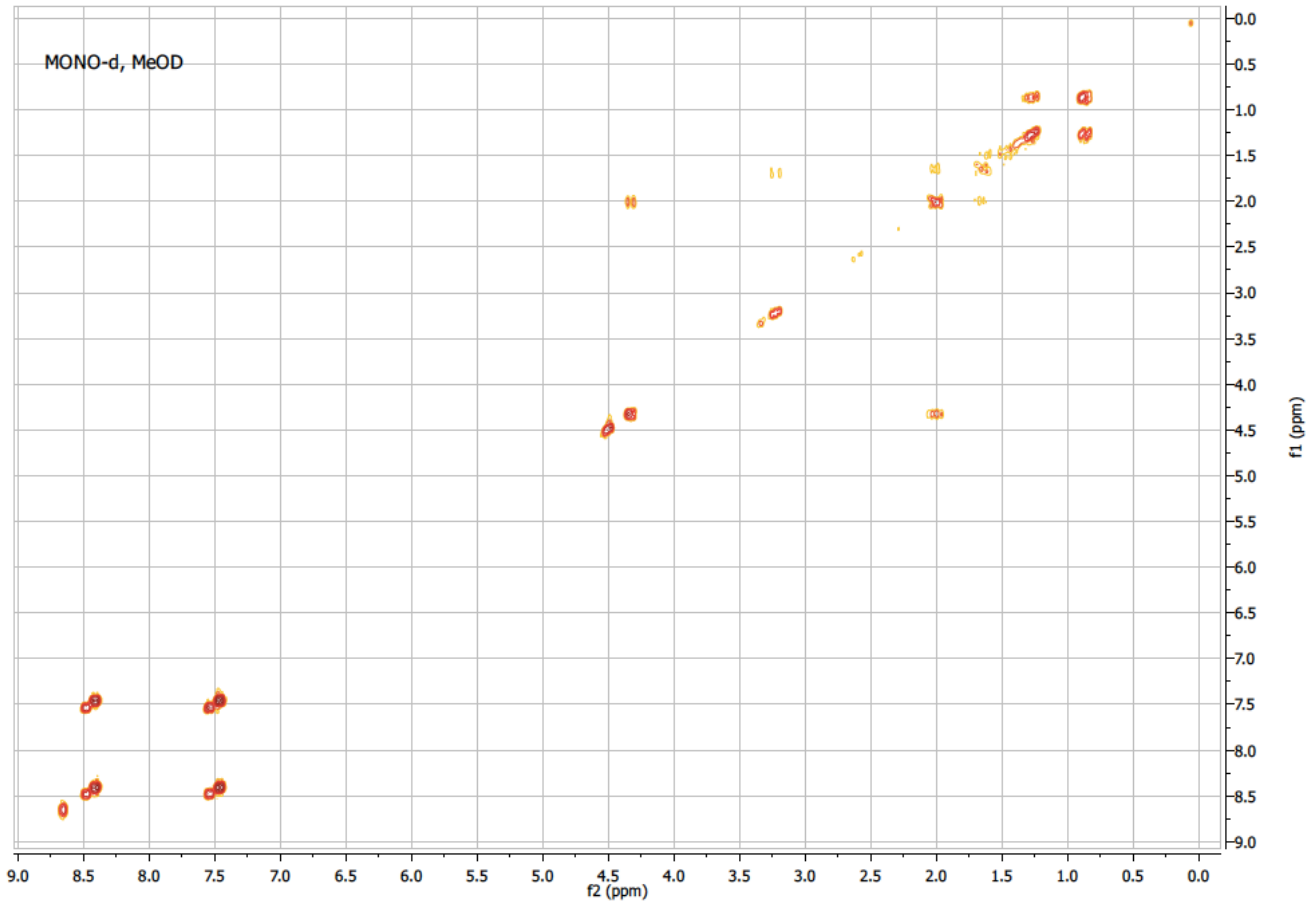

Figure S32. COSY spectrum of compound **7** (300 MHz, MeOD).

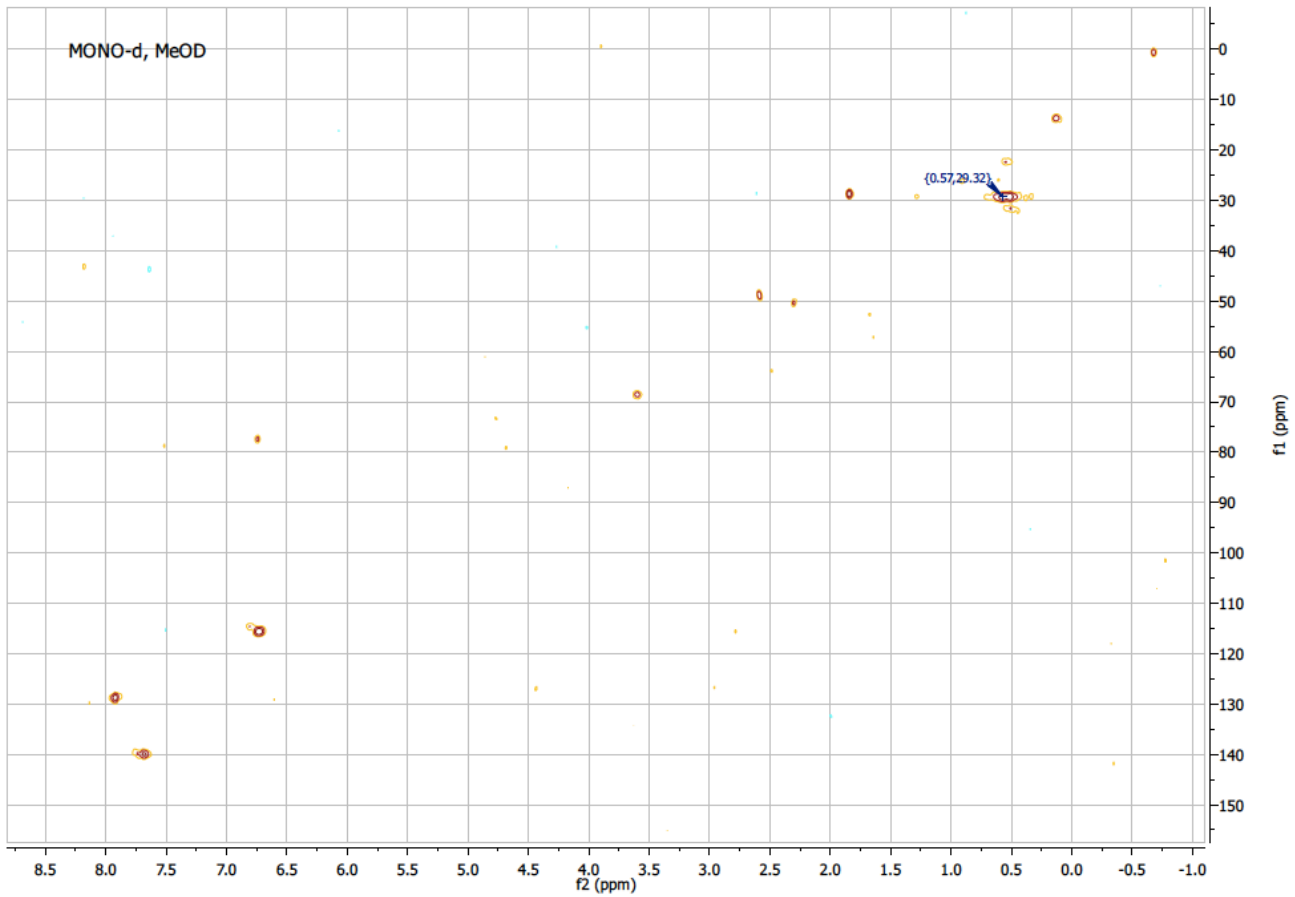

Figure S33. HSQC spectrum of compound **7** (300 MHz, MeOD).

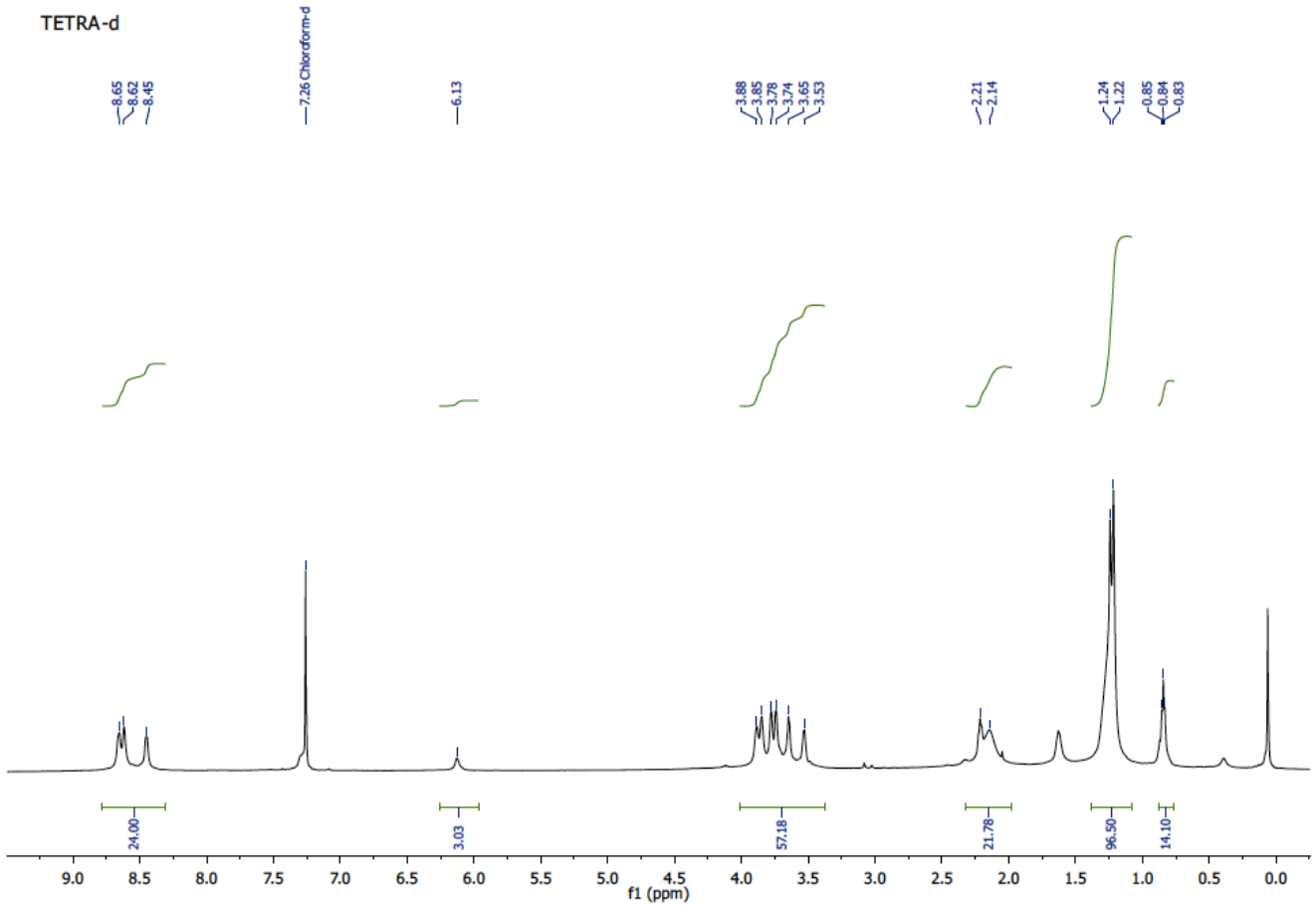

Figure S34. ^{1}H spectrum of compound **8** (600 MHz, $CDCl_3$).

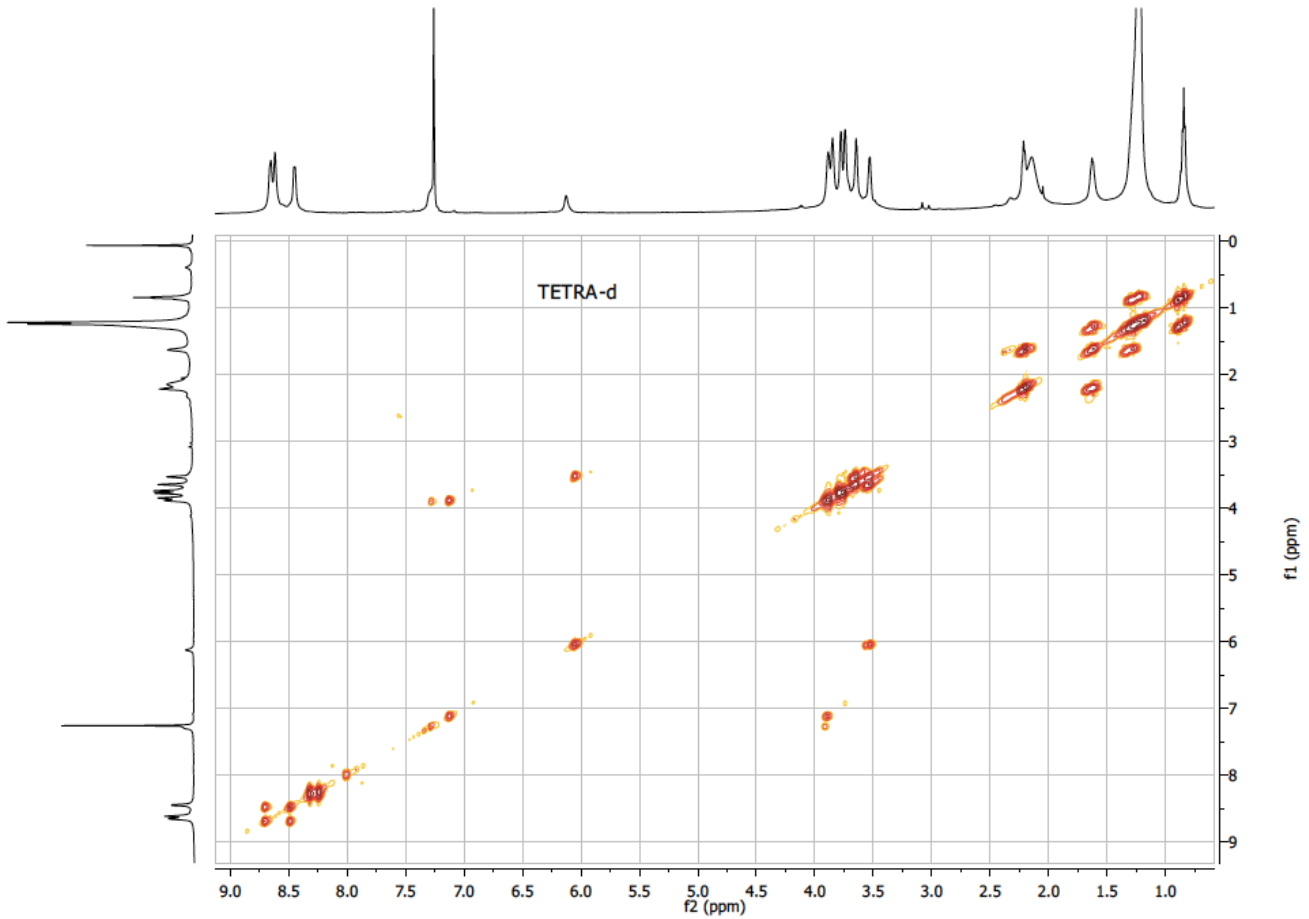

Figure S35. COSY spectrum of compound **8** (600 MHz, $CDCl_3$).

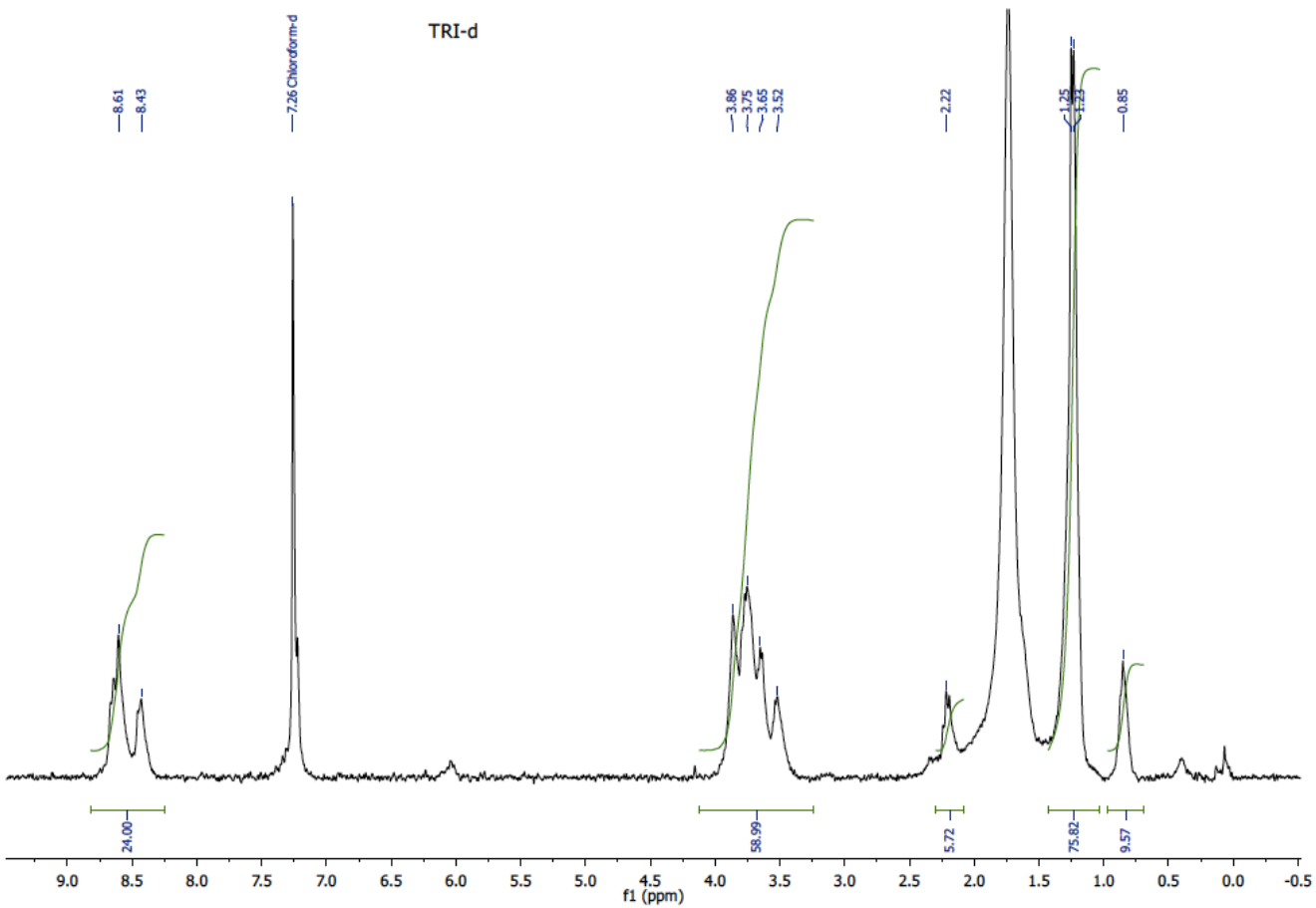

Figure S36. ^{1}H spectrum of compound **9** (300 MHz, $CDCl_3$).

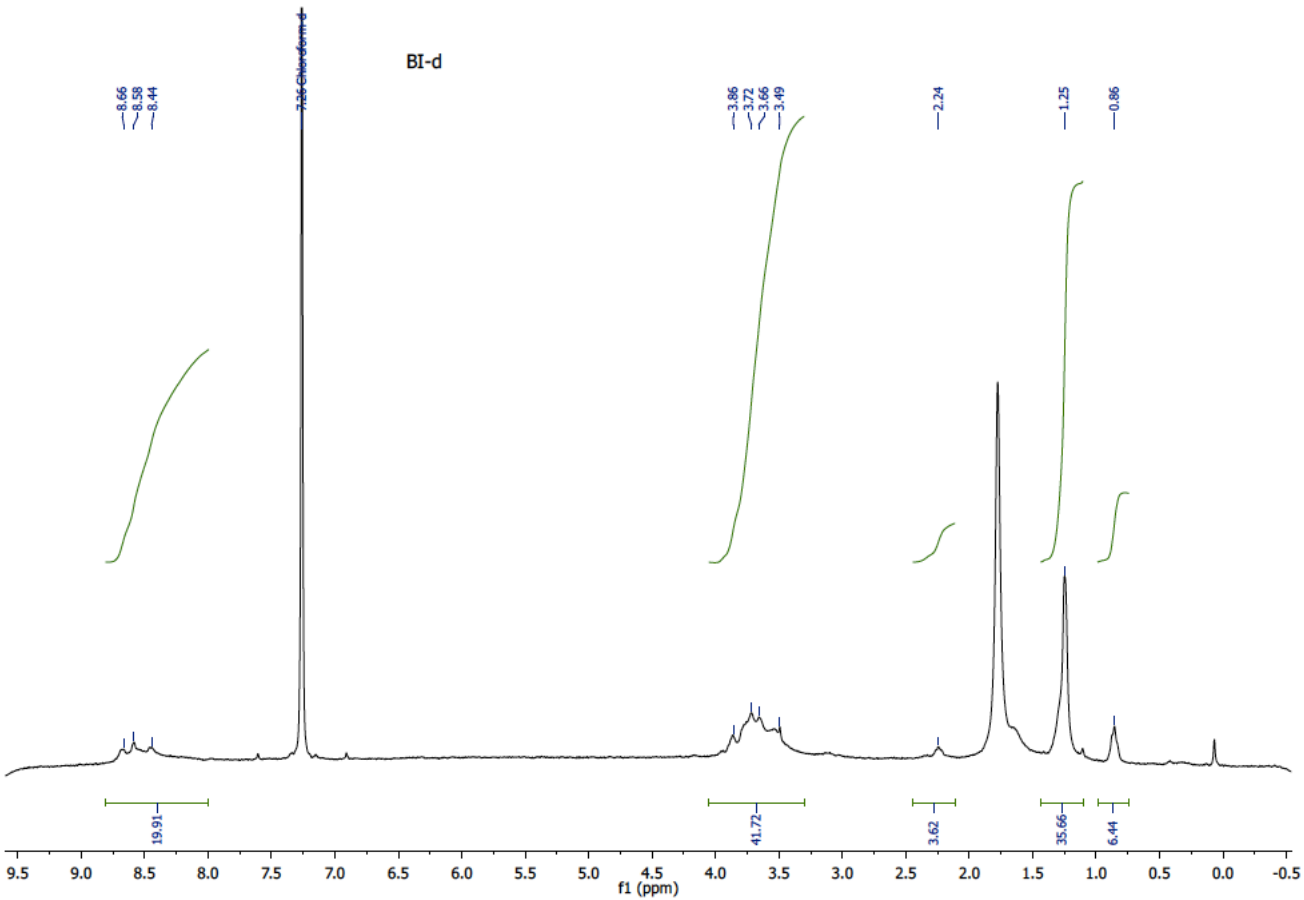

Figure S37. ^{1}H spectrum of compound **10** (300 MHz, $CDCl_3$).

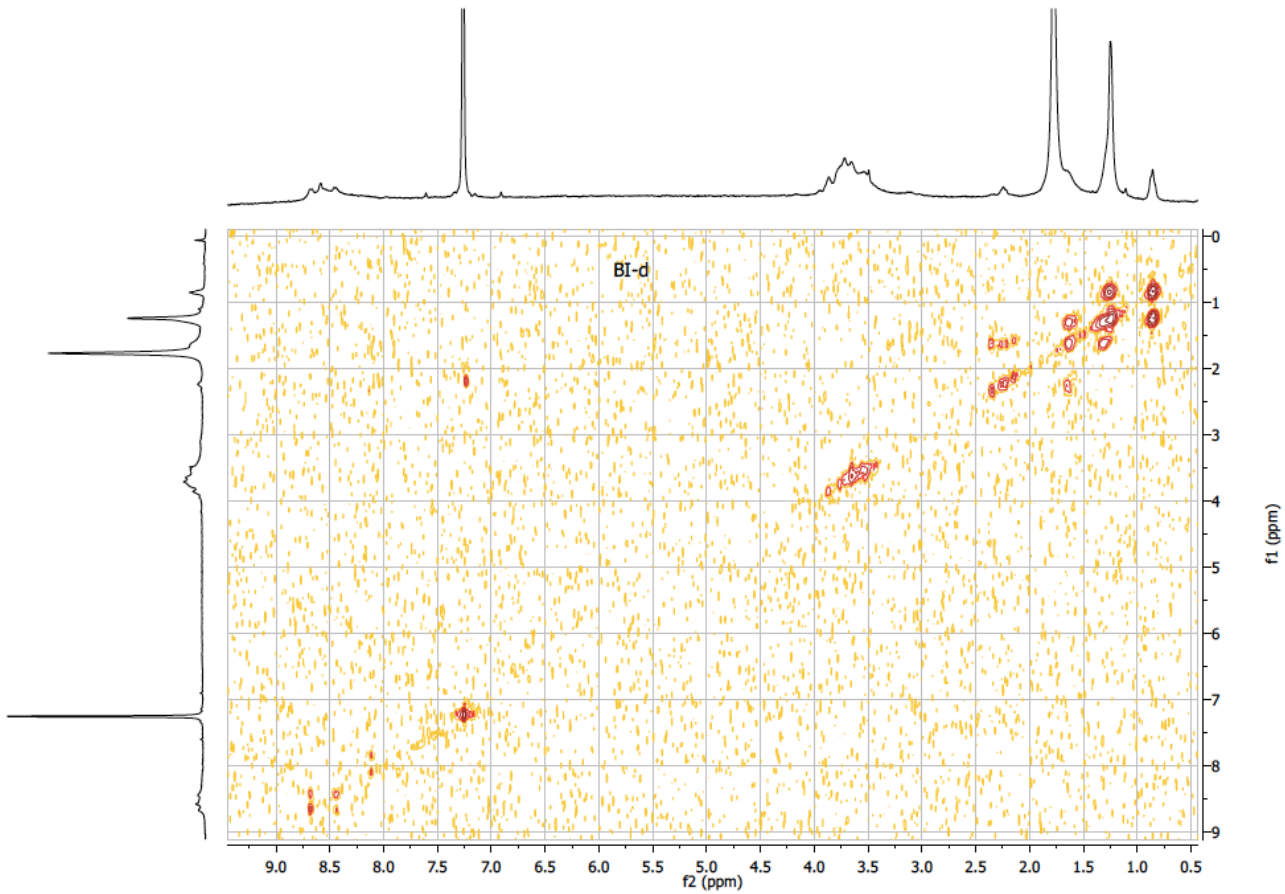

Figure S38. COSY spectrum of compound **10** (300 MHz, $CDCl_3$).

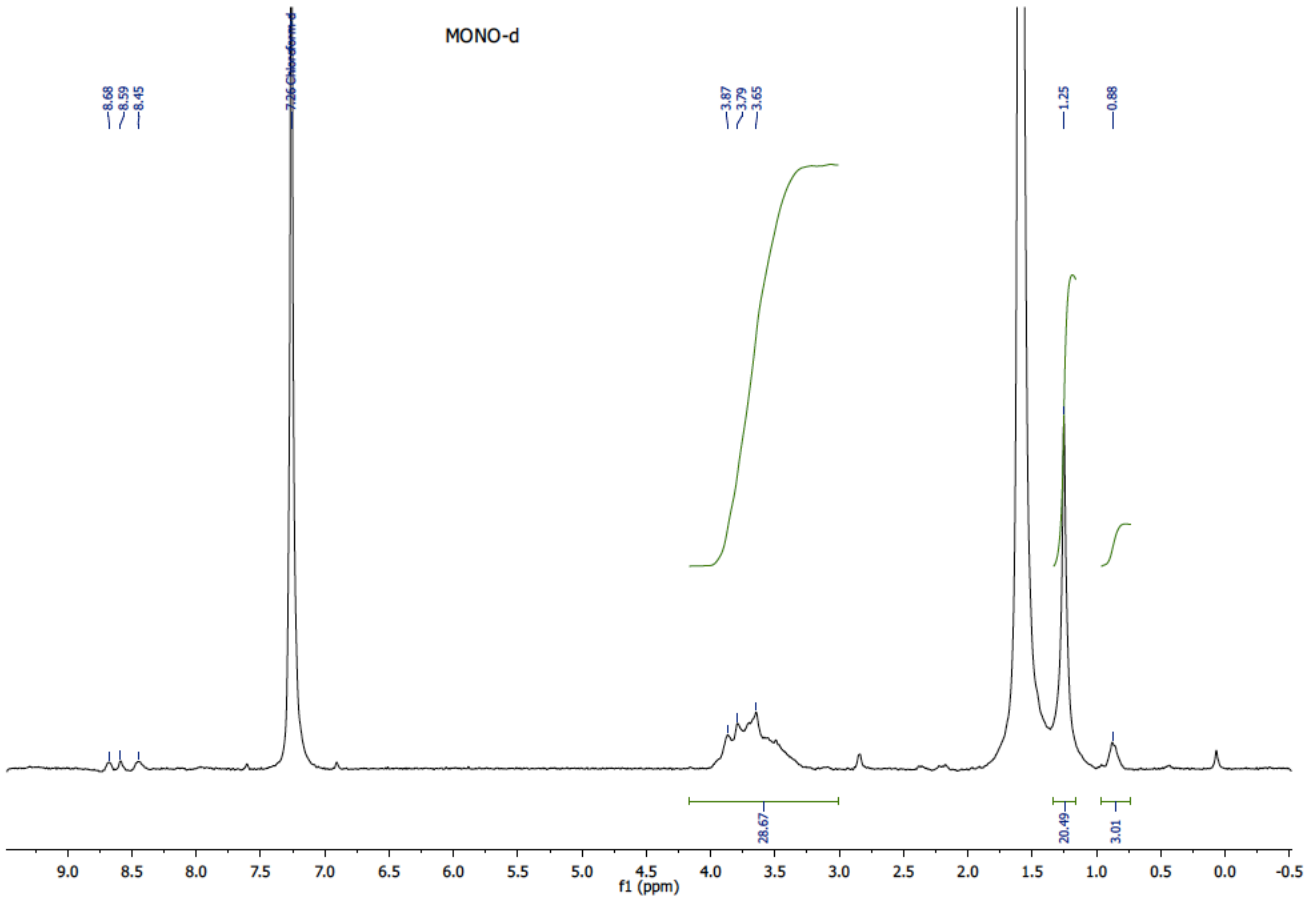

Figure S39. ^{1}H spectrum of compound **11** (300 MHz, $CDCl_3$)

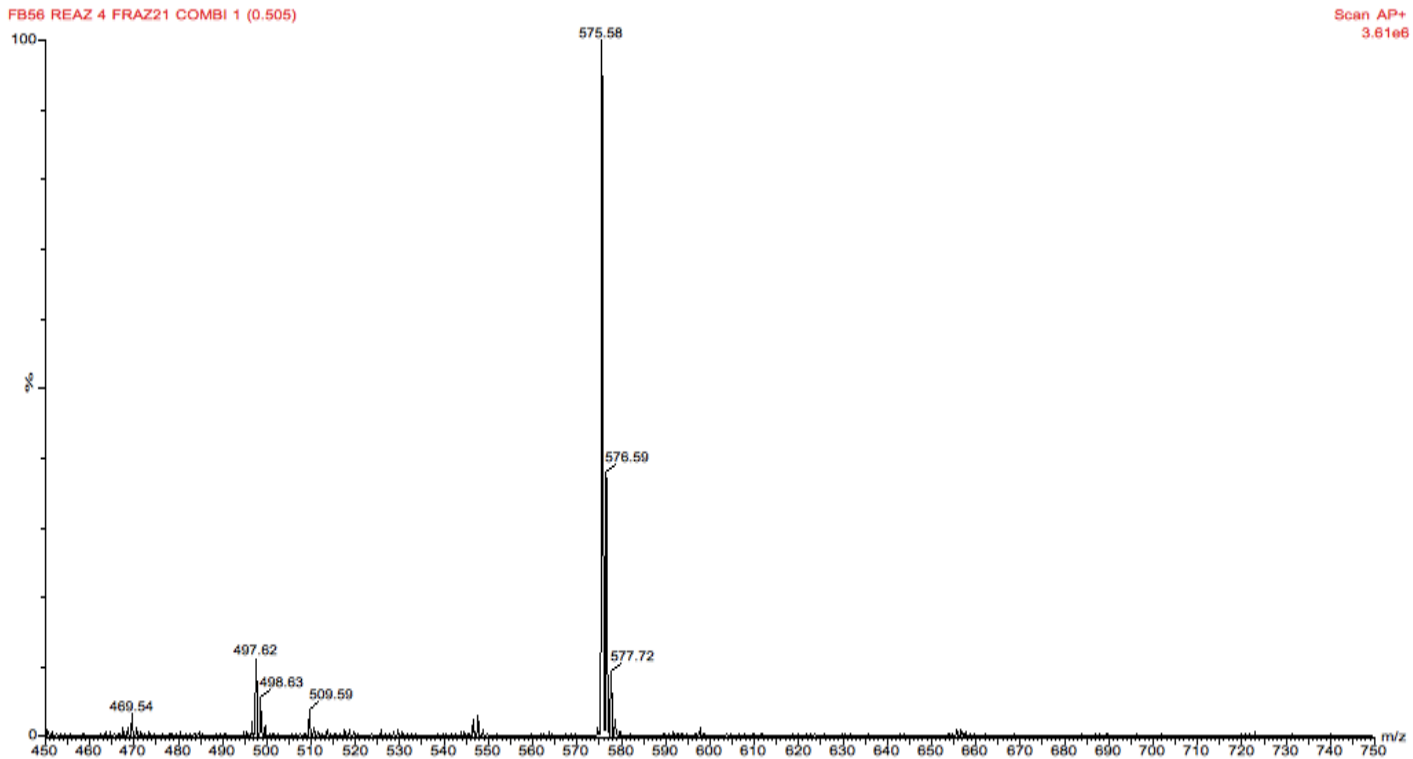

Figure S40. MS spectrum of compound **1**.

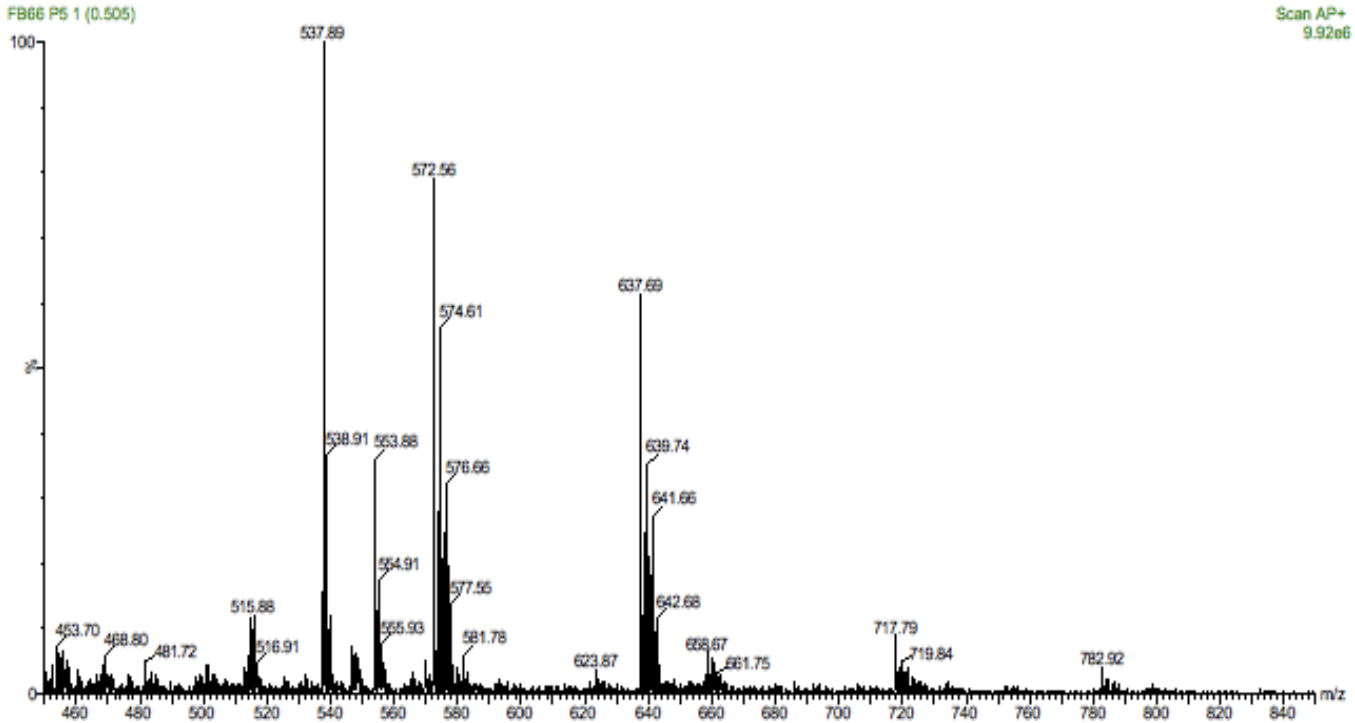

Figure S41. MS spectrum of compound **1-Zn**.

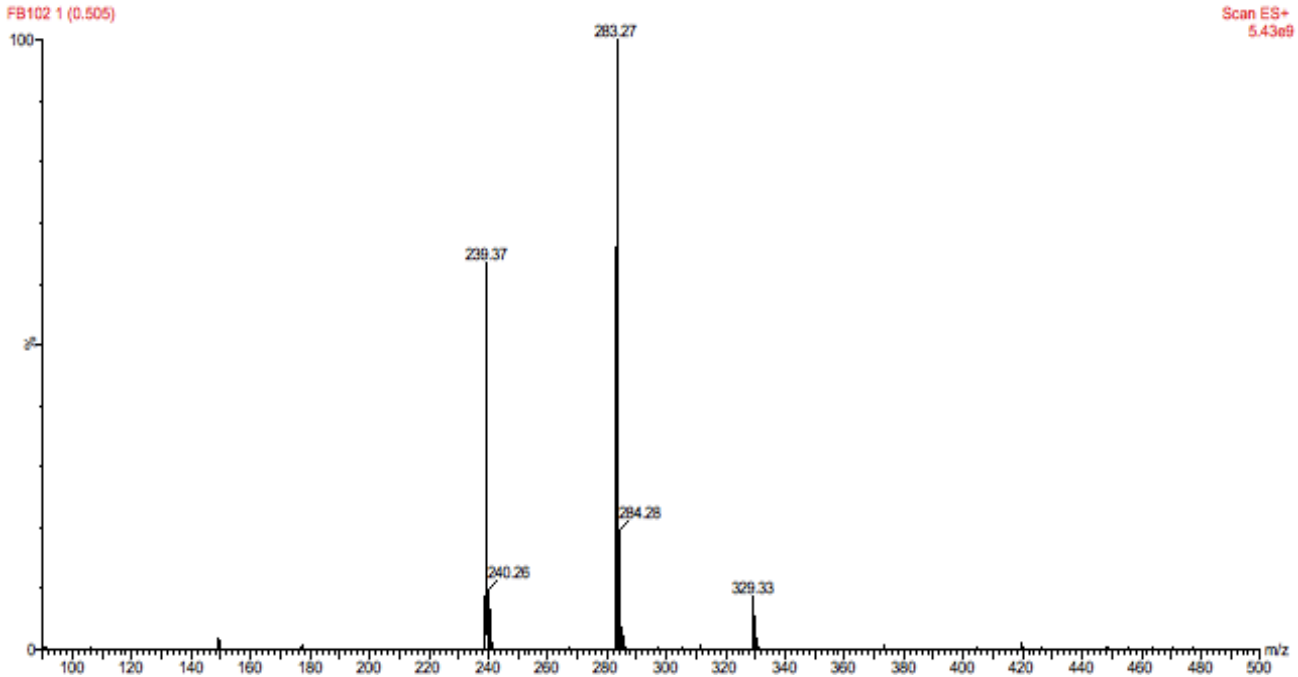

Figure S42. MS spectrum of compound **a**.

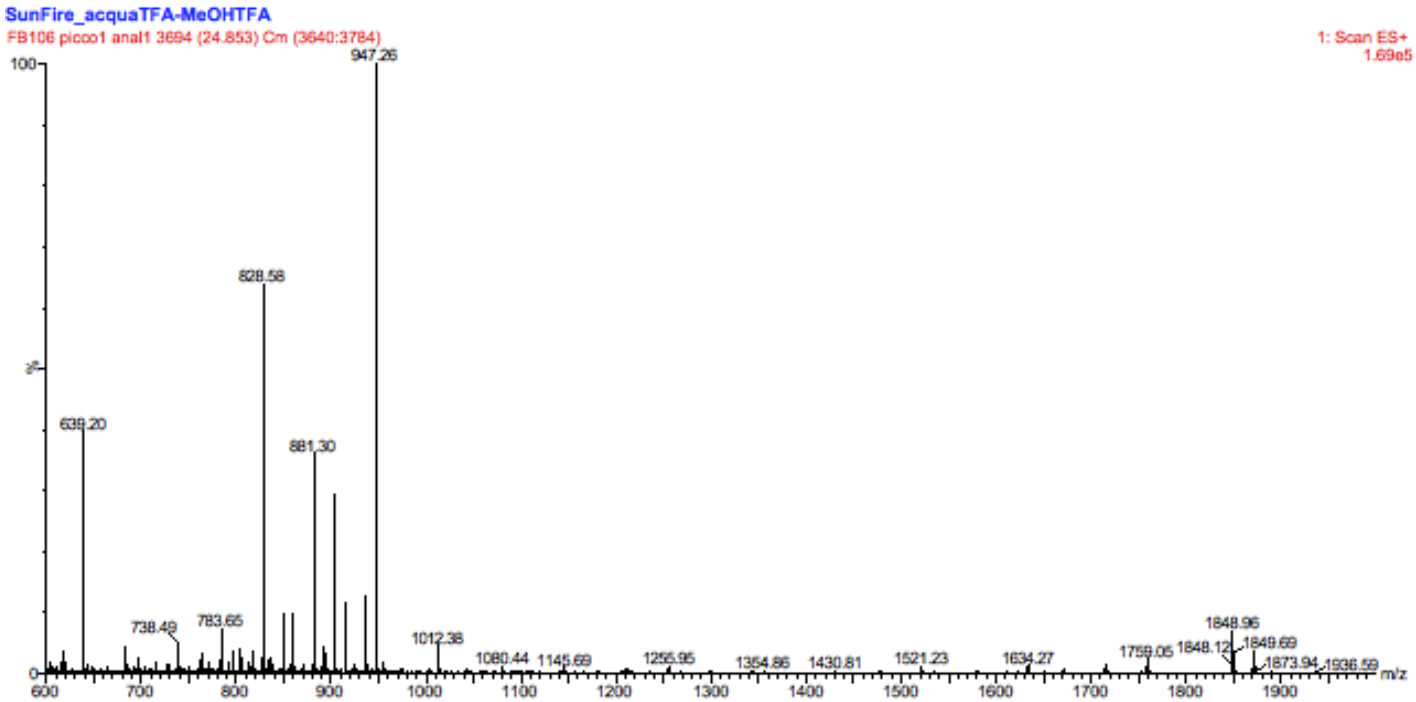

Figure S43. MS spectrum of compound **b** (from analytic analysis).

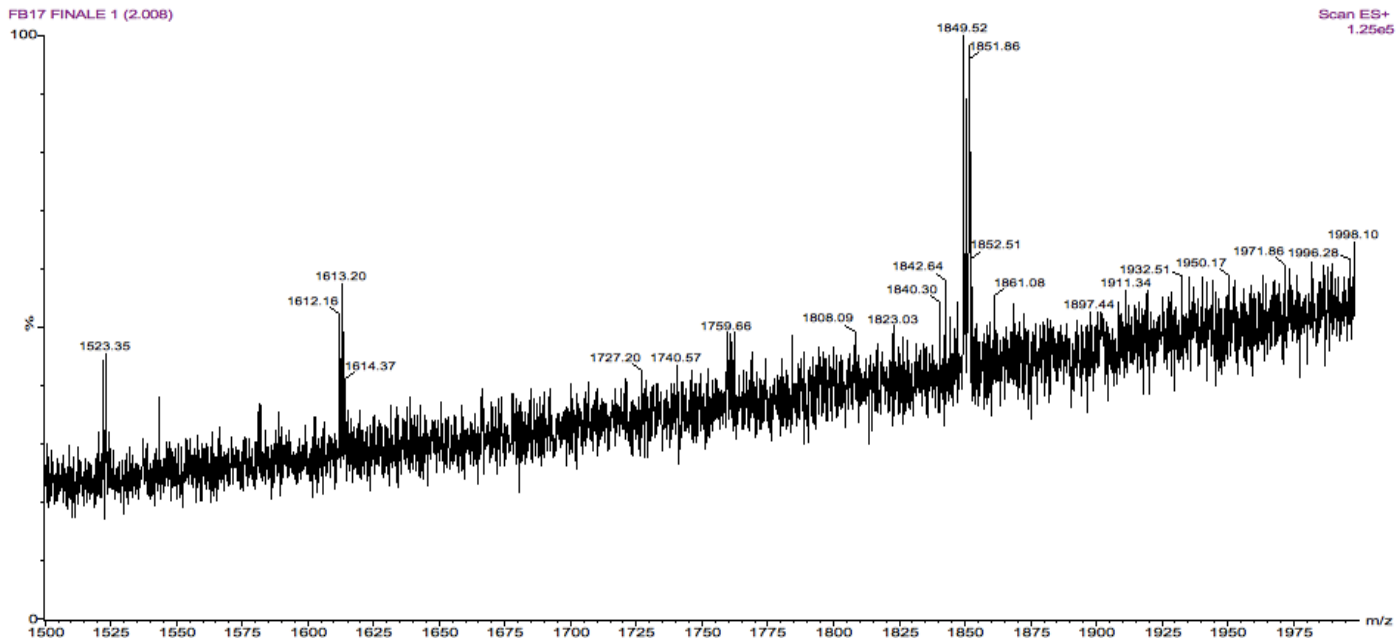

Figure S44. MS spectrum of compound **b**.

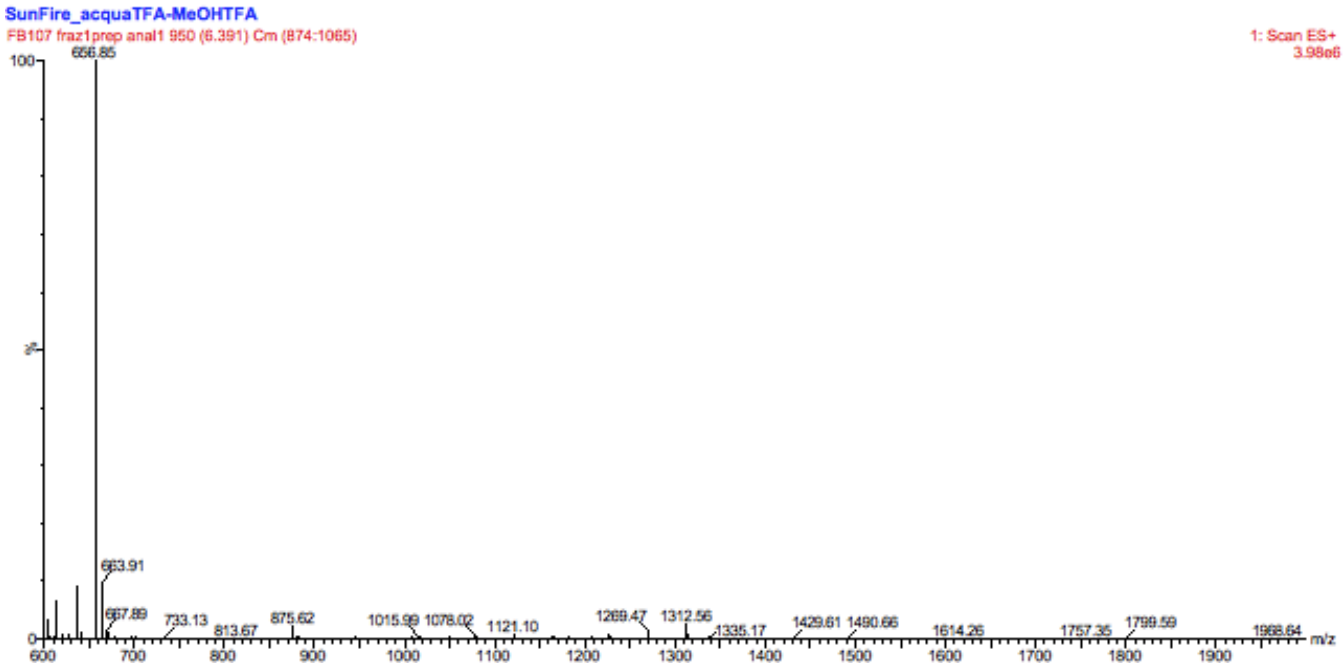

Figure S45. MS spectrum of compound **c** (from analytic analysis).

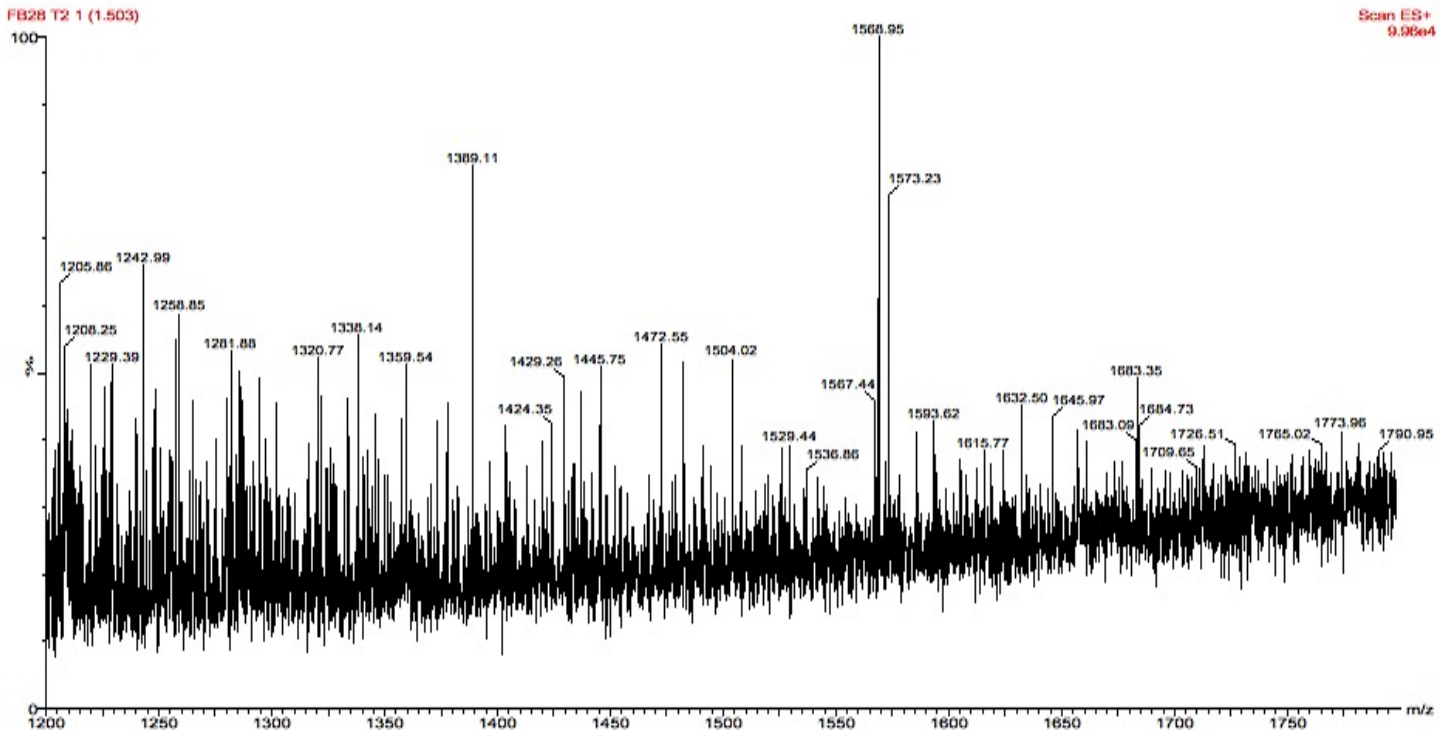

Figure S46. MS spectrum of compound **2**.

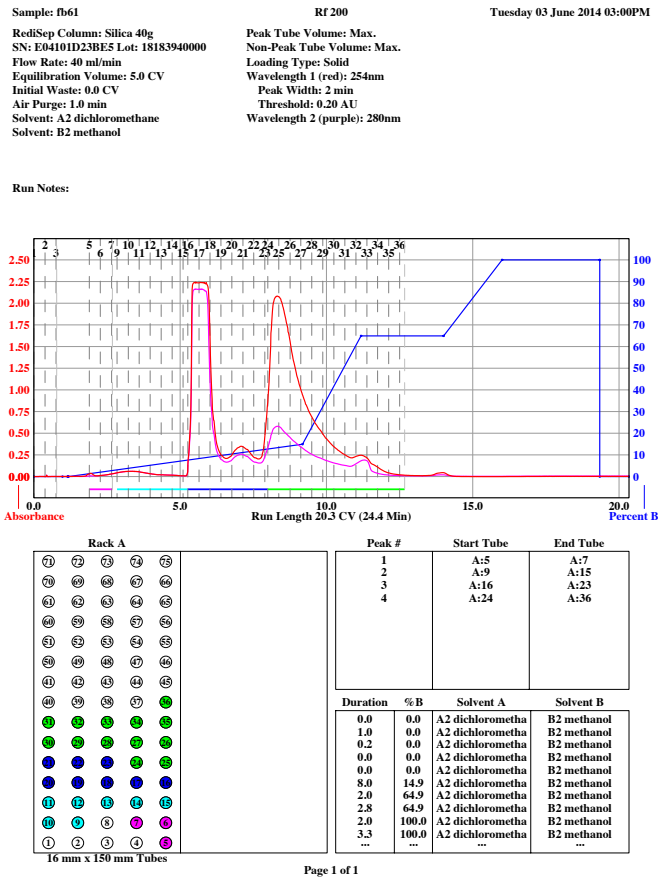

Figure S47. Combi*flash* separation of compound **b**.

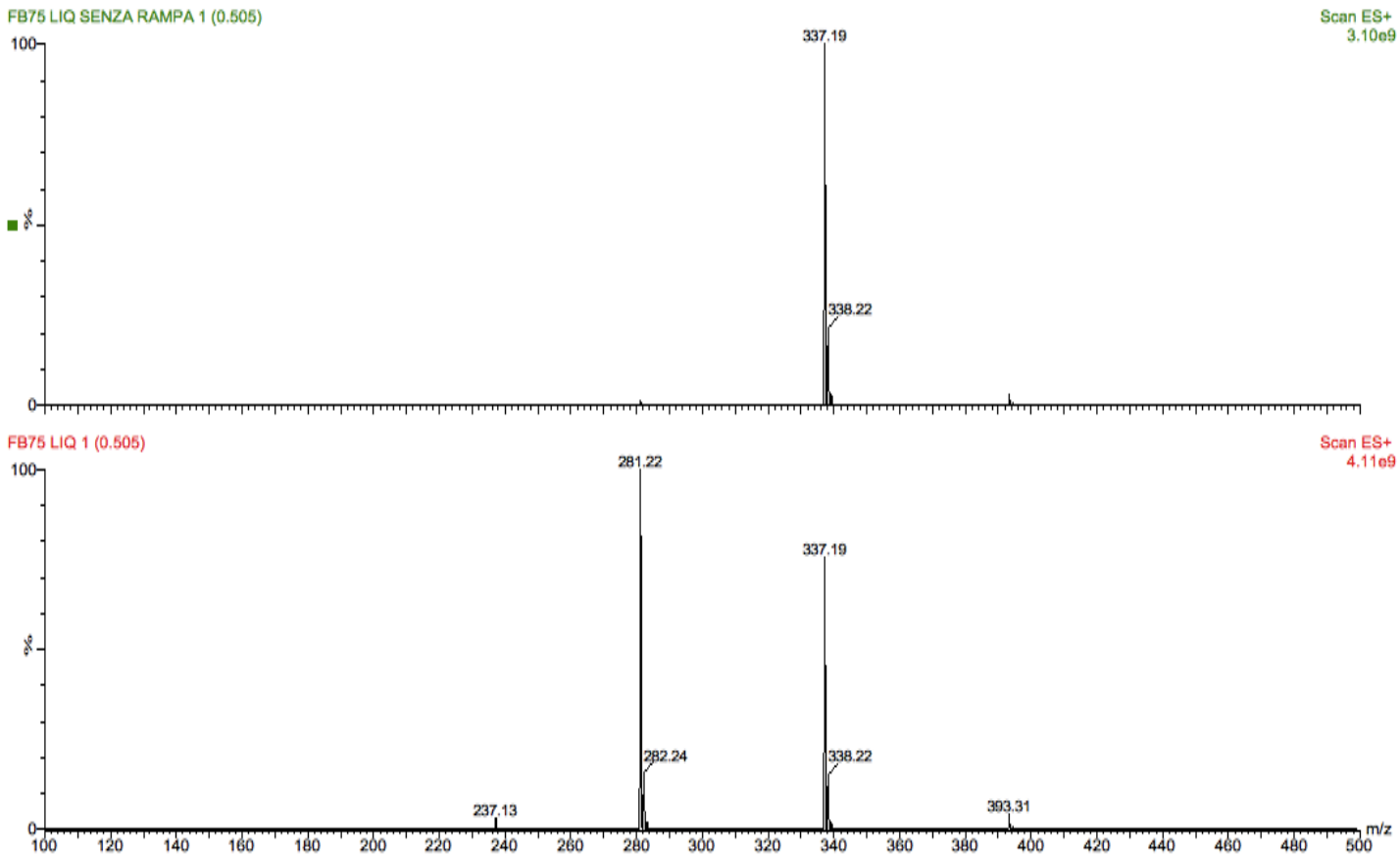

Figure S48. MS spectrum of compound **d**.

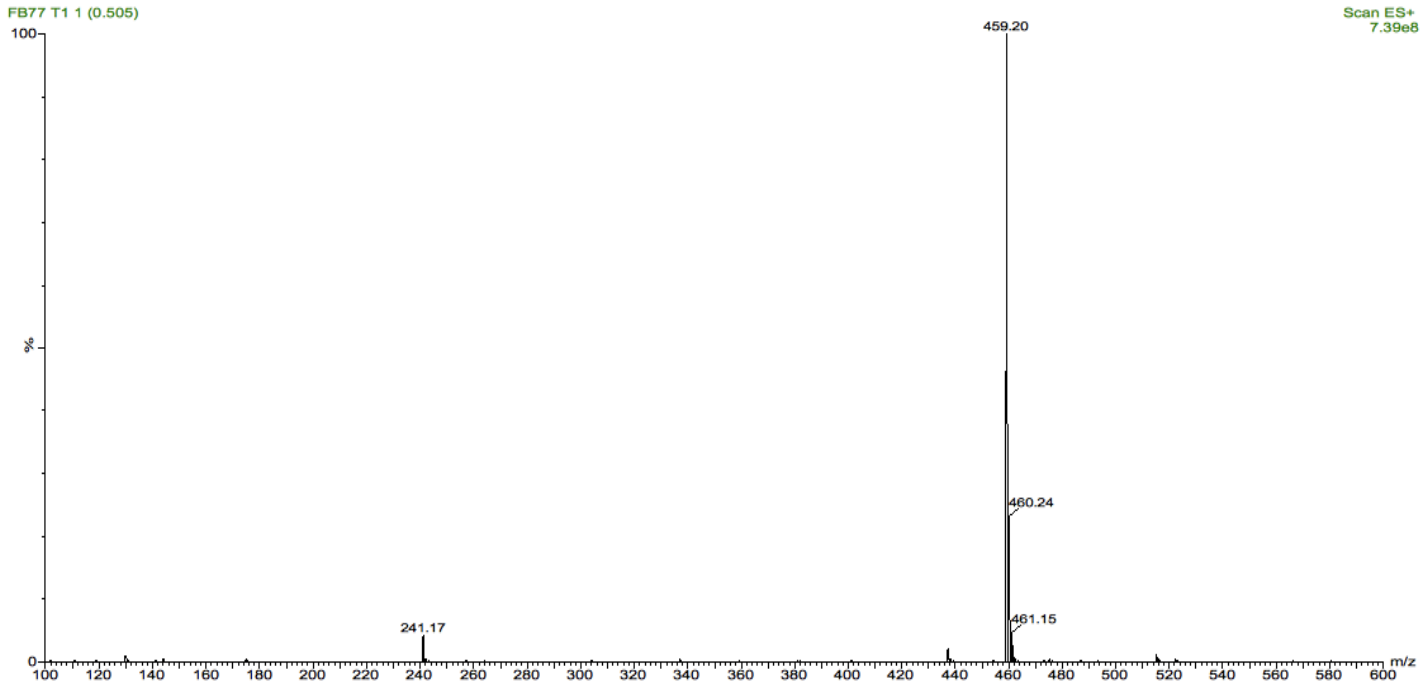

Figure S49. MS spectrum of compound **e**.

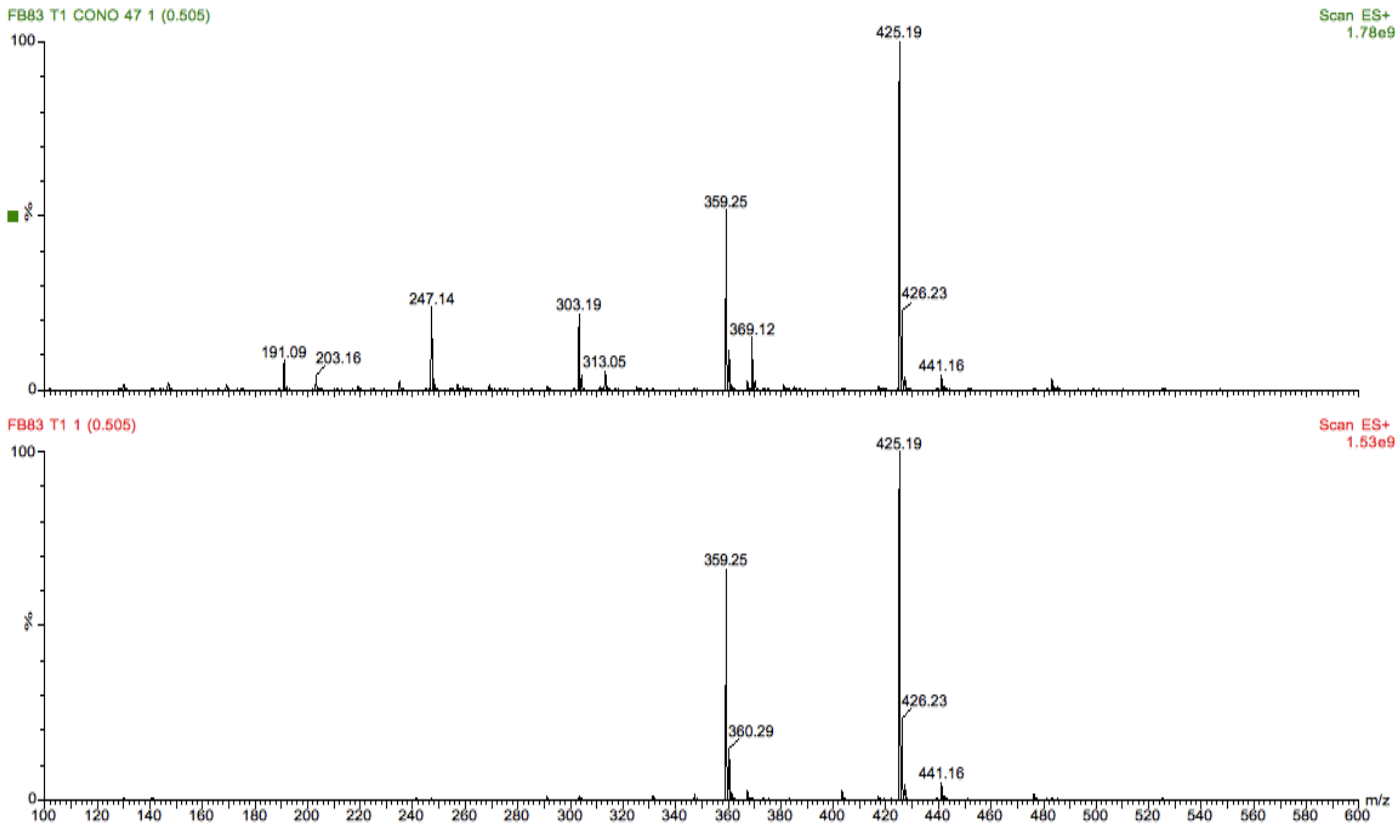

Figure S50. MS spectrum of compound **f**.

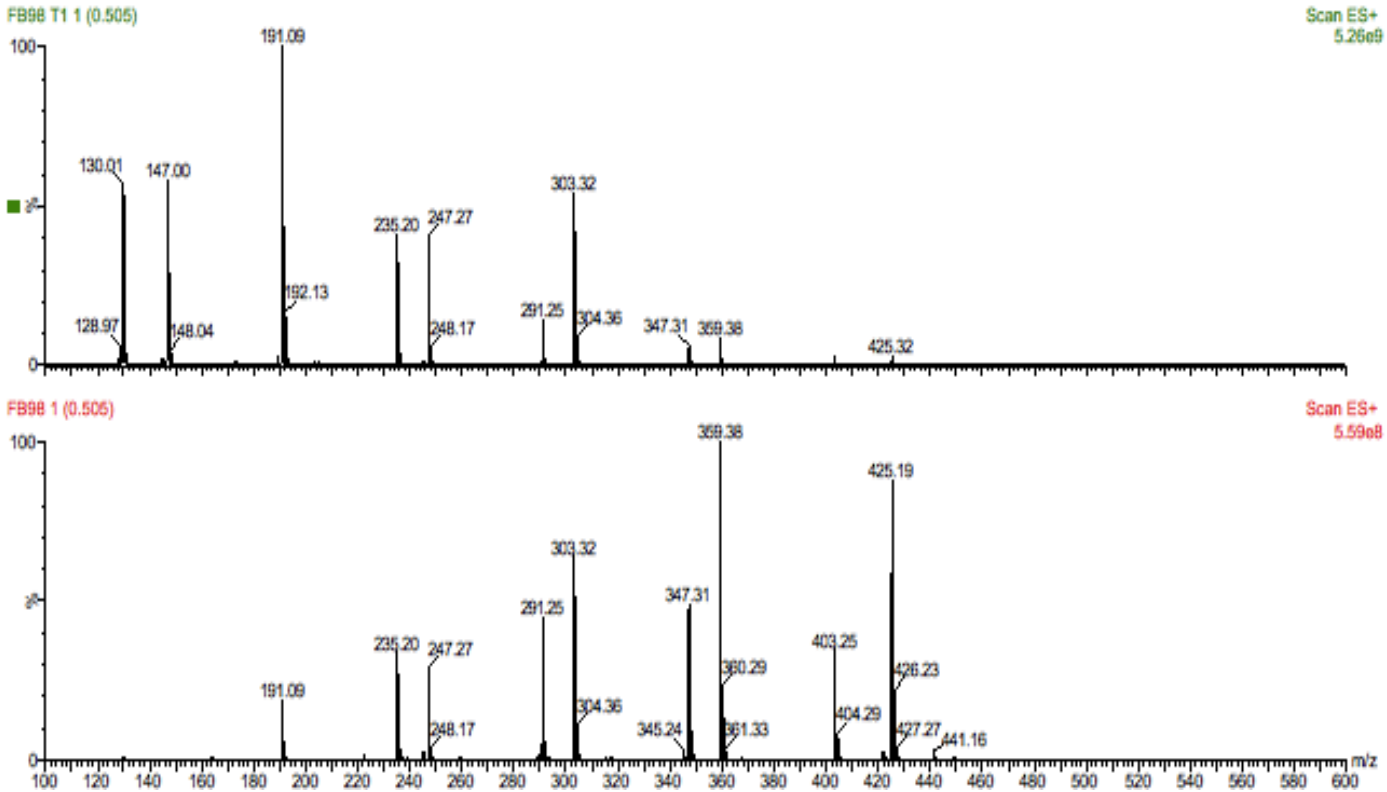

Figure S51. MS spectrum of compound **f** before (bottom) and after acidification (top).

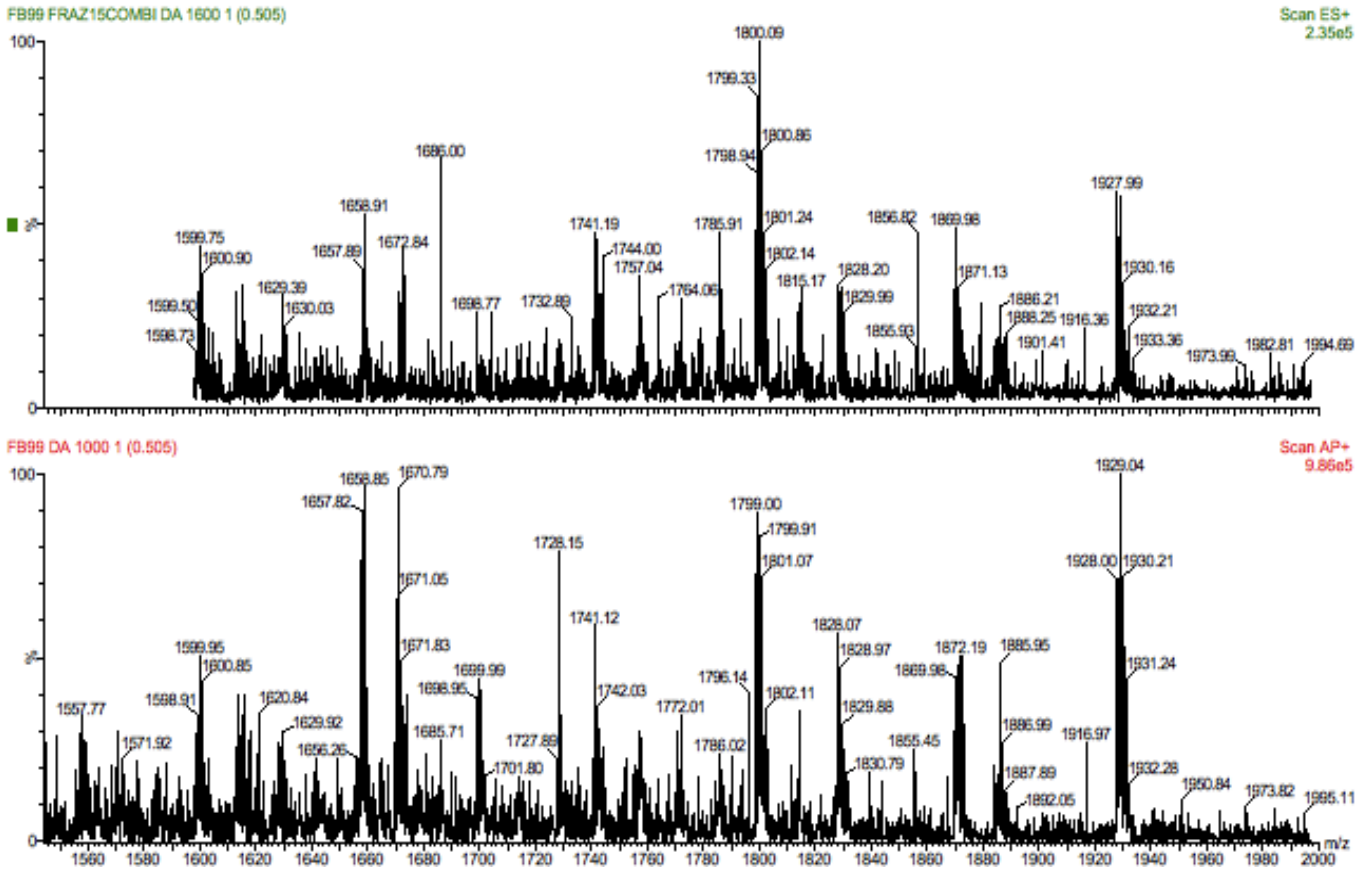

Figure S52. MS spectrum of compound **g**.

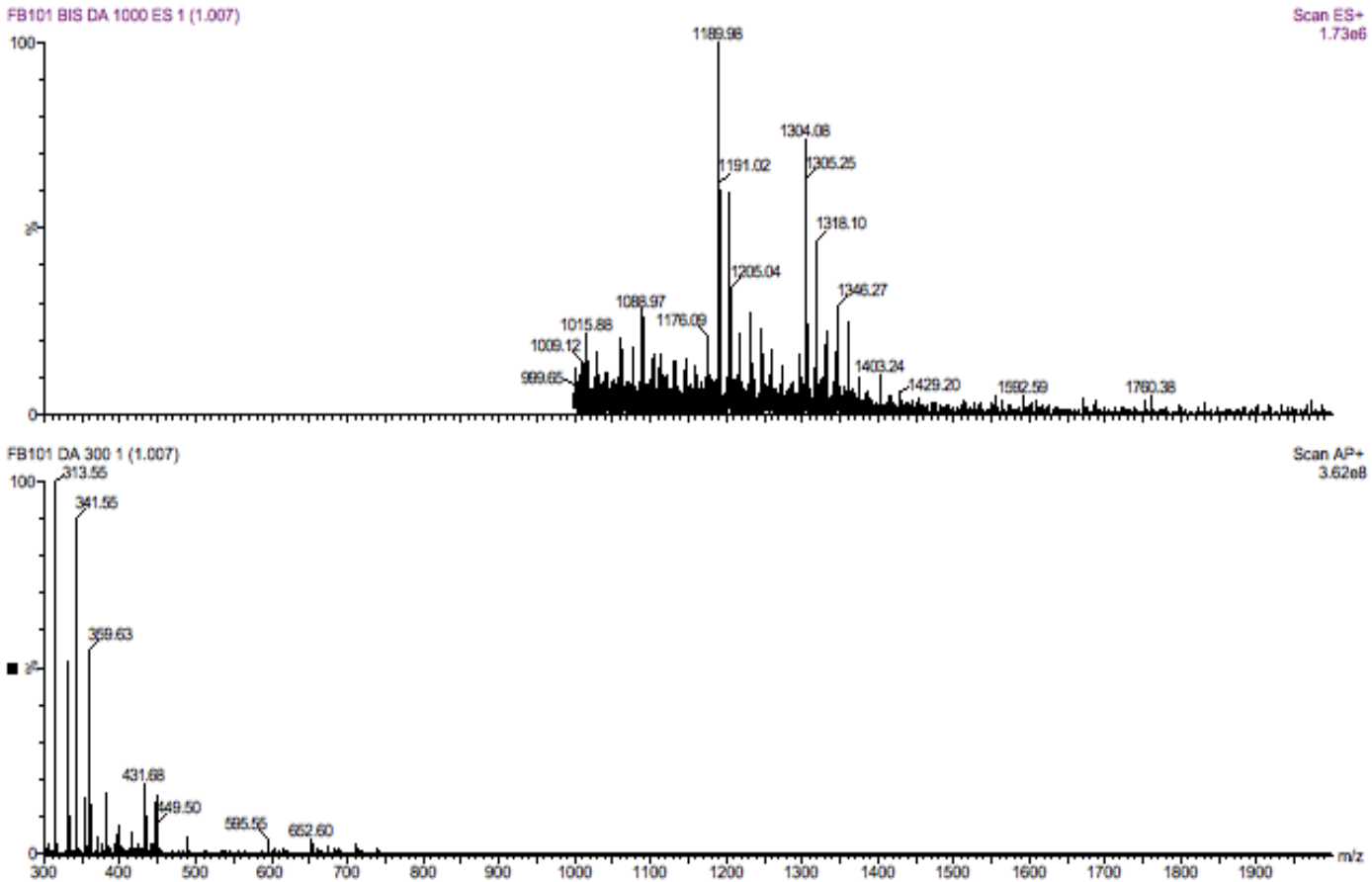

Figure S53. MS spectrum of compound **3**.

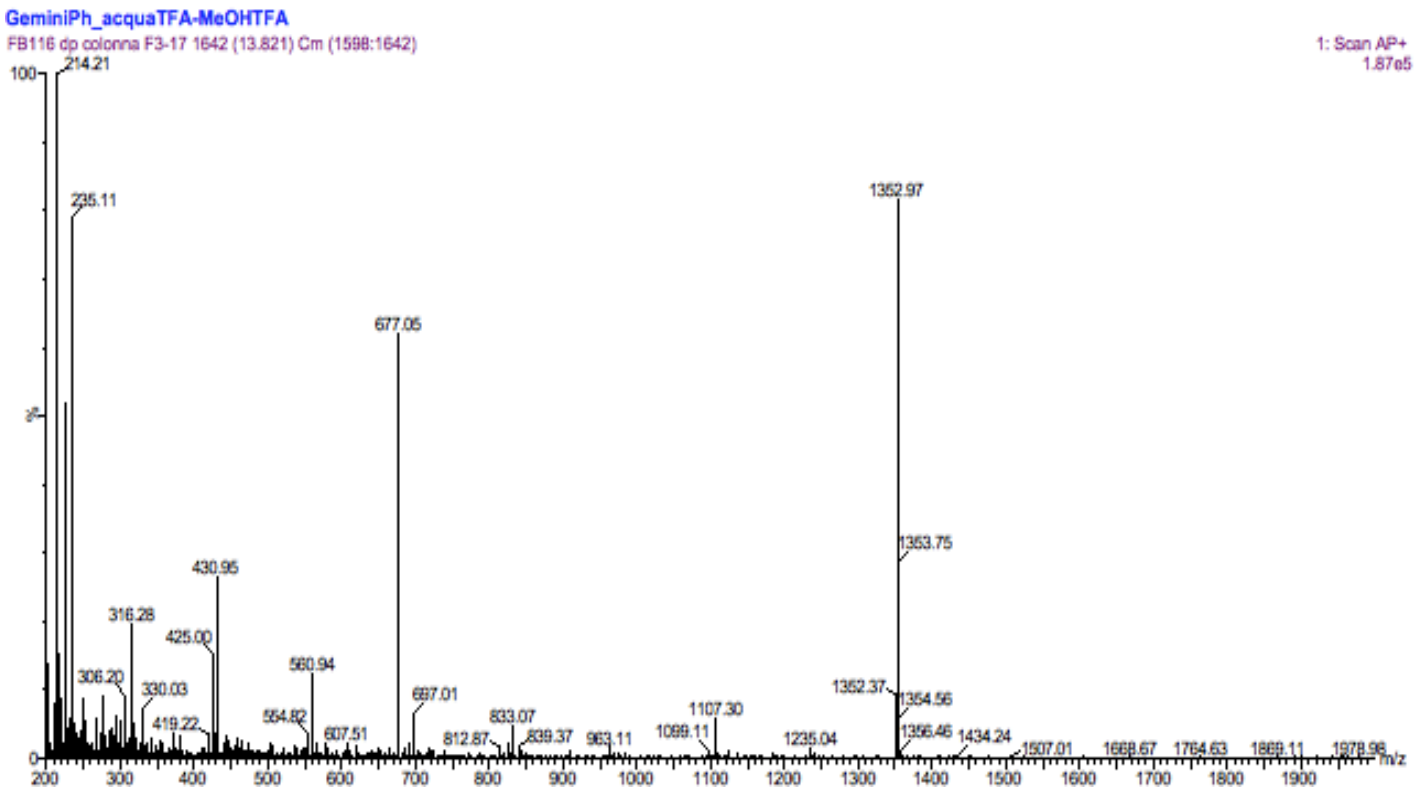

Figure S54. MS spectrum of compound **4 (Tetra-d)** (from analytic analysis).

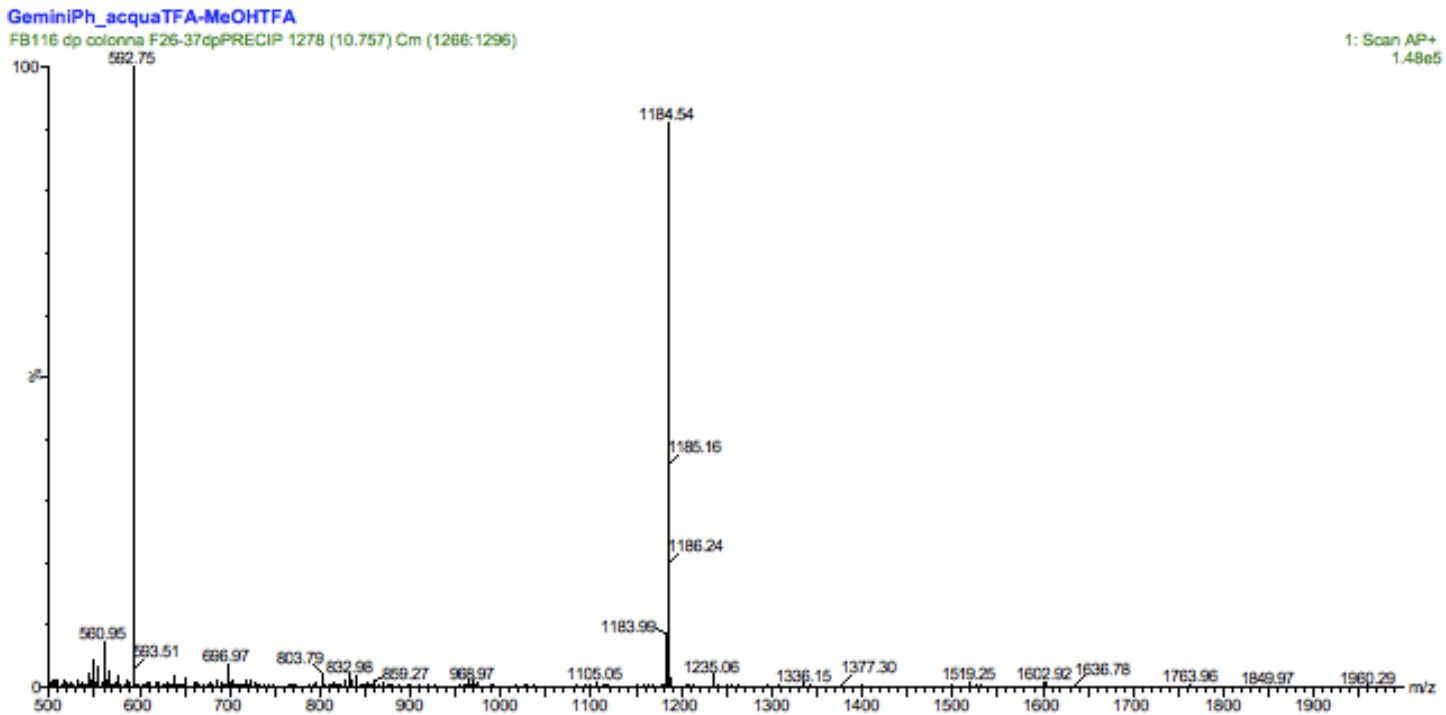

Figure S55. MS spectrum of compound **5 (Tri-d)** (from analytic analysis).

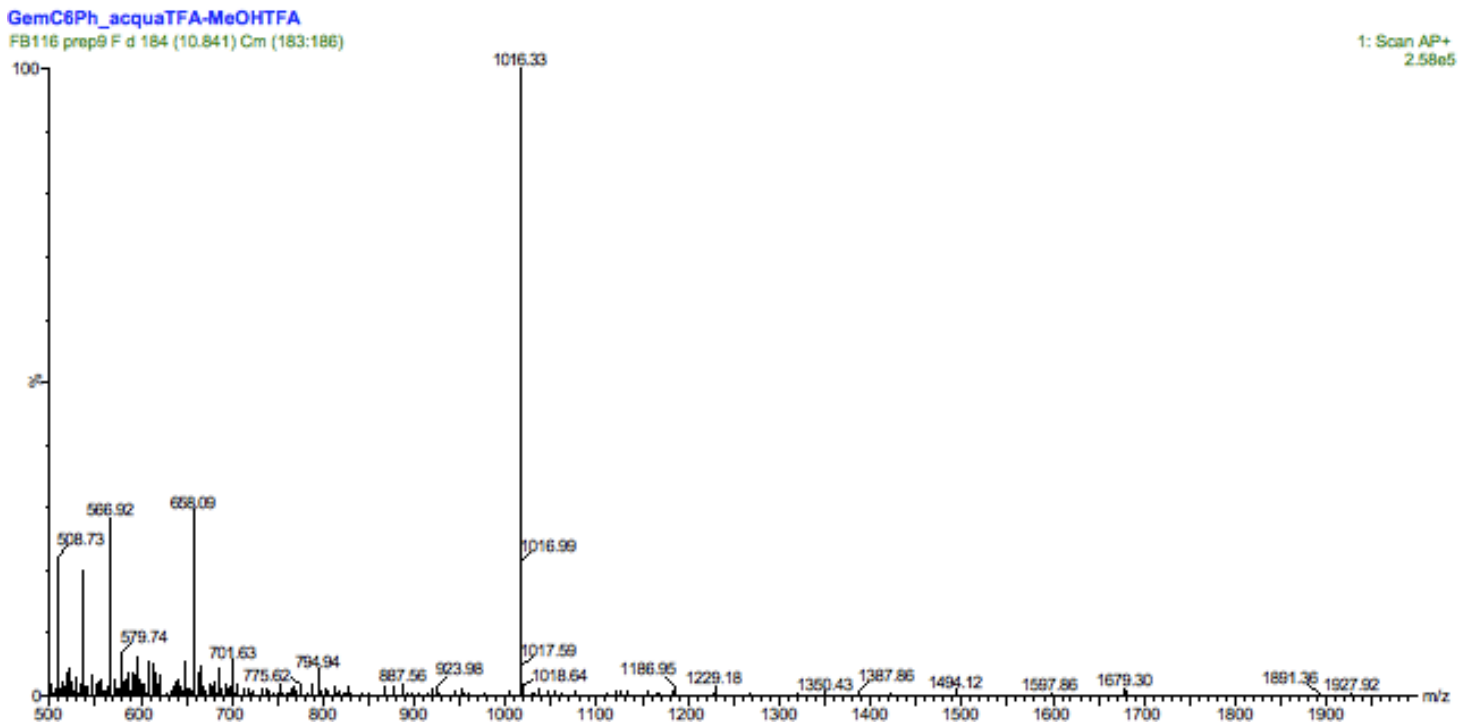

Figure S56. MS spectrum of compound **6/6-bis** (from prep analysis).

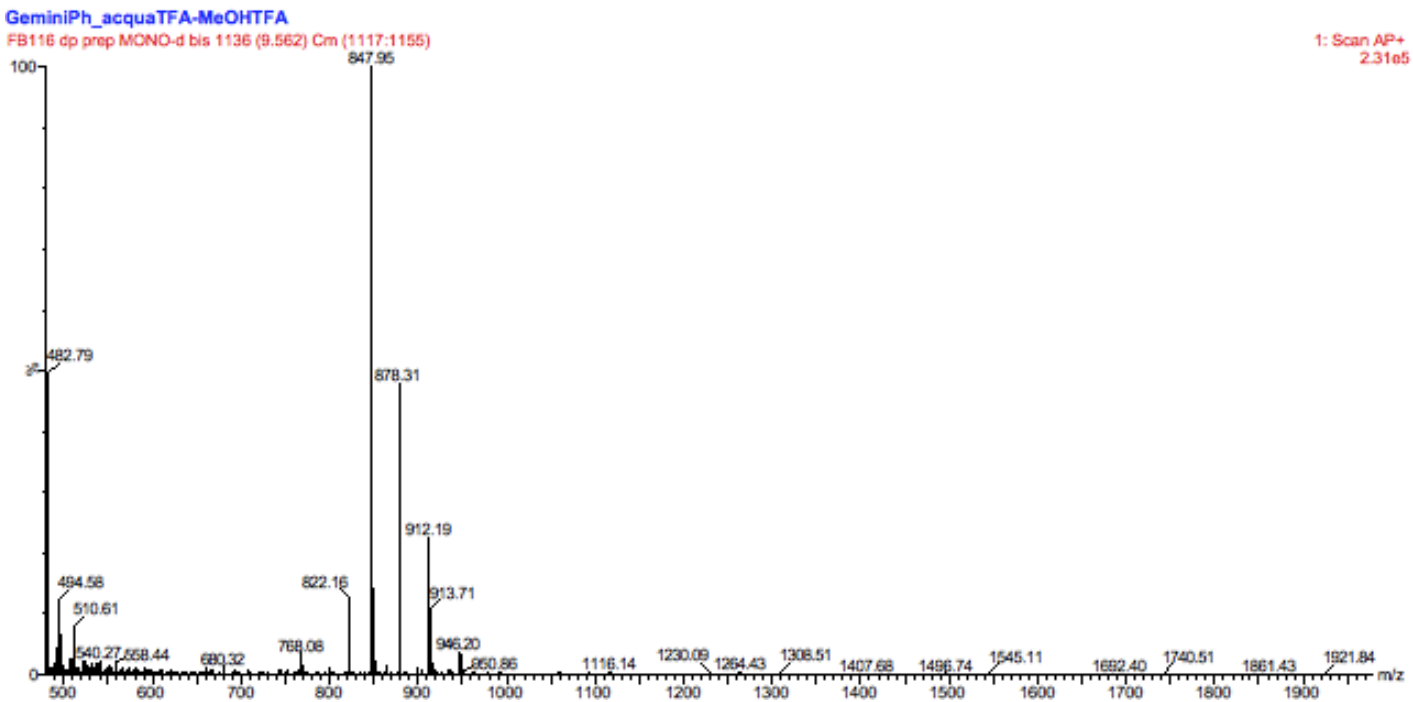

Figure S57. MS spectrum of compound **7** (from analytic analysis).

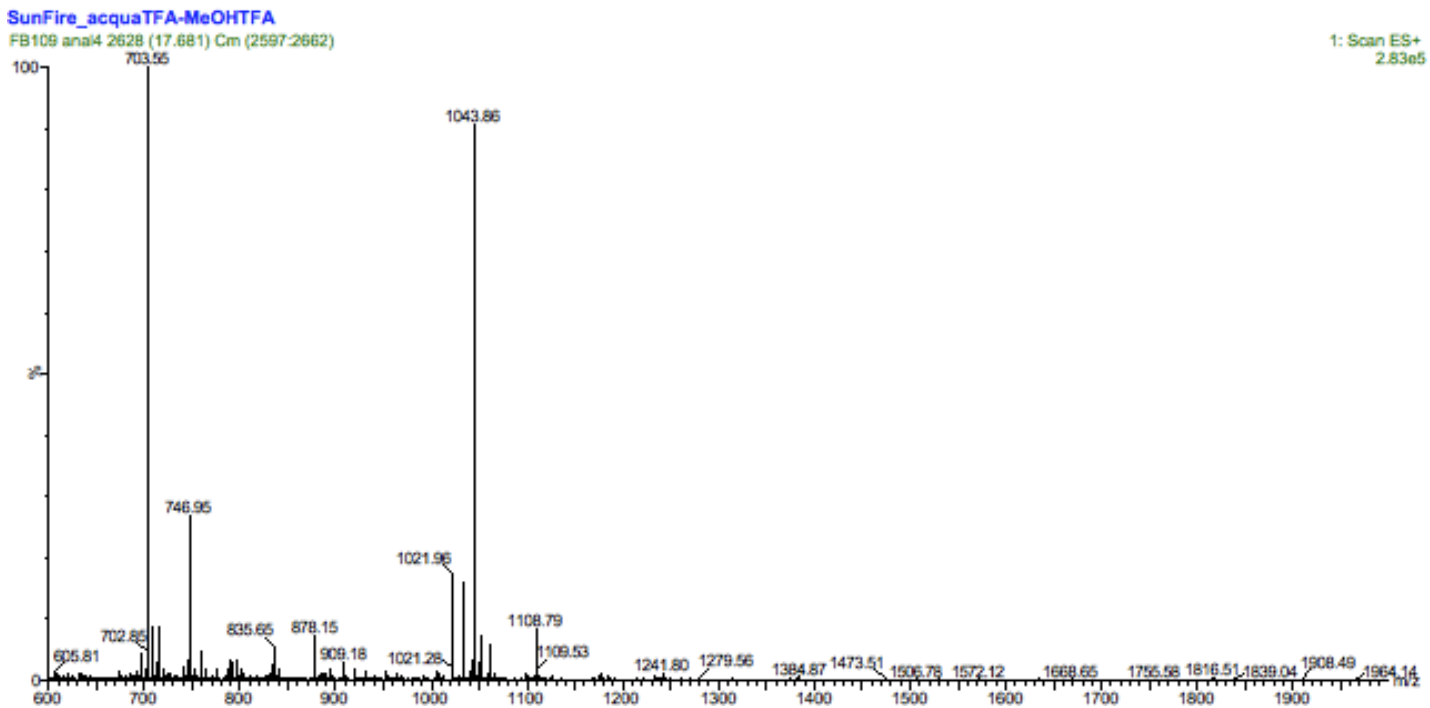

Figure S58. MS spectrum of compound **8.**

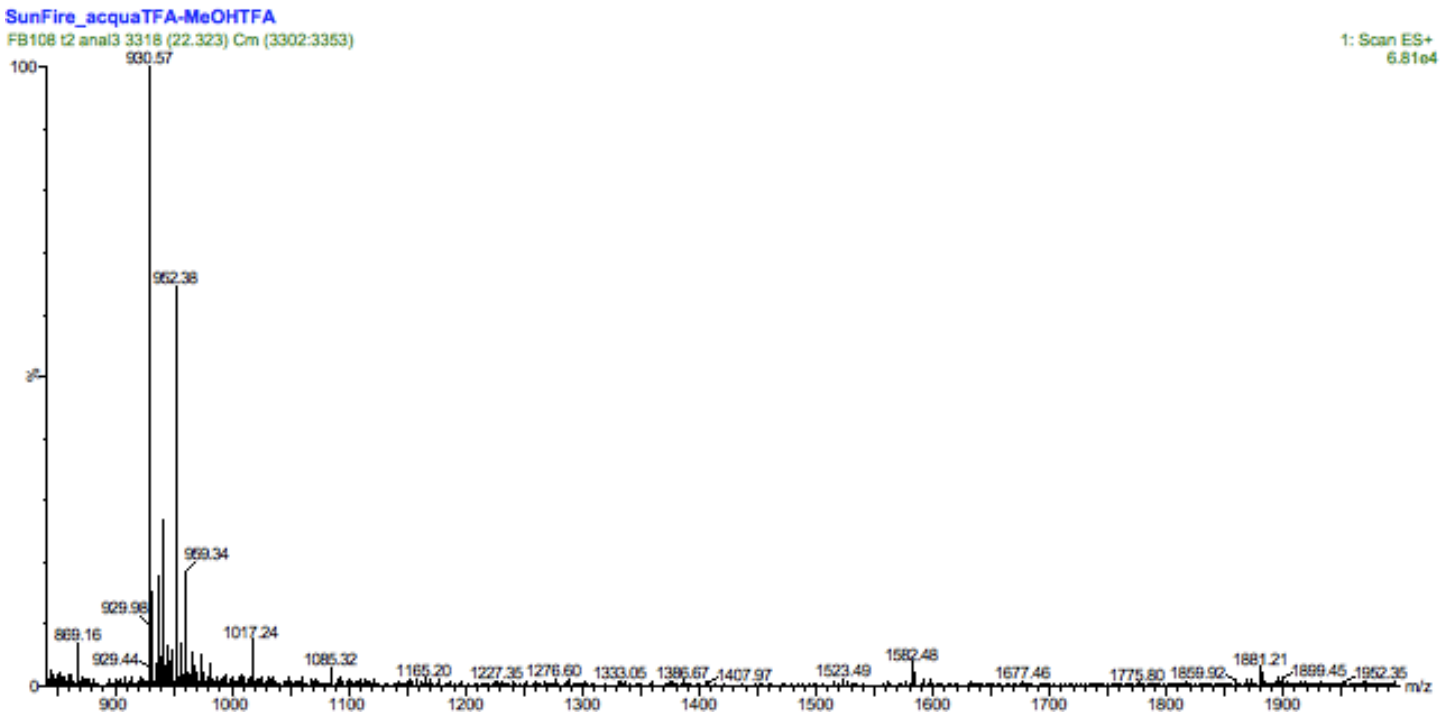

Figure S59. MS spectrum of compound **9** (from analytic analysis).

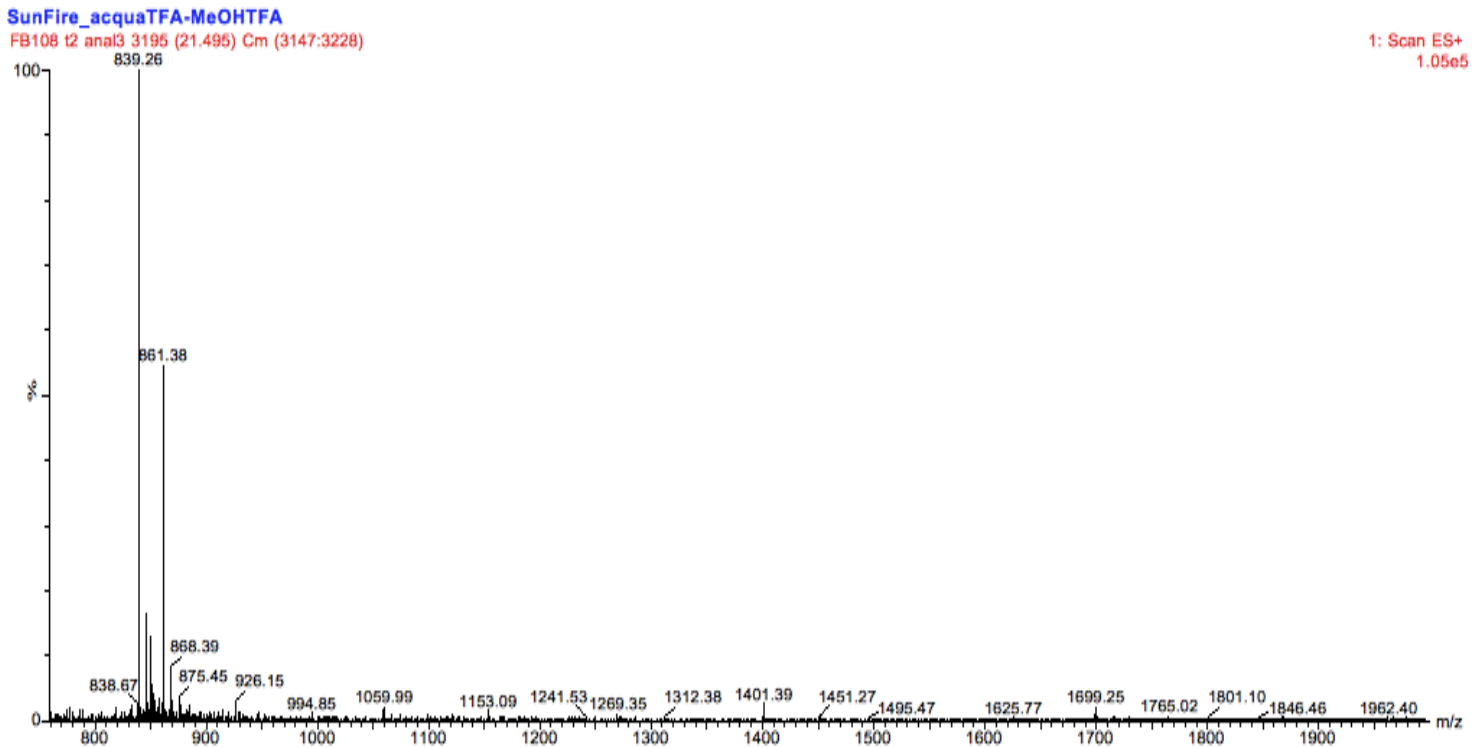

Figure S60. MS spectrum of compound **10** (from analytic analysis).

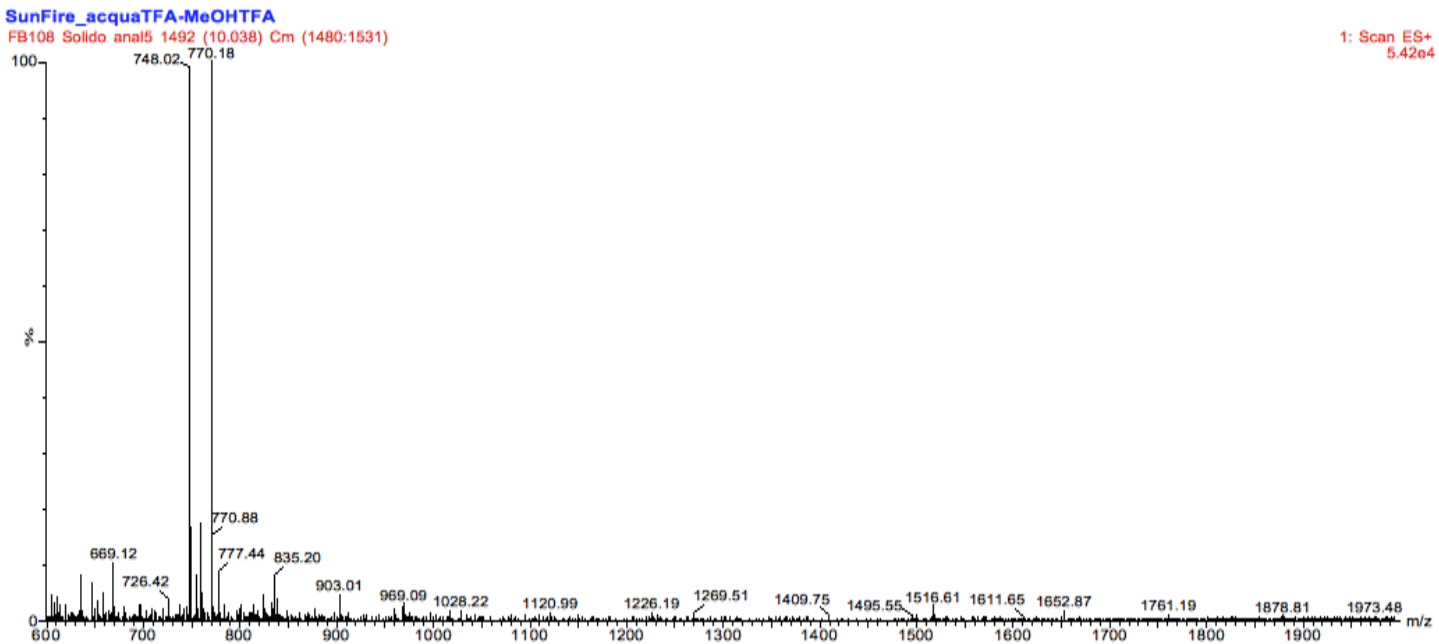

Figure S61. MS spectrum of compound **11** (from analytic analysis).

BIBLIOGRAPHY

1. Rosenthal, I.; Sostaric, J. Z.; Riesz, P., Sonodynamic therapy--a review of the synergistic effects of drugs and ultrasound. *Ultrason Sonochem* **2004,** *11* (6), 349-63.
2. Kuroki, M.; Hachimine, K.; Abe, H.; Shibaguchi, H.; Kuroki, M.; Maekawa, S.; Yanagisawa, J.; Kinugasa, T.; Tanaka, T.; Yamashita, Y., Sonodynamic therapy of cancer using novel sonosensitizers. *Anticancer Research* **2007,** *27* (6a), 3673-3677.
3. Jun, Y.; Ayumu, A.; Shin, Y.; Shin-ichiro, U., Efficient Generation of Cavitation Bubbles in Gel Phantom by Ultrasound Exposure with Negative-Followed by Positive-Peak-Pressure-Emphasized Waves. *Japanese Journal of Applied Physics* **2013,** *52* (7S), 07HF11.
4. Yumita, N.; Iwase, Y.; Nishi, K.; Komatsu, H.; Takeda, K.; Onodera, K.; Fukai, T.; Ikeda, T.; Umemura, S.; Okudaira, K.; Momose, Y., Involvement of reactive oxygen species in sonodynamically induced apoptosis using a novel porphyrin derivative. *Theranostics* **2012,** *2* (9), 880-8.
5. Li, Y.; Su, X.; Wang, X.; Leung, A. W.; Xu, C.; Wang, P.; Liu, Q., Cytotoxic Effect of Protoporphyrin IX to Human Leukemia U937 Cells under Ultrasonic Irradiation. *Cellular Physiology and Biochemistry* **2014,** *33* (4), 1186-1196.
6. Canaparo, R.; Varchi, G.; Ballestri, M.; Foglietta, F.; Sotgiu, G.; Guerrini, A.; Francovich, A.; Civera, P.; Frairia, R.; Serpe, L., Polymeric nanoparticles enhance the sonodynamic activity of meso-tetrakis (4-sulfonatophenyl) porphyrin in an in vitro neuroblastoma model. *International Journal of Nanomedicine* **2013,** *8*, 4247-4263.
7. Serpe, L.; Canaparo, R.; Berta, L.; Bargoni, A.; Zara, G. P.; Frairia, R., High Energy Shock Waves and 5-Aminolevulinic for Sonodynamic Therapy: Effects in a Syngeneic Model of Colon Cancer. *Technology in Cancer Research & Treatment* **2011,** *10* (1), 85-93.
8. Yano, T.; Hatogai, K.; Morimoto, H.; Yoda, Y.; Kaneko, K., Photodynamic therapy for esophageal cancer. *Ann Transl Med* **2014,** *2* (3), 29.
9. Brown, S. B.; Brown, E. A.; Walker, I., The present and future role of photodynamic therapy in cancer treatment. *Lancet Oncol* **2004,** *5* (8), 497-508.
10. G.Kuiper, Physics of cavitation: GAS CONTENT AND NUCLEI. In *Cavitation in Ship Propulsion*, 2010; pp 9-79.
11. Chen, H.; Zhou, X.; Gao, Y.; Zheng, B.; Tang, F.; Huang, J., Recent progress in development of new sonosensitizers for sonodynamic cancer therapy. *Drug Discovery Today* **2014,** *19* (4), 502-509.
12. Wan, G.-Y.; Liu, Y.; Chen, B.-W.; Liu, Y.-Y.; Wang, Y.-S.; Zhang, N., Recent advances of sonodynamic therapy in cancer treatment. *Cancer Biology & Medicine* **2016,** *13* (3), 325-338.
13. Shibaguchi, H.; Tsuru, H.; Kuroki, M.; Kuroki, M., Sonodynamic cancer therapy: a non-invasive and repeatable approach using low-intensity ultrasound with a sonosensitizer. *Anticancer Res* **2011,** *31* (7), 2425-9.

14. Dolmans, D. E. J. G. J.; Fukumura, D.; Jain, R. K., Photodynamic therapy for cancer. *Nat Rev Cancer* **2003,** *3* (5), 380-387.
15. Kinsella, T. J.; Colussi, V. C.; Oleinick, N. L.; Sibata, C. H., Photodynamic therapy in oncology. *Expert Opinion on Pharmacotherapy* **2001,** *2* (6), 917-927.
16. Yumita, N.; Nishigaki, R.; Umemura, K.; Umemura, S., Hematoporphyrin as a Sensitizer of Cell-Damaging Effect of Ultrasound. *Japanese Journal of Cancer Research* **1989,** *80* (3), 219-222.
17. Xu, H.; Zhang, X.; Han, R.; Yang, P.; Ma, H.; Song, Y.; Lu, Z.; Yin, W.; Wu, X.; Wang, H., Nanoparticles in sonodynamic therapy: state of the art review. *RSC Advances* **2016,** *6* (56), 50697-50705.
18. Castano, A. P.; Demidova, T. N.; Hamblin, M. R., Mechanisms in photodynamic therapy: part one—-photosensitizers, photochemistry and cellular localization. *Photodiagnosis and photodynamic therapy* **2004,** *1* (4), 279-293.
19. Boissenot, T.; Bordat, A.; Fattal, E.; Tsapis, N., Ultrasound-triggered drug delivery for cancer treatment using drug delivery systems: From theoretical considerations to practical applications. *J Control Release* **2016,** *241*, 144-163.
20. Qian, X.; Zheng, Y.; Chen, Y., Micro/Nanoparticle-Augmented Sonodynamic Therapy (SDT): Breaking the Depth Shallow of Photoactivation. *Advanced Materials* **2016,** *28* (37), 8097-8129.
21. Boissenot, T.; Bordat, A.; Fattal, E.; Tsapis, N., Ultrasound-triggered drug delivery for cancer treatment using drug delivery systems: From theoretical considerations to practical applications. *Journal of Controlled Release* **2016,** *241*, 144-163.
22. Yumita, N.; Okudaira, K.; Momose, Y.; Umemura, S.-i., Sonodynamically induced apoptosis and active oxygen generation by gallium–porphyrin complex, ATX-70. *Cancer Chemotherapy and Pharmacology* **2010,** *66* (6), 1071-1078.
23. Allison, R. R.; Downie, G. H.; Cuenca, R.; Hu, X.-H.; Childs, C. J. H.; Sibata, C. H., Photosensitizers in clinical PDT. *Photodiagnosis and Photodynamic Therapy* **2004,** *1* (1), 27-42.
24. Yano, T.; Hatogai, K.; Morimoto, H.; Yoda, Y.; Kaneko, K., Photodynamic therapy for esophageal cancer. *Annals of Translational Medicine* **2014,** *2* (3), 29.
25. Brown, S. B.; Brown, E. A.; Walker, I., The present and future role of photodynamic therapy in cancer treatment. *The Lancet Oncology* **2004,** *5* (8), 497-508.
26. Allison, R. R.; Downie, G. H.; Cuenca, R.; Hu, X. H.; Childs, C. J.; Sibata, C. H., Photosensitizers in clinical PDT. *Photodiagnosis Photodyn Ther* **2004,** *1* (1), 27-42.
27. Xiong, W.; Wang, P.; Hu, J.; Jia, Y.; Wu, L.; Chen, X.; Liu, Q.; Wang, X., A new sensitizer DVDMS combined with multiple focused ultrasound treatments: an effective antitumor strategy. *Sci Rep* **2015,** *5*, 17485.
28. Dougherty, T. J.; Gomer, C. J.; Henderson, B. W.; Jori, G.; Kessel, D.; Korbelik, M.; Moan, J.; Peng, Q., Photodynamic Therapy. *Journal of the National Cancer Institute* **1998,** *90* (12), 889-905.
29. Ma, L.; Moan, J.; Berg, K., Evaluation of a new photosensitizer, meso-tetra-hydroxyphenyl-chlorin, for use in photodynamic therapy: A comparison of its photobiological properties with those of two other photosensitizers. *International Journal of Cancer* **1994,** *57* (6), 883-888.

30. Boyle, R. W.; Dolphin, D., Structure and Biodistribution Relationships of Photodynamic Sensitizers*. *Photochemistry and Photobiology* **1996,** *64* (3), 469-485.
31. Peng, Q.; Berg, K.; Moan, J.; Kongshaug, M.; Nesland, J. M., 5-Aminolevulinic Acid-Based Photodynamic Therapy: Principles and Experimental Research. *Photochemistry and Photobiology* **1997,** *65* (2), 235-251.
32. Kennedy, J. C.; Pottier, R. H.; Pross, D. C., Photodynamic therapy with endogenous protoporphyrin. *Journal of Photochemistry and Photobiology B: Biology* **1990,** *6* (1), 143-148.
33. Yang, X.; Palasuberniam, P.; Kraus, D.; Chen, B., Aminolevulinic Acid-Based Tumor Detection and Therapy: Molecular Mechanisms and Strategies for Enhancement. *International Journal of Molecular Sciences* **2015,** *16* (10), 25865-25880.
34. Wolf, P.; Kerl, H., Photodynamic Therapy with 5-Aminolevulinic Acid - a Promising Concept for the Treatment of Cutaneous Tumors. *Dermatology* **1995,** *190* (3), 183-185.
35. Elfsson, B.; Wallin, I.; Eksborg, S.; Rudaeus, K.; Ros, A. M.; Ehrsson, H., Stability of 5-aminolevulinic acid in aqueous solution. *Eur J Pharm Sci* **1999,** *7* (2), 87-91.
36. Kloek, J.; Beijersbergen van Henegouwen, G. M. J., Prodrugs of 5-Aminolevullinic Acid for Photodynamic Therapy. *Photochemistry and Photobiology* **1996,** *64* (6), 994-1000.
37. Peng, Q.; Warloe, T.; Berg, K.; Moan, J.; Kongshaug, M.; Giercksky, K. E.; Nesland, J. M., 5-aminolevulinic acid-based photodynamic therapy - Clinical research and future challenges. *Cancer-Am Cancer Soc* **1997,** *79* (12), 2282-2308.
38. Peng, Q.; Moan, J.; Warloe, T.; Vladimir, I.; Steen, H. B.; Bjorseth, A.; Nesland, J. M., Build-up of esterified aminolevulinic-acid-derivative-induced porphyrin fluorescence in normal mouse skin. *J Photoch Photobio B* **1996,** *34* (1), 95-96.
39. Gerscher, S.; Connelly, J. P.; Griffiths, J.; Brown, S. B.; MacRobert, A. J.; Wong, G.; Rhodes, L. E., Comparison of the pharmacokinetics and phototoxicity of protoporphyrin IX metabolized from 5-aminolevulinic acid and two derivatives in human skin in vivo. *Photochemistry and Photobiology* **2000,** *72* (4), 569-574.
40. Kloek, J.; Akkermans, W.; van Henegouwen, G. M. J. B., Derivatives of 5-aminolevulinic acid for photodynamic therapy: Enzymatic conversion into protoporphyrin. *Photochemistry and Photobiology* **1998,** *67* (1), 150-154.
41. Gaullier, J. M.; Berg, K.; Peng, Q.; Anholt, H.; Selbo, P. K.; Ma, L. W.; Moan, J., Use of 5-aminolevulinic acid esters to improve photodynamic therapy on cells in culture. *Cancer Res* **1997,** *57* (8), 1481-1486.
42. Solban, N.; Rizvi, I.; Hasan, T., Targeted photodynamic therapy. *Lasers in Surgery and Medicine* **2006,** *38* (5), 522-531.
43. Li, P. X.; Mu, J. H.; Xiao, H. L.; Li, D. H., Antitumor effect of photodynamic therapy with a novel targeted photosensitizer on cervical carcinoma. *Oncol Rep* **2015,** *33* (1), 125-132.
44. Chen, B.; Pogue, B. W.; Hasan, T., Liposomal delivery of photosensitising agents. *Expert Opinion on Drug Delivery* **2005,** *2* (3), 477-487.
45. Lutsenko, S. V.; Feldman, N. B.; Finakova, G. V.; Posypanova, G. A.; Severin, S. E.; Skryabin, K. G.; Kirpichnikov, M. P.; Lukyanets, E. A.; Vorozhtsov, G. N.,

Targeting phthalocyanines to tumor cells using epidermal growth factor conjugates. *Tumor Biol* **1999,** *20* (4), 218-224.
46. Zhang, M.; Zhang, Z. H.; Blessington, D.; Li, H.; Busch, T. M.; Madrak, V.; Miles, J.; Chance, B.; Glickson, J. D.; Zheng, G., Pyropheophorbide 2-deoxyglucosamide: A new photosensitizer targeting glucose transporters. *Bioconjugate Chem* **2003,** *14* (4), 709-714.
47. Subramoney, S., Novel nanocarbons - Structure, properties, and potential applications. *Advanced Materials* **1998,** *10* (15), 1157-+.
48. Boehm, H. P., Clauss, A., Fischer, G.O., Hofmann, U., The adsorption behavior of very thin carbon films. *Journal of Inorganic and General Chemistry ZAAC* **1962,** *316* (3-4), 119-127.
49. Park, S.; Ruoff, R. S., Chemical methods for the production of graphenes. *Nat Nano* **2009,** *4* (4), 217-224.
50. Bhuyan, M. S. A.; Uddin, M. N.; Islam, M. M.; Bipasha, F. A.; Hossain, S. S., Synthesis of graphene. *International Nano Letters* **2016,** *6* (2), 65-83.
51. Moon, H. K.; Lee, S. H.; Choi, H. C., In Vivo Near-Infrared Mediated Tumor Destruction by Photothermal Effect of Carbon Nanotubes. *Acs Nano* **2009,** *3* (11), 3707-3713.
52. Avouris, P.; Chen, Z. H.; Perebeinos, V., Carbon-based electronics. *Nat Nanotechnol* **2007,** *2* (10), 605-615.
53. Ago, H.; Petritsch, K.; Shaffer, M. S. P.; Windle, A. H.; Friend, R. H., Composites of Carbon Nanotubes and Conjugated Polymers for Photovoltaic Devices. *Advanced Materials* **1999,** *11* (15), 1281-1285.
54. Umeyama, T.; Imahori, H., Carbon nanotube-modified electrodes for solar energy conversion. *Energ Environ Sci* **2008,** *1* (1), 120-133.
55. Kostarelos, K.; Lacerda, L.; Pastorin, G.; Wu, W.; Wieckowski, S.; Luangsivilay, J.; Godefroy, S.; Pantarotto, D.; Briand, J. P.; Muller, S.; Prato, M.; Bianco, A., Cellular uptake of functionalized carbon nanotubes is independent of functional group and cell type. *Nat Nanotechnol* **2007,** *2* (2), 108-113.
56. Bianco, A.; Kostarelos, K.; Prato, M., Making carbon nanotubes biocompatible and biodegradable. *Chem Commun* **2011,** *47* (37), 10182-10188.
57. Iijima, S., Helical microtubules of graphitic carbon. *Nature* **1991,** *354* (6348), 56-58.
58. Iijima, S.; Ichihashi, T., Single-shell carbon nanotubes of 1-nm diameter. *Nature* **1993,** *363* (6430), 603-605.
59. Guo, T.; Nikolaev, P.; Rinzler, A. G.; Tomanek, D.; Colbert, D. T.; Smalley, R. E., Self-Assembly of Tubular Fullerenes. *J Phys Chem-Us* **1995,** *99* (27), 10694-10697.
60. Journet, C.; Maser, W. K.; Bernier, P.; Loiseau, A.; delaChapelle, M. L.; Lefrant, S.; Deniard, P.; Lee, R.; Fischer, J. E., Large-scale production of single-walled carbon nanotubes by the electric-arc technique. *Nature* **1997,** *388* (6644), 756-758.
61. Endo, M.; Takeuchi, K.; Igarashi, S.; Kobori, K.; Shiraishi, M.; Kroto, H. W., The production and structure of pyrolytic carbon nanotubes (PCNTs). *Journal of Physics and Chemistry of Solids* **1993,** *54* (12), 1841-1848.
62. Nehoff, H.; Parayath, N. N.; Domanovitch, L.; Taurin, S.; Greish, K., Nanomedicine for drug targeting: strategies beyond the enhanced permeability and retention effect. *International Journal of Nanomedicine* **2014,** *9*, 2539-2555.

63. Sawant, R. R.; Torchilin, V. P., Challenges in Development of Targeted Liposomal Therapeutics. *The AAPS Journal* **2012,** *14* (2), 303-315.
64. Sercombe, L.; Veerati, T.; Moheimani, F.; Wu, S. Y.; Sood, A. K.; Hua, S., Advances and Challenges of Liposome Assisted Drug Delivery. *Frontiers in Pharmacology* **2015,** *6*, 286.
65. Meunier, F.; Prentice, H. G.; Ringdén, O., Liposomal amphotericin B (AmBisome): safety data from a phase II/III clinical trial. *Journal of Antimicrobial Chemotherapy* **1991,** *28* (suppl_B), 83-91.
66. Andrea, M., U.S. Food and Drug Administration Approval of AmBisome (Liposomal Amphotericin B) for Treatment of Visceral Leishmaniasis. *Clinical Infectious Diseases* **1999,** *28* (1), 42-48.
67. Juster-Reicher, A.; Leibovitz, E.; Linder, N.; Amitay, M.; Flidel-Rimon, O.; Even-Tov, S.; Mogilner, B.; Barzilai, A., Liposomal Amphotericin B (AmBisome) in the Treatment of Neonatal Candidiasis in Very Low Birth Weight Infants. *Infection* **2000,** *28* (4), 223-226.
68. Mukherjee, S.; Ray, S.; Thakur, R. S., Solid Lipid Nanoparticles: A Modern Formulation Approach in Drug Delivery System. *Indian Journal of Pharmaceutical Sciences* **2009,** *71* (4), 349-358.
69. Müller, R. H.; Mäder, K.; Gohla, S., Solid lipid nanoparticles (SLN) for controlled drug delivery – a review of the state of the art. *European Journal of Pharmaceutics and Biopharmaceutics* **2000,** *50* (1), 161-177.
70. Blasi, P.; Giovagnoli, S.; Schoubben, A.; Ricci, M.; Rossi, C., Solid lipid nanoparticles for targeted brain drug delivery. *Adv Drug Deliver Rev* **2007,** *59* (6), 454-477.
71. Cacciatore, I.; Ciulla, M.; Fornasari, E.; Marinelli, L.; Di Stefano, A., Solid lipid nanoparticles as a drug delivery system for the treatment of neurodegenerative diseases. *Expert Opinion on Drug Delivery* **2016,** *13* (8), 1121-1131.
72. Pattni, B. S.; Chupin, V. V.; Torchilin, V. P., New Developments in Liposomal Drug Delivery. *Chemical Reviews* **2015,** *115* (19), 10938-10966.
73. Allen, T. M.; Cullis, P. R., Liposomal drug delivery systems: from concept to clinical applications. *Adv Drug Deliv Rev* **2013,** *65* (1), 36-48.
74. Anderson, C. R.; Hu, X.; Tlaxca, J.; Decleves, A.-E.; Houghtaling, R.; Sharma, K.; Lawrence, M.; Ferrara, K.; Rychak, J. J., Ultrasound Molecular Imaging of Tumor Angiogenesis with an Integrin Targeted Microbubble Contrast Agent. *Investigative radiology* **2011,** *46* (4), 215-224.
75. Ferrara, K.; Pollard, R.; Borden, M., Ultrasound microbubble contrast agents: fundamentals and application to gene and drug delivery. *Annu Rev Biomed Eng* **2007,** *9*, 415-47.
76. Klibanov, A. L., Microbubble contrast agents: targeted ultrasound imaging and ultrasound-assisted drug-delivery applications. *Invest Radiol* **2006,** *41* (3), 354-62.
77. Blomley, M. J.; Cooke, J. C.; Unger, E. C.; Monaghan, M. J.; Cosgrove, D. O., Microbubble contrast agents: a new era in ultrasound. *BMJ* **2001,** *322* (7296), 1222-5.
78. Tsutsui, J. M.; Xie, F.; Porter, R. T., The use of microbubbles to target drug delivery. *Cardiovascular Ultrasound* **2004,** *2*, 23-23.

79. Wang, Y.; Li, X.; Zhou, Y.; Huang, P.; Xu, Y., Preparation of nanobubbles for ultrasound imaging and intracelluar drug delivery. *International Journal of Pharmaceutics* **2010,** *384* (1–2), 148-153.
80. Martins, S.; Sarmento, B.; Ferreira, D. C.; Souto, E. B., Lipid-based colloidal carriers for peptide and protein delivery - liposomes versus lipid nanoparticles. *International Journal of Nanomedicine* **2007,** *2* (4), 595-607.
81. Thukral, D. K.; Dumoga, S.; Mishra, A. K., Solid Lipid Nanoparticles: Promising Therapeutic Nanocarriers for Drug Delivery. *Curr Drug Deliv* **2014,** *11* (6), 771-791.
82. Uner, M.; Yener, G., Importance of solid lipid nanoparticles (SLN) in various administration routes and future perspectives. *International Journal of Nanomedicine* **2007,** *2* (3), 289-300.
83. Wissing, S. A.; Kayser, O.; Muller, R. H., Solid lipid nanoparticles for parenteral drug delivery. *Adv Drug Deliver Rev* **2004,** *56* (9), 1257-1272.
84. Ruckmani, K.; Sivakumar, M.; Ganeshkumar, P. A., Methotrexate loaded solid lipid nanoparticles (SLN) for effective treatment of carcinoma. *J Nanosci Nanotechno* **2006,** *6* (9-10), 2991-2995.
85. Wong, H. L.; Bendayan, R.; Rauth, A. M.; Li, Y. Q.; Wu, X. Y., Chemotherapy with anticancer drugs encapsulated in solid lipid nanoparticles. *Adv Drug Deliver Rev* **2007,** *59* (6), 491-504.
86. Adler, A. D.; Longo, F. R.; Finarelli, J. D.; Goldmacher, J.; Assour, J.; Korsakoff, L., A simplified synthesis for meso-tetraphenylporphine. *The Journal of Organic Chemistry* **1967,** *32* (2), 476-476.
87. Lindsey, J. S.; Schreiman, I. C.; Hsu, H. C.; Kearney, P. C.; Marguerettaz, A. M., Rothemund and Adler-Longo reactions revisited: synthesis of tetraphenylporphyrins under equilibrium conditions. *The Journal of Organic Chemistry* **1987,** *52* (5), 827-836.
88. Lindsey, J. S.; Hsu, H. C.; Schreiman, I. C., Synthesis of tetraphenylporphyrins under very mild conditions. *Tetrahedron Letters* **1986,** *27* (41), 4969-4970.
89. Dolphin, D., Porphyrinogens and porphodimethenes, intermediates in the synthesis of meso-tetraphenylporphins from pyrroles and benzaldehyde. *Journal of Heterocyclic Chemistry* **1970,** *7* (2), 275-283.
90. Arsenault, G. P.; Bullock, E.; MacDonald, S. F., Pyrromethanes and Porphyrins Therefrom1. *Journal of the American Chemical Society* **1960,** *82* (16), 4384-4389.
91. Rothemund, P., Porphyrin Studies. III.1 The Structure of the Porphine2 Ring System. *Journal of the American Chemical Society* **1939,** *61* (10), 2912-2915.
92. Vicente, M. d. G. H.; Smith, K. M., Syntheses and Functionalizations of Porphyrin Macrocycles. *Current organic synthesis* **2014,** *11* (1), 3-28.
93. Bonar-Law, R. P., Porphyrin Synthesis in Surfactant Solution: Multicomponent Assembly in Micelles. *J Org Chem* **1996,** *61* (11), 3623-3634.
94. Gonsalves, A. M. d. A. R.; Varejão, J. M. T. B.; Pereira, M. M., Some new aspects related to the synthesis of meso-substituted porphyrins. *Journal of Heterocyclic Chemistry* **1991,** *28* (3), 635-640.
95. Vieira Ferreira, L. F.; Ferreira, D. P.; Oliveira, A. S.; Boscencu, R.; Socoteanu, R.; Ilie, M.; Constantin, C.; Neagu, M., Synthesis, photophysical and cytotoxicity

evaluation of A3B type mesoporphyrinic compounds. *Dyes and Pigments* **2012,** *95* (2), 296-303.
96. Ball, R. H.; Dorough, G. D.; Calvin, M., A Further Study of the Porphine-like Products of the Reaction of Benzaldehyde and Pyrrole. *Journal of the American Chemical Society* **1946,** *68* (11), 2278-2281.
97. Treibs, A.; Haberle, N., [Concerning the synthesis and the electron spectrum of ms-substituted porphine]. *Justus Liebigs Ann Chem* **1968,** *718*, 183-207.
98. Gupta, I.; Ravikanth, M., Synthesis of meso-furyl porphyrins with N4, N3S, N2S2 and N3O porphyrin cores. *Tetrahedron* **2003,** *59* (32), 6131-6139.
99. Bosca, F.; Tagliapietra, S.; Garino, C.; Cravotto, G.; Barge, A., Extensive methodology screening of meso-tetrakys-(furan-2-yl)-porphyrin microwave-assisted synthesis. *New J Chem* **2016,** *40* (3), 2574-2581.
100. Henriques, C. A.; Pinto, S. M.; Aquino, G. L.; Pineiro, M.; Calvete, M. J.; Pereira, M. M., Ecofriendly porphyrin synthesis by using water under microwave irradiation. *ChemSusChem* **2014,** *7* (10), 2821-4.
101. de Sousa Healy, M.; Rest, A. J., Role of metal salts in the synthesis of 1,1,7,7,13,13,19,19-octamethyl-[1.1.1.1](2,5)furanophan. *Journal of the Chemical Society, Chemical Communications* **1981,** (4), 149-150.
102. Wei, L.; Wang, B.; Wang, Q.; Li, L.-J.; Yang, Y.; Chen, Y., Effect of Centrifugation on the Purity of Single-Walled Carbon Nanotubes from MCM-41 Containing Cobalt. *The Journal of Physical Chemistry C* **2008,** *112* (45), 17567-17575.
103. Turci, F.; Corazzari, I.; Alberto, G.; Martra, G.; Fubini, B., Free-Radical Chemistry as a Means to Evaluate Lunar Dust Health Hazard in View of Future Missions to the Moon. *Astrobiology* **2015,** *15* (5), 371-380.
104. Mason, T. J.; Lorimer, J. P.; Bates, D. M.; Zhao, Y., Dosimetry in sonochemistry: the use of aqueous terephthalate ion as a fluorescence monitor. *Ultrason Sonochem* **1994,** *1* (2), S91-S95.
105. Derycke, A. S. L.; de Witte, P. A. M., Liposomes for photodynamic therapy. *Adv Drug Deliver Rev* **2004,** *56* (1), 17-30.
106. Perera, R. H.; Wu, H.; Peiris, P.; Hernandez, C.; Burke, A.; Zhang, H.; Exner, A. A., Improving performance of nanoscale ultrasound contrast agents using N,N-diethylacrylamide stabilization. *Nanomedicine* **2017,** *13* (1), 59-67.
107. Krupka, T. M.; Solorio, L.; Wilson, R. E.; Wu, H.; Azar, N.; Exner, A. A., Formulation and Characterization of Echogenic Lipid–Pluronic Nanobubbles. *Molecular Pharmaceutics* **2010,** *7* (1), 49-59.
108. Wu, H.; Rognin, N. G.; Krupka, T. M.; Solorio, L.; Yoshiara, H.; Guenette, G.; Sanders, C.; Kamiyama, N.; Exner, A. A., Acoustic Characterization and Pharmacokinetic Analyses of New Nanobubble Ultrasound Contrast Agents. *Ultrasound in Medicine & Biology* **2013,** *39* (11), 2137-2146.
109. Qian, X.; Zheng, Y.; Chen, Y., Micro/Nanoparticle-Augmented Sonodynamic Therapy (SDT): Breaking the Depth Shallow of Photoactivation. *Adv Mater* **2016,** *28* (37), 8097-8129.
110. Wan, G. Y.; Liu, Y.; Chen, B. W.; Liu, Y. Y.; Wang, Y. S.; Zhang, N., Recent advances of sonodynamic therapy in cancer treatment. *Cancer Biol Med* **2016,** *13* (3), 325-338.

111. Wang, H.; Wang, P.; Li, L.; Zhang, K.; Wang, X.; Liu, Q., Microbubbles Enhance the Antitumor Effects of Sinoporphyrin Sodium Mediated Sonodynamic Therapy both In Vitro and In Vivo. *Int J Biol Sci* **2015,** *11* (12), 1401-9.
112. Gao, J.; Wang, Z.; Wang, J.; Jin, X.; Guo, Y.; Li, K.; Li, Y.; Kang, P., Review article. *Spectrochimica Acta Part A: Molecular and Biomolecular Spectroscopy* **2011,** *79* (5), 849-857.
113. Gao, J. Q.; Wang, Z. Q.; Wang, J.; Jin, X. D.; Guo, Y. W.; Li, K.; Li, Y.; Kang, P. L., Spectroscopic studies on interaction and sonodynamic damage of metallochlorophyllin (Chl-M (M = Fe, Zn and Cu)) to protein under ultrasonic irradiation. *Spectrochim Acta A* **2011,** *79* (5), 849-857.
114. Ebermann, R.; Alth, G.; Kreitner, M.; Kubin, A., Natural products derived from plants as potential drugs for the photodynamic destruction of tumor cells. *J Photoch Photobio B* **1996,** *36* (2), 95-97.
115. Keren, N.; Gong, H. S.; Ohad, I., Oscillations of Reaction-Center-Ii D1-Protein-Degradation in-Vivo Induced by Repetitive Light-Flashes - Correlation between the Level of Rcii-Q(B)(-), and Protein-Degradation in Low-Light. *J Biol Chem* **1995,** *270* (2), 806-814.
116. Wang, J.; Guo, Y. W.; Gao, J. Q.; Jin, X. D.; Wang, Z. Q.; Wang, B. X.; Li, K.; Li, Y., Detection and comparison of reactive oxygen species (ROS) generated by chlorophyllin metal (Fe, Mg and Cu) complexes under ultrasonic and visible-light irradiation. *Ultrason Sonochem* **2011,** *18* (5), 1028-1034.
117. Makadia, H. K.; Siegel, S. J., Poly Lactic-co-Glycolic Acid (PLGA) as Biodegradable Controlled Drug Delivery Carrier. *Polymers* **2011,** *3* (3), 1377-1397.
118. Fessi, H.; Puisieux, F.; Devissaguet, J. P.; Ammoury, N.; Benita, S., Nanocapsule formation by interfacial polymer deposition following solvent displacement. *International Journal of Pharmaceutics* **1989,** *55* (1), R1-R4.